A multi-disciplinary approach: How aqueous minerals hold the key to understanding the climate and habitability of terrestrial planets

Thesis by

Eva L. Scheller

In Partial Fulfillment of the Requirements for
the Degree of
Doctor of Philosophy

Caltech

CALIFORNIA INSTUTE OF TECHNOLOGY
Pasadena, California

2022
Defended February 24, 2022

Eva L. Scheller
ORCID: 0000-0002-9981-5802

ACKNOWLEDGEMENTS

First, I would like to acknowledge my three advisers that made this thesis possible. Bethany – thank you for your scientific and leadership advice throughout the years guiding me through learning how to write papers, proposals, presentations. It has helped me accomplish more than I ever dreamt of. Thanks for giving me the opportunity to pursue my intellectual curiosities and to work on extraordinary projects and join the Perseverance rover team. It is clear that you go out of your way for your students, and I will always appreciate and remember that. John G. – thank you for taking me under your wings as an Earthling-Martian hybrid like yourself and introducing me to new aspects of science that paralleled my main research program. Thanks for your patience in advising me through critical periods of my life from science to COVID lockdown to learning more about diversity, equity, and inclusion in America. John Eiler – thank you for your incredible patience in teaching the fundamentals of clumped isotopes to someone that unexpectedly got dumped into the field. Your guidance made it possible for me to enter a new field. Even though it was difficult I would not trade that for anything. Now to my committee members. Ed – I will never forget that you were the first to ever give me the opportunity to pursue research in America. Coming from such a tiny country and humble beginnings, I was so grateful for the opportunity to finally prove myself, and I will always remember that. Thanks for your advices over the years. George – thank you for always being a shoulder to lean on scientifically and for navigating the program in times when things were hard and seemed insurmountable. You're an incredibly caring mentor that goes out of your way for students. In summary, each part of my committee has played an integral role in my PhD, and I'm thankful to have had their guidance throughout these four and a half years. I extend also, of course, my thanks to my undergraduate advisors and mentors who got me here in the first place – Tod Waight, Kjartan Kinch, Minik Rosing, but especially Tais Dahl. Thank you for your mentorship over the years and providing the stepping stones that led me to this PhD.

In addition, I have had many non-faculty mentors over the years that were integral in mentoring me. Chapters 4 & 5 of this thesis would not have been possible without Miquela Ingall's continuous support and mentorship of me as well as Nami Kitchen's, Uri Ryb's, and Hao Xie's support and intellectual guidance. Chapter 2 would not have been possible without Jay Dickson's continuous support in teaching how to get my computer to do the thing it was supposed to do. I thank Rebecca Greenberger for her amazing job as a lab manager, field trip organizer, stand-in advisor, and scientific sparring partner. I want to thank also my collaborators Renyu Hu, Yuk Yung, and in particular Danica Adams for assisting my research for Chapter 7 and for their team-work. Much of my PhD has also been shaped through my interactions with incredible mentors and collaborators on the Perseverance team. In particular, I thank Katie Stack for her many aspects of support over the years and always looking out for me, which I am truly grateful for. Chapter 6 of this thesis would not have been possible without the amazing SHERLOC team and Joby Razzell Hollis', Pan Conrad's, but in particular Andrew Steele's incredible mentorship and continuous support of me. I thank in particular Luther Beegle, Rohit Bhartia, and the rest of the SHERLOC team for always welcoming me and supporting me. Last, I want to thank the entire Mastcam-Z team for their team work during my time working with the Perseverance rover.

I want to thank the Caltech international student office and international student council for always doing their best to make international students feel at home in America, to help us navigate a new culture, society, and complex ever-changing visa rules during the COVID lockdown. I thank Ulrika Terrones, Loreta Young, Jen Shechet, Julie Lee, Mark Garcia for their support in so many different ways over the years. Special thanks go to Janice Grancich for the many lab equipment purchases, reimbursements, but most of all always anticipating when students are going to botch a car on a field trip!

The time during my PhD was definitely made better by the amazing group members that have supported, mentored, and assisted me throughout the years, including Daven Quinn, Ted Present, Kelsey Moore,

ABSTRACT

Understanding the interplay between geological processes and the climate within the ancient pasts of terrestrial planets holds the key to deciphering what makes terrestrial planets habitable. The climates of both Mars and Earth were drastically different in their ancient pasts. Liquid water once flowed on Mars ~3-4 Ga, creating fluvial valleys and aqueous minerals, until Mars dried out to the desert planet we know today. During the Pleistocene (~ 2.6 Ma – 11.7 ka) and Neoproterozoic (640-710 Ma), Earth experienced widespread glaciations and even a global glaciated state, respectively. Aqueous minerals, such as clays and carbonates, record the history of their aqueous environments and can be used to track these dramatic changes in climate and environment. In Chapter 2, I use hyperspectral infrared imagery and high-resolution images retrieved by the Mars Reconnaissance Orbiter to characterize the lithology of some of the oldest Noachian ~3.8-4.1 Ga crust exposed on Mars. I document eight geological units and features that will be studied with the Perseverance rover and record the presence of pyroxene-bearing igneous crustal materials, aqueous environments that led to widespread clay formation, and basin-forming impact processes that brecciated the crust. Associated younger Noachian-aged magnesium carbonate-bearing geological units will also be studied and sampled with the Perseverance rover. In Chapter 3, I review magnesium carbonate formation on Earth and Mars and find that textures of nodules, crusts, veins, sparry crystals, and thrombolites/stromatolites, their associated host lithologies and related secondary mineralogy can be used to distinguish between formation within weathering, lacustrine, hydrothermal, diagenetic, or microbially influenced aqueous environments, respectively, with rover analyses. Laboratory analysis of stable and radiogenic isotopes of returned samples will allow us to analyze the surface temperature and atmospheric isotopic composition of ancient Mars. In Chapter 4, I characterize the paragenesis of hydrated carbonates. In frigid environments, carbonates form in hydrated species known as monohydrocalcite (MHC) and ikaite that transform to calcite upon heating. Through petrographic analysis of Pleistocene ikaite pseudomorphs and a review of more ancient examples, I define a new carbonate microtexture, *guttulatic calcite*, which is diagnostic for carbonate dehydration and can be used to document frigid temperature conditions. In Chapter 5, I characterize the stable carbon, oxygen ($\delta^{18}O_{CARB}$), and clumped (Δ_{47}) isotope systematics of hydrated carbonates. Through heating experiments of modern MHC, I measure and model change in $\delta^{18}O_{CARB}$ and Δ_{47} signatures facilitated by equilibrium exchange as MHC is dehydrated. Using the determined correction for dehydration overprint allows reconstruction of precursor ikaite formation temperatures and isotopic signatures. The textural and isotopic proxies can now be used for reconstructing temperatures and isotopic signatures within Pleistocene and Neoproterozoic sedimentary deposits. In Chapter 6, I use the Perseverance rover's SHERLOC instrument's deep-UV Raman and fluorescence spectroscopy to discover evidence for two potentially habitable ancient aqueous environments that contain aromatic organic compounds. Spectral and textural observations of the olivine-carbonate assemblage within Jezero crater, Mars reveal carbonation of ultramafic protolith. A separate, later brine formed sulfate-perchlorate mixtures in void spaces. Fluorescence signatures consistent with multiple types of aromatic organic compounds occur throughout these samples, preserved in minerals related to both aqueous processes. These organic-mineral associations indicate that aqueous alteration processes led to the preservation and possibly formation of organic compounds on Mars. In Chapter 7, I model the global water budget and hydrogen isotopic composition (D/H) of Mars, using measured constraints from geomorphology, atmospheric escape rates, volcanic degassing processes, crust volatile content, and D/H. In my simulations, I find that chemical weathering sequestered a 0.1-1 km global equivalent layer of water, decreasing the volume of water participating in the hydrological cycle by 40 to 95% over the Noachian (~3.7-4 Ga) period, reaching present-day values by ~3 Ga. Between 30 and 99% of Martian water was sequestered through crustal hydration, demonstrating that irreversible chemical weathering can increase the aridity of terrestrial planets. In summary, this PhD thesis demonstrates that the formation of aqueous minerals is a major control on terrestrial planet climates and that aqueous minerals can be used to track the conditions of their formation environments.

PUBLISHED CONTENT AND CONTRIBUTIONS

<u>Chapter 2 is published as:</u> Scheller, E. L., & Ehlmann, B. L. (2020). Composition, stratigraphy, and geological history of the Noachian Basement surrounding the Isidis impact basin. *Journal of Geophysical Research: Planets*, *125*, e2019JE006190. DOI: 10.1029/2019JE006190.

> E. L. Scheller and B. L. Ehlmann conceived the study. E. L. Scheller performed all data analysis and wrote the manuscript with help from B. L. Ehlmann.

<u>Chapter 3 is published as:</u> Scheller, E. L. et al., (2021). Formation of magnesium carbonates on Earth and implications for Mars. *Journal of Geophysical Research: Planets*, *126*(7), e2021JE006828. DOI: /10.1029/2021JE006828.

> All authors conceived the study, performed analysis, and wrote the manuscript with leadership by E. L. Scheller, who was supported by J. Grotzinger.

<u>Chapter 4 is published as:</u> Scheller, E. L., Grotzinger, J., & Ingalls, M. (2021). Guttulatic calcite: A carbonate microtexture that reveals frigid formation conditions. *Geology*. DOI: 10.1130/G49312.1.

> E. L. Scheller and J. Grotzinger conceived the study. E. L. Scheller performed all data analysis and wrote the manuscript with help from all authors.

<u>Chapter 5 is submitted as:</u> Scheller, E. L., Ingalls, M., Eiler, J., Grotzinger, J. & Ryb, U. The mechanisms and stable-isotope effects of transforming hydrated carbonate into calcite. *Geochimica et Cosmochimica Acta.*

> All authors conceived the study. E. L. Scheller performed all experiments and wrote the manuscript with help from all authors.

<u>Chapter 6 is in review as:</u> Scheller, E. L. & Razzell Hollis, J. et al., Aqueous alteration processes and implications for organic geochemistry in Jezero crater, Mars. *Science*.

> E. L. Scheller, J. Razzell Hollis, A. Steele, E. Cardarelli, L. Beegle, and R. Bhartia conceived the study together. E. L. Scheller and J. Razzell Hollis contributed equally to data analysis and writing the manuscript with major contributions from A. Steele and E. Cardarelli and organizational leadership of E. L. Scheller. The SHERLOC instrument was originally proposed by L. Beegle and R. Bhartia. All authors contributed to writing and/or editing the manuscript.

<u>Chapter 7 is published as:</u> Scheller, E. L., Ehlmann, B. L., Hu, R., Adams, D. J., & Yung, Y. L. (2021). Long-term drying of Mars by sequestration of ocean-scale volumes of water in the crust. *Science*, *372*, 56-62. DOI: 10.1126/science.abc7717.

> E. L. Scheller, B. L. Ehlmann, and R. Hu conceived the study. E. L. Scheller performed the main modelling work with contributions from D. J. Adams and Y. L. Yung. E. L. Scheller wrote the manuscript with help from all authors.

TABLE OF CONTENTS

TABLE OF CONTENTS (CONT.)

TABLE OF CONTENTS (CONT.)

TABLE OF CONTENTS (CONT.)

TABLE OF CONTENTS (CONT.)

LIST OF ILLUSTRATIONS

LIST OF ILLUSTRATIONS (CONT.)

LIST OF ILLUSTRATIONS (CONT.)

LIST OF TABLES

LIST OF ACRONYMS

ACI   Autofocus Context Imager

ALH84001   Allan Hills 84001 (Mars meteorite name)

BSE   Backscattered Electron Imaging

CCD   Charge-coupled Device

CDES   Carbon Dioxide Equilibrium Scale (a reference frame for clumped isotope measurements)

CPX   Clinopyroxene (pyroxene mineral with monoclinic crystal structure)

CRISM   Compact Reconnaissance Imaging Spectrometer for Mars

DEM   Digital Elevation Model

D/H   Deuterium-to-hydrogen isotope ratio

DIC   Dissolved Inorganic Carbon

DUV   Deep ultraviolet

EDS   Energy Dispersive X-ray Spectroscopy

ENVI   Environment for Visualizing Images (a spectral image processing software)

Fm   Formation

GEL   Global Equivalent Layer

GIS   Geographic Information System (a geospatial image processing software)

HCP   High-Ca pyroxene (pyroxene mineral with a particular infrared spectral characteristic)

HDR   High-dynamic Range (a specific measurement mode of the SHERLOC instrument)

HG   Heated gasses

HiRISE   High Resolution Imaging Science Experiment

KINETICS   A 1D photochemical model developed by the Yung group at Caltech

LCP   Low-Ca pyroxene (pyroxene mineral with a particular infrared spectral characteristic)

LIBS   Laser-induced Break-down Spectroscopy

Linkham THMS600   A cryogenic stage for the Rossmann lab Raman spectrometer

M2020   Mars 2020 mission, now known as Perseverance rover mission

MAVEN   Mars Atmosphere and Volatile EvoluioN spacecraft

MHC   Monohydrocalcite

MOLA   Mars Orbiter Laser Altimeter

MSL   Mars Science Laboratory (also known as Curiosity rover mission)

MSR   Mars Sample Return

NWA 7034   Northwest Africa 7034 (Mars meteorite name)

OPX   Orthopyroxene (pyroxene mineral with orthorhombic crystal structure)

OSGEARTH   Open Scene Graph Earth (a 3D mapping Engine for geospatial data)

PANalytical X'Pert Pro   The Caltech XRD instrument

PDS   Planetary Data System

Reinshaw inVia Oontor   The Rossmann lab Raman spectrometer

PIXL   Planetary Instrument for X-ray Lithochemistry

REE   Rare Earth Element

ROI   Region of Interest

PXRD   Powder X-ray Diffraction

SAM   Sample Analysis at Mars

SEM   Scanning Electron Microscopy

SHERLOC   The Scanning Habitable Environments with Raman & Luminescence for Organics & Chemicals

SMOW   Standard Mean Ocean Water

SNR   Signal-to-noise ratio

SOCET SET   Geospatial intelligence software for 3D visualization

SOL   One full Mars day

SPICAM   Ultraviolet and Infrared Atmospheric Spectrometer

SuperCam   A laser spectrometer and infrared spectrometer on the Perseverance rover

THEMIS   Thermal Emission Imaging System

ThermoScientific MAT253   Mass spectrometer for isotope ratio analyses

TLS   Tunable Laser Spectrometer

UV   Ultraviolet

VPDB   Vienna Pee Dee Belemnite

WATSON   Wide-Angle Topographic Sensor for Operations and eNgineering

XRD   X-ray Diffraction

Chapter 1

INTRODUCTION

The overall goal of this thesis is to understand how geological processes that result in aqueous mineral formation affected the evolution in climate and habitability of Earth and Mars, and how these same minerals can be used as archives of these climatic changes. This thesis addresses a sub-category of more specific questions, including: (1) How did Mars' ancient ~ 4 Ga crust form, what is its composition, and how can it be studied with the Perseverance rover? (2) How did Martian carbonates form, and how can they be studied with the Perseverance rover and laboratory analysis upon sample return to Earth? (3) How can we recognize carbonate diagenesis in the sedimentary record, and how do we correct for diagenetic overprints in the isotopic composition of carbonates from both Earth and Mars? (4) What were past aqueous environments on Mars like and were they potentially habitable? (5) How did aqueous mineral formation early in Mars' geological history affect the planet's climate and habitability potential, and can this explain why Mars differs from Earth?

1.1 Mars' geological history

Through accumulation of planetary datasets spanning telescopic, orbital satellite, landing probe experiments, in-situ rover analysis, and meteoritic laboratory techniques, it has become evident that the ancient Martian surface had liquid that formed rivers, lakes, and aqueous minerals (such as clays, carbonates, and sulfates) (Bibring et al,. 2007; Grotzinger et al, 2014; Ehlmann and Edwards, 2014). Many of the ancient aqueous environments investigated with orbital satellites and rovers even reveal environments with habitable conditions for putative Martian biota (Fairen et al., 2010; Grotzinger et al., 2014; Farley et al., 2020). Hence, ancient Mars may have had a comparable surface environment to that of the Earth's. However, current Mars presents as an arid, inhospitable planetary surface with its H_2O primarily locked up as ice deposits (e.g. Christensen, 2006). The early Martian time period in which vast regions of clay formation and ancient fluvial systems occurred is referred to as the Noachian period (> ~3.7 Ga) (Ehlmann et al., 2011; Carr and Head, 2010; Tanaka et al., 2014; Ehlmann et al., 2016). The past 3 Ga years are referred to as the Amazonian period and present little geomorphological and mineralogical evidence for the presence of liquid water (Carr and Head, 2010; Fassett et al., 2014; Tanaka et al., 2014). During the middle transitional period, the Hesperian (~ 3-3.7 Ga), Mars did have active outflow channels, lake environments, even possible oceans, and formed aqueous minerals in a more limited extend compared to the Noachian (Carr and Head, 2003; Ehlmann et al., 2011; Grotzinger et al., 2014; Ehlmann

et al., 2016; Turbet et al., 2017). Because of these orbital and rover observations, it is thought that the Martian climate changed over time. A warmer and wetter Mars, either sustained or episodic, has been proposed for the Noachian periods, whereas the Hesperian has been proposed to represent the transition towards a colder and more arid climate (Wordsworth et al., 2016). The reasons for these climatic transitions are still obscure and have generated multiple hypotheses, including but not limited to geological H_2 production on early Mars causing collision-induced absorption heating (Ramirez et al., 2014; Tosca et al., 2014; Wordsworth et al., 2021), production of other greenhouse gasses on early Mars (Pollack et al., 1987; Yung et al., 1997; Wordsworth et al., 2017), and/or gradual loss of the Martian atmosphere through either atmospheric loss or sequestration in carbonate deposits (Hu et al., 2015; Heard and Kite, 2020).

The questions then become: What were the processes that controlled this divergence of the Martian surface environment, climate, and its potential habitability in comparison to Earth? And could life have arisen on ancient Mars and be preserved today? The aqueous mineralogy on Mars holds part of the answers to these questions. H_2O- and OH-bearing minerals have been proposed to have sequestered Martian water (Mustard et al., 2019; Scheller et al., 2021), while carbonate minerals have been proposed to have sequestered the Martian atmospheric CO_2 (Hu et al., 2015; Heard and Kite, 2020). Such geological processes are common on Earth; however, the presence of tectonics makes the crustal sequestration of these important volatiles a cyclical phenomenon, whereas this was not the case on Mars (e.g. Korenaga, 2012; Lammer et al,. 2013). Thesis Chapters 2, 3, 6, and 7 address both how the formation of these minerals could have affected Martian climate and habitability, but also how current and future studies of these materials with the Perseverance rover may further elucidate these processes.

1.2 Jezero Crater: Preparing for current and future investigations

Jezero crater, a 49 km diameter impact crater, is the landing site of the Perseverance rover, which landed on Mars in February 2021 (Farley et al., 2020). Jezero crater is situated within the intersection of the Isidis Planitia, Nili Fossae, and North East Syrtis regions within the rim of the Isidis impact basin (Farley et al., 2020; Scheller et al., 2021). The primary mission of the Perseverance rover will occur inside of the crater, while the extended mission of the rover will occur within the Nili Planum area of NE Syrtis outside of the crater (Farley et al., 2020). Jezero crater was selected as the Perseverance rover landing site due to the fact that it contains geomorphological evidence for a paleolake basin and includes remnants of a delta fan (Goudge et al., 2015; Farley et al., 2020). Fine-grained clay mineral-bearing layered deposits within delta deposits on Earth are conducive to preserve biosignatures and are prime target on Mars for rover analysis and sampling for return to Earth (Ehlmann et al., 2008; Farley et al., 2020; Mangold et al., 2021).

Aside from the delta deposits, however, the Jezero crater and its watershed within the NE

Syrtis/Nili Fossae regions preserve an elaborate stratigraphy and geological units that are uniquely preserved on Mars. Surrounding regions that form the watershed and are cross-cut by younger fluvial system that fed the Jezero paleolake, include geological units referred to as the Noachian Basement Group, the regional Olivine-carbonate unit, and the Mafic Capping Unit (Ehlmann and Mustard, 2012; Goudge et al., 2015; Bramble et al., 2017; Scheller et al., 2021). The Noachian Basement Group is the subject of Chapter 2, and orbital spectroscopy reveals a piece of ancient (>4-3.8 Ga) crust with igneous and aqueous alteration mineralogy that was heavily deformed by the Isidis impact (Mustard et al., 2009; Ehlmann and Mustard, 2012; Goudge et al., 2015; Scheller et al., 2021). The overlying regional Olivine-carbonate unit (~3.8 Ga) is the subject of Chapter 3, as it retains the largest deposit of carbonates on Mars (Ehlmann et al., 2008; Kremer et al., 2020), which is a prime target for analysis and sampling in order to understand the Martian atmosphere and biosignature preservation (Farley et al., 2020). Little is known about the nature of the Mafic Capping Unit that caps these two older geological deposits, but it retains pyroxene mineral signatures from orbital spectroscopy (Goudge et al., 2015; Bramble et al., 2017). Each of these units will be explored during the Perseverance rover extended mission (Farley et al., 2020; Simon et al., 2020).

The insides of the Jezero crater also reveal a complex stratigraphy. It is comprised by the Crater Floor Fractured Rough unit (CFFr) or Maaz Formation, which contains pyroxene-bearing materials believed to be igneous. Crater counting of this unit resulted in approximate ages of ~2.3-2.6 Ga (Goudge et al., 2015; Shahrzad et al., 2019; Holm-Alwmark et al., 2020). In addition, the Jezero crater contains the Crater Floor Fractured 1 unit (CF-F1) or Seitah Formation, which contains olivine and carbonate and appears similar in composition and geomorphology to the regional Olivine-carbonate unit (Stack et al., 2020). It is generally thought that the Seitah Fm is older and underlying that Maaz Fm although this is still the subject of investigation of the Perseverance rover. Last, putative shoreline deposits containing olivine, carbonate, and clays flank the Jezero crater rim (Stack et al., 2020; Horgan et al., 2020; Brown et al., 2020; Tarnas et al., 2021). These crater floor units, which had largely unknown origins, but were initially proposed to potentially be of igneous and possibly volcanic in origin (Goudge et al., 2015), are currently being investigated by the Perseverance rover as it makes way to the delta and are the subject of Chapter 6.

1.3 Carbonate diagenesis: **Why we need to recognize it**

Carbonates within the sedimentary record are powerful proxies for the ancient processes that controlled the carbon cycle of terrestrial planets. Specifically petrography, mineralogical, and isotopic study of stable carbon, oxygen, and clumped isotopes can be utilized to unravel the conditions in which carbonates formed within aqueous environments as well as the preservation of biosignatures, such as microfossils and organics matter. For example, carbonate mineralogy and petrography have been used to reveal global

trends in marine pH and saturation conditions throughout geological history (Grotzinger and Reed, 1983; Grotzinger and James, 2000; Grotzinger and Knoll, 1995). Carbonate carbon and oxygen have been used to track changes in Earth's climate, oceanographic conditions, and changes in the global biosphere in numerous studies, too many to summarize here (e.g. Marshall, 1992; Kump and Arthur, 1999). Clumped isotope compositions are a relatively new tool that can be used to directly determine carbonate formation temperatures and the isotopic composition of the precipitating waters. However, diagenesis, which often involves dissolution, recrystallization, replacement, and/or cementation through interaction with secondary waters, has the capacity to change both carbonate macro- and microtextures as well as recorded stable isotopic compositions (e.g. Armenteros, 2010). Previous studies have had an intense focus on the relationship between the dominant carbonate species, aragonite, calcite, and dolomite, and how these may replace each other through diagenetic processes.

In Chapter 4 and 5, I focus instead on the lesser known species of hydrated carbonates that form only in near-freezing marine and lacustrine natural environments <9°C (Huggett et al,. 2005; Field et al., 2017). Due to their limited stability fields, hydrated carbonates, in particular calcite pseudomorphs after ikaite, have been used as paleotemperature proxies within ancient sedimentary records, most famously for the Neoproterozoic period that involved global glaciations (James et al., 2005; Dempster and Jess, 2015; Wang et al., 2020). It is a particular macrotexture of bi-pyramidal or stellate cm-scale crystals with microtextural evidence for calcite replacement that has been used to infer an ikaite precursor and associated frigid conditions within ancient deposits (James et al., 2005; Dempster and Jess, 2015; Wang et al., 2020). The dehydration process and replacement of ikaite, therefore, is a diagenetic process that can alter texture and isotopic compositions, rendering current interpretations of their anhydrous carbonate transformation products inconclusive. Chapter 4 and 5 addresse how new petrographic and isotopic methodology to identify and quantitatively correct for this diagenetic overprint.

Furthermore, as delineated in Chapter 3, the Perseverance rover is analyzing and sampling carbonates from the Jezero crater that will be subjects for similar petrographic and isotopic analyses. Measurements of isotopic compositions of carbonates will yield direct insight into the composition of the ancient Martian atmosphere and the geological and atmospheric processes that shaped it (Niles et al., 2013; Hu et al., 2015). However, carbonates from Mars are also likely to have been subjected to diagenetic processes and unravelling these, in similar style as we have done on Earth, will be crucial for their interpretation.

1.4 Thesis contents

Chapter 2 investigates the composition of the ancient crust on Mars, the Noachian Basement Group, that is situated within the Jezero crater watershed and the extended mission area of the Perseverance rover. I use hyperspectral infrared imagery and high-resolution images retrieved by the Mars Reconnaissance

Orbiter to characterize the lithology of some of the oldest ~3.8-4.1 Ga crust exposed within the solar system. This study investigates the question of what geological processes affected and shaped the composition of this ancient crust. I document eight geological units and features that record the presence of low-Ca pyroxene-bearing igneous crustal materials, aqueous environments that led to widespread Fe/Mg-smectite and kaolinite formation, and basin-forming impact processes that brecciated the crust to form extensive graben systems and megabreccia blocks (1 m – 1 km in diameter). Furthermore, I constrain the presence of these materials within the traverse area for the Perseverance rover extended mission and address which outstanding scientific questions can be addressed by analyzing these materials. This work lead to the development of potential traverse routes during the Strategic Planning of the Perseverance rover (Simon et al., 2020).

Chapter 3 provides an interdisciplinary review of the most up-to-date knowledge on magnesium carbonate formation on both Earth and Mars. Magnesium carbonates, a relatively rare carbonate species on Earth primarily associated with aqueous alteration environments within ultramafic deposits, have been found to be the predominant carbonate species on Mars. The study particularly investigates what clues to Martian climatic history, surface temperature conditions, and biosignature preservation can be unlocked with rover studies and laboratory studies of returned samples of these carbonates. Specifically, these carbonates are currently being analyzed and sampled by the Perseverance rover (Farley et al., submitted; Scheller et al., submitted). We find that on Earth, magnesium carbonates textures of nodules, crusts, veins, sparry crystals, and thrombolites/stromatolites, their associated host lithologies and related secondary mineralogy can be used to distinguish between formation within weathering, lacustrine, hydrothermal, diagenetic, or microbially influenced aqueous environments, respectively, with rover analyses. Laboratory analysis of stable and radiogenic isotopes of returned samples will allow us to analyze surface temperature, atmospheric isotopic compositions, and the geochronological age of carbonates on ancient Mars.

Chapter 4-5 provides the first paragenetic and isotopic documentation of dehydration diagenesis of hydrated carbonates, including ikaite and monohydrocalcite (MHC). The studies address whether ikaite pseudomorphs and their isotopic compositions can be used to reconstruct the paleotemperature conditions of their precursor formation environments. Through petrographic analysis of Pleistocene ikaite pseudomorphs and a review of more ancient examples, I define a new carbonate microtexture, *guttulatic calcite*, which is diagnostic for carbonate dehydration and can be used to document frigid temperature conditions. I propose that the documentation of the paragenetic sequence in guttulatic calcite can be used as a new tool to document ikaite pseudomorphs and dehydration diagenetic processes within the sedimentary record. I also characterize the stable carbon, oxygen ($\delta^{18}O_{CARB}$), and clumped (Δ_{47}) isotope systematics of hydrated carbonates. Through heating experiments of modern MHC from the Ikka Fjord,

Greenland, I measure and model change in $\delta^{18}O_{CARB}$ and Δ_{47} signatures facilitated by equilibrium exchange as MHC is dehydrated. Using the determined correction for dehydration overprint allows reconstruction of precursor formation temperatures and isotopic signatures. The textural and isotopic proxies together can now be used for reconstruction of precursor temperatures and isotopic signatures that corrects for diagenetic overprints within carbonates from for example Pleistocene and Neoproterozoic sedimentary deposits.

Chapter 6 uses Raman and fluorescence spectroscopy for the first time on another planetary body through the Perseverance rover's SHERLOC instrument to characterize the presence of minerals and organic compounds within the Jezero crater floor units, now called the Maaz Fm and Seitah Fm. The investigation was designed to address what types of ancient aqueous environments were present within Jezero crater and whether they were habitable and/or contained biosignatures. The first retrieved Raman spectroscopy results contain evidence of carbonate-forming aqueous alteration of an ultramafic protolith, a process known as carbonation on Earth. Furthermore, SHERLOC identified a mineral assemblage of Na-perchlorate and Ca-sulfate mixed within void spaces in the interior of basaltic rocks that also reflects either formation through a brine or at least mobilization of these salts through a liquid. Last, all of the rocks investigated contained fluorescence signatures consistent with organic compounds. The more intense fluorescence signatures, interestingly, correlated with aqueous minerals suggesting that these played a role in their preservation and/or formation and that these aqueous environments could potentially have been habitable.

Chapter 7 addresses the implications of the developing overarching story of how Martian aqueous mineral formation affected the planet's climate, habitability, and its diverging evolution in surface environments compared to Earth. It poses and answers the question: Did the formation of hydrated minerals affect the Martian hydrosphere through their formation? Did it cause the loss of Mars' water and the planet's transition to a dry state with decreased habitability potential? Simultaneously, the study addresses a great paradox within multiple fields of Martian research. Geological studies point to a large volume of liquid water on ancient Mars, while atmospheric modelling of Mars' hydrogen isotopic composition (D/H) only allows for a small amount of water loss, and satellite measurements of very limited exospheric H loss points to an even smaller amount of water loss accounted for by atmospheric processes. I modeled the global water budget and hydrogen isotopic composition (D/H) of Mars, using measured constraints from geomorphology, atmospheric escape rates, volcanic degassing processes, crust volatile content, and D/H. In my simulations, I find that chemical weathering sequestered a 0.1-1 km global equivalent layer of water, decreasing the volume of water participating in the hydrological cycle by 40 to 95% over the Noachian (~3.7-4 Ga) period, reaching present-day values by ~3 Ga. Between 30 and 99% of Martian water was sequestered through crustal hydration, demonstrating that irreversible chemical

weathering can increase the aridity of terrestrial planets.

Chapter 8 summarizes the major findings presented in the thesis and addresses outstanding questions.

References

Armenteros, I. (2010). Diagenesis of carbonates in continental settings. *Developments in Sedimentology*, *62*, 61-151.

Bibring, J. P. et al., (2006). Global mineralogical and aqueous Mars history derived from OMEGA/Mars Express data. *Science*, *312*(5772), 400-404.

Bramble, M. S. et al., (2017). The geological history of northeast Syrtis Major, Mars. *Icarus*, *293*, 66-93.

Brown, A. J. et al., (2020). Olivine-carbonate mineralogy of the Jezero Crater Region. *Journal of Geophysical Research: Planets*, *125*(3), e2019JE006011.

Carr, M. H., & Head III, J. W. (2003). Oceans on Mars: An assessment of the observational evidence and possible fate. *Journal of Geophysical Research: Planets*, *108*(E5).

Carr, M. H., & Head III, J. W. (2010). Geologic history of Mars. *Earth and Planetary Science Letters*, *294*(3-4), 185-203.

Christensen, P. R. (2006). Water at the poles and in permafrost regions of Mars. *Elements*, *2*(3), 151-155.

Dempster, T., & Jess, S. A. (2015). Ikaite pseudomorphs in Neoproterozoic Dalradian slates record Earth's coldest metamorphism. *Journal of the Geological Society*, *172*(4), 459 464.

Ehlmann, B. L. et al., (2008). Clay minerals in delta deposits and organic preservation potential on Mars. *Nature Geoscience*, *1*(6), 355-358.

Ehlmann, B. L. et al., (2011). Subsurface water and clay mineral formation during the early history of Mars. *Nature*, *479*(7371), 53-60.

Ehlmann, B. L., & Mustard, J. F. (2012). An in-situ record of major environmental transitions on early Mars at Northeast Syrtis Major. *Geophysical Research Letters*, *39*(11).

Ehlmann, B. L., & Edwards, C. S. (2014). Mineralogy of the Martian surface. *Annual Review of Earth and Planetary Sciences*, *42*, 291-315.

Ehlmann, B. L. et al., (2016). The sustainability of habitability on terrestrial planets: Insights, questions, and needed measurements from Mars for understanding the evolution of Earth like worlds. *Journal of Geophysical Research: Planets*, *121*(10), 1927-1961.

Fairén, A. G. et al., (2010). Astrobiology through the ages of Mars: The study of terrestrial analogues to understand the habitability of Mars. *Astrobiology*, *10*(8), 821-843.

Farley, K. A. et al., (2020). Mars 2020 mission overview. *Space Science Reviews*, *216*(8), 1-41.

Farley, K. et al. (submitted) Aqueously-altered igneous and sedimentary rocks on the floor of Jezero crater, Mars. *Science*.

Fassett, C. I. et al., (2014). An extended period of episodic northern mid-latitude glaciation on Mars during the Middle to Late Amazonian: Implications for long-term obliquity history. *Geology*, *42*(9), 763-766.

Field, L. P. et al., (2017). Unusual morphologies and the occurrence of pseudomorphs after ikaite (CaCO3· 6H2O) in fast growing, hyperalkaline speleothems. *Mineralogical Magazine*, *81*(3), 565-589.

Goudge, T. A. et al., (2015). Assessing the mineralogy of the watershed and fan deposits of the Jezero crater paleolake system, Mars. *Journal of Geophysical Research: Planets*, *120*(4), 775-808.

Grotzinger, J. P., & Reed, J. F. (1983). Evidence for primary aragonite precipitation, lower Proterozoic (1.9 Ga) Rocknest dolomite, Wopmay orogen, northwest Canada. *Geology*, *11*(12), 710-713.

Grotzinger, J. P., & James, N. P. (2000). Precambrian carbonates: Evolution of understanding. *Society of Sedimentary Geology Special Publication, 67.*

Grotzinger, J. P., & Knoll, A. H. (1995). Anomalous carbonate precipitates: Is the Precambrian the key to the Permian? *Palaios*, 578-596.

Grotzinger, J. P. et al., (2014). A habitable fluvio-lacustrine environment at Yellowknife Bay, Gale Crater, Mars. *Science*, *343*(6169).

Heard, A. W., & Kite, E. S. (2020). A probabilistic case for a large missing carbon sink on Mars after 3.5 billion years ago. *Earth and Planetary Science Letters*, *531*, 116001.

Holm-Alwmark, et al., (2021). Stratigraphic relationships in Jezero crater, Mars–constraints on the timing of fluvial-lacustrine activity from orbital observations. *Journal of Geophysical Research: Planets*, e2021JE006840.

Horgan, B. H. et al., (2020). The mineral diversity of Jezero crater: Evidence for possible lacustrine carbonates on Mars. *Icarus*, *339*, 113526.

Hu, R. et al., (2015). Tracing the fate of carbon and the atmospheric evolution of Mars. *Nature Communications*, *6*(1), 1-9.

Huggett, J. M. et al., (2005). The petrology of ikaite pseudomorphs and their diagenesis. *Proceedings of the Geologists' Association*, *116*(3-4), 207-220.

James, N. P. et al., (2005). Glendonites in Neoproterozoic low-latitude, interglacial, sedimentary rocks, northwest Canada: Insights into the Cryogenian ocean and Precambrian cold-water carbonates. *Geology*, *33*(1), 9-12.

Kite, E. S. et al., (2020). Methane release on Early Mars by atmospheric collapse and atmospheric reinflation. *Planetary and Space Science*, *181*, 104820.

Korenaga, J. (2012). Plate tectonics and planetary habitability: Current status and future challenges. *Annals of the New York Academy of Sciences*, *1260*(1), 87-94.

Kump, L. R., & Arthur, M. A. (1999). Interpreting carbon-isotope excursions: Carbonates and organic matter. *Chemical Geology*, *161*(1-3), 181-198.

Lammer, H. et al., (2013). Outgassing history and escape of the Martian atmosphere and water inventory. *Space Science Reviews*, *174*(1), 113-154.

Mangold, N. et al., (2021). Perseverance rover reveals an ancient delta-lake system and flood deposits at Jezero crater, Mars. *Science*, *374*(6568), 711-717.

Marshall, J. D. (1992). Climatic and oceanographic isotopic signals from the carbonate rock record and their preservation. *Geological Magazine*, *129*(2), 143-160.

Mustard, J. F. et al., (2009). Composition, morphology, and stratigraphy of Noachian crust around the Isidis basin. *Journal of Geophysical Research: Planets*, *114*(E2).

Mustard, J. F. (2019). Sequestration of volatiles in the Martian crust through hydrated minerals: A significant planetary reservoir of water. In *Volatiles in the Martian Crust* (pp. 247 263). Elsevier.

Niles, P. B. et al., (2013). Geochemistry of carbonates on Mars: Implications for climate history and nature of aqueous environments. *Space Science Reviews*, *174*(1), 301-328.

Pollack, J. B. et al., (1987). The case for a wet, warm climate on early Mars. *Icarus*, *71*(2), 203 224.

Ramirez, R. M. et al., (2014). Warming early Mars with CO_2 and H_2. *Nature Geoscience*, *7*(1), 59-63.

Scheller, E. L. et al., (2021). Long-term drying of Mars by sequestration of ocean-scale volumes of water in the crust. *Science*, *372*(6537), 56-62.

Scheller, E. L. & Razzel Hollis, J. (submitted). Aqueous alteration processes and implications for organic geochemistry in Jezero crater, Mars. *Science*.

Shahrzad, S. et al., (2019). Crater statistics on the dark-toned, mafic floor unit in Jezero Crater, Mars. *Geophysical Research Letters*, *46*(5), 2408-2416.

Simon, J. et al., Characterizing the Stratigraphy of the Nili Planum Region outside Jezero crater: Implications for Mars 2020 Strategic Planning, LPSC 52 (2021).

Stack, K. M. et al., (2020). Photogeologic map of the perseverance rover field site in Jezero Crater constructed by the Mars 2020 Science Team. *Space Science Reviews*, *216*(8), 1-47.

Tanaka, K. L. et al., (2014). The digital global geologic map of Mars: Chronostratigraphic ages, topographic and crater morphologic characteristics, and updated resurfacing history. *Planetary and Space Science*, *95*, 11-24.

Tarnas, J. D. et al., (2021). Characteristics, Origins, and Biosignature Preservation Potential of Carbonate-Bearing Rocks Within and Outside of Jezero Crater. *Journal of Geophysical Research: Planets*, *126*(11), e2021JE006898.

Tosca, N. J. et al., (2018). Magnetite authigenesis and the warming of early Mars. *Nature Geoscience*, *11*(9), 635-639.

Turbet, M. (2017). 3D modelling of the climatic impact of outflow channel formation events on early Mars. *Icarus*, *288*, 10-36.

Wang, Z. et al., (2020). Wide but not ubiquitous distribution of glendonite in the Doushantuo Formation, South China: Implications for Ediacaran climate. *Precambrian Research*, *338*, 105586.

Wordsworth, R. D. (2016). The climate of early Mars. *Annual Review of Earth and Planetary Sciences*, *44*, 381-408.

Wordsworth, R. D. et al., (2017). Transient reducing greenhouse warming on early Mars. *Geophysical Research Letters*, *44*(2), 665-671.

Wordsworth, R. D. et al., (2021). A coupled model of episodic warming, oxidation and geochemical transitions on early Mars. *Nature Geoscience*, *14*(3), 127-132.

Chapter 2

Composition, Stratigraphy, and Geological History of the Noachian Basement Surrounding the Isidis Impact Basin

Eva L. Scheller[1] and Bethany L. Ehlmann[1,2]

[1]Division of Geological and Planetary Sciences, California Institute of Technology, Pasadena, California, USA.

[2]Jet Propulsion Laboratory, California Institute of Technology, Pasadena, California, USA.

2.1 Abstract

The western part of the Isidis basin structure hosts a well-characterized Early Noachian to Amazonian stratigraphy. The Noachian Basement comprises its oldest exposed rocks (Early to Mid-Noachian), and was previously considered a single LCP- and Fe/Mg-smectite-bearing unit. Here, we divide the Noachian Basement Group into 5 distinct geological units (Stratified Basement Unit, Blue Fractured Unit, Mixed Lithology Plains Unit, LCP-bearing Plateaus Unit, Fe/Mg-smectite-bearing Mounds Unit), 2 geomorphological features (megabreccia and ridges), and a mineral deposit (kaolinite-bearing bright materials), based on geomorphology, spectral characteristics, and stratigraphic relationships. Megabreccia contain four different pre-Isidis lithologies, possibly including deeper crust or mantle materials, formed through mass-wasting associated with transient crater collapse during Isidis basin formation. The Fe/Mg-smectite-bearing Stratified Basement Unit and LCP-bearing Blue Fractured Unit likewise represent pre-Isidis units within the Noachian Basement Group. Multiple Fe/Mg-smectite-bearing geological units with different stratigraphic positions and younger kaolinite-bearing bright materials indicate several aqueous alteration episodes of different ages and styles. Units with slight changes in pyroxene spectral properties suggest a transition from low-Ca pyroxene-containing materials to those with higher proportions of pyroxenes higher in Ca and/or glass that could be related to different impact- and/or igneous processes, or provenance. This long history of Noachian and potentially Pre-Noachian geological processes, including impact basin formation, aqueous alteration, and multiple igneous and sedimentary petrogeneses, records changing ancient Mars environmental conditions. All units defined by this study are available 20 km outside of Jezero crater for in-situ analysis and sampling during a potential extended mission scenario for the Mars 2020 rover.

2.2 Plain language summary

The Isidis basin's Noachian Basement Group is a collection of geological materials that are among the oldest rocks exposed on the Martian surface (>3.8 billion years old). We have characterized their spectral signatures and appearances using instruments on the Mars Reconnaissance Orbiter. The Noachian Basement Group contains 8 different geological categories of rocks formed at different times and by different processes. One of these categories is megabreccia, which are blocks of rocks created when a meteorite impact formed the 1900-km Isidis impact basin. The megabreccia contain materials from deep within Mars and likely formed during enormous landslides after the impact. The spectral properties of the megabreccia reveal that they contain four different types of rock that must have originated before the Isidis impact basin formed. Through investigations of the 3-dimensional relationships between our 8 categories of geological materials, we observe that they record multiple distinct water-rich environments, multiple igneous processes, and giant impact processes, during an ancient time period that we know little about. Furthermore, all 8 different rock categories can be studied and sampled with the next Mars rover,

set to launch in 2020, which will answer outstanding questions about the climate, astrobiology, and geological processes on early Mars.

2.3 Introduction

Understanding the geological history of the ancient Pre-Noachian to Mid-Noachian crust on Mars is imperative as it includes processes such as impact basin formation, igneous petrogenesis, climate evolution, and ancient aqueous environments that are essential for understanding the origin, early evolution, and habitability of terrestrial planets. This time period encompasses rocks formed >3.82 Ga (Werner and Tanaka, 2011; Mandon et al., 2019). However, few well-exposed and well-preserved examples of Pre-Noachian to Noachian-aged crust exist on Mars and other solar system bodies. The NW region of the Isidis basin, a 1900-km, 3.96-3.97 Ga (Fassett & Head, 2011; Werner, 2008), Early-Mid Noachian impact basin structure on the crustal dichotomy boundary (Ritzer and Hauck, 2009), provides a window into the geological history of ancient Mars that is exceptionally well-preserved compared to rocks of the same age on Mars and Earth (Fig. 2.1).

The NW Isidis basin region includes Nili Fossae, NE Syrtis, and the Jezero crater watershed and contains a well-characterized Noachian to Amazonian stratigraphy (Fig. 2.1) (Bramble et al., 2017; Ehlmann et al., 2009; Ehlmann & Mustard, 2012; Goudge et al., 2015; Mangold et al., 2007; Mustard et al., 2007; 2009; Quinn & Ehlmann, 2019a). The lowermost part of this stratigraphy is the > ~600 m thick Noachian Basement Group (Bramble et al., 2017; Ehlmann and Mustard; 2012; Goudge et al., 2015; Mangold et al., 2007; Mustard et al., 2009). Regionally, the Noachian Basement Group is overlain by the olivine-carbonate-bearing fractured unit, various high-Ca pyroxene-bearing materials often referred to as the mafic cap unit, a sedimentary unit of layered sulfates, and Hesperian-age (Hiesinger, 2004) Syrtis Major lava flows. Previous studies using infrared remote sensing have determined that the Noachian Basement contains low-Ca pyroxenes (LCP), Fe/Mg-smectite, and kaolinite (Ehlmann et al., 2009; Ehlmann & Mustard, 2012; Mangold et al., 2007; Michalski et al., 2010; Mustard et al., 2009). Additionally, the Noachian Basement includes a variety of geomorphological features such as ridges (Pascuzzo et al., 2019; Saper & Mustard, 2013), smooth plains, knobby plains, mounds, and megabreccia (Bramble et al., 2017).

In addition to recording ancient aqueous environments and igneous petrogenesis, the Noachian Basement Group also records processes forming the Isidis basin. In particular, its megabreccia have been proposed to have formed by the Isidis impact (Mustard et al., 2009). However, previous literature has neither considered the exact formation mechanism of megabreccia nor the location of other Isidis impact products such as melt sheet and ejecta. Currently, the formation processes of multi-ring impact basins are not well-understood as they are primarily based on models with few opportunities for constraints through field studies. Hydrocode and other modelling efforts have been performed primarily for lunar impact

basins (Johnson et al., 2016; Schultz & Crawford, 2016) and the Chixulub impact basin (Baker et al., 2016; Collins et al., 2002). Study of lunar impact basins through satellite observations and sample analysis (Howard, Wilhelms, & Scott, 1974) and studies of the three largest impact basins on Earth (150-300 km diameters), including Vredefort (Reimold & Gibson, 1996), Sudbury (Riller, 2005), and the Chixulub drilling project (Morgan et al., 2016), have also contributed significantly to our understanding of impact basin formation processes. Hence, the Isidis Noachian Basement Group on Mars provides an extraordinary opportunity to further our understanding of these impact basin formation processes.

Although the diversity of the Noachian Basement Group has been evaluated in previous literature, the collective stratigraphic and geological histories of these various compositional and geomorphic units
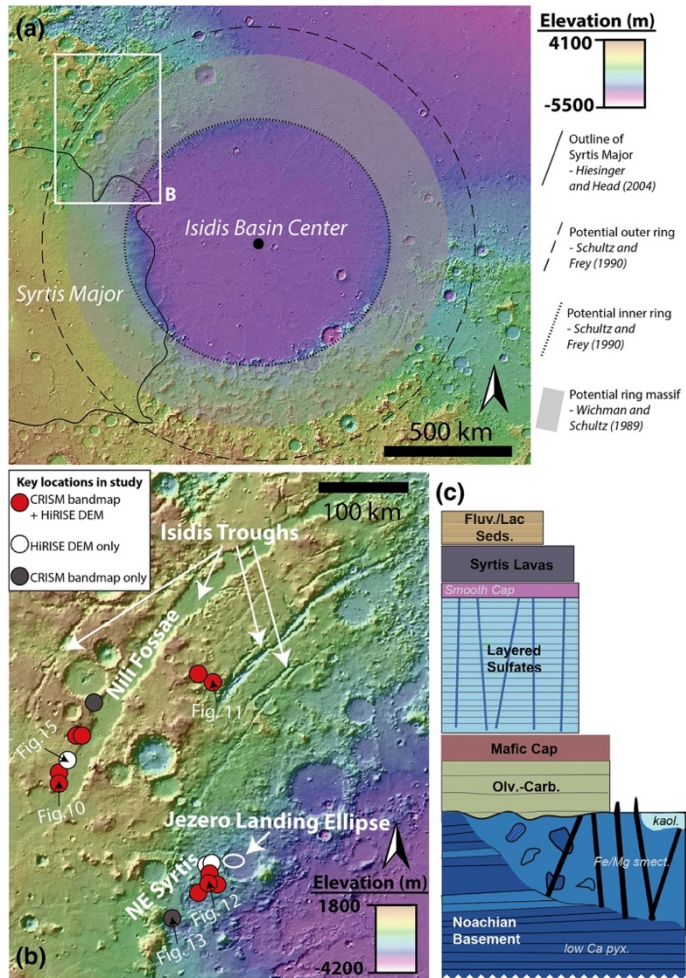
Fig. 2.1: Overview of study area. (A) MOLA topography map of Isidis basin and Syrtis Major. Outlines refer to suggested impact basin features from previous literature. White box denotes position of panel B. (B) Map of main study area. Circles refer to key stratigraphic locations used in this study. Red circles refer to the position of CRISM bandmaps with HiRISE DEMs, white circles refer to HiRISE DEMs only, and the grey circle refers to CRISM bandmap only. The location of data shown in Fig. 2.10-2.15 are indicated with black arrows. (C) Regional stratigraphy of study area within panel B. The regional stratigraphy represents a summarization of Mustard et al. (2009), Ehlmann and Mustard (2012), Goudge et al. (2015), Bramble et al. (2017), and Quinn and Ehlmann (2019a).

within the Noachian Basement Group have not been determined. In this study, we use combined mineralogical-, geomorphological-, and stratigraphic analysis in order to define units, their stratigraphic position, and, where possible, their formation history within the Noachian Basement Group. We intentionally adopt the nomenclature of "Group" to describe the basement because it formed during a time interval prior to formation of younger units in the regional stratigraphy but is clearly comprised of multiple distinctive units with different ages and formation processes. Furthermore, we investigate the geographical distribution of the Isidis megabreccia, some of the oldest rocky materials exposed on solar system terrestrial planets, for the first time, and systematically classify the megabreccia lithologies. We test between the multiple megabreccia formation hypotheses (ballistic ejecta, melt flows, crater floor/peak fracturing, gravitational flows), using the characteristics of distribution, texture, lithology, and block size of megabreccia that are expected to differ between formation mechanisms (Table 2.1). In turn, this provides constraints on the preservation (shock pressure, temperature, strain) of the Pre-Noachian or Early Noachian materials within the megabreccia. We evaluate the potential presence of Isidis impact melt and ejecta in the new geological units defined in this study. Lastly, we provide a detailed map of the occurrence of these materials within potential driving distance of the Mars 2020 rover.

Table 2.1: Expected characteristics of megabreccia deposits from four known megabreccia formation mechanisms.

Formation mechanism	Distribution	Texture/Lithology	Block sizes	References
Ballistic ejecta	- Circumferential to outer and inner crater ring - Extend >2 crater radii	- Multitude of textures/lithologies - Potential sorting of textures/lithologies with distance	- Potential dependency on distance from crater center	*e.g. Hörz, 1982*
Ground-hugging, Ejecta-related Melt flows	- Not necessarily circumferential - Should extend beyond the outer ring - Occurs locally	- Significant melt component - Flow/dike/pseudotachylite structures	- No particular expectations	*e.g. Komatsu et al., 2007; Osinski et al., 2011*
Crater floor/central peak fracturing and/or melt sheet formation	- Occurs within inner ring or central peak	- Uplifted/faulted blocks - Pre-impact lithologies - Should be in matrix of melt	- Primarily large blocks (100s of meters)	*e.g. Caudill et al., 2012; Schultz et al., 1976; Quantin et al., 2011; Krüger et al., 2016*
Gravitational flow during crater collapse	- Circumferential to inner crater rim - Occurs primarily within transient crater and faulted region (likely between outer and inner ring)	- Multitude of textures/lithologies - Evidence for ground transport - No spatial sorting, complete heterogeneity	- Potential dependency on elevation but not distance	*e.g. Belza et al., 2012; Stöffler et al., 2004; Trowbridge et al., 2019*

2.4 Methods

The composition and geomorphology of the Noachian Basement in the study area were analyzed using data from the Context Camera (CTX; Malin et al., 2007), High Resolution Imaging Science Experiment (HiRISE; McEwen et al., 2007), Mars Orbiter Laser Altimeter (MOLA; Zuber, 1992), Compact Reconnaissance Imaging Spectrometer for Mars (CRISM; Murchie et al., 2007), and Thermal Emission

Imaging System (THEMIS; Christensen et al., 2004) data sets (Table 2.2), incorporated into an ArcGIS database. CRISM images were also analyzed in the ENVI software package.

Table 2.2: Data sets with their related online repositories and references used in this study

Dataset name	Online Repository	Reference
HiRISE RDR	Planetary Data System (PDS)	McEwen et al. (2007)
CRISM TRR3, MSP, and MSW	Planetary Data System (PDS)	Murchie et al. (2007)
MOLA global mosaic	Planetary Data System (PDS)	Zuber et al. (1992)
CTX global mosaic	Murray Lab/ArcGIS online	Dickson et al. (2019)
THEMIS Day/Night time global mosaic	ASU Mars Global Data Sets	Edwards et al. (2011)

2.4.1 Megabreccia distribution map

Within ~900 HiRISE images, we searched for large blocks, >1 m, within a radial distance of 500-2000 km from the crater center, including the northwestern and south rim but excluding areas dominated by Syrtis Major and the Northern Plains (Fig. 2.1.A). In the Nili Fossae and NE Syrtis areas, we searched Noachian Basement units that were mapped by Bramble et al. (2017) and Goudge et al. (2015). Our mapping criteria for megabreccia were: 1) occurrence within Noachian Basement and underlying the olivine-carbonate unit, 2) no association with ejecta blankets of other craters, 3) albedo contrast to surrounding matrix, 4) textural contrast to surrounding matrix, and 5) distinct blocky shape (typically angular or sub-rounded). Our mapping efforts are limited by the availability of HiRISE grayscale and color data (megabreccia are easier to observe in color data, Fig. 2.3), exposure of the basement units (significantly better near grabens due to erosion), and dust/sand cover. Regions south and east within the Isidis structure have much less HiRISE coverage than the western part of the Isidis structure. In addition, much of the basement in these regions is observed in visible image data to be mantled by fine-grained materials, consistent with THEMIS thermal inertia data (Bishop et al., 2013). HiRISE that we requested of Noachian regions near Libya Montes (as defined by Bishop et al., 2013) had a thick cover of fine-grained materials, obscuring any bedrock.

Outlining all individual clasts of all 173 megabreccia-bearing outcrops was beyond the scope of this study; however, we outlined all individual block clasts above HiRISE resolution within 13 outcrops (totaling 4600 individual block clasts), representative of the 13 different distance and elevations bins from the Isidis crater center and tabulated their size characteristics (Fig. 2.5). The largest outcrop(s) within each distance and elevation bin (Fig. 2.5) were chosen for this outlining. The reported block size of these 4600 individual block clasts represents a maximum length that was calculated by constructing a minimum enveloping circle to each megabreccia outline and calculating

the diameter of this circle. In addition, we calculated the planar distance between the Isidis crater center and the center of the minimum enveloping circle of each megabreccia.

Megabreccia block sizes were then binned according to planar distance from Isidis crater center and MOLA elevation for construction of boxplots in order to investigate changes in megabreccia block sizes with crater distance and elevation. These binned block-size data were examined via box plots created with the Python seaborn module (Waskom et al., 2017) in order to investigate any systematic changes in the median, quartiles, and ranges with distance or elevation. In addition, all of the block size distributions within distance and elevation bins were subjected to pairwise Mann-Whitney U-test using the SciPy module (Jones et al., 2001) in order to test for any nonparametric differences between these distributions. Subsequently, the binned block-size distributions were fitted with skewed normal distributions and lognormal distributions using the SciPy module in order to investigate any systematic changes to the mean, mode, variance, skewness, kurtosis, and overall shapes of distributions with distance and elevation.

2.4.2 Megabreccia lithologies

CRISM covers 12 outcrops of megabreccia that were analyzed block by block through single-pixel study (Fig. 2.2). As megabreccia blocks were generally below CRISM resolution, we also used HiRISE color data in order to analyze megabreccia. Following instructions by Eliason et al. (2007) and using GDAL, HiRISE color DN were corrected to: $\frac{I}{F*\cos(\theta)}$, where I is the measured radiance, F is the radiance of the sun, and θ is the sun angle. All megabreccia within 8 different HiRISE color images were outlined individually, and the three band values of the HiRISE color rasters were extracted for each pixel within this outline using arcpy tool Extract by Mask. For each pixel, we calculated band ratios of IR/RED, IR/BG, and BG/RED as suggested in Delamere et al. (2010). In addition, we calculated the slope, angle, and area of each HiRISE color band profile (Fig. 2.2) through trigonometric formulas. Variations in these 6 parameters are typically due to absorptions associated with Fe^{2+} and Fe^{3+} in minerals (Fig. 2.2). We created 2D histograms of all pixel values for these 6 different parameters, identified megabreccia classes based on manually selected clusters, and then determined which visual colors from Fig. 2.2 correlated with clusters and certain parameter values. Additionally, we analyzed 4 HiRISE color images that contained a variety of Noachian Basement Group units and the olivine-carbonate unit, defined using CRISM and HiRISE, using the same color parameterization.

Furthermore, we verified that results in HiRISE color parameter space reflect changes in lithology rather than changes in lighting and geometry. First, we analyzed 3 different HiRISE color images (ESP_047049_2015, ESP_045137_2015, and ESP_045071_2015) acquired over the same area at different times. The point clouds and 2D histograms of these 3 images were compared visually. No

significant differences were noted between these 3 different point clouds and 2D histograms. Second, we compared HiRISE color results of the same megabreccia in direct sunlight and shadow. The area of profiles were affected slightly by shadow effects, although this difference is much smaller than the observed parameter differences between clusters in our 2D histograms. Shadowed megabreccia appeared to have approximately the same values in all other parameters as megabreccia in sunlight.

Many megabreccia outcrops included multiple blocks of different color/albedo and textural
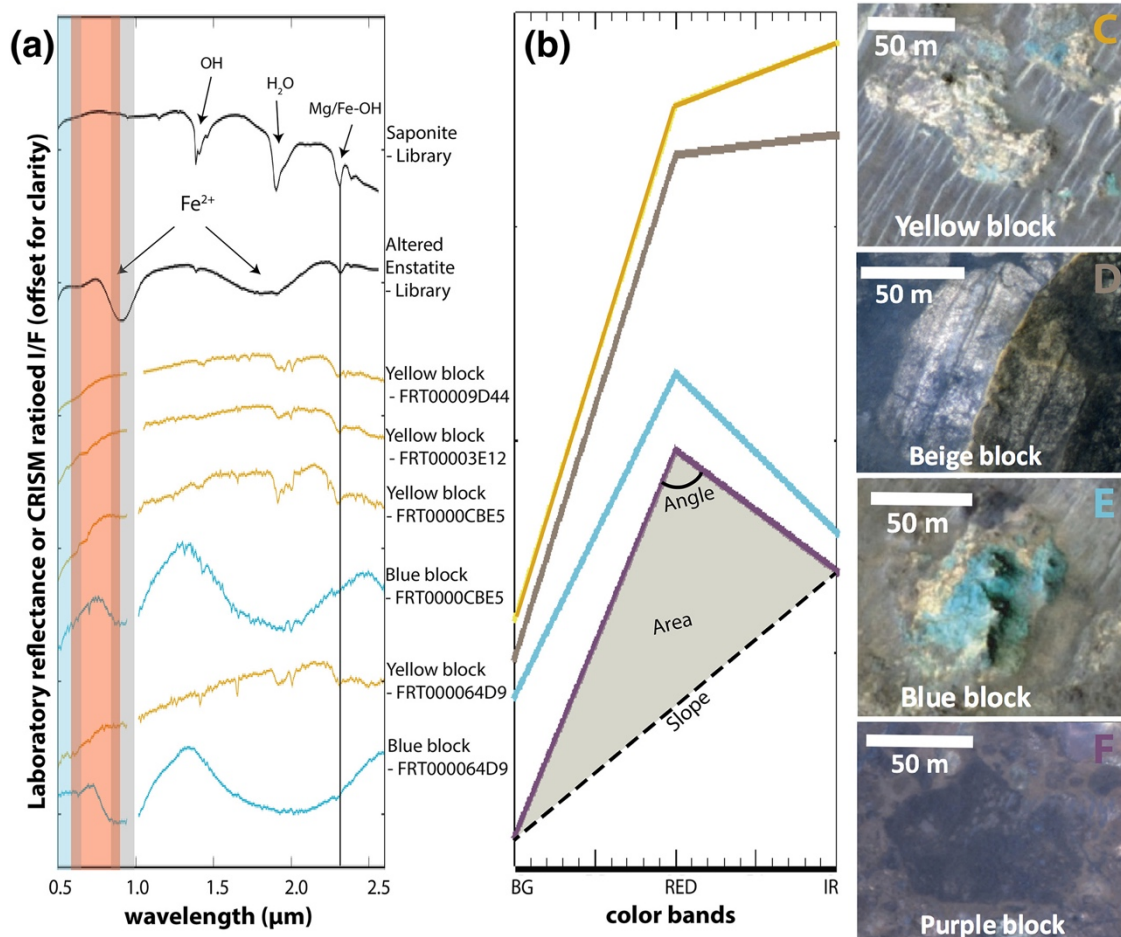
Fig. 2.2: Spectroscopy of Martian megabreccia. (A) CRISM spectra of 6 different megabreccia blocks from four different outcrops compared to two library spectra of saponite (Mg-smectite) and altered enstatite (LCP) from the USGS spectral library (Clark et al., 1993). Wavelength intervals colored blue, red and grey correspond to the wavelength intervals of BG, RED, and IR bands of HiRISE color images. Center coordinate(s) of block(s) within CRISM image(s) FRT00009D44 is 20°2'10.15"N, 73°40'51.02"E, FRT00003E12 is 22°11'22.01"N, 77°4'24.28"E, FRT0000CBE5 are 17°17'34.46"N, 76°17'54.60"E and 17°17'33.32"N, 76°17'59.31"E, and FRT000064D9 are 21°6'5.22"N, 74°14'15.19"E and 21°6'26.69"N, 74°14'13.99"E. (B) Average HiRISE color band profiles of four different megabreccia blocks corresponding to blocks shown in C-F. C and E are from HiRISE image ESP_047049_2015), D is from ESP_033572_1995 and F is from ESP_037185_2010These HiRISE color band profiles were parameterized through band ratios, slope (black stippled line), area (grey shaded area), and angle (solid black line).

properties. For blocks with HiRISE color coverage, the presence of blocks with visual color in the standard HiRISE IR-Red-BG product was recorded: blue/green (here called "blue"), yellow, beige, and purple. This color classification was done by eye for individual outcrops. Outcrops were classified based on whether they contained blocks of only a single color or multiple colors. We determined the textural properties by visual inspection: layered or not; uniformity or heterogeneity of albedos (labelled "monomict" and "polymict"), and proximity of adjacent blocks. Layered materials only exhibited albedo differences, not color differences, and could be classified with one color. We extracted longitude and latitude coordinates and elevation for each megabreccia outcrops from MOLA data (SimpleCylindrical_Mars map projection).

2.4.3 Defining geological units

Approximately 30 CRISM TRR3 images covering the western rim of the Isidis basin structure were analyzed in order to define spectral characteristics of the Noachian Basement These 30 CRISM images were chosen because they were the only high-resolution CRISM images within the study region (Fig. 2.1B), covering the Noachian Basement Group, that contained both L- and S-data (Murchie et al., 2007). In addition, 5 multispectral CRISM images (MSP and MSW) were used for the construction of a map west of Jezero and north of NE Syrtis due to lack of high-resolution CRISM images (see section 2.4.5). The 30 CRISM TRR3, 4 MSW, and single MSP images (Murchie et al., 2007) were processed using the CRISM Analysis Toolkit 7.4 in ENVI (Morgan et al., 2009). Data were converted to $\frac{I}{F*cos(\theta)}$, as defined in section 2.4.2, using procedures described in Murchie et al. (2007). Subsequently, the data was atmospherically corrected using the volcano scan correction (McGuire et al., 2009) and projected (Morgan et al., 2009; Murchie et al., 2016). Minimal processing of CRISM images was performed, usually relying solely on pixel averages of regions of interests with spectra ratioed to a spectrally bland unit within the same column. In some cases, noise reduction was performed using methods by Pan et al. (2017). CRISM bandmaps were constructed using band parameters from Pelkey et al. (2007), Viviano-Beck et al. (2014), and Carter et al. (2013).

In addition, we calculated a custom band parameter for distinguishing LCP signatures, a spectral centroid, corresponding to the wavelength position of the maximum between 1 μm and 2 μm. The spectral centroid is defined as: $Centroid = \frac{\sum_{i=1}^{N} I_i \lambda_i}{\sum_{i=1}^{N} I_i}$. Here i refers to each of the N number of bands used for this calculation. I refers to the intensity of the reflectance value for each band, while λ refers to the wavelength value of each band. We used all bands between the fixed range of 1 μm to 2 μm for this calculation in order to track the position of maximum reflectance between the 1 μm and 2 μm absorptions. This band parameter was designed as we observed a minor change in LCP spectral characteristics correlating with geomorphology. The compositional significance of the LCP centroid was evaluated by investigating the

centroid positions of previously published laboratory spectra of pyroxenes with different compositions (Klima et al., 2011). In addition, the centroid positions of calculated linear mixtures of LCP with regional dune materials, previously published laboratory Fe/Mg-smectite (Fox et al., 2019), and previously published Fe-rich glass spectra (Cannon et al., 2017) were compared with the Mars CRISM data.

When present, CRISM bandmaps and corresponding HiRISE were analyzed together in order to define subunits within the Noachian Basement. Detailed manual co-registration between CRISM and HiRISE was performed for 12 key locations (Fig. 2.1). We evaluated the following characteristics in HiRISE in order to characterize Noachian Basement units/features: albedo, texture, HiRISE color, smoothness/roughness, relative crater densities, topographic expression, and thickness. Geological units were defined to be materials of the same lithology with a defined volume and clear contact with other units. Geomorphological features were defined to be materials of the same lithology or collection of lithologies with a singular geomorphological expression that did not have a clear contact with other units, e.g. ridges and blocks, but rather appeared to be within units. Lastly, we use the term mineral deposits to categorize kaolinite-bearing bright materials (see section 2.5.2.7), as these could be identified via spectral characteristics but did not have consistent geomorphic or stratigraphic characteristics.

2.4.4 Stratigraphy and structural analyses

Stratigraphic analyses were based primarily on visual inspection of HIRISE DEMs. We constructed one HiRISE DEM through SOCET SET (Kirk et al., 2009). This study also used a number of HiRISE DEMs covering NE Syrtis and the Mars 2020 Midway landing ellipse made available to the Mars 2020 Science Team by the Murray Lab at Caltech and processed through the NASA Ames Stereo Pipeline (Beyer et al., 2018). Furthermore, we constructed 6 HiRISE DEMs through the Ames Stereo Pipeline, primarily for visual inspection (Fig. 2.1). All visual inspections were performed using OSGEARTH that renders HiRISE DEMs at full resolution. Measurements and elevation profiles were performed in ArcGIS. Subsequently, two of these HiRISE DEMs were used to calculate orientations (strike, dip, angular errors) of layers within stratified parts of the Noachian Basement and the contact between megabreccia and this stratification. These orientation calculations were performed through the attitude software package developed by Quinn and Ehlmann (2019b).

2.4.5 Geological map of Noachian Basement accessible to a Mars 2020 extended mission

The geological units of the Noachian Basement Group were mapped with HiRISE data at 1:5,000 resolution for the area between NE Syrtis and the western Jezero rim that could constitute an extended mission area for Mars 2020 and that is within the safe Midway landing ellipse presented at the Mars-2020 workshops (Farley et al., 2018) (Figure 20). The map in the vicinity of the NE Syrtis ellipse was adapted from mapping of the Noachian Basement geomorphological units by Bramble et al. (2017) at 1:1000 resolution. However, changes, additions, and reclassifications were made to the original Bramble et al.

(2017) map in order to align the map with the specific geologic units defined within this study. Mapping of the megabreccia and megabreccia lithologies within this map were performed using methods of section 2.5.1.2. Because hyperspectral CRISM data are not available and the spatial resolution of CRISM multispectral data was too coarse for the scale of spatial variability of units in most cases, distinguishing between knobby parts of Mixed Lithology Plains Unit and LCP-bearing Plateaus Unit (see section 2.5.2) was not entirely possible and has been left ambiguous within the map. Low resolution multispectral CRISM data (MSW and MSP) were used to look for strong LCP-signatures. Strong LCP-signatures were occasionally found and the area was subsequently mapped as LCP-bearing Plateaus Unit. However, the spatial resolution (~100-200 m/pixel) was generally too low to distinguish outcrops of the LCP-bearing Plateaus Unit that usually only have a lateral extent of a couple of hundred meters, so rover-scale investigations would likely reveal more geological unit diversity than that delineable from orbit. In comparison, the Blue Fractured Unit was easily distinguishable due to its distinct texture and blue color.

2.5 Results

2.5.1 Megabreccia

Megabreccia occur within the Noachian Basement in outcrops of a single to thousands of <1-433 m size angular to sub-rounded blocks. These blocks have a variety of textures but all have a sharp albedo and texture contrast with surrounding matrix materials. Outcrops with megabreccia blocks are usually highly eroded exposing a flat cross-section of the original block. However, less eroded, protruding blocks do occur occasionally (Goudge et al., 2015).

2.5.1.1 Megabreccia map

Our final map of megabreccia consisted of 173 megabreccia deposits within the NW part of the Isidis crater structure, assessed within 10^6 km^2 of HiRISE images (Fig. 2.3). We only found megabreccia in the NW region between the putative outer and inner ring (Fig. 2.1 and Fig. 2.3). Previous studies have observed spectroscopic signatures in the southern part of the Isidis impact structure, identical to the Noachian Basement and olivine-carbonate in the NW region of the study area (Bishop et al., 2013; Mustard et al., 2009). However, the exposure is considerably worse. We searched south and east of the Isidis basin structure, but due to thick, fine-grained covers within this region (see section 2.4.1), it remains indeterminate whether megabreccia are present. We did not positively locate any megabreccia in our search of ~80,000 km^2 of HiRISE cover in the southern part of the Isidis structure (Fig. 2.3). The prior detection by Tornabene et al. (2013) (Fig. 2.3) is associated with Duvolo crater and, therefore, not necessarily associated with the Noachian Basement Group.

We generated five classifications of megabreccia outcrops on the basis of block distribution and textural properties (Fig. 2.4). "Densely packed blocks" are outcrops where blocks occur in contact with each
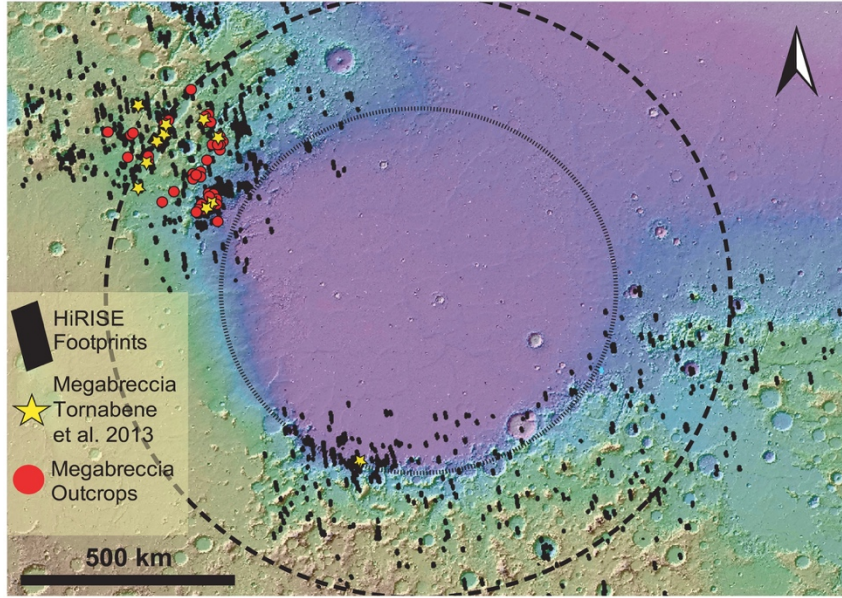
Fig. 2.3: Map of all 173 megabreccia cataloged in this study within the Noachian Basement Group (red circles, overlapping at this spatial scale) along with megabreccia locations compiled in Tornabene et al. (2013) (yellow starts). Inferred inner and outer ring of Isidis basin from Fig. 2.1 shown as black stippled lines. All analyzed HiRISE image footprints in black.

other. "Scattered blocks" are outcrops where blocks do not occur in contact with each other, and "single blocks" are a single megabreccia block with no association to larger exposures (Fig. 2.4). Second, densely packed blocks can appear "monomict" or "polymict" depending on the number of distinct lithologies present based on albedo or HiRISE color properties (Fig. 2.3). Third, certain polymict blocks exhibit layering with meters to tens of meter scale banding of material with alternating colors or albedos (Fig. 2.4). The spatial distributions of these textures were investigated in 3D and plan view as a function of radial distance to Isidis crater center and elevation (Fig. 2.4). The different textural types of megabreccia had no obvious trends in their distribution and occur throughout the study area, particularly where eroded scarps provide a window in to the Noachian Basement (Fig. 2.4).

Megabreccia blocks have an overall size range of 1.3-433 m with a median of 11.5 m. Block sizes have similar characteristics (quartiles and ranges) at different distances from the crater center and elevation intervals with no apparent trends (Fig. 2.5). We performed a Mann-Whitney U test in order to determine whether there were changes in the non-parametric distributions of block sizes within different bin-intervals. Most pairs of block distributions achieved a p-value <0.05 suggesting that block size distributions within bins are statistically different. Skewed normal and lognormal distributions were used to model distributions within each distance and elevation bins to investigate trends together with boxplots. Although the distribution parameters are statistically different, the median, quartiles, ranges, mean, mode,
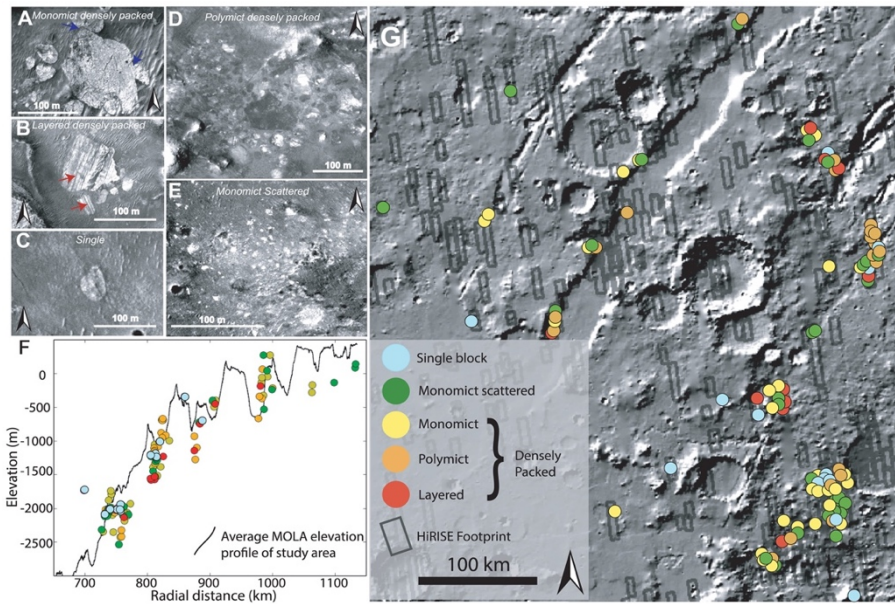
Fig. 2.4: Examples of (A) monomict, densely packed megabreccias (ESP_033572_1995). (B) layered, densely packed megabreccia as indicated by red arrows (ESP_035062_1995), (C) single megabreccia (ESP_053523_1985), (D) polymict, densely packed megabreccia (ESP_037185_2010), and (E) scattered megabreccia (PSP_008861_2000). (F) Megabreccia outcrops of different textures plotted by radial distance from the center of Isidis basin and MOLA elevation. The black line in the background represents the average MOLA elevation profile of the study area. (G) Megabreccia outcrops of different textures plotted in plan-view with MOLA background. All HiRISE footprints studied are outlined in dark grey.
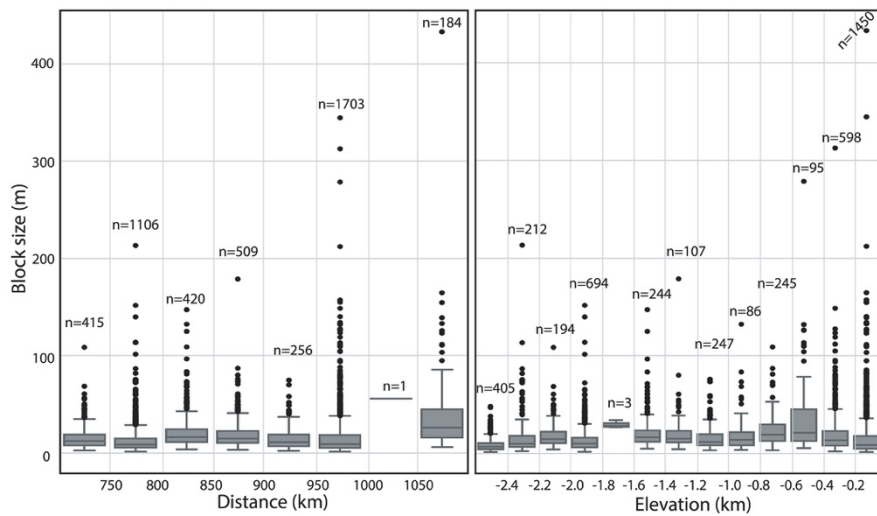
Fig. 2.5: Boxplots of 4,600 megabreccia block sizes within each distance and elevation bin. The gray box encompasses the interquartile range (IQR) including the 25th (Q1) and 75th percentiles (Q3). The black line in the box indicates the median. Whiskers show lower (Q1–1.5 × IQR) and upper (Q3 + 1.5 × IQR) range of boxplots. Gray dots show all megabreccia points outside the lower and upper range. The number of megabreccia within each bin is denoted above each boxplot. Note that certain bins at 1,000–1,050 km and elevation of −1.8 to −1.6 km have too few megabreccia to construct proper boxplots and may be disregarded.

23

variance, skewness, kurtosis, and overall shapes of distributions of boxplots and distributions do not appear to exhibit any systematic changes with increasing distance to crater or elevation (Fig. 2.5). In summary, each bin has a statistically different distribution compared to the others, but the differences were not systematic with increasing distance or elevation.

2.5.1.2 Megabreccia lithologies

Analysis of 12 separate exposures of megabreccia with CRISM reveal that LCP- and Fe/Mg-smectite occur in megabreccia materials, as reported previously (Mustard et al., 2009) (Fig. 2.2). Eight separate exposures of megabreccia from 8 different HiRISE color images reveal that at least four different clusters
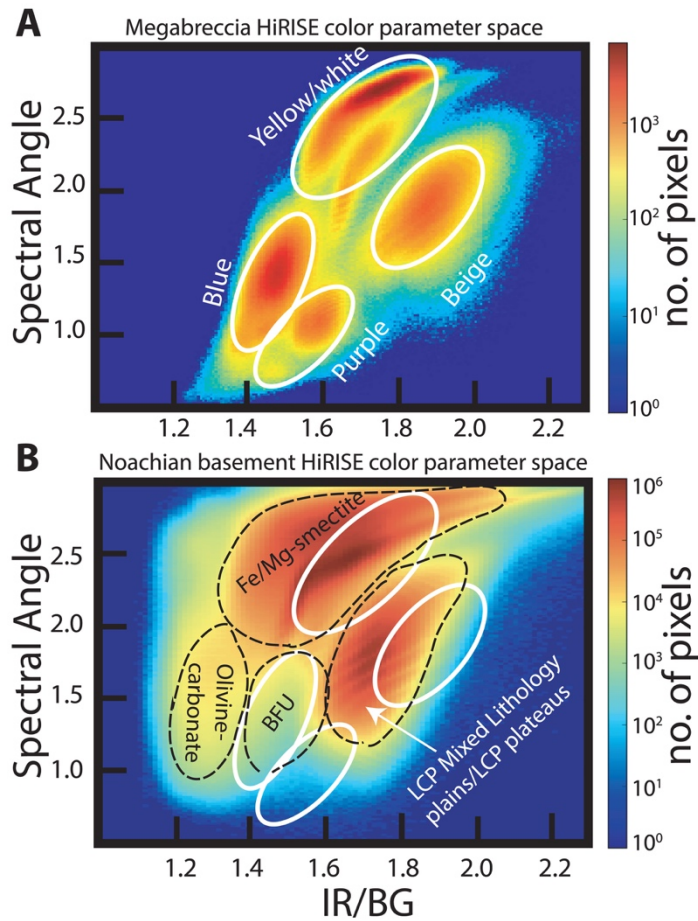
Fig. 2.6: Megabreccia color classification histograms. (A) 2D histogram of IR/BG band ratio and spectral angle from HiRISE color parameterization scheme from Fig. 2. Data includes only megabreccia blocks from 8 different images that each contained a variety of different colored clasts. The megabreccia HiRISE color parameter space shows four main lithological clusters (white lines) that correlate with yellow/white, blue, beige, and purple visual colors from Fig. 2. HiRISE images used are ESP_016153_2005, ESP_022601_1975, ESP_033572_1995, ESP_037185_2010, ESP_037541_2010, ESP_047049_2015, ESP_047339_1980, and PSP_002888_2025. (B) 2D histogram of IR/BG band ratio and spectral angle from entire HiRISE images containing Noachian Basement and olivine-carbonate units. Here, clusters (black stippled lines) were related to olivine-carbonate, Blue Fractured Unit (BFU), general Fe/Mg-smectite signatures in CRISM, and LCP-bearing Mixed Lithology Plains Unit and/or LCP-bearing Plateaus Unit. HiRISE images used are a portion of ESP_016153_2005, ESP_027691_2025, ESP_047049, and ESP_053655_1985.

of HiRISE color properties occur (Fig. 2.6). We observed that one cluster always correlated with the visual color of blue, while another always correlated with the visual color of purple. The two last clusters correlated with yellow/white colors, although one of the clusters represented blocks of a more beige nuance (Fig. 2.6.A). The frequency distribution of color properties within the yellow/white blocks class may indicate two distinct subclasses (Fig. 2.6.A). Yellow/white megabreccia blocks were Fe/Mg-smectite-bearing while blue megabreccia blocks were LCP-bearing when CRISM data were available over large blocks, as also previously reported in Mustard et al., (2009) (Fig. 2.2). Beige blocks did not have any CRISM coverage. In the few cases where purple blocks had CRISM coverage, the megabreccia did not occur in sizes large enough to obtain CRISM spectra (>18 m). Hence, beige and purple block lithologies are clearly distinct in HiRISE color but are unconstrained by VSWIR spectra.

Comparison between HiRISE color properties of Noachian Basement units and megabreccia (Fig.
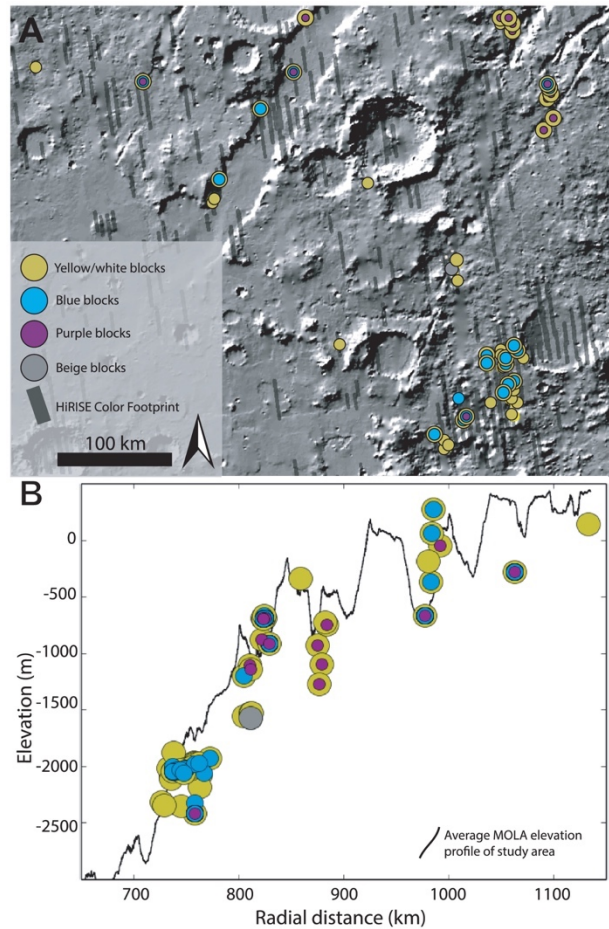
Fig. 2.7: Distribution of megabreccia colors. (A) Megabreccia outcrops of different visual HiRISE color (yellow/white, blue, purple, and beige colors) properties plotted in plan-view with MOLA hillshade background. Outcrops with multiple colored circles represent outcrops that include blocks of multiple color properties. HiRISE color footprints in dark grey. (B) Megabreccia outcrops of different color properties plotted by radial distance and MOLA elevation. Outcrops with multiple colored circles represent outcrops that include blocks of multiple color properties. The black line in the background represents the average MOLA elevation profile of the study area.

2.6B) show that blue megabreccia blocks have similar HiRISE color properties and CRISM spectral characteristics as the Blue Fractured Unit (see section 2.5.2). Similarly, yellow/white megabreccia mostly share HiRISE color properties with Fe/Mg-smectite-bearing Stratified Basement Unit and Mixed Lithology Plains Unit on a regional scale (see section 2.5.2). The purple and beige megabreccia blocks are clearly distinct in color properties and are not represented in the larger basement units.

The spatial distributions of the megabreccia color classes were investigated visually for spatial patterns or groupings (Fig. 2.7). Most megabreccia exposures were dominated by yellow/white colored blocks. Beige megabreccia blocks were not easily distinguishable from yellow/white properties by visual inspection. In our quantification and classification maps, beige blocks only appeared in one out of the 8 HiRISE color images processed within our study's scope. Through quantified processing of all megabreccia-containing HiRISE color images by hand-mapping individual blocks, future studies could likely locate more beige megabreccia blocks. Generally, differently colored megabreccia appeared to occur directly juxtaposed next to each other throughout the study area where exposures of megabreccia are seen with no visual evidence of spatial groupings or changes with distance from the basin center or depth.

2.5.2 Geological units of the Noachian Basement Group

Based on coupled HiRISE, HiRISE DEM, and CRISM analyses, we define 5 distinct geological units within the Noachian Basement Group: Stratified Basement Unit, Blue Fractured Unit, Fe/Mg-smectite-bearing Mounds Unit, Mixed Lithology Plains Unit, LCP-bearing Plateaus Unit; 2 geomorphological features, megabreccia (see section 2.5.1) and ridges; and one mineral deposit type, kaolinite-bearing bright materials. All geological units, geomorphological features, and mineral deposits of the Noachian Basement Group defined within this study are shown in Table 2.3 and characteristic spectra are shown in Fig. 2.8.

2.5.2.1 Stratified Basement Unit

The Stratified Basement Unit (SBU) consists of materials of different albedos, layered at ~10-m scale. Its exposures extend over several kilometers, while individual layers can be traced over several hundreds of meters up to one kilometer (Fig. 2.9). The SBU is typically only exposed in graben walls, although a few examples occur in eroded flat terrains as well. Graben exposures of SBU typically underlie 100s of meters of overlying units. A total of 19 different exposures of SBU were observed throughout the NW part of the Isidis impact structure (Fig. 2.9) with horizontal extents ranging over 0.2-8 km. The total thicknesses of these layered packages range between 50-450 m. Single SBU exposures consist of between 6-20 layers with a range of layer thicknesses from 8-42 m. It is likely that certain layer boundaries are not resolved at

Table 2.3: Summary table of geological units (plain text), geomorphological features (in italics), and mineral deposit (in italics and bold) within the Noachian Basement.

Unit/Feature Name	Acronym	CRISM Composition	Geomorphology	Stratigraphic level/Time order	Relevant figure(s)
Stratified Basement Unit	SBU	Fe/Mg-smectite	Individual layers have a thickness of 8-42 m Between 6-20 layers in each exposure Exposures have a horizontal extent of 300 m to 10 km	Lower	Fig. 2.8-9
Blue Fractured Unit	BFU	LCP (low centroid) Occasional, minor Fe/Mg-smectite	Highly fractured polygonal patches of bedrock Distinct blue color in HiRISE	Lower	Fig. 2.8-10
Fe/Mg-smectite Mounds Unit	SmMU	Fe/Mg-smectite	Topographic highs with sharp contact to the Mixed Lithology Plains Unit Ridged and knobby mounds	Unknown - potentially lower	Fig. 2.8, 2.12
Megabreccia	*MB*	*LCP (low centroid) Fe/Mg-smectite Unknown for beige- and purple-colored blocks in HiRISE*	*Angular or sub-rounded blocks with abrupt textural contrast to surrounding matrix materials Distinct blue, yellow, beige, and purple colors in HiRISE*	*Lower-middle depending on outcrop relationship with SBU and MLPU*	*Fig. 2.8, 2.14-15*
Mixed Lithology Plains Unit	MLPU	Mixture of LCP (high centroid) and Fe/Mg-smectite	Low-lying plains Generally heterogeneous with fractured, knobby, or smooth terrains	Middle	Fig. 2.8, 2.10-12
LCP-bearing Plateaus Unit	LPU	LCP (middle centroid); no evidence of alteration	Topographic highs Smooth, flat plateaus	Upper	Fig. 2.8, 2.10-12
Ridges	*R*	*Fe/Mg-smectite*	*Semi-linear ridges May occur in 6 different geometric configurations (Pascuzzo et al., 2019) Bright white or yellow in HiRISE*	*Younger - no known contact to LPU, SmMU, and KBM*	*Fig. 2.8, 2.16*
Kaolinite-bearing bright materials	**KBM**	**Kaolinite**	**Irregular, bright, white patches of 100s of meters**	**Younger - younger than LPU**	**Fig. 2.8, 2.13**

27
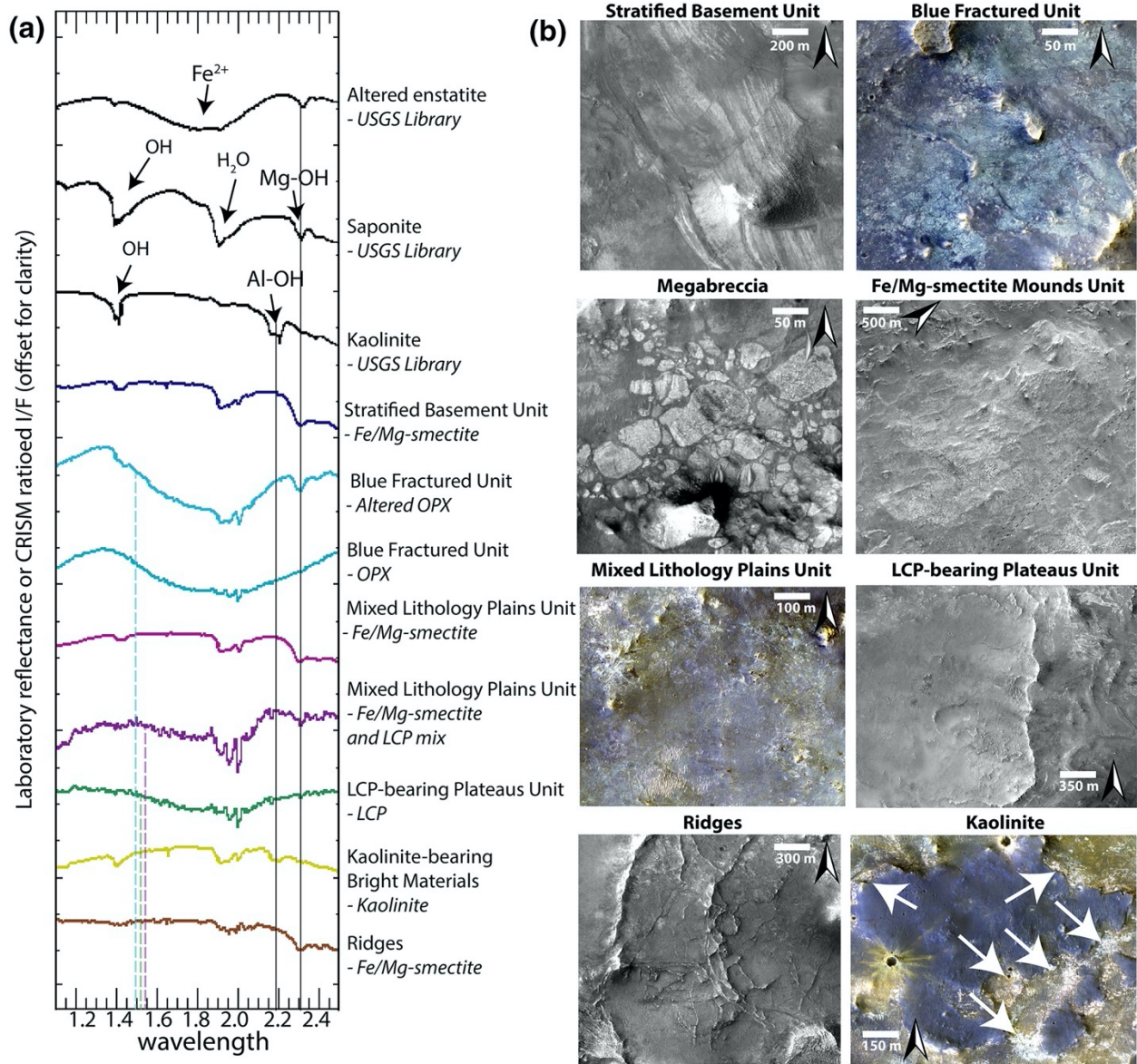
Fig. 2.8: All defined geological units and their spectroscopic signatures. (A) Locations of Stratified Basement Unit (SBU) outcrops within the study area shown in white dots. Grey rectangles are HiRISE footprints. Locations B, C, and D refer to the position of panel B, C, and D. (B) SBU outcrop within the wall of the fossae. Block arrows show the location of two faults causing the offset of layers within the Stratified Basement Unit from HiRISE ESP_019476_2005. (C) Examples of similar SBU outcrops with multiple layers in Northeast graben wall from HiRISE ESP_032227_2040. (D) Example of SBU within the wall of the fossae from HiRISE ESP_016153_2005. Blue arrows point towards bluish layers in HiRISE color. Here, Fe/Mg-smectite-bearing layers appear white. Note that bluish layers and SBU appear to be interlayered. Apparent folding in outcrops is the result of exposure and not a result of deformation (see section 2.5.2.1).

HiRISE resolution. Nine of these 19 exposures of Stratified Basement Unit had CRISM coverage and were found to be dominated by Fe/Mg-smectite compositions (Fig. 2.8). The layers are often displaced along faults that formed after the deposition of the SBU in its current position (Fig. 2.9.B). In addition, the faults of the Nili Fossae graben itself cross-cut the layers of SBU (Fig. 2.9.B-D). As noted by Mustard et al. (2009), bluish units are occasionally within yellow/white layers of the SBU (Fig. 2.9.D). These units have the same spectral signature as Blue Fractured Unit (section 2.5.2.2) with minor Fe/Mg-smectite components in CRISM (Fig. 2.8). Additionally, HiRISE color analyses show that bluish layered materials have color properties similar to BFU cluster in Fig. 2.6.B, whereas all other SBU materials have color properties similar to the Fe/Mg-smectite cluster in Fig. 2.6.B.

Orientations of layers and contact segments were measured over exposures of several kilometers in Nili Fossae graben walls. The strikes of layers in the SBU (n=60) were N-S strike range (300-58º) with a westward shallow dip with a range of 2-26˚ and a median 10˚. A few anomalous exposures of megabreccia blocks underlie the SBU (Fig. 2.15.C). The contact segments (n=6) between SBU and underlying megabreccia blocks had a similar N-S strike range (299-42º) with a westward shallow dip with a range of 7-14˚ and a median of 12˚. In order to achieve an average of orientations for all layers and contact segments, we excluded high error fit data and stacked measurement segments for a single calculation (Quinn and Ehlmann, 2019b). The stacked solution for SBU orientation is a strike of 0˚ and westward dip of 4˚ (rake error, θ_{max}=17º), while the contact between the SBU and anomalous underlying megabreccia is a strike of 19˚ and westward dip of 9˚ (θ_{max}=8º). While some of the layers appear deformed or folded (e.g. Fig. 2.9.D and Fig. 2.15.C), we determined using HiRISE orthophotos draped over HiRISE DEMs, contour lines, and fitting of planes to layers that the apparent folding was a viewing geometry effect due to the curved nature of the exposure and overhead view.

2.5.2.2 Blue Fractured Unit

The Blue Fractured Unit (BFU) consists of a generally bright, highly fractured texture that appears primarily blue in HiRISE color, i.e., it has diminished NIR and Red albedo relative to typical Martian materials (Fig. 2.8-10). The BFU is usually exposed as relatively small patches (~100-500 m) within the Mixed Lithology Plains Unit, but outcrops of several kilometers are also observed (section 2.5.2.4; Fig. 2.10.F, Fig. 2.20). No craters are observed within these small units. The contact between the BFU and other parts of the Noachian Basement Group is sharp. However, due to the limited spatial extent and erosion of BFU, we do not see any of these contacts exposed in three dimensions, so the nature of the contact relationships is challenging to assess.

Compositionally, the Blue Fractured Unit has a characteristic LCP-dominated spectrum with a very deep Fe^{2+}-related absorption band (Fig. 2.8). The spectral characteristics of the three LCP-bearing units defined within this study are distinguishable by the spectral centroid between 1 and 2 μm (Fig. 2.8).
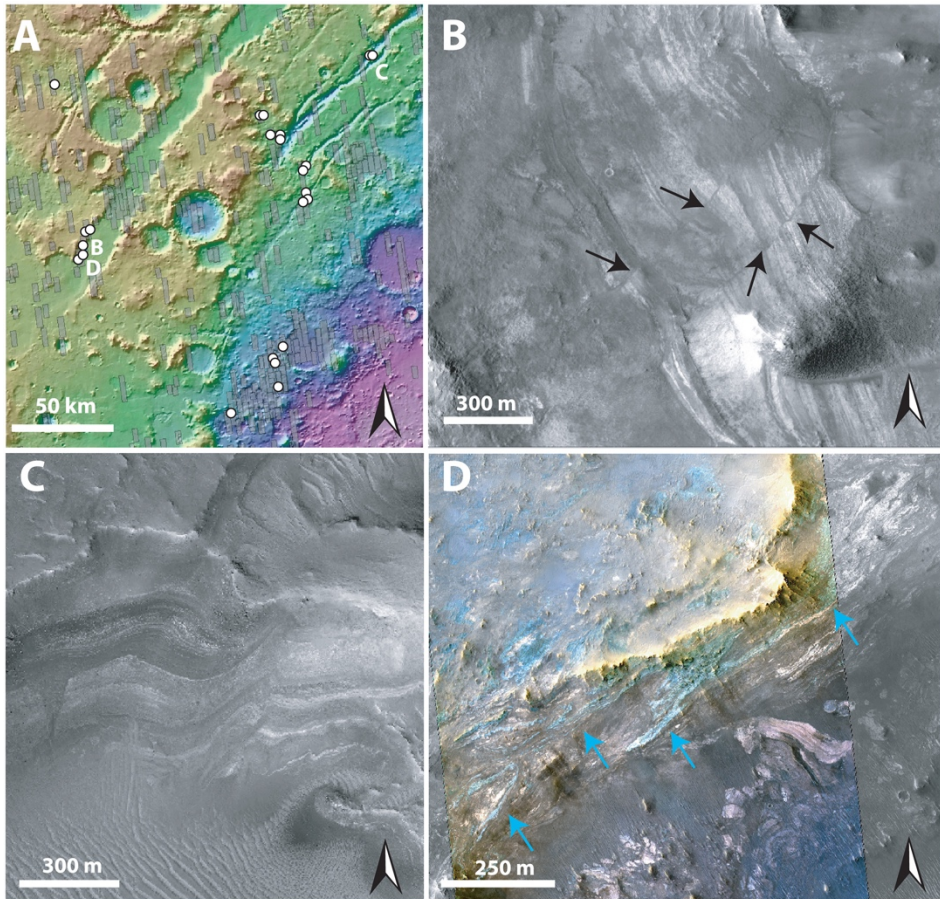
Fig. 2.9: HiRISE images of Stratified Basement Unit. (A) Locations of Stratified Basement Unit (SBU) outcrops within the study area shown in white dots. Grey rectangles are HiRISE footprints. Locations B, C, and D refer to the position of panel B, C, and D. (B) SBU outcrop within the wall of the fossae. Block arrows show the location of two faults causing the offset of layers within the Stratified Basement Unit from HiRISE ESP_019476_2005. (C) Examples of similar SBU outcrops with multiple layers in Northeast graben wall from HiRISE ESP_032227_2040. (D) Example of SBU within the wall of the fossae from HiRISE ESP_016153_2005. Blue arrows point towards bluish layers in HiRISE color. Here, Fe/Mg-smectite-bearing layers appear white. Note that bluish layers and SBU appear to be interlayered. Apparent folding in outcrops is the result of exposure and not a result of deformation (see section 2.5.2.1).

Boxplots of the centroids show that the interquartile ranges for centroids of BFU, LCP-bearing Plateaus Unit, and Mixed Lithology Plains Unit are separated, although there is some minor overlap between the full ranges of centroids between the 3 different geological units (Fig. 2.18). The median spectral centroid of this LCP band in BFU is 1.535 μm, which is the lowest, compared to other LCP-compositions in the Noachian Basement Group (Fig. 2.8). Usually, the BFU does not appear to contain Fe/Mg-smectite in CRISM spectra. However, minor Fe/Mg-smectite signatures can occasionally occur (Fig. 2.8). The distinct composition, textural expression, clear contacts, occasional volumetric and km-scale outcrops, and a variety of different morphological expressions suggest that the Blue Fractured Unit is a geological unit.
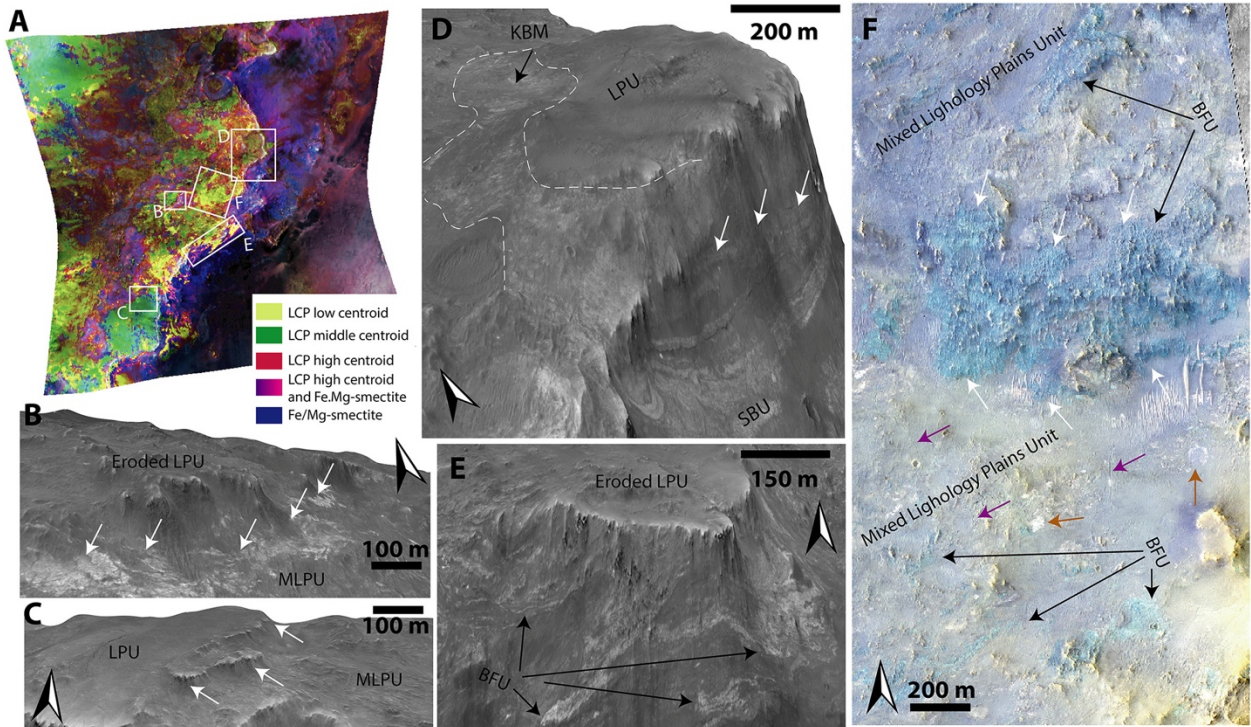
Figure 2.10: CRISM bandmap and HiRISE DEM images of Noachian Basement stratigraphic relationships. (A) Bandmap of CRISM image FRT00009D44 where R: LCPINDEX, G: LCP centroid custom parameter, B: D2300. White rectangles show the locations of HiRISE images in panels B-F. (B) Eroded remnants of LCP-bearing Plateaus Unit that have a gradual contact between a particularly bright Fe/Mg-smectite-bearing part of Mixed Lithology Plains Unit. (C) Example of LPU elevated compared to MLPU with well-defined edge of plateau (white arrows) with break in slope to MLPU (D) LPU elevated above Stratified Basement Unit exposed in the largest Nili Fossae trough. Additionally, a front of kaolinite-bearing bright materials occur on the edge of the LPU. (E) Eroded LPU overlying Stratified Basement with bluish layers. The same location in HiRISE color can be seen in Fig. 9.D. (F) Particularly resistant example of Blue Fractured Unit forming a full outcrop that stands out compared to surrounding MLPU. Note that the mineralogical boundary between MLPU and BFU is sharp (white arrows). Several smaller angular blocks of BFU can be observed within the MLPU. Examples of putative megabreccia blocks eroded flat occur within the MLPU as well (brown arrows). Large fractures can be observed in the MLPU (purple arrows). All HiRISE images are from HiRISE ESP_016153_2005. All examples from HiRISE DEM have been vertically exaggerated by 3.

2.5.2.3 Fe/Mg-smectite-bearing Mounds Unit

The Fe/Mg-smectite-bearing Mounds Unit (SmMU) occurs near the proposed landing ellipse in NE Syrtis and southwest of the proposed ellipse surrounded by the Syrtis lavas (Ehlmann & Mustard, 2012; Bramble et al., 2017; Quinn and Ehlmann, 2019a). Similar to geomorphic features also noted by Bramble et al (2017), the SmMU always occurs as km-scale diameter mounds protruding with a vertical elevation of up to around ~50 m above the surroundings, which are primarily composed of Fe/Mg-smectite from CRISM observations (Fig. 2.12). These mounds usually have a sharp compositional, sometimes sharp topographical, and potentially stratigraphic contact (Fig. 2.12.E) with the generally flat-lying adjacent

Mixed Lithology Plains Unit, suggesting that they form a geological unit with a singular geomorphological mode of occurrence (Fig. 2.12).

2.5.2.4 Mixed Lithology Plains Unit

The most extensive parts of the Noachian Basement Group consist largely of eroded plains (Fig. 2.10-12). This Mixed Lithology Plains Unit (MLPU) are usually dominated by a spectral mixture of minor LCP and
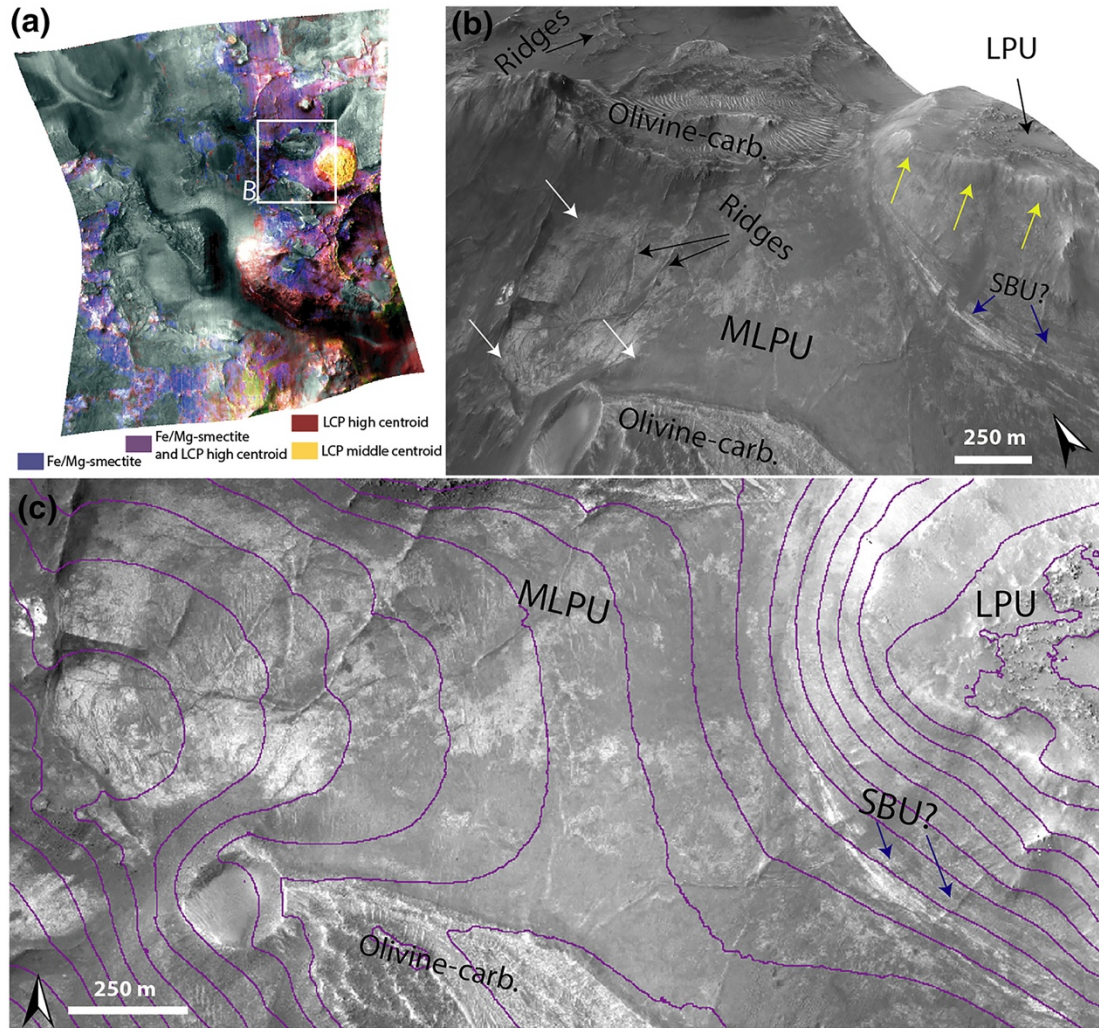
Figure 2.11: CRISM bandmap and HiRISE DEM images of Noachian Basement stratigraphic relationships. (A) Bandmap of CRISM image FRT0000B438 where R: LCPINDEX, G: LCP centroid custom parameter, B: D2300. White rectangle shows the position of panel B. (B) Example of contact between LCP-bearing Plateaus Unit and Mixed Lithology Plains Unit (yellow arrows), where LPU is elevated compared to MLPU. Note albedo transitions in MLPU correlate roughly with stronger/weaker Fe/Mg-smectite signatures in the CRISM bandmap, although the textural change is diffuse and smooth (white arrows). Ridges appear to be cross-cutting part of the MLPU (black arrows). We also observe a transition between MLPU to a putative outcrop of Stratified Basement Unit underlying the LPU (blue arrows). HiRISE image from ESP_027691_2025. (C) 2D-view of the same area as panel B with superimposed contour lines with 20 meter intervals. This sections highlights the ambiguous contact between the Stratified Basement Unit and MLPU in smaller outcrops. Here, both units appear to occupy the same topographic interval.
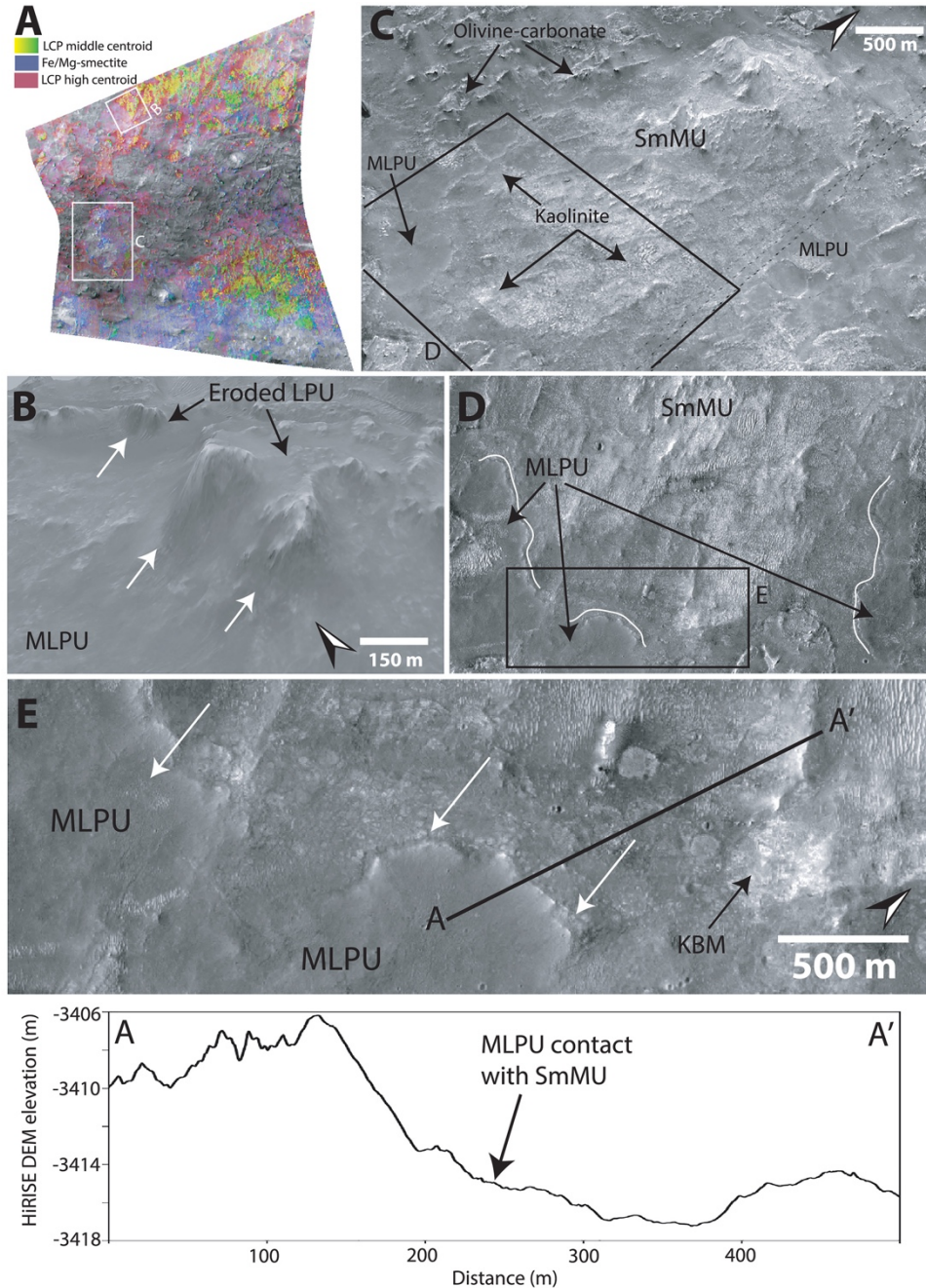
Figure 2.12: CRISM bandmap and HiRISE DEM images of Noachian Basement stratigraphic relationships. (A) Bandmap of CRISM image FRT0000161EF, where R: LCPINDEX, G: LCP centroid custom parameter, B: D2300. White rectangles show the location of HiRISE images in subsequent panels. (B) Contact between eroded remnants of the LCP-bearing Plateaus Unit and Mixed Lithology Plains Unit in NE Syrtis from HiRISE ESP_015942_1980. (C) Fe/Mg-smectite Mound Unit from HiRISE ESP_016931_1980. Stippled black lines are the image seam between HiRISE images ESP_016931_1980 and HiRISE ESP_015942_1980. Olivine-carbonate appears as minor mesas (large black arrows). Notice minor patches of kaolinite that occur at the edges of SmMU (large black arrows). Black rectangle shows position of panel D. (D) Contact between SmMU and MLPU outlined in white lines. Black rectangle shows position of panel E. (E) MLPU appears in sharp contact with the SmMU exhibiting a lobate morphology (white arrows). HiRISE DEM elevation profile line segment A-A' shows the steep scarp of lobate MLPU contact to base of SmMU with 10 m elevation drop. All examples from the two HiRISE DEMs have been vertically exaggerated by 3.

33

Fe/Mg-smectite components (Fig. 2.8). The compositional transitions are diffuse in CRISM bandmaps, and there are no significant geomorphological distinctions between plains of different compositions at HiRISE-scale, although some albedo contrasts may occur (Fig. 2.10-12). The LCP spectral signature has subdued band depths compared to the absorptions of Blue Fractured Unit (Fig. 2.8). The median spectral centroid of typical MLPU LCP is higher, ~1.549 μm, than other LCP-bearing units within the study area. Certain parts of the Mixed Lithology Plains Unit appear to be associated primarily with LCP while other parts appear to be associated primarily with Fe/Mg-smectite. Mixing with Fe/Mg-smectite does not affect the position of the centroid much (Fig. 2.18), see section 2.6.2. The full range of the LCP centroid is larger for MLPU compared to LCP-bearing Plateaus Unit and Blue Fractured Unit, which is unsurprising due to the vast size and heterogeneity of the unit (Fig. 2.18). However, the interquartile ranges of the MLPU are clearly at longer wavelengths than the interquartile ranges of LCP-bearing Plateaus and Blue Fractured Unit (Fig. 2.18). In addition, bandmaps utilizing the LCP centroid parameter easily delineate the morphological features that are characteristic for each unit (Fig. 2.10.A).

In general, the Mixed Lithology Plains Unit are characterized by laterally extensive plains with little topographic relief that occur in between megabreccia outcrops and other mound-, plateau-, and mesa-forming units. The MLPU is texturally smooth with the exception of occasional polygonal fracturing (10s of meters in length). In general, only smaller craters (10s of meters to 100s of meters) or no craters at all are observed superposed on the MLPU. Large parts of the MLPU are featureless. However, the albedo and color of the MLPU can vary at the HiRISE-scale. Bright circular features and irregular bright patches are sometimes observed although these textural features appear to have similar elevations with no significant geological contacts. (Fig. 2.10-12).

We determine that the Mixed Lithology Plains Unit should be defined as its own unit. This is based on the fact that MLPU has an identifiable lithology with spectral signatures (high centroid LCP and Fe/Mg-smectite mixtures) unique to this unit, a thickness, and contacts to the Stratified Basement Unit, LCP-bearing Plateaus Unit, and Fe/Mg-smectite-bearing Mounds Unit (see subsections of section 2.5.2). However, the occasional entrainment of blocks/patches of megabreccia and Blue Fractured Unit within the MLPU convolutes the distinction between these 3 units/features (e.g. Fig 2.10.F). Megabreccia generally occur within the Mixed Lithology Plains Unit as blocks. Hence, megabreccia are considered to be a geomorphological feature contained within the MLPU. However, the Blue Fractured Unit is sometimes of large spatial extent with defined volume and contact relationships, necessitating its own unit definition (section 2.5.2.2). Completely unambiguous 3-dimensional exposures of the Mixed Lithology Plains Unit are rare, but a few MLPU exposures in grabens have a thickness of 10s of meters to 100 meters with sharp transitions and contacts with underlying Stratified Basement Unit (Fig. 2.10.A and Fig. 2.15.C). In a few exposures, the contact between MLPU and SBU is ambiguous but suggestive of MLPU

surrounding the SBU (Fig. 2.11.B-C). Interpretation of the origin of the complex MLPU is further described in 4.3.4.

2.5.2.5 LCP-bearing Plateaus Unit

The LCP-bearing Plateaus Unit (LPU) generally occurs as elevated plateaus or mesas with a horizontal extent of 100s of meters (Fig. 2.10-12). The plateau surfaces are smooth and featureless with few craters. In some cases, the LCP-bearing Plateaus Unit is heavily eroded into smaller uneven, ridged surfaces even though they are still elevated from the Mixed Lithology Plains Unit. The LCP-bearing Plateaus Unit has a distinct LCP spectral signature from the two other LCP-bearing geological units. The LPU have a median spectral centroid of ~1.544 μm, intermediate between the Blue Fractured Unit spectral signature and the Mixed Lithology Plains Unit (Fig. 2.8). In addition, the LPU do not exhibit any Fe/Mg-smectite or hydration signatures, not even occasionally (Fig. 2.8). Typically the LPU are 10-40 m thick, and there is a sharp break in slope at the contact with the underlying Mixed Lithology Plains Unit (Fig. 2.10.C). The slopes of LPU-associated plateaus are often obscured and usually have some debris cover but do not appear to shed boulders. In certain cases, the slopes may be highly eroded (Fig. 2.12.B). However, highly eroded parts of the LPU are not to be confused with the Fe/Mg-smectite-bearing Mounds Unit. Eroded parts of the LPU still maintain steep slopes and their characteristic LCP compositions, whereas the Fe/Mg-smectite-bearing mounds are much larger (km-scale) with more gradual slopes and characteristic
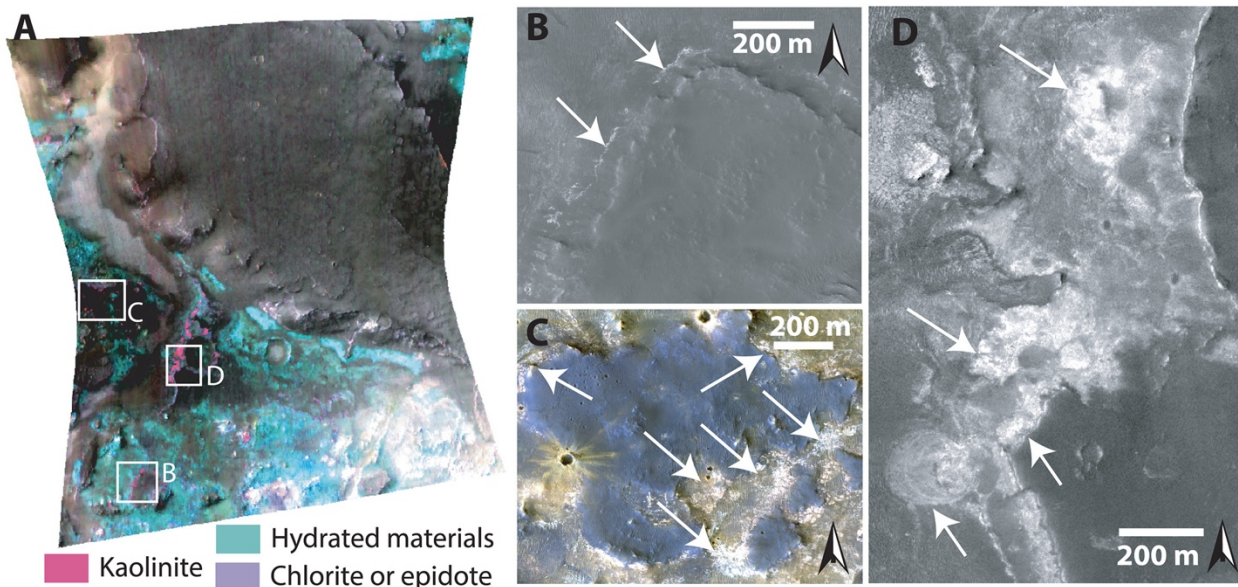
Fig. 2.13: CRISM bandmap and HiRISE DEM images of kaolinite. (A) CRISM bandmap image FRT0000CBE5 of parameters R:BD2.17 μm, G: D2.30 μm, and B: D2.32 μm from Carter et al. (2013). Pink color denotes kaolinite, turquoise color denotes materials containing hydrated minerals including both Noachian Basement and Olivine-carbonate Unit, purple denotes the presence of either chlorite or epidote (Carter et al. (2013)). (B) Kaolinite present as a layer overlain by a mafic mesa from HiRISE PSP_010206_1975. (C) Example of most general appearance of kaolinite as bright, irregular patches from HiRISE PSP_010206_1975. (D) Example of bright circular features of kaolinite from HiRISE ESP_022601_1975.

Fe/Mg-smectite compositions. Due to the fact that the LCP-bearing Plateaus Unit has a distinct composition, characteristic contacts to SBU and MLPU, and diminished susceptibility to erosion that results in well-formed plateaus, eroded plateaus, and ridged plateaus, we define the LPU to be a geological unit.

2.5.2.6 Ridges

Geomorphological features that occur as ridges in the Noachian Basement Group have been characterized quite thoroughly geomorphologically and compositionally in previous literature (Saper et al., 2013; Bramble et al., 2017; Pascuzzo et al., 2019). The ridges features refer to elevated curvilinear-linear features that cross-cut most of the Noachian Basement Group units (Fig. 2.11 and Fig. 2.16). Pascuzzo et al. (2019) noted that there are six different geomorphological types of ridges based on different geometric configurations. We refer to Pascuzzo et al. (2019) for images and descriptions of these. The ridges have all been observed to be composed of Fe/Mg-smectite-bearing materials that typically have weaker absorption minima compared to the host rock (Pascuzzo et al., 2019). We have observed ridges within or cross-cutting SBU, BFU, megabreccia, and MLPU (Fig. 2.16).

2.5.2.7 Kaolinite-bearing bright materials

Kaolinite-bearing bright materials (KBM) have been described in various previous contributions that have noted they may be a weathering front or a unit of altered materials of distinct composition from the rest of
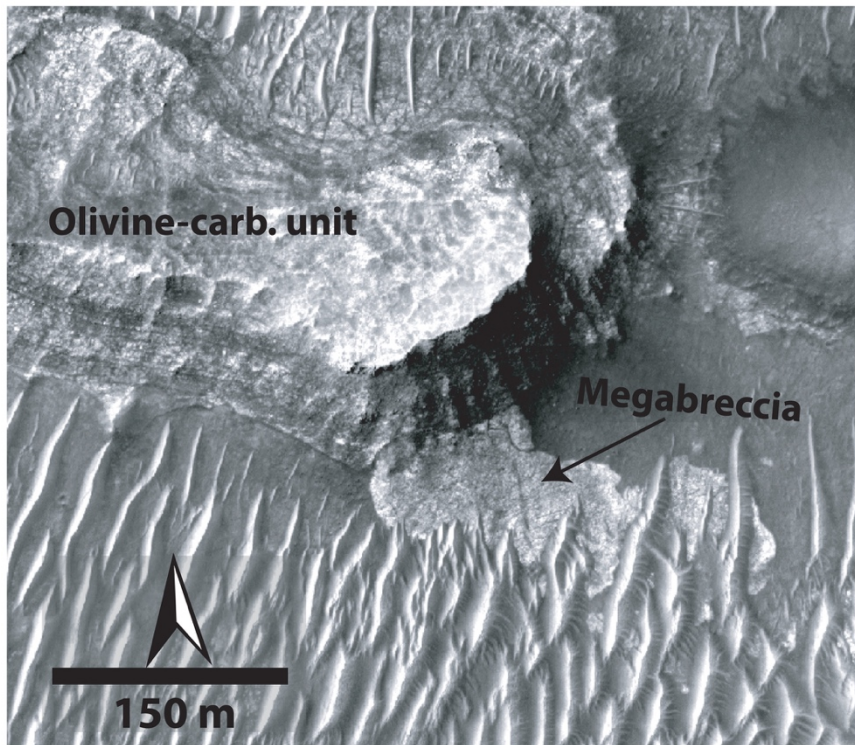
Fig. 2.14: Megabreccia underlying olivine-carbonate unit from HiRISE ESP_035062_1995. There is no accompanying CRISM but the olivine-carbonate unit is defined in Goudge et al. (2015) and is consistent with its morphologic expression.

the Noachian Basement Group (Mustard et al., 2009; Ehlmann et al., 2009; Ehlmann & Mustard, 2012; Bramble et al., 2017). In this study, kaolinite-bearing bright materials are observed to have a variety of geomorphological expressions. KBM are always bright in HiRISE and white in HiRISE color. They occur in small patches ~100 m across up to patchy exposures with km-wide extent. These kaolinite-bearing bright materials sometimes have an irregular expression with diffuse or gradual contacts to surrounding materials (Fig. 2.10.D and Fig. 2.13.C). However, our studies find that kaolinite-bearing bright materials can also occur as a ~5 m thick layer in a mesa and as circular features with semi-concentric layering (Fig. 2.13), although KBM are generally superficial (<2 m thick). The KBM classify neither as a geological unit nor as a geomorphological feature as they typically lack clear stratigraphic contacts, 3-dimensionality of exposure, and a consistent identifiable geomorphological expression. Instead, we classify kaolinite-bearing bright materials as mineral deposits that are primarily identified based on composition in CRISM. The KBM appear to be at a higher stratigraphic level than Stratified Basement Unit (Fig. 2.10.D). We observe that KBM have formed within or on Fe/Mg-smectite Mounds Unit (Fig. 2.12.C), Mixed Lithology Plains Unit, and LCP-bearing Plateaus Unit (Fig. 2.10.D).

2.5.3 Stratigraphic relationships

The 5 geological units have defined contacts in HiRISE DEMs that appear to be systematic throughout the western part of the Isidis structure as examined at 14 key locations (Fig. 2.1). A synthesis of our stratigraphic analysis has been visualized through a schematic cross-section of the area (Fig. 2.17). Stratified Basement Unit and Blue Fractured Unit always occur in lowermost parts of the basement stratigraphy. In a single outcrop, bluish materials similar to BFU in composition and texture are interlayered with SBU (Fig. 2.9.D). This would suggest that BFU and SBU are at a stratigraphically similar level and possibly related, although determining this would require additional HiRISE data along the Nili Fossae scarps.

Megabreccia also appear to be a geomorphological feature of similar relative emplacement age as the lowermost units. Megabreccia are always observed to clearly underlie the Olivine-Carbonate Unit, and we did not find any megabreccia outcrops where this contact is ambiguous (Fig. 2.14). Additionally, no Olivine-Carbonate Unit compositional elements are found within megabreccia (Fig. 2.6). However, while some megabreccia deposits overlie parts of the Stratified Basement Unit, other megabreccia appear to underlie parts of the SBU (Fig. 2.15). In certain cases, the contact between megabreccia and SBU is obscured as both materials have eroded to a flat plane. In these cases, it cannot be distinguished whether one is overlying the other or whether exposures are adjacent. Certain megabreccia blocks exhibit layering as described in Mustard et al. (2009) (Fig. 2.4).
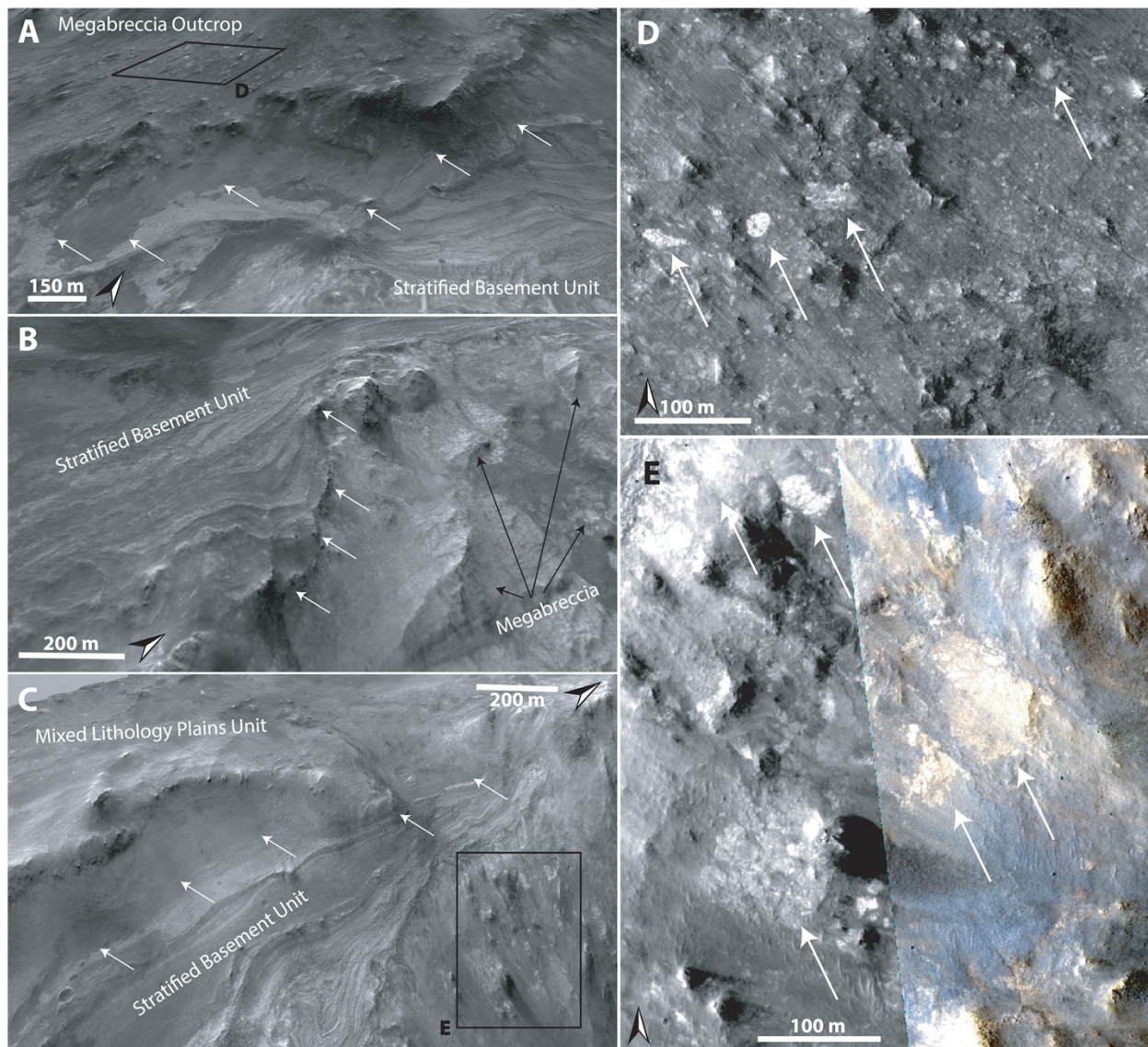
Fig. 2.15: Noachian Basement exposures in the western Nili Fossae graben wall from HiRISE ESP_019476_2005. (A) Uppermost megabreccia outcrops within MLPU overlie Stratified Basement Unit, marked with white arrows. Black rectangle is showing location of panel D. (B) Large megabreccia blocks appear to underlie SBU. The contact between SBU and underlying megabreccia is marked with white arrows. (C) MLPU overlie SBU. The contact between SBU and MLPU is marked with white arrows. Note smaller megabreccia blocks occur vertically below the SBU in the graben wall, although no clear contact is exposed. Black rectangle is showing location of panel E. (D) View of megabreccia blocks (white arrows) present within the megabreccia exposure in panel A. (E) View of megabreccia (white arrows) present within the megabreccia exposure in panel C.

As noted in Mustard et al. (2009), the scale of layering between layered megabreccia (meters scale) and SBU (10s of m scale) does appear to different. Hence, it is not clear if potential layered megabreccia precursor rock and SBU may be related to each other. For example, the Stratified Basement Unit could be larger sections of intact crust than the megabreccia, disrupted but preserved. In addition, blue megabreccia blocks appear to be similar to the Blue Fractured Unit (Fig. 2.6). Hence, assuming the megabreccia blocks derive from BFU, the Blue Fractured Unit must have formed prior to formation of the megabreccia and is therefore stratigraphically below megabreccia deposits containing blue blocks.

The Stratified Basement Unit typically underlies the Mixed Lithology Plains Unit with a sharp contact in well-exposed km-scale outcrops (Fig. 2.15.C). In a few cases, MLPU may appear to surround SBU (Fig. 2.11), although these smaller outcrops cannot be interpreted with certainty. This could potentially suggest that minor parts of SBU are incorporated within MLPU similar to the entrainment of megabreccia and patches of BFU within the MLPU (Fig. 2.10.F). There is a clear stratigraphic relationship between LCP-bearing Plateaus Unit and Mixed Lithology Plains Unit. The LCP-bearing Plateaus Unit is always elevated and appears to overlie MLPU with a diffuse and often covered contact (Fig. 2.10-12). Additionally, no megabreccia are observed within or in contact with the LCP-bearing Plateaus Unit as megabreccia generally occur at a lower topographic and stratigraphic level.

The youngest features in the geological sequence of events are kaolinite-bearing bright materials and ridges. Ridges directly cross-cut Stratified Basement Unit, Blue Fractured Unit, megabreccia, and Mixed Lithology Plains Unit (Fig. 2.11, 2.16). However, no contact has been observed between ridges and LCP-bearing Plateaus Unit nor ridges and kaolinite-bearing bright materials, so their relative stratigraphic relationships are still uncertain. Kaolinite-bearing bright materials typically appear topographically higher than both Mixed Lithology Plains Unit and Stratified Basement Unit, although no stratigraphic contact is clearly observed (Fig. 2.10.D). In certain cases, KBM occur in the same plane as Mixed Lithology Plains Unit with a diffuse contact. We also observed that KBM have formed with a similar irregular expression and diffuse contact on eroded parts of the LCP-bearing Plateaus Unit and Fe/Mg-smectite-bearing Mounds Unit (Fig. 2.10.D, 2.12), suggesting that they have a relatively younger stratigraphic age. Megabreccia also appear to be unaffiliated with kaolinite deposits (Fig. 2.2) except for one block in the Jezero crater rim (see 4.6), although kaolinite cannot be readily distinguished from Fe/Mg-smectite in the HiRISE color classification scheme.

The most stratigraphically inscrutable geological unit is the Fe/Mg-smectite-bearing Mounds Unit. It does appear older than kaolinite-bearing bright materials (Fig. 2.12). However, the outcrops of this unit primarily occur in NE Syrtis and have no observed or resolvable contact with the Stratified Basement Unit, Blue Fractured Unit, megabreccia, and LCP-bearing Plateaus Unit. The contact between Fe/Mg-smectite-bearing Mounds Unit and Mixed Lithology Plains Unit is quite sharp compositionally
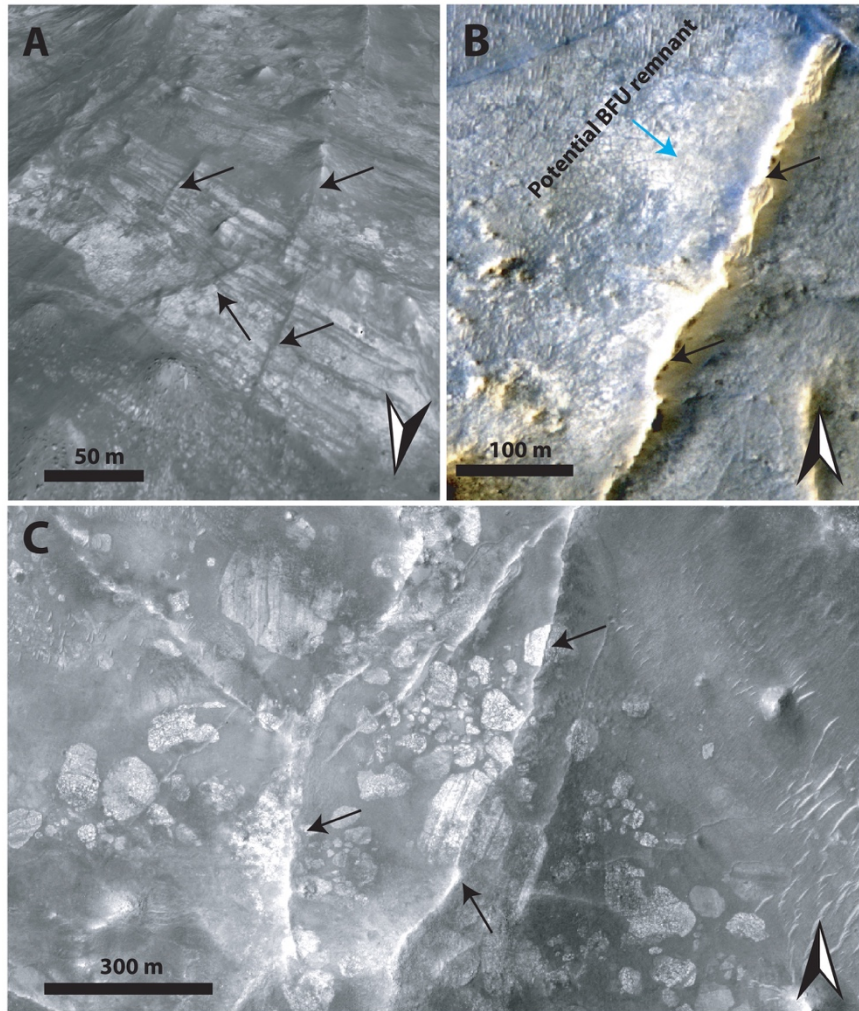
Fig. 2.16: Megabreccia relationship with ridges. (A) Ridges (black arrows) cross-cutting Stratified Basement Unit (PSP_002176_2025). (B) Ridge (black arrows) cross-cutting a putative exposure of Blue Fractured Unit (blue arrow) (ESP_052020_1985). (C) Ridges (black arrows) cross-cutting megabreccia (ESP_033572_1995).

(Fig. 2.12). In several locations, we observe an elevation drop of ~10-20 m from the top of the MLPU to the bottom of the SmMU (e.g. Fig. 2.12.E). Furthermore, the terminal parts of the MLPU appear lobate at these contacts suggesting that the MLPU may be embaying the SmMU (Fig. 2.12). This would make SmMU stratigraphically older than MLPU.

2.6 Discussion

2.6.1 Defining the Noachian Basement Group: Comparison to previous studies.

In previous studies, the Noachian Basement has generally been treated as a single mineralogically and geomorphologically heterogeneous unit. Here, we define a basement group with 5 geological units, 2 geomorphological features, and a mineral deposit based on compositional, textural, and stratigraphic contacts.
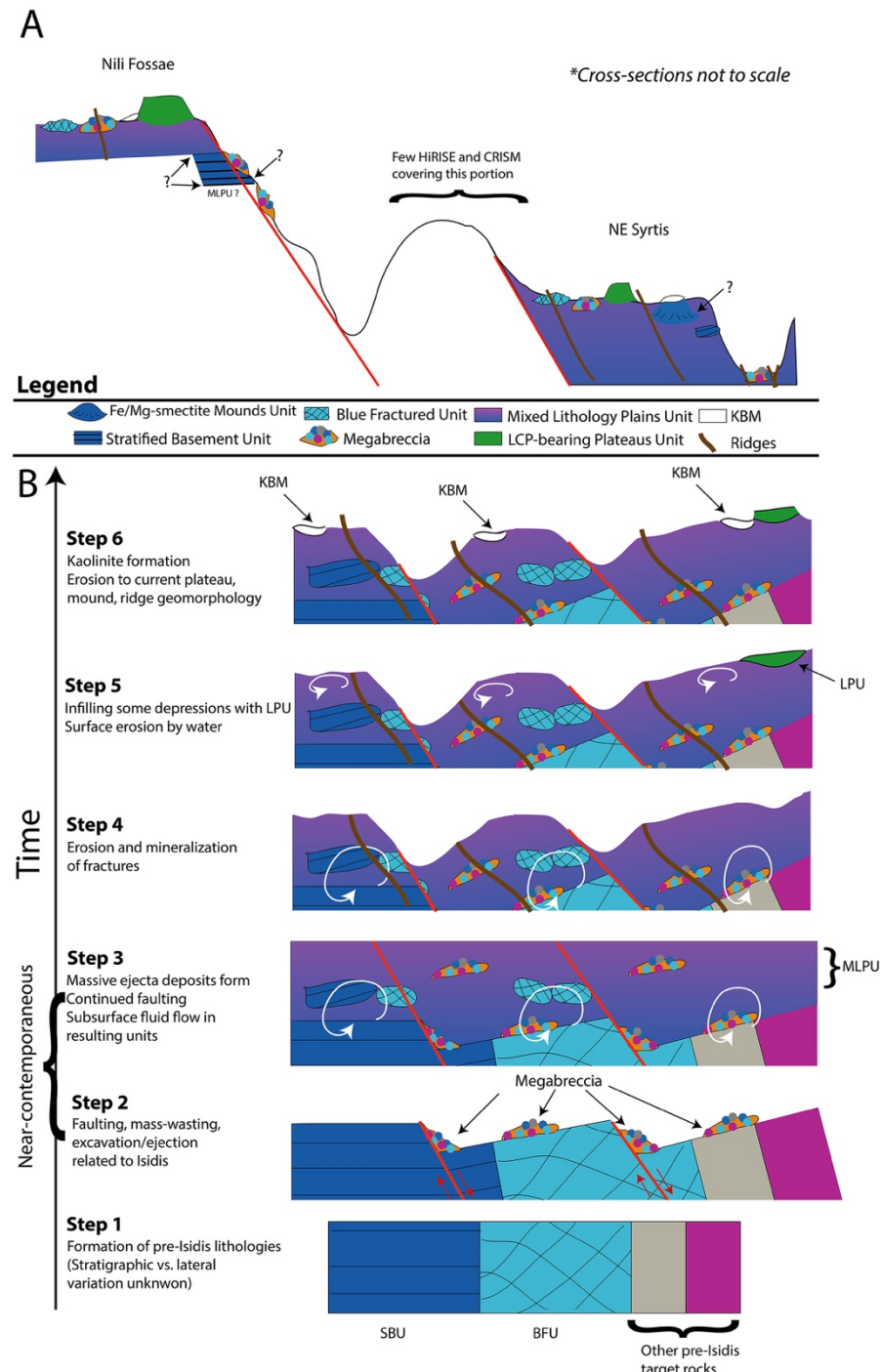
Fig. 2.17: Schematic regional stratigraphy of the Noachian Basement based on key locations in Nili Fossae and NE Syrtis. The lowermost units/features include Blue Fractured Unit, Stratified Basement Unit, megabreccia, and Mixed Lithology Plains Unit. The LCP-bearing Plateaus Unit appear to be stratigraphically above these units. Ridges are observed to cross-cut all of the lowermost units. Kaolinite-bearing bright materials (KBM) has been observed to form on LPU, Fe/Mg-smectite Mounds Unit, and MLPU. Question marks denote unresolved questions on the nature of individual contacts through lack of unambiguous contact exposures. These include the contact between BFU and MLPU, BFU and SBU, megabreccia and SBU, SmMU and MLPU, and the diffuse transition between LCP-dominated and Fe/Mg-smectite-dominated parts of the MLPU.

41

Mustard et al. (2009) noted that certain parts of the Noachian Basement were either LCP-, Fe/Mg-smectite, or kaolinite-bearing, which is similar to the spectral diversity that we have observed (Fig. 2.8). The LCP originally described in Mustard et al. (2009) is similar to the Blue Fractured Unit and LCP-bearing Plateaus Unit materials, which we clearly delineate as two different units formed at different times and occupying different stratigraphic positions. Fe/Mg-smectite from Mustard et al. (2009) includes both the Stratified Basement Unit and Mixed Lithology Plains Unit. At 5-m/pixel CTX-scale, Goudge et al. (2015) divided the Noachian Basement in Dusty Massive Basement, Altered Basement, and Ridged Altered Basement, which we all consider Mixed Lithology Plains Unit, with and without cross-cutting ridges. By contrast, our unit definitions make finer compositional distinctions and ridges are considered features. The geomorphological units defined in Bramble et al. (2017) are the most similar to our geological units. Bramble et al. (2017) defined Smooth and Knobby Plains Units similar to the Mixed Lithology Plains Unit in this study and Raised Linear Ridges Unit similar to Mixed Lithology Plains Unit with cross-cutting ridges. In addition, Bramble et al. (2017) defined Crustal Mounds/Large Crustal Mounds Units that encompass the two distinct LCP-bearing Plateaus Unit and Fe/Mg-smectite-bearing Mounds Unit defined in this study. Our study subdivides these because their mineralogy, physical expression, and stratigraphic position are distinct. It was suggested that kaolinite-bearing parts of the Noachian Basement formed later than Fe/Mg-smectite-bearing parts (Carter et al., 2014; Ehlmann et al., 2011, 2009). Likewise, it has been suggested that the ridges are a younger feature forming after the Isidis impact (Pascuzzo et al., 2019). Both are confirmed within this study. However, a series of new enigmatic geomorphological expressions including circular layered structures suggest that further study is needed to explain the full diversity in geomorphological expression of the kaolinite-bearing bright materials and that these may not be a discrete geologic unit, hence our classification here as a mineral deposit (Fig. 2.13).

2.6.2 Origin of spectral differences between LCP-bearing units

The centroid between 1 and 2 μm roughly indicates pyroxene compositions as the centers of the 1 and 2 μm Fe-related absorption bands shift when the compositions of pyroxenes change (Fig. 2.18.A-B). Orthopyroxenes (OPX) and LCP have lower wavelength centroids than high-Ca pyroxenes (HCP). However, other materials with Fe-related absorptions such as Fe-bearing smectites and Fe-bearing glasses may affect the centroid, if mixed with pyroxenes. In addition, dunes in the study area have Fe-related absorptions, and different bedrock-sand proportions within pixels could give rise to a shift in the centroid. From investigation of calculated linear mixtures with Fe/Mg-smectites (Fox et al., 2017), glasses (Cannon et al., 2017), sand from the study area and three different pyroxene compositions (OPX, LCP, and HCP; Klima et al., 2011), it appears that mixing with Fe-bearing glasses is likely to affect the centroid position (Fig. 2.18.C). Higher glass content gives rise to higher centroid position. In contrast, mixing with sand does not give rise to much change in the centroid position (Fig. 2.18.C). Mixing with Fe/Mg-smectites

can give rise to increase or decrease in centroid position depending on smectite composition (Fig. 2.18.C). We observe slight correlation between the centroid position and the D2300 band parameter that evaluates the depth of a Fe/Mg-smectite-related absorption at 2.3 μm (Pelkey et al., 2007) within altered Blue Fractured Unit (Fig. 2.18.D). This suggests that some higher centroid positions within BFU could be driven by mixture with Fe-rich smectites. However, large parts of Blue Fractured Unit, Mixed Lithology
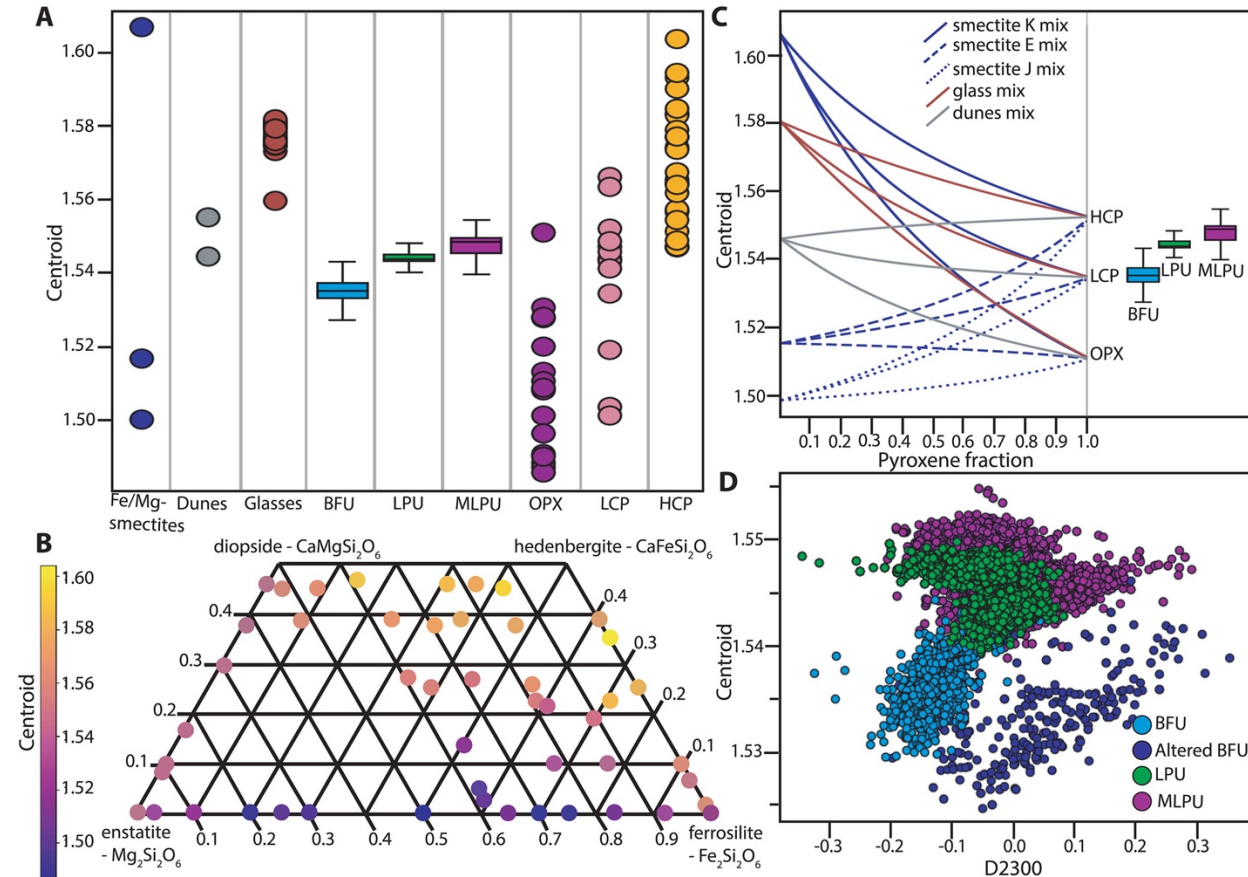
Fig. 2.18: Analysis of pyroxene centroid positions. (A) Centroid positions between 1 and 2 μm for a variety of materials. Dots show Fe/Mg-smectites of 3 different compositions from Fox et al. (2019) (navy), dunes from the study area (gray), Fe-bearing glasses from Cannon et al. (2017) (maroon), orthopyroxenes (OPX) from Klima et al. (2007) (magenta), low Ca-pyroxenes (LCP; red) and high Ca-pyroxenes (HCP; burnt orange) from Klima et al. (2011). Box plots show centroid of Blue Fractured Unit (BFU), LCP-bearing Plateaus Unit (LPU), and Mixed Lithology Plains Unit (MLPU) from two different CRISM scenes in NE Syrtis (FRT000161EF, Fig. 12) and Nili Fossae (FRT00009D44, Fig. 10). (B) Centroid positions of pyroxenes with different compositions from Klima et al. (2007) and Klima et al. (2011) plotted in pyroxene quadrilateral. Note that an increase in Ca content generally causes a higher centroid position. (C) Mixing lines for pyroxenes of three different compositions (OPX, LCP, and HCP) with the 3 different Fe/Mg-smectites from Fox et al. (2019), a representative glass from Cannon et al. (2017), and representative dune composition. Smectite K, E, and J refers to smectite of compositions $Ca_{0.23}[Fe_{2.51}Al_{0.26}Mg_{0.12}][Si_{3.51}Al_{0.49}]O_{10}(OH)_2$, $Ca_{0.40}[Fe^{III}_{1.06}Mg_{0.93}Al_{0.15}][Si_{3.70}Al_{0.30}]O_{10}(OH)_2$, and $Ca_{0.37}[Fe^{III}_{0.27}Mg_{2.31}Al_{0.08}][Si_{3.60}Al_{0.40}]O_{10}(OH)_2$ respectively. Boxplots of BFU, LPU, and MLPU are shown to the side for easy comparison. (D) Plots of centroid position and the D2300 band parameter from Pelkey et al. (2007) for pixels of BFU, altered BFU, LPU, and MLPU from the two different CRISM scenes.

Plains Unit, and all of LCP-bearing Plateaus Unit do not appear to have correlated centroid position and D2300 parameter value. In addition, we observed no correlation between centroid position and BD1900 parameter value. This suggests that mixing the Fe/Mg-smectite is not the primary control on LCP centroid position changes between the three LCP-bearing units.

Hence, the major changes between the centroid position of Blue Fractured Unit, LCP-bearing Plateaus Unit, and Mixed Lithology Plains Unit are most likely related to changes in pyroxene compositions or glass content. In this case, BFU would have the least Ca-containing pyroxenes or the least Fe-bearing glass content. The MLPU would have the highest Ca-containing pyroxenes or the highest Fe-bearing glass content. A single ultramafic or basaltic Martian meteorite can contain a variety of pyroxenes, including both pigeonites and augites, and different levels of glass contents (Papike et al., 2009). Therefore, it is unclear from a petrogenetic perspective what causes the difference in LCP between the 3 units from an orbital scale. However, the distinct stratigraphic contacts and morphological variability in combination with differing pyroxene composition and/or changing proportions of glass content points to a different origin or change in depositional/emplacement regime of the three LCP-bearing units.

2.6.3 Isidis impact processes

2.6.3.1 Megabreccia formation mechanisms

Megabreccia are formed through many processes such as impact cratering, volcanic caldera collapse, tectonic processes, mass-wasting processes, and glacial activity. The size of megabreccia blocks, reaching ~ 400 m, their distribution within a region of Isidis-related concentric ring grabens, and the presence of compositional and textural elements similar to the surrounding Noachian Basement favor formation by the Isidis impact (Fig. 2.1, 2.3). Proposed ice-related processes in Isidis Planitia during 3-2.8 Ga (Guidat et al., 2015; Souček et al., 2015) and glacial features in Nilosyrtis (Johnsson et al., 2019) have no association with megabreccia.

Impact cratering is observed to produce impact megablocks or megabreccia (meter to 100 m-scale sized breccia blocks) in both simple and complex craters on Earth (e.g., Hörz, 1982; Osinski et al., 2005; Vishnevsky & Montanari, 2007), the Moon (e.g., Mustard et al., 2011; Stöffler et al., 2012), and elsewhere on Mars (e.g., Caudill et al., 2012; Grant et al., 2008; Tornabene et al., 2013). In particular, megabreccia are associated with ballistic ejecta, melt sheet and melt flows, crater floor and peak fracturing, and gravitational flows in association with crater collapse, fall back, and modification (Table 2.1). Our observations are most compatible with formation through gravitational flows associated with transient crater collapse due to the observed extent of megabreccia, the high heterogeneity of megabreccia materials, the large block size, and lack of distance-dependency for megabreccia block sizes. In addition, we do observe some rounding of megabreccia blocks in between primarily angular blocks. Data from

terrestrial landslides and avalanches suggest that occasional sub-rounding/rounding may occur through abrasion processes (Dufresne, Bösmeier, & Prager, 2016; Krieger, 1977). Mass-wasting deposits in certain cases exhibit inverse grading due to kinetic sieving (Gray & Hutter, 1997; Gray & Thornton, 2005), which we did not observe (Fig. 2.5). Megabreccia cannot be exclusively related to tectonic processes associated with faulting and graben formation because >100 megabreccia outcrops are unrelated to any graben/fault structures of the Nili Fossae (Fig. 2.4), but faulting and slumping can be potential mechanisms for creating gravitational flows during transient collapse as discussed in section 2.6.3.3 (Fig. 2.19).

Other formation processes can be excluded based on the extent of megabreccia, as megabreccia are observed outside the proposed inner ring but within the proposed outer ring of the Isidis impact basin (Fig. 2.1 and Fig. 2.3). Crater floor/peak fracturing and a primary melt sheet (see section 2.6.2.3) would form within the inner ring, while ballistic ejecta and ejecta-associated melt flows would have an extent outside the outer ring (Barlow, 2005; Osinski, 2006; 2011; Weiss & Head, 2014). In the case of a melt flows and melt sheet origin, one might expect megabreccia to be associated with melt flow structures, such as a melt matrix, melt injections, pseudotachylitic textures, and/or lobate flow structures. Additionally, one might expect block sizes to be dependent on distance from the crater center if formed through ballistic ejecta (Oberbeck, 1975), and we did not observe such a relationship (Fig. 2.5).

2.6.3.2 Megabreccia lithologies and relationship to the basement

Quantitative investigation of HiRISE color properties showed at least four different lithologies within the megabreccia. From parallel analysis of CRISM spectra, the blue megabreccia with LCP materials are similar to the Blue Fractured Unit within the Noachian Basement Group (Fig. 2.6), and yellow/white materials are similar to other Fe/Mg-smectite-bearing materials in the Noachian Basement Group (Fig. 2.6). This indicates that blue megabreccia blocks were potentially sourced from Isidis target rock similar to Blue Fractured Unit. Yellow/white megabreccia lithologies could potentially have been sourced from any of the older Fe/Mg-smectite-bearing units (Stratified Basement Unit or Fe/Mg-smectite-bearing Mounds) but the exact relationship to Fe/Mg-smectite-bearing Noachian Basement Group units are undetermined, as all materials with Fe/Mg-smectite signatures plot similarly in the examined parameter spaces on a regional scale (Fig. 2.6). In contrast, beige and purple megabreccia materials appear to be different from any surface-exposed regional Noachian Basement units, suggesting that these megabreccia blocks are pre-Isidis lithologies not represented in the Noachian Basement Group and are Pre-Noachian or Early Noachian materials.

2.6.3.3 Testing Impact Models: How do transient craters collapse?

Traditionally, two different models for the formation of peak-ring basins and their transient crater collapse have been considered (Baker et al., 2016; Morgan et al., 2016). The main difference between

these two different models is the nature of the central uplift and its collapse (Baker et al., 2016; Morgan et al., 2016). Conceptual models based on observational evidence, suggest that the transient cavity may inwardly collapse along a series of faults (Baker et al., 2016), giving rise to massive mass-wasting from the outside inward (Fig. 2.19). Additionally, we may expect uplift in association with the central peak of the basin that could also cause mass-wasting. In contrast, hydrocode models of Orientale (Johnson et al., 2016) and Chixulub (Collins et al., 2002; Morgan et al., 2016) show that outward gravitational flow due to collapse of a transient central peak structure is the primary source of material in basin-scale impact craters at the distances at which we observe megabreccia (Fig. 2.19). In both scenarios, gravitational flows are the primary depositional mechanism of megabreccia blocks in the area between the inner and outer rings of the impact basin, which is supported by the observed attributes of megabreccia in this study. However, what differs are the stratigraphic levels from which the materials participating in the gravitational flows are derived.

In hydrocode-based models described above (Collins et al., 2002; Johnson et al., 2016; Morgan et al., 2016), we may expect deep crustal/mantle materials to be present within megabreccia, including from
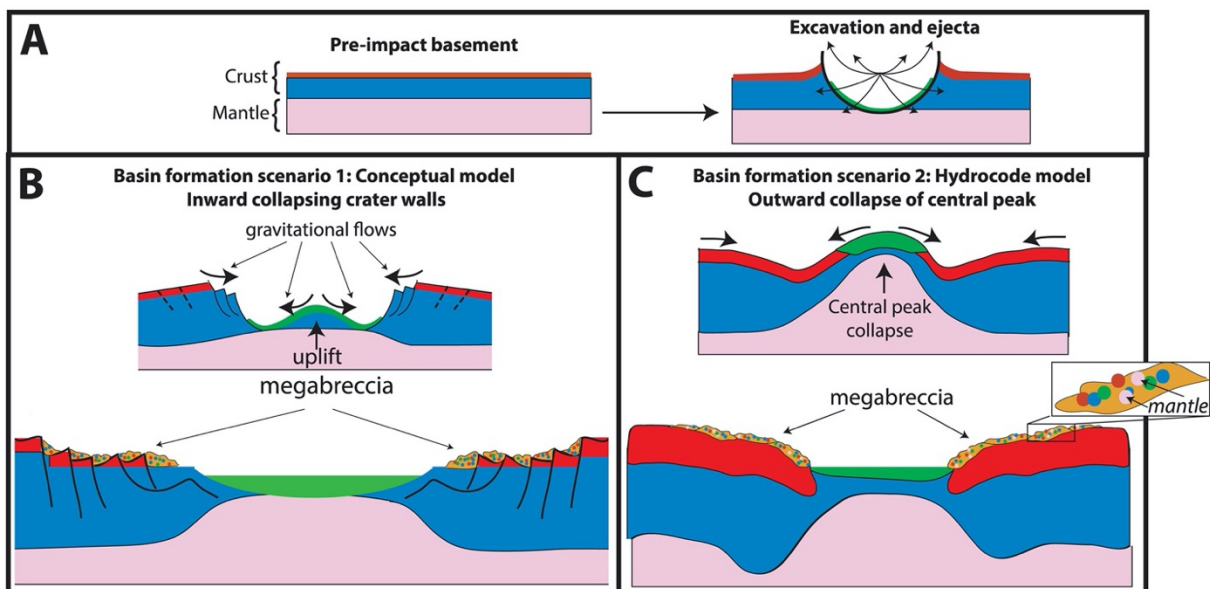
Figure 2.19: Schematic of proposed megabreccia formation mechanisms. (A) Schematic showing a two-layer crust (red and blue layers) and mantle (pink layers) that is impacted, creating a transient crater and ejecta during the excavation stage. (B) One of several possible basin-forming scenarios where collapse of the transient is inward (Baker et al., 2013). This is presumably related to a central uplift and inward collapsing walls through faulting and graben formation. Black arrows signify the predominant directions of which gravitational flows may occur. Following the inward collapse, the impact structure would consist of a series of faults and grabens associated with primarily shallow crustal megabreccia from gravitational flows. Impact melt sheets (green) are also expected to have formed, predominantly within the central basin area. (C) Another of several possible basin-forming scenarios where collapse of the transient crater occurs outward (Baker et al., 2013). From hydrocode model results, we may expect the central peak to collapse outward. The putative flow associated with this collapse is possibly able to form megabreccia, which would be more deeply derived.

the maximum depth of excavation (Fig. 2.19). The smaller Orientale basin (~860 km diameter) is modelled to retain materials from 55 km depth (mantle depth) in the collapse flow (Johnson et al., 2016), while the much smaller Chixulub crater (~200 km diameter) is modelled to retain materials from 10 km depth (mid-crustal depth) in the collapse flow (Morgan et al., 2016). Similar models of Isidis basin suggest that materials of >30 km depth (mantle depth) could be retained within the collapse flow (Trowbridge et al., 2019). In contrast, megabreccia formed through faulting and landslides from massive rock slope failure along the transient crater walls would represent primarily shallower materials (Fig. 2.19). Hence, understanding the source depth of megabreccia materials will test between these two proposed models for impact basin formation. A number of orbital detections of impact megabreccia associated with lunar impact basins have revealed compositions similar to deep crustal or mantle materials containing predominantly Mg-rich LCP and olivine in a few cases (Bretzfel et al., 2019; Klima et al., 2011; Pieters et al., 1997; Yamamoto et al., 2010), suggesting that basin-scale impacts may excavate deep crust/mantle materials.

From the four lithologies determined in this study, blue blocks have LCP spectral signatures with Fe^{2+}-related absorptions (Fig. 2.2 and Fig. 2.6). Although the high resolution spectral signatures of purple blocks are unknown, their HiRISE color profiles have low spectral angles and IR/BG (Fig. 2.6) that are usually related to Fe^{2+} crystal field splitting absorptions that predominantly occur in mafic minerals (Fig. 2.2 and Fig. 2.6). Based on the spectral signatures, purple and blue blocks are candidates for recording igneous materials. Furthermore, materials similar to purple blocks are not present within the other Noachian Basement Group unit. Hence, blue and purple megabreccia provide intriguing targets for the Mars 2020 rover instrument suite that could confirm/disprove the potential presence of deeply sourced materials within such igneous rocks, which we expect from models, meteorites, and orbital observations.

2.6.3.4 Impact melt and ejecta

An impact basin as large as the Isidis basin is likely to have produced vast amounts of melt, excavated materials, and ejecta. However, no units within the study area clearly record such processes. In our study, we find 3 units (Blue Fractured Unit, Mixed Lithology Plains Unit, and LCP-bearing Plateaus Unit) that could potentially represent impact melt bearing materials.

Current understanding of the extent of impact melt sheets is primarily based on well-exposed lunar basins and Chixulub. Most impact models and empirical observations of lunar basins and Chixulub concur that the thickest melt sheet is retained within the central depression of the impact basin (inside the inner ring) (Cintala & Grieve, 1998; Hurwitz & Kring, 2014; Morgan et al., 2016; Potter et al., 2012; Spudis et al., 2014; Vaughan et al., 2013). Hence, it appears that the primary impact melt sheet produced by the Isidis basin is not exposed within the Noachian Basement Group, as all of these units extend from the inner ring to and possibly beyond the outer ring of the structure (Fig. 2.1 and Fig. 2.19). Although by

analogy with the lunar basin Orientale, melt deposits have been proposed around the Nili Fossae (Mustard et al., 2007). Future work may consider if any geological unit closer to the inner ring (Fig. 2.1) is a candidate for the Isidis melt sheet.

However, melt related to the Isidis impact may be present in the form of excavated material, melt-rich ground-hugging flows (Osinski, Tornabene, & Grieve, 2011), smaller melt pools, and/or veneer associated with for example terracing (Cintala & Grieve, 1998). All of these units are expected to be thinner but reach larger radial distances than the central melt sheet. The Mixed Lithology Plains Unit are a candidate unit to represent a mixture of excavated, brecciated, and ejected material that is likely to contain components of melt. The unit appears geomorphologically and spectrally heterogeneous, including fractures, entrained blocks, and zones of clay formation. In addition, terminal parts of the Mixed Lithology Plains Unit appear lobate in certain cases (Fig. 2.12). This may also explain why megabreccia and parts of Blue Fractured Unit (potentially excavated target rock) appear to occur wihin a matrix of Mixed Lithology Plains Unit.

The LCP-bearing Plateaus Unit appears to have a more limited spatial extent than the Mixed Lithology Plains Unit. Impact melt processes such as melt pool formation associated with terracing and/or other melt trapping mechanisms (e.g. topographic depressions) could be responsible for smaller concentrations of melt-rich materials. Succeeding formation of these pools, the inversion of topography would presumably be caused by differential erosion. Another possibility is limited melt-rich ejecta flow forming plateaus. Analysis of Noachian Basement outside the Isidis impact structure would aid in understanding whether LCP-bearing Plateaus Unit are indeed related to the Isidis impact or have formed through a separate volcanic and/or sedimentary process. Future modelling efforts determining the extent and thickness of deposits related to the impact melt, excavation, ejecta, and gravitational flow processes during the Isidis impact would greatly improve our understanding of the units defined within the Noachian Basement Group and further our understanding of basin-scale impacts on Mars in general. Furthermore, examining these units in situ with the Mars-2020 rover, would likely definitively determine their emplacement mechanism and whether they are melt/ejecta rocks.

2.6.3.5 Several episodes of megabreccia formation?

The contact between megabreccia and the Stratified Basement Unit in certain, anomalous outcrops is enigmatic, as we observe that megabreccia blocks appear to both overlie SBU within MLPU but also underlie SBU over sections of several kilometers (Fig. 2.15). The SBU is unlikely to have formed concurrently with megabreccia as several boulder-less layers (6-20) with albedo contrast and extent to outer ring are not consistent with formation through impact melt sheet, layered ejecta, or mass-wasting processes. It is more likely, that the SBU represents a faulted (Fig. 2.9.B) but relatively intact piece of the pre-Isidis crust. If the contact between SBU and underlying megabreccia is stratigraphic, this implies that

megabreccia in the study area could potentially have two different ages (syn-Isidis and pre-Isidis). However, the contact could also be an erosional construct, allowing SBU to appear topographically above megabreccia while stratigraphically underlying megabreccia. Neither an erosional contact nor a stratigraphic boundary between SBU and underlying megabreccia can be excluded based on calculated orientations due to uncertainty associated with measurements. Determining the nature of this contact would benefit from acquiring additional stereo HiRISE images of the Western scarp of Nili Fossae where this contact may be exposed.

2.6.4 History of Hydrated Minerals and Aqueous Processes

Local abrupt color, albedo, spectral, and texture changes between Fe/Mg-smectite-bearing lithologies in yellow megabreccia and immediately surrounding Mixed Lithology Plains Unit indicate that they formed separately (Fig. 2.2, Fig. 2.4, Fig. 2.10.F, Fig. 2.15.D). If Fe/Mg-smectite within megabreccia and MLPU formed in a single event, color and spectral characteristics would be expected to be the same. Therefore, Fe/Mg-smectite within megabreccia most likely represent older aqueously altered target rock, while Fe/Mg-smectite within MLPU represent younger materials. Fe/Mg-smectite-bearing units lower in the stratigraphy (Stratified Basement Unit and possibly Fe/Mg-smectite Mounds Unit) differ in character compared to MLPU and predate MLPU. They potentially represent regions of intact pre-Isidis Fe/Mg-smectite-bearing Noachian basement. These materials could be retained within target rock recorded in megabreccia, although this relationship cannot be determined from orbit with certainty. Ridges are young features that cross-cut and thus formed after the formation of the SmMU, BFU, megabreccia blocks, and MLPU. Pascuzzo et al. (2019) found that all ridges contain Mg-smectite and/or mixed talc-saponite clay compositions and proposed that ridges most likely formed through shallow clastic intrusions or mineralization in fluid flows of subsurface fractures. Last, kaolinite-bearing bright materials in/on the MPLU are compositionally distinct and younger than most Fe/Mg-smectite-bearing materials (see section 2.5.3).

From these observations, we propose that the Noachian Basement Group records at least 4 events of hydrated mineral formation: (1) pre-Isidis Fe/Mg-smectite formation in target rock (possibly SBU and SmMU) that are now megabreccia blocks; (2) at least one and possibly several episodes of Fe/Mg-smectite formation within potential syn- Isidis impact deposits (MPLU); (3) contemporaneous or subsequent Fe/Mg-smectite formation in cross-cutting fractures that now form ridges; and (4) kaolinite formation. Other questions regarding the history of hydrated mineral formation within the Noachian Basement Group are not resolvable from orbit because the mineral assemblages and rock textures are not known. Key questions include 1) Does the nature of the aqueous processes recorded each unit differ? 2) For each unit, were hydrated minerals formed as the result of a primary aqueous depositional environment or the result of diagenetic or hydrothermal processes? 3) What was the timing and nature of fluids

leading to mineralization now exposed in ridges? 4) What was the timing and nature of the spatially restricted kaolinite-forming events? The various hydrated mineral-bearing lithologies provide intriguing targets for analysis and sampling with the Mars 2020 mission in order to deconvolve the complex aqueous history within the Noachian Basement Group.

2.6.5 Geological history of the Noachian Basement: Preferred interpretation

The 8 geological units and features of the Noachian Basement Group undoubtedly record a very long history of impact, igneous, and aqueous processes that happened over different geological time intervals from the Pre-Noachian or Early Noachian to Mid-Noachian. Stratified Basement Unit and potentially Fe/Mg-smectite Mounds Unit represent relatively intact but deformed pieces of pre-Isidis crust. Due to their Fe/Mg-smectite compositions (Fig. 2.6), Stratified Basement Unit, Fe/Mg-smectite Mounds Unit, and pre-Isidis target rock recorded within yellow megabreccia blocks either formed in or were affected by an aqueous environment before the formation of Isidis-related megabreccia and Mixed Lithology Plains Unit. Likewise, the Blue Fractured Unit was a target rock that predates the Isidis impact and was highly affected by the Isidis impact causing brecciation and excavation of the unit resulting in the patchy and blocky nature of the unit.

Following formation of these pre-Isidis units, megabreccia and the Mixed Lithology Plains Unit likely formed in association with the Isidis impact. Megabreccia most likely represent gravitational flows associated with transient crater collapse. Some of Blue Fractured Unit and pre-Isidis Fe/Mg-smectite-bearing target rocks are recorded in blue and yellow megabreccia lithologies along with 2 unknown lithological components (beige, purple) that are pre-Isidis. Entrainment of excavated target rock and megabreccia materials, heterogeneity, and the occasional lobate morphological expression of the Mixed Lithology Plains Unit suggest that this unit may record a mixture of expected impact processes such as excavation, ejecta, and melt flows. These materials must have subsequently interacted with fluids causing a larger portion of these materials to become Fe/Mg-smectite-bearing. The LCP-bearing Plateaus Unit postdates megabreccia and the Mixed Lithology Plains Unit, forming a younger unit of different spectral signature than Blue Fractured Unit and MLPU that did not have contact with fluids. Preferred candidate processes for the LCP-bearing Plateau Unit formation include later melt pools or flows associated with the Isidis impact, although additional study is needed to confirm this and other igneous/sedimentary processes cannot be excluded.

The formation of ridges follows the formation of the Stratified Basement Unit, Blue Fractured Unit, megabreccia, and Mixed Lithology Plains Unit, postdating the Isidis impact through shallow clastic intrusions or mineralization in fluid flows of subsurface fractures, affecting all units stratigraphically below the LCP-bearing Plateaus Unit. Likewise, kaolinite-bearing bright materials postdate the Isidis impact and formed in a separate, younger aqueous environment compared to pre-Isidis and syn-Isidis

units. There is no direct contact between ridges and kaolinite-bearing bright materials, but their respective lithologies suggest that they formed in separate aqueous environments.

2.6.6 Implications for Mars 2020 rover

The Mars 2020 instrument suite is likely to encounter eroded sediments or cobbles of Noachian Basement Group units within the walls and/or sedimentary materials within Jezero crater because the Jezero watershed includes large areas of Noachian Basement Group units (Goudge et al., 2015). In addition, the entire Noachian Basement Group may be explored in situ with a ~20-km extended mission that would take the Mars 2020 rover west of the Jezero rim (Fig. 2.20), answering many outstanding questions both about the regional geology and about ancient terrestrial planetary processes in general (Table 2.4).

First, identifying excavated mantle materials within megabreccia would have implications not only for Mars mantle petrology and understanding the composition of the Martian mantle and resulting melting pathways but also for our understanding of basin-scale impact models. The presence or non-presence of mantle materials within megabreccia would provide an important depth constraint to excavation for basin-scale impact models. Blue, yellow, and purple megabreccia lithologies are present in an extended mission traverse (Fig. 2.20). Megabreccia, including one kaolinite block, are even present in the rim of Jezero crater although it cannot be discerned whether these were formed through the Jezero crater or the Isidis basin. In addition, it is highly likely that the Noachian Basement Group records impact melt from the Isidis basin in one of its three LCP-bearing units.

The Mars 2020 rover would also be able to analyze the Mixed Lithology Plains Unit, LCP-bearing Plateaus Unit, megabreccia, and Blue Fractured Unit that may provide examples of geological units with different igneous origins or at least different aqueous alteration processes. The importance of understanding the igneous compositions of the Noachian Basement is furthered by the presence of HCP higher in the regional stratigraphy, often referred to as the mafic cap unit in literature (Fig. 2.1) (Mustard et al., 2009; Ehlmann et al., 2009; Goudge et al., 2015; Bramble et al., 2017). From orbital data and petrological modelling efforts, it has been suggested that there was a global transition from LCP-dominated to HCP-dominated igneous compositions on the Martian surface related to thermal evolution of the Martian mantle (Mustard et al., 2005; Baratoux et al., 2013). The 3 different LCP-bearing Noachian Basement units may potentially also record changes in composition from lithologies containing more Fe-rich LCP compositions to lithologies containing more Ca-rich LCP compositions. However, due to the uncertainties regarding the spectral signatures of these materials discussed above, this cannot be confirmed from orbit. However, this can be confirmed by analysis with instruments on the Mars 2020 rover. Therefore, analyzing and understanding the Noachian Basement LCP-bearing units, their relationship to each other, and their transition to the younger HCP-bearing units may have implications for understanding the Martian mantle evolution, its melting processes, and surface volcanism on Mars.
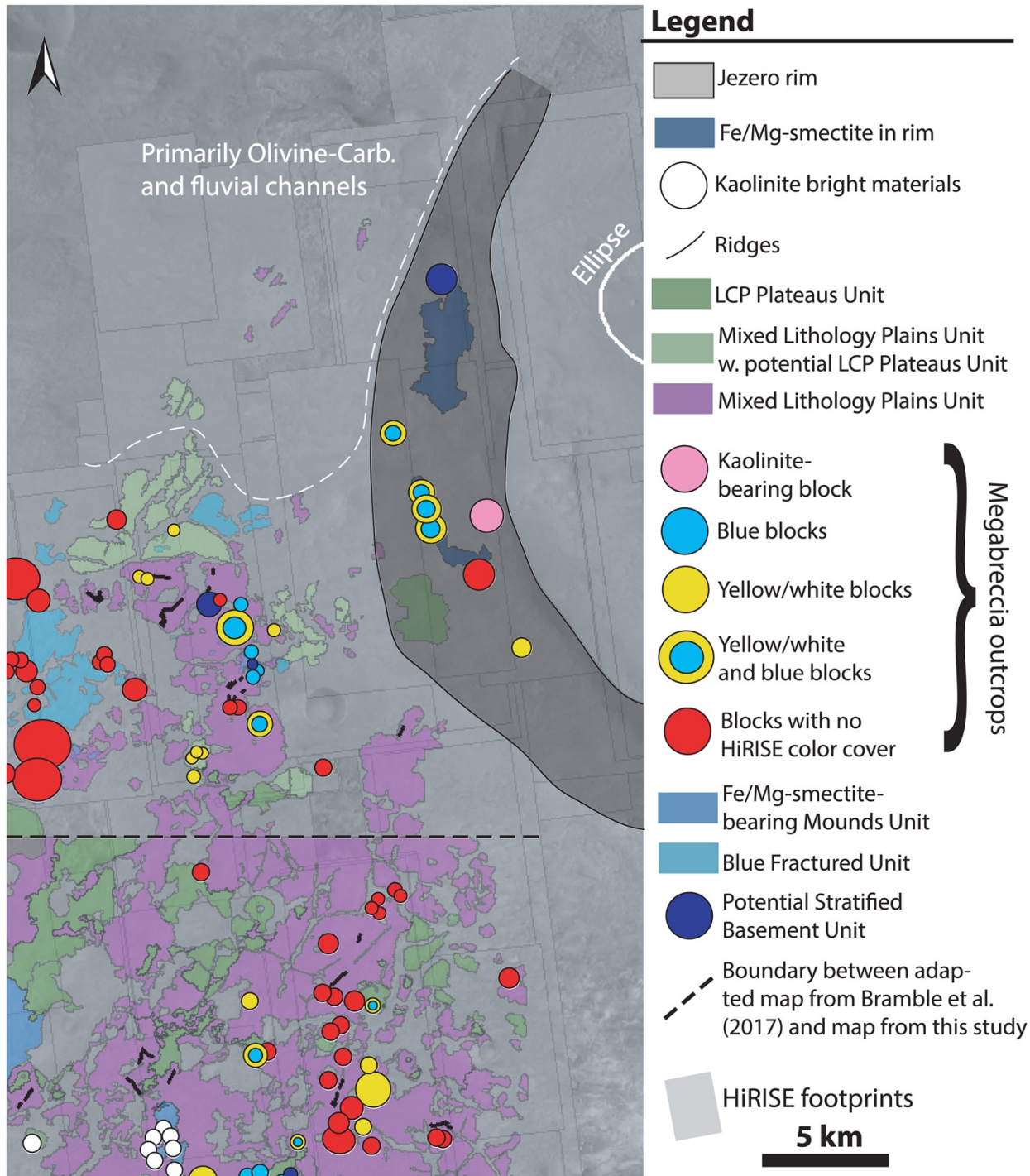
Figure 2.20: Partial map of Noachian Basement Group units and features within an area accessible by the Mars 2020 extend mission. Map of NE Syrtis (separated by black stippled line) is from Bramble et al. (2017) but adapted and modified to fit the terminology presented in this study. Megabreccia mapping scheme is based on visual characterization of HiRISE color images (see Fig. 7). Note that the Jezero rim (grey shaded area) may contain areas similar to Noachian Basement Group such as LCP-bearing Plateaus Unit and Fe/Mg-smectite-bearing parts of the rim, but these are more complicated and presumably disrupted by the Jezero impact. Mixed Lithology Plains Unit with features of geomorphological similarity to LCP-bearing Plateaus Unit but no high-resolution CRISM coverage are mapped separately in light green.

Table 2.4: Summary table of geological units and related science questions within an extended mission from Jezero crater.

Unit Name	Distance to Jezero ellipse	Science objectives/questions at units
Kaolinite-bearing bright materials	~ 9 km	- Detailed mineralogical and chemical analysis of Kaolinite-bearing bright materials will reveal how the related aqueous environment(s) differed or were similar to the environment(s) that formed Fe/Mg-smectite.
Ridges	~22 km	- Detailed mineralogical and chemical analysis of materials within ridges may reveal the chemistry and temperature of fluid flow within ridges. - Understanding the chemistry of fluids may help us understand the habitability potential of these fracture systems.
LCP-bearing Plateaus Unit	~ 13 km	- Analyzing the texture of LCP-bearing Plateaus Unit with Mars 2020 cameras may reveal whether the LCP-bearing Plateaus Unit have an impact, sedimentary, and/or igneous origin. - Detailed mineralogical and chemical study will reveal what type of environment the LCP-bearing Plateaus Unit formed in (e.g. lava flow, impact melt flow, lithified sandstone, etc.)
Mixed Lithology Plains Unit	~ 9 km	- Analyzing the texture of the Mixed Lithology Plains Unit with the Mars 2020 cameras will reveal whether the Mixed Lithology Plains Unit is an impact product or formed through a different processes. - Detailed mineralogical and chemical study of the hydrated materials within the Mixed Lithology Plains Unit with the Mars 2020 instrument suite may reveal the aqueous environment(s) that formed them. - Analysis of these aqueous environment(s) will help us understand ancient Mars habitability and climate .
Fe/Mg-smectite in the Jezero rim	~ 6 km	- Detailed mineralogical and chemical study of the hydrated materials within the Fe/Mg-smectite Mounds Unit with the Mars 2020 instrument suite may reveal the aqueous environment(s) that formed them. - Analysis of these aqueous environment(s) will help us understand ancient Mars habitability and climate .
Megabreccia	~ 9 km	- Detailed mineralogical and chemical study will reveal the composition of the earliest Martian crust that are captured within megabreccia materials. - Determining the source depth of megabreccia materials will enable us to test between impact basin models.
Blue Fractured Unit	~ 18 km	- Detailed mineralogical and chemical study with the Mars 2020 instrument suite can easily determine whether the Blue Fractured Unit is deep crustal/mantle materials or other igneous materials. - Sampling and in-situ analysis of the Blue Fractured Unit will potentially inform us on the deep crustal/mantle composition of Mars and/or other igneous petrogenetic processes.
Potential Stratified Basement Unit	~7 km	- Analyzing sedimentary or volcanic layers in the Stratified Basement Unit will inform interpretations of the depositional environments and processes by which layers and extensive Fe/Mg-smectite clays formed within the Stratified Basement Unit. - Analysis of these aqueous environment(s) will help us understand ancient Mars habitability and climate.

Lastly, the Mars 2020 rover will be able to provide detailed analyses of petrographic texture, composition, mineral assemblages, stratigraphy and thus infer habitability and environmental transitions recorded by the several units in the Noachian Basement Group with hydrous materials, including Stratified Basement Unit, Mixed Lithology Plains Unit, Fe/Mg-smectite-bearing megabreccia, ridges, and kaolinite-bearing bright materials. First, the origin of layering in smectite-bearing pre-Isidis Stratified Basement Unit could be sedimentary or volcanic. Second, the Mixed Lithology Plains Unit appears to represent a spatially extensive aqueous environment, and it still remains to be answered why hydrated mineralogy formed on such a large scale on Noachian Mars and whether this was impact-related. The vast Fe/Mg-smectite formation on Mars has had many explanations proposed in previous literature, including subsurface alteration, hydrothermalism, burial metamorphism/diagenesis, and pedogenetic processes (Ehlmann and

Mustard, 2012; Ehlmann et al., 2011; Mustard et al., 2009; Viviano et al., 2013). Detailed mineralogical, chemical, and textural studies of these units will reveal the temperature and fluid chemistry of formation, testing between these different aqueous environments. The megabreccia may preserve very ancient pre-Isidis water-related processes. The ridges, in contrast, represent a separate syn- or post-Isidis episode of fluid flow, possibly unrelated to the original Fe/Mg-smectite. Last, the relationship between Fe/Mg-smectite clays and overlying kaolinite-bearing bright materials observed in the study area may reveal hints to similar relationships observed globally when studied in situ (Carter et al., 2015; Ehlmann et al., 2011). Hence, the many units with hydrous minerals in the Noachian Basement Group record multiple different aqueous environments on ancient Mars that will be revealed through in-situ analysis and sample return.

2.7 Conclusions

We define the oldest, lowermost stratigraphy west of the Isidis basin to be a Noachian Basement Group comprised of 5 distinct geological units (Stratified Basement Unit, Blue Fractured Unit, Mixed Lithology Plains Unit, LCP-bearing Plateaus Unit) and 2 geomorphological features (megabreccia and ridges) and 1 mineral deposit (kaolinite-bearing bright materials). The stratigraphically lowermost units are the Stratified Basement Unit, Blue Fractured Unit, and pre-Isidis megabreccia materials. The Stratified Basement Unit contains Fe/Mg smectite-bearing materials layered (6-20 layers/exposure) at scales of 10s of meters or less. The Blue Fractured Unit contains polygonally fractured terrain containing low-Ca pyroxene with strong Fe^{2+} absorptions and little to no alteration. The overlying Mixed Lithology Plains Unit is in the middle of the stratigraphy and contains vast, usually smooth plains of LCP and Fe/Mg-smectite mixed together with diffuse boundaries between LCP-dominated and Fe/Mg-smectite-dominated parts of the plains. The Mixed Lithology Plains Unit also sometimes contains megabreccia and patches of Blue Fractured Unit. Stratigraphically above the Mixed Lithology Plains Unit is the LCP-bearing Plateaus Unit: flat, raised plateaus that contain large areas of completely unaltered LCP. Fe/Mg-smecite-bearing ridges and kaolinite-bearing bright materials occur within the Mixed Lithology Plains Unit and likely represent the youngest features in the Basement Group.

The megabreccia are observed primarily within the NW part of the Isidis basin structure 500-1000 km from the crater center within the Mixed Lithology Plains Unit. They are angular to sub-rounded, have diverse block packing density, are sometimes layered, and block lithology is often heterogeneous within a single outcrop. Through parameterization of HiRISE color images, we find four different lithologies indicated by yellow/white, blue, beige, and purple colors in HiRISE false-color. CRISM data show yellow/white and blue materials contain Fe/Mg-smectite and Blue Fractured Unit-type LCP, respectively. However, beige and purple megabreccia do not occur at a sufficient spatial scale in any areas with CRISM coverage to examine their composition and are likely distinctive pre-Isidis materials (Pre-

Noachian or Early Noachian). Block sizes of megabreccia ranged from 1.3-433 m with a median of 11.5 m with no clear correlation to distance from crater center or elevation. Taken together, the heterogeneity, sedimentological properties, block size, and spatial extent/distribution of megabreccia appear to be most compatible with formation through gravitational flows resulting from collapse of the transient crater during Isidis basin formation.

The LCP-bearing Plateaus Unit, Mixed Lithology Plains Unit, and Blue Fractured Unit all contain LCP but differ in spectral characteristics related to either pyroxene composition (high- vs. low-Ca) and/or glass content. This suggests that at least 3 different types of LCP-bearing lithologies have formed at different stratigraphic times. These have also undergone different degrees of aqueous alteration within the Noachian Basement Group. Similarly, 4 aqueous alteration events of (1) pre-Isidis Fe/Mg-smectite formation, (2) Fe/Mg-smectite formation within potential impact deposits, (3) Fe/Mg-smectite formation in fractures forming ridges, and (4) kaolinite formation, are responsible for formation of hydrated mineralogy within the Stratified Basement Unit, Fe/Mg-smectite-bearing Mounds Unit, Mixed Lithology Plains Unit, ridges, and kaolinite-bearing bright materials.

Outstanding questions include 4 major topics. (1) What was the duration and evolution of aqueous processes giving rise to hydrated mineralogy of different stratigraphic ages stretching from the Pre-Noachian or Early Noachian to Mid-Noachian? (2) What igneous or impact process(es) formed LCP, potentially OPX, within the pre-Isidis crust? (3) Do megabreccia contain mantle materials and what does that tell us about the Martian interior? (4) What processes of 1900-km Isidis impact basin formation are recorded within the Noachian Basement Group and does this match predictions of current basin formation models? Many of these questions are answerable with in situ exploration and sampling by the Mars-2020 mission in an extended mission taking the rover ~20 km from the Jezero landing ellipse.

References

Baker, D. M. H., Head, J. W., Collins, G. S., & Potter, R. W. K. (2016). The formation of peak-ring basins: Working hypotheses and path forward in using observations to constrain models of impact-basin formation. *Icarus*, *273*, 146–163. https://doi.org/10.1016/j.icarus.2015.11.033

Barlow, N. G. (2005). A review of Martian impact crater ejecta structures and their implications for target properties. *Special Paper 384: Large Meteorite Impacts III*, *384*, 433–442. https://doi.org/10.1130/0-8137-2384-1.433

Belza, J., Goderis, S., Keppens, E., Vanhaecke, F., & Claeys, P. (2012). An emplacement mechanism for the mega-block zone within the Chicxulub crater, (Yucatán, Mexico) based on chemostratigraphy. *Meteoritics and Planetary Science*, *47*(3), 400–413. https://doi.org/10.1111/j.1945-5100.2012.01345.x

Beyer, R. A., Alexandrov, O., & McMichael, S. (2018). The Ames Stereo Pipeline: NASA's open source

software for deriving and processing terrain data. *Earth and Space Science, 5*(9), 537-548.

Bretzfelder, J. M., Klima, R. L., Greenhagen, B. T., Buckowski, D. L., Cartwright, S. F. A., Moriarty, D. P., Ernst, C. M., and Petro, N. E. (2019). Comparative spectral analysis of three distinct Lunar basins. *LPSC L #1933*.

Bishop, J. L., Tirsch, D., Tornabene, L. L., Jaumann, R., McEwen, A. S., McGuire, P. C., … Neukum, G. (2013). Mineralogy and morphology of geologic units at Libya Montes, Mars: Ancient aqueously derived outcrops, mafic flows, fluvial features, and impacts. *Journal of Geophysical Research E: Planets*, *118*(3), 487–513. https://doi.org/10.1029/2012JE004151

Bramble, M. S., Mustard, J. F., & Salvatore, M. R. (2017). The geological history of Northeast Syrtis Major, Mars. *Icarus*, *293*, 66–93. https://doi.org/10.1016/j.icarus.2017.03.030

Cannon, K. M., Mustard, J. F., Parman, S. W., Sklute, E. C., Dyar, M. D., & Cooper, R. F. (2017). Spectral properties of Martian and other planetary glasses and their detection in remotely sensed data. *Journal of Geophysical Research: Planets, 122*(1), 249-268

Carter, J., Loizeau, D., Mangold, N., Poulet, F., & Bibring, J. P. (2014). Widespread surface weathering on early Mars: A case for a warmer and wetter climate. *Icarus*, *248*, 373–382. https://doi.org/10.1016/j.icarus.2014.11.011

Carter, J., Poulet, F., Murchie, S., & Bibring, J. P. (2013). Automated processing of planetary hyperspectral datasets for the extraction of weak mineral signatures and applications to CRISM observations of hydrated silicates on Mars. *Planetary and Space Science, 76*, 53-67

Caudill, C. M., Tornabene, L. L., McEwen, A. S., Byrne, S., Ojha, L., & Mattson, S. (2012). Layered MegaBlocks in the central uplifts of impact craters. *Icarus*, *221*(2), 710–720. https://doi.org/10.1016/j.icarus.2012.08.033

Christensen, P. R., Jakosky, B. M., Kieffer, H. H., Malin, M. C., McSween, Jr., H. Y., Nealson, K., … Ravine, M. (2004). The Thermal Emission Imaging System (THEMIS) for the Mars 2001 Odyssey Mission. *Space Science Reviews*, *110*(1–2), 85–130. https://doi.org/10.1023/b:spac.0000021008.16305.94

Cintala, M. J., & Grieve, R. A. F. (1998). Scaling impact melting and crater dimensions:Implications for the lunar cratering record. *Meteoritics and Planetary Science*, *33*(4), 889–912. https://doi.org/10.1111/j.1945-5100.1998.tb01695.x

Clark, R. N., Swayze, G. A., Gallagher, A. J., King, T. V. V., & Calvin, W. M. (1993). The U.S. Geological Survey, Digital Spectral Library: Version 1 : 0.2 to 3.0 μm. *U.S. Geological Survey Open File Report 93-592*.

Collins, G. S., Melosh, H. J., Morgan, J. V., & Warner, M. R. (2002). Hydrocode simulations of Chicxulub crater collapse and peak-ring formation. *Icarus*, *157*(1), 24–33.

https://doi.org/10.1006/icar.2002.6822

Delamere, W. A. et al. (2010). Color imaging of Mars by the high resolution imaging science experiment (HiRISE). *Icarus, 205*(1), 38-52.

Dickson, J., Kerber, A., Fassett, C. I., Ehlmann, B. L. (2018). A global, blended CTX mosaic of Mars with vectorized seam mapping: A new mosaicking pipeline using principles of non-destructive image editing. *LPSC XLIX #2083.*

Dufresne, A., Bösmeier, A., & Prager, C. (2016). Sedimentology of rock avalanche deposits – Case study and review. *Earth-Science Reviews*, *163*, 234–259. https://doi.org/10.1016/j.earscirev.2016.10.002

Edwards, C. S., Nowicki, K. J., Christensen, P. R., Hill, J., Gorelick, N., & Murray, K. (2011). Mosaicking of global planetary image datasets: 1. Techniques and data processing for Thermal Emission Imaging System (THEMIS) multi-spectral data. *Journal of Geophysical Research E: Planets*, *116*(E10008). https://doi.org/10.1029/2010JE003755

Ehlmann, B. L., & Mustard, J. F. (2012). An in-situ record of major environmental transitions on early Mars at Northeast Syrtis Major. *Geophysical Research Letters*, *39*(11). https://doi.org/10.1029/2012GL051594

Ehlmann, B. L., Mustard, J. F., Murchie, S. L., Bibring, J. P., Meunier, A., Fraeman, A. A., & Langevin, Y. (2011). Subsurface water and clay mineral formation during the early history of Mars. *Nature*, *479*(7371), 53–60. https://doi.org/10.1038/nature10582

Ehlmann, B. L., Mustard, J. F., Swayze, G. A., Clark, R. N., Bishop, J. L., Poulet, F., … Murchie, S. L. (2009). Identification of hydrated silicate minerals on Mars using MRO-CRISM: Geologic context near Nili Fossae and implications for aqueous alteration. *Journal of Geophysical Research E: Planets*, *114*(E2). https://doi.org/10.1029/2009JE003339

Eliason, E., Becker, L., Anderson, J., Sides, S. (2007). Software Interface Specification for HiRISE Reduced Data Record Products. JPL Document Number D-32006.

Farley, K., Williford, K, & Stack Morgan, K. (2018). Science Objectives, Landing Site Working Group Operation Scenarios, and Site Assessment Criteria. 4th Landing site workshop for the Mars 2020 rover mission. https://marsnext.jpl.nasa.gov/workshops/2018-10/PRESENTATIONS/m2020_lsw_day1_04_farley.pdf

Fassett, C. I., & Head, J. W. (2011). Sequence and timing of conditions on early Mars. *Icarus*, *211*(2), 1204–1214. https://doi.org/10.1016/j.icarus.2010.11.014

Fox, V. K., Kupper, R. J., Ehlmann, B. L., Catalano, J. G., Nickerson, R. D., Katz, S. M., White, A. A. (2019). Characterization of synthetic Fe3+-Fe2+-Al-Mg smectites. *LPSC L #2132*

Frey, H. (2008). Ages of very large impact basins on Mars: Implications for the late heavy bombardment in the inner solar system. *Geophysical Research Letters*, *35*(13).

https://doi.org/10.1029/2008GL033515

Goudge, T. A., Mustard, J. F., Head, J. W., Fassett, C. I., & Wiseman, S. M. (2015). Assessing the mineralogy of the watershed and fan deposits of the Jezero crater paleolake system, Mars. *Journal of Geophysical Research: Planets*, *120*(4), 775–808. https://doi.org/10.1002/2014JE004782

Grant, J. A., Irwin, R. P., Grotzinger, J. P., Milliken, R. E., Tornabene, L. L., McEwen, A. S., … Thomson, B. J. (2008). HiRISE imaging of impact megabreccia and sub-meter aqueous strata in Holden Crater, Mars. *Geology*, *36*(3), 195–198. https://doi.org/10.1130/G24340A.1

Gray, J. M. N. T., & Hutter, K. (1997). Pattern formation in granular avalanches. *Continuum Mechanics and Thermodynamics*, *9*(6), 341–345. https://doi.org/10.1007/s001610050075

Gray, J. M. N. T., & Thornton, A. R. (2005). A theory for particle size segregation in shallow granular free-surface flows. *Proceedings of the Royal Society A: Mathematical, Physical and Engineering Sciences*, *461*(2057), 1447–1473. https://doi.org/10.1098/rspa.2004.1420

Guidat, T., Pochat, S., Bourgeois, O., & Souček, O. (2015). Landform assemblage in Isidis Planitia, Mars: Evidence for a 3 Ga old polythermal ice sheet. *Earth and Planetary Science Letters*, *411*, 253–267. https://doi.org/10.1016/j.epsl.2014.12.002

Hiesinger, H. (2004). The Syrtis Major volcanic province, Mars: Synthesis from Mars Global Surveyor data. *Journal of Geophysical Research*, *109*(E1). https://doi.org/10.1029/2003je002143

Hörz, F. (1982). Ejecta of the Ries Crater, Germany. In *Geological implications of impacts of large asteroids and comets on the Earth* (pp. 39–55). https://doi.org/10.1130/spe190-p39

Howard, K. A., Wilhelms, D. E., & Scott, D. H. (1974). Lunar basin formation and highland stratigraphy. *Reviews of Geophysics*, pp. 309–327. https://doi.org/10.1029/RG012i003p00309

Hurwitz, D. M., & Kring, D. A. (2014). Differentiation of the South Pole-Aitken basin impact melt sheet: Implications for lunar exploration. *Journal of Geophysical Research E: Planets*, *119*(6), 1110–1133. https://doi.org/10.1002/2013JE004530

Johnson, B. C., Blair, D. M., Collins, G. S., Melosh, H. J., Freed, A. M., Taylor, G. J., … Zuber, M. T. (2016). Formation of the Orientale lunar multiring basin. *Science*, *354*(6311), 441–444. https://doi.org/10.1126/science.aag0518

Johnsson, A., Raack, J., Hauber, E. (2019) Possible recessional moraines in the Nilosyrtis Mensae region, Mars. *LPSC L #3085*

Jones, E., et al. (2001). SciPy: Open source scientific tools for Python, v1.1.0. Online. http://www.scipy.org/

Kirk, R. L., Howington-Kraus, E., Rosiek, M. R., Anderson, J. A., Archinal, B. A., Becker, K. J., … McEwen, A. S. (2009). Ultrahigh resolution topographic mapping of Mars with MRO HiRISE stereo images: Meter-scale slopes of candidate Phoenix landing sites. *Journal of Geophysical*

Research E: Planets, *113*(E3). https://doi.org/10.1029/2007JE003000

Klima, R. L., Pieters, C. M., Boardman, J. W., Green, R. O., Head, J. W., Isaacson, P. J., … Tompkins, S. (2011). New insights into lunar petrology: Distribution and composition of prominent low-Ca pyroxene exposures as observed by the Moon Mineralogy Mapper (M3). *Journal of Geophysical Research E: Planets*, *116*(E6). https://doi.org/10.1029/2010JE003719

Klima, R. L., Pieters, C. M., & Dyar, M. D. (2007). Spectroscopy of synthetic Mg-Fe pyroxenes I: Spin-allowed and spin-forbidden crystal field bands in the visible and near-infrared. *Meteoritics & Planetary Science, 42*(2), 235-253

Komatsu, G., Ori, G. G., Di Lorenzo, S., Rossi, A. P., & Neukum, G. (2007). Combinations of processes responsible for Martian impact crater "layered ejecta structures" emplacement. *Journal of Geophysical Research E: Planets*, *112*(E6). https://doi.org/10.1029/2006JE002787

Krieger, M. H. (1977). Large landslides, composed of megabreccia, interbedded in Miocene basin deposits, southeastern Arizona. *United States Geological Survey Professional Paper*.

Krüger, T., van der Bogert, C. H., & Hiesinger, H. (2016). Geomorphologic mapping of the lunar crater Tycho and its impact melt deposits. *Icarus*, *273*, 164–181. https://doi.org/10.1016/j.icarus.2016.02.018

Malin, M. C., Bell, J. F., Cantor, B. A., Caplinger, M. A., Calvin, W. M., Clancy, R. T., … Wolff, M. J. (2007). Context Camera Investigation on board the Mars Reconnaissance Orbiter. *Journal of Geophysical Research E: Planets*, *112*(E5). https://doi.org/10.1029/2006JE002808

Mandon, L., Quantin, C., Thollot, P., Mangold, N., Lozac'h, L., Dromart, G., Beck, P., Dehouck, E., Breton, S., Millot, C. & Volat, M. (2019). Refining the age, emplacement and alteration scenarios of the olivine-rich unit in the Nili Fossae region, Mars. *Icarus*, *336*(113436).

Mangold, N. et al. (2007). Mineralogy of the Nili Fossae region with OMEGA/Mars Express data: 2. Aqueous alteration of the crust. *Journal of Geophysical Research: Planets, 112*(E8).

McEwen, A. S., Eliason, E. M., Bergstrom, J. W., Bridges, N. T., Hansen, C. J., Delamere, W. A., … Weitz, C. M. (2007). Mars reconnaissance orbiter's high resolution imaging science experiment (HiRISE). *Journal of Geophysical Research E: Planets*, *112*(E5). https://doi.org/10.1029/2005JE002605

McGuire, P. C., Bishop, J. L., Brown, A. J., Fraeman, A. A., Marzo, G. A., Frank Morgan, M., et al. (2009). An improvement to the volcano-scan algorithm for atmospheric correction of CRISM and OMEGA spectral data. *Planetary and Space Science, 57*(7), 809–815.

Michalski, J., Poulet, F., Bibring, J. P., & Mangold, N. (2010). Analysis of phyllosilicate deposits in the Nili Fossae region of Mars: Comparison of TES and OMEGA data. *Icarus, 206(*1), 269-289.

Morgan, F., Seelos, F., Murchie, S., and the CRISM team (2009). CRISM Data User's Workshop CAT

Tutorial. PDS Geoscience, Washington University of St. Louis.

Morgan, J. V., Gulick, S. P. S., Bralower, T., Chenot, E., Christeson, G., Claeys, P., … Zylberman, W. (2016). The formation of peak rings in large impact craters. *Science*, *354*(6314), 878–882. https://doi.org/10.1126/science.aah6561

Murchie, S., Guinness, E., & Slavney, S. (2016). CRISM data product software interface specification. PDS. https://pds-geosciences.wustl.edu/mro/mro-m-crism-2-edr-v1/mrocr_0001/document/crism_dpsis.pdf

Murchie, S., Arvidson, R., Bedini, P., Beisser, K., Bibring, J. P., Bishop, J., … Wolff, M. (2007). Compact Connaissance Imaging Spectrometer for Mars (CRISM) on Mars Reconnaissance Orbiter (MRO). *Journal of Geophysical Research E: Planets*, *112*(E5). https://doi.org/10.1029/2006JE002682

Mustard, J. F., Ehlmann, B. L., Murchie, S. L., Poulet, F., Mangold, N., Head, J. W., … Roach, L. H. (2009). Composition, morphology, and stratigraphy of Noachian crust around the Isidis basin. *Journal of Geophysical Research E: Planets*, *114*(E2). https://doi.org/10.1029/2009JE003349

Mustard, John F., Pieters, C. M., Isaacson, P. J., Head, J. W., Besse, S., Clark, R. N., … Tompkins, S. (2011). Compositional diversity and geologic insights of the Aristarchus crater from Moon Mineralogy Mapper data. *Journal of Geophysical Research E: Planets*, *116*(5), 1–17. https://doi.org/10.1029/2010JE003726

Oberbeck, V. R. (1975). The role of ballistic erosion and sedimentation in lunar stratigraphy. *Reviews of Geophysics*, *13*(2), 337–362. https://doi.org/10.1029/RG013i002p00337

Osinski, G. R. (2006). Effect of volatile and target lithology on the generation and emplacement of impact crater fill and ejecta deposits on Mars. *Meteoritics and Planetary Science*, *41*(10), 1571–1586. https://doi.org/10.1111/j.1945-5100.2006.tb00436.x

Osinski, G. R. et al. (2005). Geological overview and cratering model for the Haughton impact structure, Devon Island, Canadian High Arctic. *Meteoritics and Planetary Science*, *40*(12), 1759–1776. https://doi.org/10.1111/j.1945-5100.2005.tb00145.x

Osinski, G. R., Tornabene, L. L., & Grieve, R. A. F. (2011). Impact ejecta emplacement on terrestrial planets. *Earth and Planetary Science Letters*, *310*(3–4), 167–181. https://doi.org/10.1016/j.epsl.2011.08.012

Pan, L., Ehlmann, B. L., Carter, J., & Ernst, C. M. (2017). The stratigraphy and history of Mars' northern lowlands through mineralogy of impact craters: A comprehensive survey. *Journal of Geophysical Research: Planets, 122*(9), 1824-1854.

Papike, J. J., Karner, J. M., Shearer, C. K., & Burger, P. V. (2009). Silicate mineralogy of martian meteorites. *Geochimica et Cosmochimica Acta, 73*(24), 7443-7485.

Pascuzzo, A. C., Mustard, J. F., Kremer, C. H., & Ebinger, E. (2019). The formation of irregular polygonal ridge networks, Nili Fossae, Mars: Implications for extensive subsurface channelized fluid flow in the Noachian. *Icarus*, *319*, 852–868. https://doi.org/10.1016/j.icarus.2018.10.020

Pelkey, S. M. et al. (2007). CRISM multispectral summary products: Parameterizing mineral diversity on Mars from reflectance. *Journal of Geophysical Research: Planets, 112*(E8).

Pieters, C. M., Tompkins, S., Head, J. W., & Hess, P. C. (1997). Mineralogy of the mafic anomaly in the South Pole-Aitken Basin: Implications for excavation of the lunar mantle. *Geophysical Research Letters*, *24*(15), 1903–1906. https://doi.org/10.1029/97GL01718

Potter, R. W. K., Collins, G. S., Kiefer, W. S., McGovern, P. J., & Kring, D. A. (2012). Constraining the size of the South Pole-Aitken basin impact. *Icarus*, *220*(2), 730–743. https://doi.org/10.1016/j.icarus.2012.05.032

Quantin, C., Flahaut, J., Clenet, H., Allemand, P., & Thomas, P. (2012). Composition and structures of the subsurface in the vicinity of Valles Marineris as revealed by central uplifts of impact craters. *Icarus*, *221*(1), 436–452. https://doi.org/10.1016/j.icarus.2012.07.031

Quinn, D. P., & Ehlmann, B. L. (2019a). The deposition and alteration history of the northeast Syrtis Major layered sulfates. *Journal of Geophysical Research. Planets. 124*(7), 1743-1782.

Quinn, D. P., & Ehlmann, B. L. (2019b). A PCA-based framework for determining remotely-ġsensed geological surface orientations and their statistical quality. Earth and Space Sciences (Hoboken, NJ), 6, 1378.

Reimold, W. U., & Gibson, R. L. (1996). Geology and evolution of the Vredefort impact structure, South Africa. *Journal of African Earth Sciences*, *23*(2), 125–162. https://doi.org/10.1016/S0899-5362(96)00059-0

Riller, U. (2005). Structural characteristics of the Sudbury impact structure, Canada: Impact-induced versus orogenic deformation - A review. *Meteoritics and Planetary Science*, *40*(11), 1723–1740. https://doi.org/10.1111/j.1945-5100.2005.tb00140.x

Ritzer, J. A., & Hauck II, S. A. (2009). Lithospheric structure and tectonics at Isidis Planitia, Mars. Icarus, 201(2), 528-539.

Saper, L., & Mustard, J. F. (2013). Extensive linear ridge networks in Nili Fossae and Nilosyrtis, Mars: Implications for fluid flow in the ancient crust. *Geophysical Research Letters*, *40*(2), 245–249. https://doi.org/10.1002/grl.50106

Schultz, P. H. (1976). Floor-fractured lunar craters. *The Moon*, *15*(3–4), 241–273. https://doi.org/10.1007/BF00562240

Schultz, P. H., & Crawford, D. A. (2016). Origin and implications of non-radial Imbrium Sculpture on the Moon. *Nature*, *535*(7612), 391–394. https://doi.org/10.1038/nature18278

Souček, O., Bourgeois, O., Pochat, S., & Guidat, T. (2015). A 3 Ga old polythermal ice sheet in Isidis Planitia, Mars: Dynamics and thermal regime inferred from numerical modeling. *Earth and Planetary Science Letters*, *426*, 176–190. https://doi.org/10.1016/j.epsl.2015.06.038

Spudis, P. D., Martin, D. J. P., & Kramer, G. (2014). Geology and composition of the orientale basin impact melt sheet. *Journal of Geophysical Research E: Planets*, *119*(1), 19–29. https://doi.org/10.1002/2013JE004521

Stöffler, D. et al. (2012). Composition and evolution of the lunar crust in the Descartes Highlands, Apollo 16. *Journal of Geophysical Research*, *90*(S02). https://doi.org/10.1029/jb090is02p0c449

Tornabene, L. L., Osinski, G. R., McEwen, A. S., Wray, J. J., Craig, M. A., Sapers, H. M., & Christensen, P. R. (2013). An impact origin for hydrated silicates on Mars: A synthesis. *Journal of Geophysical Research E: Planets*, *118*(5), 994–1012. https://doi.org/10.1002/jgre.20082

Trowbridge, A. J., Bertels, A., Hogan, B., Elliott, J., and Melosh, H. J. (2019). Excavation of Martian lower crust and mantle by the Isidis impact and implications for the Mars 2020 mission. *LPSC L #2132*.

Vaughan, W. M., Head, J. W., Wilson, L., & Hess, P. C. (2013). Geology and petrology of enormous volumes of impact melt on the Moon: A case study of the Orientale basin impact melt sea. *Icarus*, *223*(2), 749–765. https://doi.org/10.1016/j.icarus.2013.01.017

Vishnevsky, S., & Montanari, A. (2007). Popigai impact structure (Arctic Siberia, Russia): Geology, petrology, geochemistry, and geochronology of glass-bearing impactites. In *Special Paper 339: Large Meteorite Impacts and Planetary Evolution; II* (pp. 19–60). https://doi.org/10.1130/0-8137-2339-6.19

Viviano-Beck, C. E. et al. (2014). Revised CRISM spectral parameters and summary products based on the currently detected mineral diversity on Mars. *Journal of Geophysical Research: Planets, 119*(6), 1403-1431

Waskom, M. et al. (2017). seaborn: statistical data visualization, v0.8.1. Online. https://seaborn.pydata.org/

Weiss, D. K., & Head, J. W. (2014). Ejecta mobility of layered ejecta craters on Mars: Assessing the influence of snow and ice deposits. *Icarus*, *233*, 131–146. https://doi.org/10.1016/j.icarus.2014.01.038

Werner, S. C. (2008). The early martian evolution-Constraints from basin formation ages. *Icarus*, *195*(1), 45–60. https://doi.org/10.1016/j.icarus.2007.12.008

Werner, S. C., & Tanaka, K. L. (2011). Redefinition of the crater-density and absolute-age boundaries for the chronostratigraphic system of Mars. *Icarus, 215*(2), 603-607.

Yamamoto, S. et al. (2010). Possible mantle origin of olivine around lunar impact basins detected by

SELENE. *Nature Geoscience*, *3*(8), 533–536. https://doi.org/10.1038/ngeo897

Zuber, M. T. (1992). The Mars Observer laser altimeter investigation. *Journal of Geophysical Research*, *97*(E5), 7781–7797. https://doi.org/10.1029/92JE00341

Formation of Magnesium Carbonates on Earth and Implications for Mars

Eva L. Scheller[1], Carl Swindle[1], John Grotzinger[1], Holly Barnhart[1], Surjyendu Bhattacharjee[1], Bethany L. Ehlmann[1], Ken Farley[1], Woodward W. Fischer[1], Rebecca Greenberger[1], Miquela Ingalls[1,3], Peter E. Martin[1,4], Daniela Osorio-Rodriguez[1], and Ben P. Smith[1]

[1]Division of Geological and Planetary Sciences, California Institute of Technology, Pasadena, CA, USA

[2] Jet Propulsion Laboratory, California Institute of Technology, Pasadena, CA, USA.

[3]Department of Geosciences, Pennsylvania State University, State College, PA, USA.

[4]Geological Sciences Department, University of Colorado Boulder, Boulder, CO, USA.

3.1 Abstract

Magnesium carbonates have been identified within the landing site of the Perseverance rover mission. This study reviews terrestrial analog environments and textural, mineral assemblage, isotopic, and elemental analyses that have been applied to establish formation conditions of magnesium carbonates. Magnesium carbonates form in 5 distinct settings: ultramafic rock-hosted veins, the matrix of carbonated peridotite, nodules in soil, alkaline lake and playa deposits, and as diagenetic replacements within lime- and dolostones. Dominant textures include fine-grained or microcrystalline veins, nodules, and crusts. Microbial influences on formation are recorded in thrombolites, stromatolites, crinkly and pustular laminites, spheroids, and filamentous microstructures. Mineral assemblages, fluid inclusions, and carbon, oxygen, magnesium, and clumped isotopes of carbon and oxygen have been used to determine the sources of carbon, magnesium, and fluid for magnesium carbonates as well as their temperatures of formation. Isotopic signatures in ultramafic rock-hosted magnesium carbonates reveal that they form by either low-temperature meteoric water infiltration and alteration, hydrothermal alteration, or metamorphic processes. Isotopic compositions of lacustrine magnesium carbonate record precipitation from lake water, evaporation processes, and ambient formation temperatures. Assessment of these features with similar analytical techniques applied to returned Martian samples can establish whether carbonates on ancient Mars were formed at high or low temperature conditions in the surface or subsurface through abiotic or biotic processes. The timing of carbonate formation processes could be constrained by ^{147}Sm-^{143}Nd isochron, U-Pb concordia, ^{207}Pb-^{206}Pb isochron radiometric dating as well as ^{3}He, ^{21}Ne, ^{22}Ne, or ^{36}Ar surface exposure dating of returned Martian magnesium carbonate samples.

3.2 Plain language summary

Magnesium carbonate minerals rarely form large deposits on Earth, and because they constitute such a small proportion of the terrestrial carbonate record in comparison to calcium-rich carbonates, they have received little attention. In contrast, the largest carbonate deposit detected on Mars has magnesium carbonate, and it has been detected at the landing site of the 2020 mission where the Perseverance rover will collect samples for return to Earth. We synthesized the field observations and laboratory experiments that pertain to magnesium carbonates formed on Earth and find that they form in five types of environments: within veins or in the bulk volume of magnesium-rich rocks, soils, alkaline or salty lakes, and as replacements of previously formed calcium-rich carbonate minerals. Conceptually, these environments may be analogs for ancient Martian magnesium carbonate-forming environments. Magnesium carbonates formed in some environments are capable of preserving remnants of microbes, especially if magnesium carbonates formed characteristic large-scale clotted- or vertical column shapes or microscale spherical and laminated textures. If life had ever originated on Mars, these would be key

materials to investigate for biosignatures. Finally, a number of analytical techniques are discussed that can be performed on magnesium carbonate rocks collected by Perseverance when returned to Earth.

3.3 Introduction: Magnesium carbonates on Earth and Mars

The Perseverance rover will explore and sample, for eventual return to Earth, magnesium carbonates found at its Jezero crater landing site on Mars (Grant et al., 2018), motivating interest in understanding the possible formation pathways of these uncommon carbonate minerals. Terrestrial magnesium carbonate minerals include a range of anhydrous and hydrous phases. Magnesite ($MgCO_3$) is the Mg-rich endmember of carbonate minerals with a trigonal crystal structure. It forms solid-solution series and co-occurs with corresponding calcium- and iron-rich carbonate endmembers although in low-temperature surface environments the stability of the solid solution series is highly affected by kinetic effects (Morse & Mackenzie, 1990; Chai & Navrotsky, 1996). Hydrous magnesium carbonate mineral phases, such as hydromagnesite ($Mg_5(CO_3)_4(OH)_2 \cdot 4H_2O$), barringtonite ($MgCO_3 \cdot 2H_2O$), nesquehonite ($Mg(HCO_3)(OH) \cdot 2(H_2O)$), lansfordite ($MgCO_3 \cdot 5H_2O$), artinite ($Mg_2(CO_3)(OH)_2 \cdot 3H_2O$), and dypingite ($Mg_5(CO_3)4(OH)_2 \cdot 5(H_2O)$), often co-occur with magnesite (e.g. Zedef et al,. 2000; Power et al., 2009).

On Earth, the Ca-rich carbonate endmembers such as calcite ($CaCO_3$; trigonal), aragonite ($CaCO_3$; orthorhombic), and dolomite ($CaMg(CO_3)_2$; trigonal) are far more abundant than either magnesite or siderite ($FeCO_3$). Atmospheric carbon dioxide produces carbonate rock through aqueous chemical weathering. Such reactions are central to the surficial carbon cycle and rock cycle on Earth. The dominance of calcium carbonates results from the fact that modern seawater is oversaturated with calcium carbonate due to weathering of Ca-dominant silicate rocks (Walker et al., 1981) and pre-existing carbonate rocks. Ca appears to have dominated for even the earliest part of Earth history that preserves a sedimentary rock record (Grotzinger and Kasting, 1993; Grotzinger and James, 2000). Since marine sediments dominate Earth's stratigraphic record, deposits of calcium carbonate overwhelm the tiny proportion of primary magnesium carbonate precipitation on Earth.

In contrast, deposits with magnesium carbonate minerals reveal clues about past aqueous activity on the Martian surface (e.g. Edwards and Ehlmann, 2015; Ehlmann et al., 2008; McSween et al., 2014). Although Mars is currently too dry for detectable large-scale aqueous alteration at its surface, mineralogical evidence for hydrated minerals and geomorphological evidence of fluvial, glacial, and lacustrine systems indicate abundant surface waters prior to about 3.5 Ga (Carr, 1987; Hynek et al., 2010). One candidate mechanism proposed for the dramatic climatic cooling on Mars is drawdown of atmospheric CO_2 into carbonate rock (Kasting, 1991). However, despite evidence for a wetter past and the current composition of the atmosphere of ~95% CO_2, surficial carbonate rock on Mars is remarkably rare.
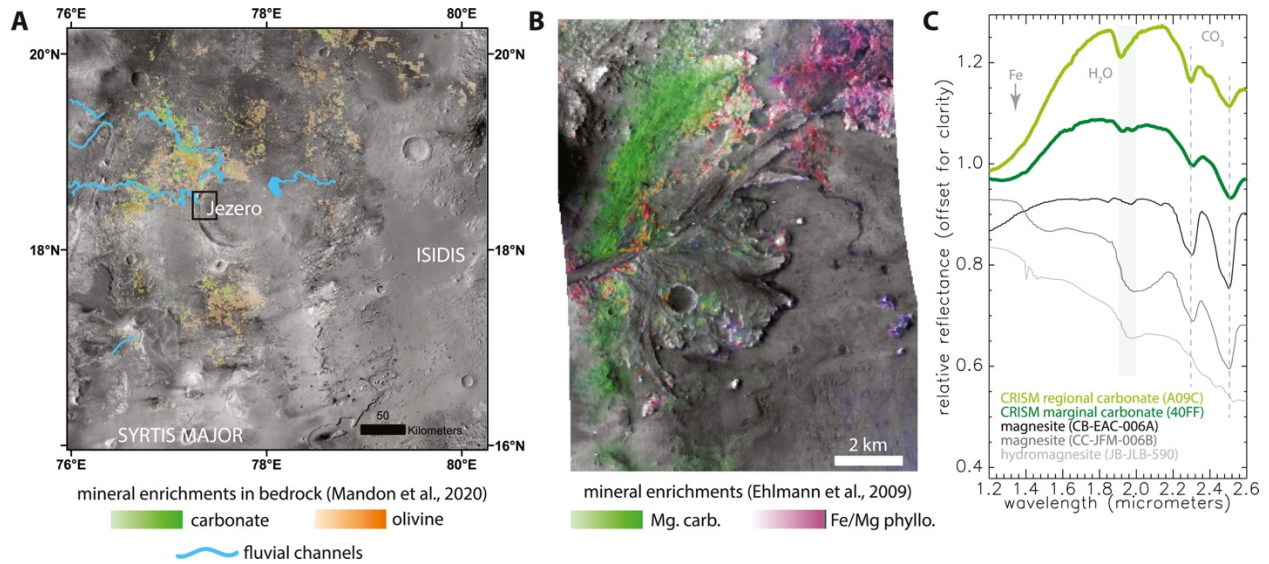
Fig. 3.1: Overview of magnesium carbonates within and surrounding Jezero crater. (A) The watershed of Jezero crater lake cross-cuts olivine-enriched bedrock, in places altered to magnesium carbonate. Map of bedrock enrichments, subsetted from Mandon et al. (2020). (B) The sediments of the western shore and delta fed by the western channel are enriched in magnesium carbonate (green), relative to the sedimentary rocks deposited by the northern channel. Map of mineral enrichments, subsetted from Ehlmann et al., (2009). (C) Infrared spectra acquired of rock units from orbit compared with spectra from the RELAB spectral library. Note: characteristic 2.3 and 2.5 micrometer absorptions associated with Mg bound to CO_3 and 1.9 micrometer absorptions associated with H_2O.

On Mars, orbital spectroscopy reveals widespread hydrated mineral phases, indicating aqueous alteration (Bibring et al., 2006; Mustard et al., 2008), including phyllosilicates, sulfates, and hydrated silica, but only limited surface exposure of carbonates (Ehlmann et al., 2008; Niles et al., 2013). Bandfield (2003) detected magnesium carbonate at the few wt% level in globally widespread Martian dust, and Boynton et al (2009) measured 3-5 wt.% calcium carbonate at the Phoenix landing site. Curiosity X-ray diffraction data and evolved gas analysis data indicate ~1 wt. % Mg, Fe carbonate in soils (Leshin et al., 2013; Archer et al., 2020). Mg-Fe carbonates were also observed at ~25 wt. % in a small, olivine/silica-rich volcaniclastic outcrop at the Spirit landing site (Morris et al., 2010). Carbonates also occur in some Martian meteorites (Niles et al 2013), including the nodules consisting of mixtures of Mg-, Fe-, and Ca-rich carbonates in ALH84001 (Valley 1997).

From orbital remote sensing, a single region of Mars (Nili Fossae) accounts for the majority of the areal fraction carbonate detections known for Mars (Ehlmann et al., 2008; Wray et al., 2016) (Fig. 3.1). A few dozen small scattered locales in the southern highlands have infrared signatures consistent with a mineral assemblage of smectite clay, chlorite, and Fe/Ca carbonate (Wray et al., 2016). The Nili Fossae carbonate is associated with an olivine-bearing unit modelled to contain 10% to 40% coarse-grained olivine and up to 20 wt.% magnesium carbonate with minor amounts of Fe/Mg phyllosilicate along with pyroxene and feldspar (Edwards and Ehlmann, 2015; Hoefen et al., 2003; Salvatore et al.,

2018; Mandon et al., 2020) (Fig. 3.1A). Ehlmann et al. (2008) concluded that the dominant cation in the carbonate is Mg, due to infrared absorption positions distinct from Ca and Fe carbonates (Fig. 3.1C) (Gaffey, 1987). The spectra additionally exhibit an H_2O absorption, particularly in the regional bedrock (Fig. 3.1C) (e.g. Ehlmann et al., 2008). Some terrestrial magnesium carbonates that are nominally anhydrous (e.g., magnesite) can exhibit H_2O absorptions (e.g. Gaffey, 1985; Leask, 2020); such absorptions are also characteristic of hydrous carbonates like hydromagnesite (Horgan et al., 2020). The presence of these carbonates could reflect alteration of the olivine unit involving surface water, shallow groundwater, or deeper hydrothermal solutions. In the primary mission, the Perseverance rover is expected to examine magnesium carbonate within crater floor units and deltaic sedimentary rocks in the Jezero crater paleolake basin (Fig. 3.1B). In an extended mission, the rover may examine magnesium carbonate in situ within the regional olivine unit.

The Mars 2020 mission is tasked with seeking the signs of life in ancient Martian environments, understanding the geological history of Mars, and preparing a collection of samples for Earth return by the future Mars Sample Return program (Williford et al., 2018). The carbonates at Jezero crater and the surrounding Nili Fossae region are key lithologies to be investigated and sampled by the Perseverance rover. Thus, the sampling efforts and subsequent analyses of Martian magnesium carbonates require an understanding of processes that form magnesium carbonates on Earth. This synthesis reviews the geological environments and physical conditions in which magnesium carbonates form on Earth in order to constrain pathways for magnesium carbonate formation in ancient Martian environments, the potential preservation of biosignatures, and the use of stable isotopic, elemental, and geochronologic systematics in their evaluation.

For this purpose, we divide the paper into sections that review the following topics: (1) Magnesium carbonate-forming environments on Earth. (2) Characteristic textures and fabrics found within different carbonate-forming enviornments on Earth and considerations of how these can be tied to interpreting formation environments. (3) Thermodynamic and kinetic conditions required to precipitate magnesium carbonates in synthetic experiments and how this can help constrain magnesium carbonate formation on Mars. (4) Results from isotopic and elemental chemistry laboratory methods and how application of these methodologies to Martian samples can aid in interpretation of formation conditions. (5) Geochronological methods that have been applied to magnesium carbonates for geochronological study of returned samples of Martian carbonates.

3.4 Geological context of magnesium carbonate formation

Magnesium carbonates on Earth (Fig. 3.2) are commonly associated with ultramafic rocks, either in (1) veins or (2) within the matrix of carbonated peridotite or, often through transport of fluids that have interacted with ultramafic rock, as authigenic precipitates, i.e., (3) nodules in soil, and in (4) alkaline lakes

and playas. A fifth occurrence (5) is within diagenetically or hydrothermally altered limestones and dolostones. Magnesite can also form within the upper mantle by transformation of subducting dolomite, and they persist to the lower mantle (Isshiki et al., 2004). However, since these mantle occurrences are not related to surface processes, we do not discuss them further. Magnesite and other products from the magnesite-siderite solid solution series can be found within igneous rocks that have a mineralogical composition of >50% carbonate minerals, also known as carbonatites (Buckley and Woolley, 1990; Zaitsev et al., 2004). Although some phases of magnesite in carbonatites have been suggested to be potential primary liquidus phases based on their characteristic euhedral crystal shape (Buckley and Woolley, 1990), experimental data suggest that magnesite can only crystallize at mantle-like pressure/depths (>20 Kb) from carbonate melts, which much more typically form Ca-rich carbonates (Irving & Wyllie, 1975; Lee et al., 2000). Instead, the carbonatite-associated magnesites formed through hydrothermal alteration or as replacements of other carbonates akin to alteration processes found within ultramafic and sedimentary carbonate rocks, described in the following sections (Buckley and Woolley, 1990; Zaitsev et al., 2004).

The primary 5 geological settings provide viable Earth analogs for the magnesium carbonate detections localized in Jezero crater and its adjacent highlands on Mars. The geologic context and textures of magnesium carbonates observed by the Perseverance rover will help determine the environmental setting of magnesium carbonate formation on ancient Mars inside and outside Jezero crater. Descriptions of magnesium carbonate systems in this section are separated into ultramafic rock-hosted, sedimentary, and impact-associated systems on Earth. Additional diagenetic, metasomatic, and metamorphic replacement environments are described in section 3.5. Finally, the section summarizes Martian occurrences of magnesium carbonates in detail for comparison with terrestrial analogue environments.

3.4.1 Ultramafic rock-hosted magnesium carbonate on Earth

Magnesite is found filling fractures in ultramafic rocks on Earth, particularly within ophiolites, where the ultramafic oceanic crust and upper mantle have been tectonically thrust onto the preexisting continental margin (e.g., Abu-Jaber and Kimberley, 1992; Schroll et al., 2002). In fact, magnesite is present in most ophiolites. Veins, carbonated peridotite matrix, and overlying pedogenic nodule-type magnesium carbonates within ultramafic rock record a range of aqueous environments and conditions ranging from deep-seated to shallow hydrothermal activity to infiltration and alteration by low-temperature meteoric fluids via fractures to low-temperature laterization and surface weathering. These give rise to characteristic and distinguishable textures such as veins, nodules, and matrix magnesium carbonates within carbonated ultramafic rock. A record of one and possibly multiple transitions of such environments on Mars would therefore yield important insights into the temperature, chemistry, and nature (surface vs. subsurface) of ancient aqueous activity on Mars.

3.4.1.1 Hydrothermal processes leading to complete and partial carbonation

A continuum exists between magnesium carbonate formation hydrothermally and by chemical weathering. The most common terrestrial setting for hydrothermal magnesium carbonate formation is in ultramafic rocks within ophiolite deposits. Here, a common pathway is first serpentinization of the ultramafic rock and later carbonation of the serpentinite (Klein and Garrido, 2011; Klein and McCollom, 2013), though the particular fluid chemistries and CO_2 availabilities determine whether serpentine or magnesite is favored. Full carbonation occurs when primary pyroxene and olivine have been completely altered and replaced by a distinct carbonate and quartz assemblage with new textures compared to the
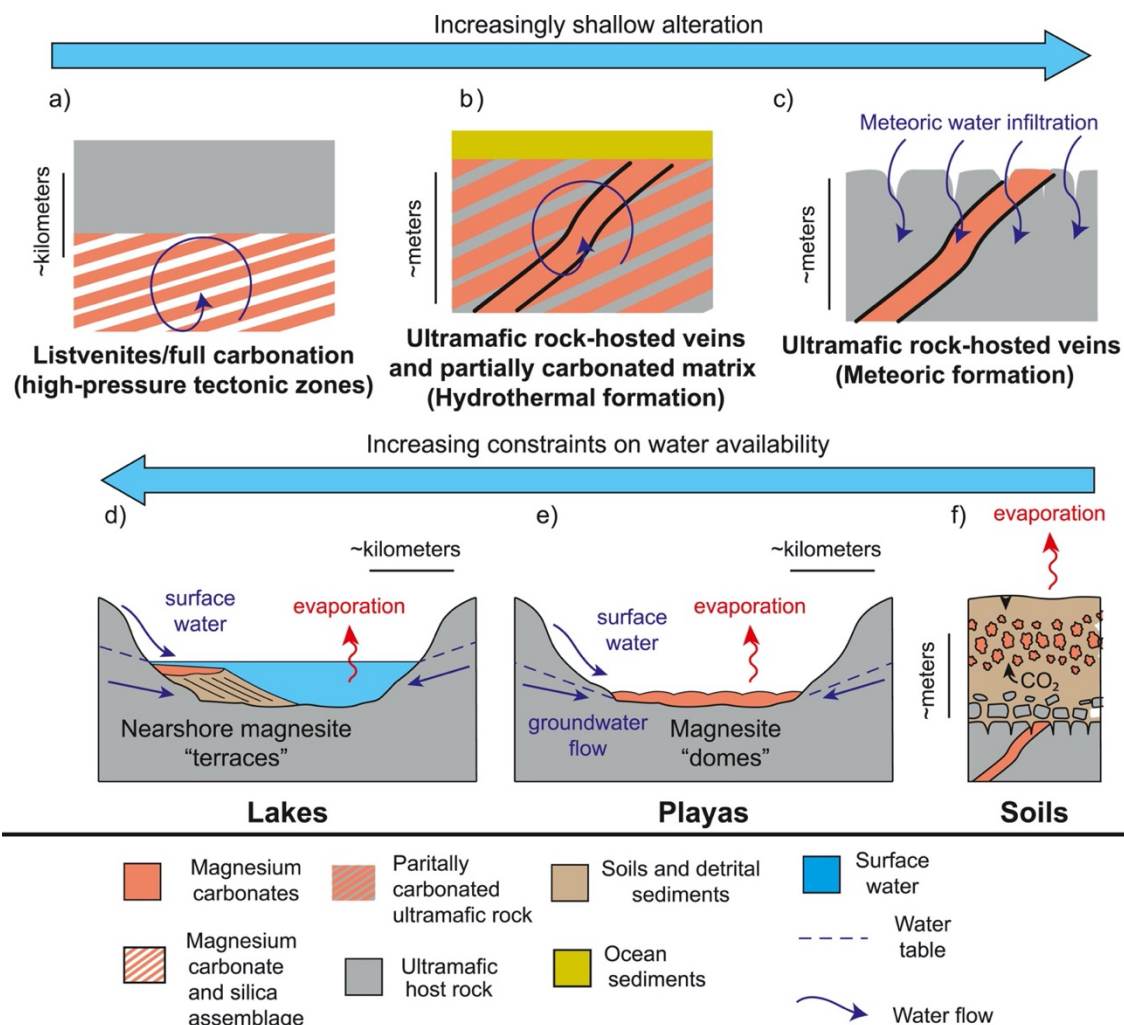
Fig. 3.2: Schematic depicting the three main ultramafic rock-hosted and three main sedimentary magnesium carbonate-forming environments on Earth. (A) magnesium carbonate and silica assemblage as alteration products in fully carbonated peridotite within subduction zones known as listvenite, magnesium carbonates as veins in ultramafic host rock formed by (B) hydrothermal alteration or (C) meteoric water infiltration, (D) magnesium carbonate terraces/stromatolites within alkaline lakes, (E) magnesium carbonate crusts in playas, and (F) magnesium carbonate nodules in soils in close association with ultramafic rock-hosted magnesite veins.

former peridotite (e.g., Halls and Zhao, 1995; Nasir et al., 2007; Falk and Kelemen, 2015). This fully carbonated quartz-carbonate rock forms via a set of dissolution-reprecipitation reactions and is called listvenite (or listwaenite). Full carbonation to listvenite typically requires high pressures of ~ 0.2-1.5 GPa, provided by slab subduction and which increase the solubility of CO_2 in fluids by orders of magnitude (Kelemen and Manning, 2015; Falk and Kelemen, 2015). Listvenites within the Advocate ophiolite, Newfoundland, Canada, Birjand ophiolite, Iran, and Semail ophiolites are all interpreted to have formed through carbonation by fluids from the subducting slab (Menzel et al., 2018; Boskabadi et al., 2020). These terrestrial listvenite-forming geologic environments form in high-pressure tectonic environments with large CO_2 sources, the combination of which is unlikely on the ancient Martian surface, which was not tectonically active (Nimmo & Stevenson, 2000). High pressures during meteorite impacts are likely too transient or would lead to melting (see section 3.4.3).

However, the solubility of CO_2 is a function of temperature, pressure, and salinity among other factors (e.g. Duan and Sun, 2003), and carbonation can also occur at lower pressures. For example, incomplete carbonation during hydrothermal alteration form a large array of mineral assemblages at much lower pressures that are plausible for Mars (<0.5 GPa; Klein and Garrido, 2011; Klein and McCollom, 2013; Grozeva et al., 2017), including but not limited to: (1) serpentine + brucite + magnesite, (2) serpentine + magnesite, (3) serpentine + talc + magnesite, (4) talc + magnesite, or soapstone (Menzel et al., 2018; Hansen et al., 2005, and Beinlich et al., 2013), as well as assemblages containing magnetite, goethite, hematite, and metal alloys (e.g., Kelemen et al., 2014). Magnesium carbonates in these rock types form veins (e.g. Boschi et al., 2009, Ashley, 1997) and also occur as part of the matrix assemblage of the ultramafic rock, typically with microcrystalline textures (Menzel et al., 2018; Hansen et al., 2005, and Beinlich et al., 2013). While discussion of the full pathway from dunite or harzburgite through intermediates to listvenite is beyond the scope of this magnesite review, we note that other minerals that co-occur with magnesite provide key information about the temperature, pressure, fluid chemistry, and redox conditions of the alteration. The complete reactions involved in the carbonation process are the subject of ongoing study (e.g., by the recent Oman Drilling Project; Kelemen et al., 2020).

Although hydrothermal magnesite occurrences in ultramafic complexes are much more common, other settings with mafic rocks do occur. For example, magnesium carbonates are found as hydrothermal alteration products in basalts within deposits in Northern Spitsbergen, Svalbard (Treiman et al., 2002). Here, they form as relatively minor precipitates in veins and may be related to alteration of the ultramafic xenoliths within the lavas.

3.4.1.2 Chemical weathering processes

At lower temperatures and in waters in contract with atmosphere, chemical weathering processes at more moderate temperatures alter ultramafic rocks. Olivine and pyroxene in the ultramafic rock are Mg-rich

and relatively Si-poor and Ca-poor. Fluids become alkaline as they react with the bedrock, and in the presence of atmospheric CO_2, Mg^{2+}- and HCO_3^--bearing fluids form from chemical weathering (e.g., Barnes and O'Neil, 1969; Neal and Stanger, 1985). These fluids tend to precipitate magnesite and occur as surface waters and shallow ground waters (e.g., Barnes and O'Neil, 1969; Kelemen et al., 2011). Upon infiltrations, the fluids change composition as dissolved CO_2 is exhausted via Mg carbonate precipitation. During low temperature serpentinization by these alkaline, now CO_2-poor waters, pyroxene alteration by hydration that produces serpentine releases Ca^{2+} (from pyroxene) and generates OH^-, yielding Ca^{2+}- and OH^-- rich waters (Barnes and O'Neil, 1969; Neal and Stanger, 1985; Kelemen and Matter, 2008; Kelemen et al., 2011). These waters precipitate calcium carbonates upon renewed contact with the atmosphere and, thus, travertine springs are a common feature of serpentinized ultramafic bodies.

The Semail ophiolite of Oman and the United Arab Emirates hosts an 8-12 km thick sequence of particularly well-studied ultramafic rock, upper mantle peridotite (e.g., Glennie et al., 1973, Searle and Cox, 1999). Magnesite is common within the ophiolite, occurring in veins that are up to a few meters thick (Fig. 3.3) (e.g., Neal and Stanger, 1984, 1985; Kelemen and Matter, 2008; Kelemen et al., 2011; Mervine et al., 2014). Neal and Stanger (1985) estimate that 80% of carbonate veins within the mantle rock of the ophiolite are magnesite. Hydromagnesite, nesquehonite, and dypingite and other related minerals (e.g. aragonite, brucite etc.) are also present as rock coatings and crusts within spring deposits (e.g., Giampouras et al., 2020). Magnesite vein outcrops are separated spatially from surface-outcropping travertines (Ca-carbonates), which formed from discharging alkaline Ca^{2+}- and OH^-- rich waters (Clark and Fontes, 1990; Kelemen et al., 2011). While the ophiolite obducted >90 Ma (Rioux et al., 2012, 2013, 2016), radiocarbon can be readily detected in carbonate veins, and dating yields ~8-45 kyr ages for most veins (Kelemen et al., 2011; Mervine et al., 2014; see section 3.9). This suggests that magnesite veins are actively forming through low temperature surface weathering (Kelemen et al., 2011).

Similarly, deep veins within the New Caledonia ophiolite contain magnesite and are interpreted to form through alteration by meteoric water, possibly associated with laterization at the surface (Fig. 3.3) (Quesnel et al., 2013, 2016; Ulrich et al., 2014). Magnesite veins up to 10-m thick within ophiolite blocks in NE Iran, such as the Derakht-Senjed deposit, are associated with the Mg-rich, Ca-poor fluids, indicative of weathering processes (Mirnejad et al., 2008; Mirnejad et al., 2015). The Attunga magnesite deposit within the Great Serpentinite Belt deposit contains veins and nodules within the ultramafic rock interpreted to have formed through weathering (e.g. Oskierski et al., 2013). Furthermore, tcharacteristic vein and stockwork magnesite have been identified in the Dinarides in the Balkan Peninsula (referred to as Yugoslavia in past literature) (Fallick et al., 1991; Jurković et al., 2012). However, studies disagree on whether these deposits originated through a hydrothermal or weathering process.

These settings of chemical weathering of ultramafic rocks were suggested as an original analog

for the Mg carbonates on Mars (Ehlmann et al., 2008), because cold temperature weathering under water-limited conditions will tend to promote magnesium carbonates but not the later stages of serpentine or calcium carbonate formation common in the water-rich terrestrial systems but not observed in associated with the deposits on Mars.

3.4.1.3 Magnesite precipitation during soil formation

Magnesium carbonates are also associated with the soils in ultramafic regions and represent a combination of chemical weathering as well as dissolution-reprecipitation reactions as meteoric fluids and organic acids from vegetation interact with ultramafic rocks. In addition to deep veins, the ophiolites in New Caledonia and Attunga, Australia are also associated with pedogenic environments directly overlying ultramafics, and are interpreted to represent surface alteration of the ultramafics (Quesnel et al., 2013; 2016; Oskierski et al., 2013). These pedogenic soils in New Caledonia and Attunga often contain nodular concretions of magnesite with cauliflower textures (Fig. 3.2-3). A similar setting is found at the Woodsreef Asbestos Mine in the Great Serpentinite Belt, Australia where hydromagnesite, magnesite, and other carbonates formed through reaction of meteoric fluids with mine tailings (Oskierski et al., 2013).

3.4.2 Sedimentary magnesium carbonate deposits on Earth

Magnesite-forming systems are often related to hydrologic conditions within broader ultramafic catchments. Permanent lakes form when evaporation is balanced by recharge from the watershed, and playas form when evaporation exceeds recharge so that the basin is intermittently dry. However, lakes and playas are similar in that dissolved ions are sourced from the surrounding watershed rather than bedrock directly underneath the deposit (Brathwaite and Zedef, 2000; Power et al., 2014). Furthermore, numerical modeling of evaporite basins has shown that even thin (10s of cm) evaporite beds require large volume of water to be flushed through the system, often exceeding the total lake volume by a factor of 1000 or more (Wood and Sandford, 1990). As such, ancient magnesite from playas or lakes could be qualitative indicators of long-term water availability and/or chemical weathering rates in the surrounding drainage area (Fig 2). In contrast, magnesite-bearing soils (Quesnel et al., 2016; Schroll 2002) are more difficult to interpret; some soils form from groundwater discharge into topographic lows (Oskierski et al., 2013), but others could be in-situ weathering products where ions are sourced directly from underlying bedrock (Fig. 3.2).

Magnesium carbonates have been observed to precipitate in perennial alkaline lakes, ephemeral playas (e.g. Mur and Upinell, 1987; Braithwaite and Zedef, 1996; Alçiçek, 2009), soils (Quesnel et al., 2013; Schroll 2002, Oskierski et al., 2013), and coastal salinas (Von der Borch, 1965) (Fig. 3.2 and 3.4). All of these lakes and playas are within or adjacent to ultramafic units. For example, Lake Salda, Turkey, contains hydromagnesite mounds, terraces, and stromatolites (Fig. 3.2 and 3.4) (Van der Borch, 1965;

Zedef et al., 1996, 2000; Russel et al., 1999). This ~200 m deep lake has waters of pH >9 (Braithwaite and Zedef, 1996), and Mg was likely sourced through the Lake Salda watershed ground and surface waters interacting with the surrounding serpentinized ultramafic rock (Zedef et al., 2000). Lake Salda has recently been revisited by Horgan et al., (2020) as an analog for the "marginal carbonates" in Jezero crater, Mars, which occupy a restricted elevation range that tracks the elevation of the delta top, suggesting a possible shoreline deposit for those carbonates (Horgan et al., 2020). At Lake Salda, hydromagnesite precipitates as coatings and cements in nearshore sediment associated with rocky shorelines and deltas (Braithewaite and Zedef, 1996). In addition, hydromagnesite comprises stromatolites in Lake Salda, which provides an analog for possible biosignature preservation on Mars (Braithwaite and Zedef, 1996; Russel et al., 1999).

Magnesium carbonate-bearing playas have been well-documented near Atlin, British Columbia (Power et al., 2007; 2014; 2019). Regional ophiolites are the likely source of Mg to these playas, and the climate is subarctic with carbonates forming at freezing conditions (Power et al., 2007, 2014, 2019); this last point is significant and means magnesium carbonates can and do form across a wide range of temperature conditions (Bosak et al., in press). This is relevant to Mars as the Martian surface temperature varies widely (-130 to 30 °C) but is generally much cooler than Earth's surface (e.g. Vasavada et al., 2017). Magnesium carbonates form low relief mounds (10s of cm) in the center of the playa (Fig. 3.4). These mounds include mixtures of magnesite and metastable magnesium carbonates such as hydromagnesite, nesquehonite, and landsfordite (Power et al., 2014). While magnesite precipitation is initiated subaqueously, mounds in the Atlin playas continued to grow and amalgamate after their emergence from the surrounding ephemeral ponds (Power et al., 2019). Exposure features in these deposits consist of polygonal desiccation cracks and "cauliflower" textures, interpreted to require limited surface water during magnesite formation (Power et al., 2014). In ephemeral systems, magnesite precipitates from playa lakes in Los Monegros, Spain, from the combination of seasonal Mg-rich brines and decaying organic matter increasing CO_2 (Mur & Urpinell, 1987).

The 2 Ga Tulomozerkskaya Formation in the Fennoscandian Shield, Scandinavia, includes five beds of magnesite interpreted to have formed in a playa or sabkha environment in which micritic magnesite diagenetically replaced dolomite and magnesite precipitated directly from brines (Melezhik et al., 2001). In this Paleoproterozoic example magnesite replacement appears to have been stimulated by evaporative modification of mixed marine-terrestrial fluids rather than weathering of ultramafic rocks. A modern analog for this type of magnesite precipitation is found in the coastal salinas of the Coorong region of South Australia (Von der Borch, 1965; Walter et al., 1973). In the ~790 Ma Skillogalee Dolomite of South Australia, finely laminated, micritic magnesite occurs rarely with mudcracks and tepee

structures indicating subaerial exposure and evaporation, but more commonly as reworked, conglomeratic intraclasts (Frank and Fielding, 2003).

3.4.3 Effects of deformation by impact shock

It is likely that areas of the ancient Martian magnesium carbonate system within the Jezero crater region have been affected by impacts. On Earth, we have observed impact structures in limestone and dolostone target rocks, but not magnesium carbonate rocks (e.g., Pohl et al., 1977; Kieffer, 1971; Metzler et al., 1988). Passage of the shock wave during impact events modifies the carbonate target rock to produce high-pressure deformation fabrics such as shatter cones and, where shock pressures are high enough, they can melt the carbonate target rock (e.g., Dence, 1971; Grieve et al., 1977). While devolatilization of carbonates was previously thought to be important, experiments and observations of terrestrial structures suggest that this process has minimal effect on Earth (Graup, 1999; Osinski and Spray, 2001; Jones et al., 2005; Bell, 2016). Instead, much of the carbonate is retained within carbonate-bearing impact melts (e.g., Graup, 1999; Osinski and Spray, 2001, Jones et al., 2005). These carbonate-bearing melts typically quench to form minerals, not glasses, and are immiscible with silicate impact melts (Freestone and Hamilton, 1980; Graup, 1999; Osinski and Spray, 2001). However, it is currently unknown how this melting process would work with the differing physical conditions of the Martian surface. Another open question is whether magnesite could form via quenching of magnesium carbonate impact melts. No such process has been observed on Earth, and the well-studied Haughton structure showed carbonate melts were Mg-poor despite melting of dolomite within the target rock (Osinski and Spray, 2001; Osinsi et al., 2005)

3.4.4 Magnesium carbonates on Mars

Orbiter-based detection of magnesium carbonates is often associated with detection of olivine-bearing rocks circumferential to the 1900-km Isidis impact basin, to the west in the Nili Fossae region and to the south in Libya Montes (Mustard et al., 2009; Bishop et al., 2013; Edwards and Ehlmann, 2015; Ehlmann et al., 2008; Bramble et al., 2017; Brown et al., 2020; Viviano et al., 2013) (Fig 1A). The olivine- and carbonate-bearing unit is typically a few to tens of meters thick and occurs in a distinctive stratigraphic position. It overlies an older, extensive low Ca-pyroxene and Fe/Mg-smectite-bearing rocks of Noachian age (>~3.8 Ga; Mandon et al., 2020; Scheller and Ehlmann, 2020) and underlies a high Ca-pyroxene-bearing mafic capping unit (Bramble et al., 2017). The olivine- and carbonate-bearing unit spans a large elevation range of more than 3 km. Formation hypotheses discussed in the literature include an olivine-bearing ashfall, lava flow, impact melt sheet, or igneous intrusion (Hamilton & Christensen, 2005; Hoefen et al., 2003; Kremer et al., 2019; Mustard et al., 2007; 2009; Tornabene et al., 2008; Brown et al., 2020).

The strong association between magnesium carbonates and ultramafic rocks on Earth suggests

that potential ultramafic materials exposed in the watershed of the Jezero basin may host magnesium carbonates similar in context to the terrestrial examples discussed above. Complicating this interpretation, however, is the fact that modeling of mineralogy from orbital infrared datasets does not yield ultramafic compositions. Original thermal infrared modeling of olivine abundance estimated 30 wt. % olivine (Hoefen et al., 2003) and later analyses showed 10-15 wt. % olivine (Salvatore et al., 2018). Joint modeling of near-infrared and thermal infrared data suggests ~25 wt.% olivine, ~30 wt.% pyroxene, and ~15 wt.% carbonate (Ehlmann and Edwards, 2015). By contrast, unserpentinized ultramafic rocks on Earth are typically >80-90% olivine and pyroxene. While it is possible that coverage by basaltic dust or sand obscures an ultramafic composition, it remains for in situ investigation to understand the composition of the rock and relationship between the olivine and carbonate. Observations of the carbonate textures, abundances of carbonate within the rocks, and whether they are vein-forming, nodule-forming, within the matrix of the olivine-bearing rock, or surficial (e.g., travertine, playa) will be critical for understanding the best terrestrial analogue environments for magnesium carbonate formation on Mars.

This laterally extensive, regional olivine-carbonate unit includes the watershed of Jezero crater within the extended mission area of Nili Planum. Similar materials are on the floor of Jezero crater and within its delta. The purest carbonate signatures regionally (i.e., lacking a Fe/Mg phyllosilicate absorption) are found in the sedimentary materials of Jezero crater (Ehlmann et al., 2008; 2009) (Fig. 3.1B-C). The olivine-carbonate unit appears to drape over the Jezero crater rim to the floor, which would demand that it postdates formation of Jezero crater (Goudge et al., 2015; Bramble et al., 2017; Kremer et al., 2019; Mandon et al., 2020; Brown et al., 2020) (Fig. 3.1). On the other hand, materials comprising the floor of Jezero could be distinctive deposits formed by sedimentation in a lake of the eroded olivine-carbonate formation. A separate magnesium carbonate-bearing unit has been hypothesized within the Jezero crater as the "margin light-toned fractured unit" in Stack et al. (2020) or "marginal carbonates" in Horgan et al. (2020) (Fig. 3.1B). This unit has a stronger signal of magnesium carbonate than deltaic sediments or other floor units within beds of consistent elevational level with close proximity to the western part of the crater rim (Fig. 3.1C). It is possible that this mode of magnesium carbonate accumulation represents authigenic precipitation from fluids that percolated down gradient in the shallow subsurface and then emerged at lake level to precipitate magnesium carbonate along the delta shoreline in a highstand position (Horgan et al., 2020). Alternatively and/or additionally, detrital carbonate grains transported from the regional olivine-carbonate unit outside Jezero crater were likely deposited fluvially in the prominent river delta in the crater (Goudge, 2015). Observations of the carbonate fabrics within the marginal carbonates of Jezero crater will likely be indicative as to whether these can be considered to be authigenic precipitants or detrital materials. Furthermore, observations of carbonate fabrics and structures

can be tied to lake history and used to distinguish between an alkaline lake environment versus playas (Fig. 3.2).

3.5 Magnesium carbonate fabrics and paragenesis

The occurrence, fabrics, paragenesis and associated mineral assemblages vary by environmental type, and environments of formation that can sometimes be inferred from these features (Table 3.1; Fig. 3.3-5). The Perseverance rover is equipped with spectroscopic and imaging instruments that are specifically designed to determine rock textures and associated mineral assemblages. Hence, rover observations of fabrics and mineral assemblages can be used to directly test between environments of formation for magnesium carbonates on ancient Mars.

3.5.1 Ultramafic rock-hosted magnesium carbonate

In ultramafic terrains, magnesite occurs primarily within secondary vein deposits (Fig. 3.3). Vein deposits from for example the Balkan Peninsula (referred to as Yugoslavia in past literature) occur at depths greater than ~80-200 meters with a thickness of up to 20 m, then grading to more abundant, thin veins (1 mm – 2 m wide) (Zachmann and Johannes, 1989). These veins are characteristically finely crystalline to microcrystalline of nm-µm scale crystals, often described as cryptocrystalline massive fabrics with occasional spheroidal textures (Fig. 3.3) (Abu-Jaber and Kimberley, 1992). The spheroidal fabric is characterized by ~3 mm aggregates of fine euhedral crystals (<1 mm) within a matrix of finer (<0.1 mm) spherical grains. At the macroscopic scale, microcrystalline magnesite is bright white. Microscopically, it exhibits a characteristic conchoidal fracture, and is devoid of fluid inclusions or pseudomorphic textures after the parental ultramafic rock (García del Real et al., 2016). The massive microcrystalline magnesite forms vein fills together with other Ca-carbonates, such as dolomite and calcite, as well as silica and serpentine within serpentinized dunite or peridotite (Abu-Jaber and Kimberley, 1992; Zachmann, 1989) (Fig. 3.3). Additionally, ultramafic rocks may host multiple episodes of vein formation in which some veins are primarily composed of calcite whereas others are primarily composed of magnesium carbonates (Streit et al., 2012; Cooperdock et al., 2020).

In carbonated ultramafic rocks, magnesium carbonates form assemblages with other Fe- and Ca-carbonates, silica, sulfides, spinel, iron oxides, fuchsite, serpentine, and talc (Boskabadi et al., 2020) and typically occur in close association with serpentinized dunite or peridotite in the (section 3.4). In carbonated ultramafic rocks, magnesium carbonate occur both as veins and within the matrix forming finely crystalline to microcrystalline or cryptocrystalline textures with nm-µm scale crystals finely
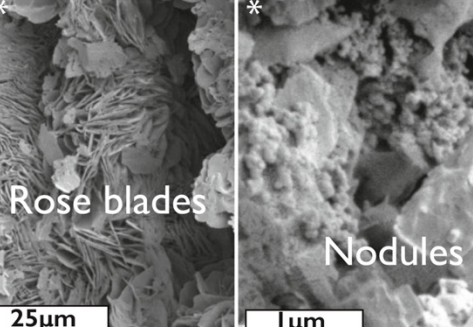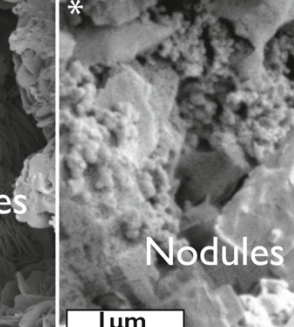
intergrown with silica and other minor phases (Boskabadi et al., 2020; Fallick et al., 2015). However, coarse magnesite crystals of 1-0.25 mm can be found in alternating layers in carbonated ultramafic rocks as well (Menzel et al., 2018). Importantly, the specific mineral assemblages found within the carbonated ultramafic rock can be used to constrain the temperature and pressure conditions of formation.

3.5.2 Sedimentary deposits

3.5.2.1 Observed fabrics and parageneses

In Late Triassic hypersaline evaporite deposits (Lugli, Morteani and Blamart, 2002) and in Holocene salt lake deposits (Mees and Keppens, 2013), magnesite and nesquehonite seem to have precipitated together with evaporitic sulfate salts and halite (Fig. 3.4). Sedimentary magnesite deposits also occur in the Precambrian rock record (Melezhik et al., 2001, Alderman and Von der Borch, 1961). Here, Ca-bearing sulfate minerals are likely absent due to both the depleted marine sulfate reservoir (compared to present day), and the seawater chemistry that favored Ca-carbonate precipitation instead of Ca-bearing sulfate (Grotzinger, 1989; Grotzinger and Kasting, 1993; Frank and Fielding, 2003).

Magnesite, hydromagnesite, dypingite, and nesquehonite assemblages have been found in playas within Atlin, British Columbia, along with aragonite, quartz, clay minerals and feldspars (Power et al.,

*Original images kindly provided by Garcia del Real from work on a compilation of study sites (e.g. del Real et al., 2016)
**Original pictures by authors of magnesite veins within serpentinite from Marlborough, Australia
***Original pictures by authors of magnesite veins in Oman ophoplite

Fig. 3.3: Key textures at micro-, meso-, and macro-scale in ultramafic terrains (upper row) and pedogenic soils overlying ultramafic terrains (lower row). Full length of hammer for scale is ~32 cm. Quarter for scale is ~2.5 cm. Pen for scale is ~10 cm. Lens cap for scale is ~5 cm.

2007). These form large, white mounds with cauliflower textures (Fig. 3.4) (Power et al., 2019). It is thought that the formation of dypingite serves as a precursor for the formation of hydromagnesite via dehydration at the playa mounds in Atlin (Power et al., 2007). Similarly, beds of magnesite, hydromagnesite, dolomite, aragonite, and gypsum are found in a series of alkaline lakes associated with the Coorong Lagoon, east coast of South Australia (Von der Bock, 1965; Warren, 1990). These carbonate assemblages form laminated or massive lake beds and nodules in siliciclastics (Warren, 1990; Rosen et al., 1988). The relative influence of marine, fluvial and groundwaters input and evaporation controlled the specific mineralogical assemblages. Mg input results from groundwaters interacting with terrestrial materials including the local Pleistocene dune system, and the relative importance of (hydro)magnesite decreases with marine influence and increases with evaporation and salinity. As Mg-enriched groundwaters feed the northern Coorong lakes, Ca-rich phases precipitate closer to inputs at lake margins, and Mg-rich phases precipitate basinward where evaporation dominates (Warren 1990).

3.5.2.2 Preservation of microbial mats

Microbial mats can be associated with hydrated magnesium carbonates in both modern and ancient environments, mostly in alkaline lakes but occasionally in hypersaline lakes as well (Fig. 3.4) (e.g. Walter et al., 1973; Renaut, 1993; Braithwaite and Zedef, 1994; Sanz-Montero and Rodríguez-Aranda, 2012; Cabestrero and Sanz-Montero, 2018; Power et al., 2019). Microbial-mat associated magnesium carbonates form laminated, clotted, and spherical textures that make up stromatolitic or thrombolitic structures (Bosak et al., in press) (Fig. 3.4). The Perseverance rover will be able to analyze for the presence of these macroscopic and microscopic microbial mat associated textures and structures (Bosak et al., in press). Although no single textural observation can be utilized to determine unequivocally that biosignatures are recorded within the magnesium carbonate deposit, the presence of these textures are indicative that sampling and subsequent laboratory measurements to understand the formation of these structures would be highly informative.

Table 3.1: Overview of all characterized magnesium carbonate textures, their associated paragenetic mineral assemblages and geological setting as described in section 3.5. Right column shows accompanying figure number with detailed textural images at micro-, meso-, and macro-scales.

Texture/crystal habit	Paragenetic mineral assemblage	Geological setting	Fig
Fine-grained or microcrystalline veins	magnesite $\pm$hydrommagnesite $\pm$ talc $\pm$ silica $\pm$ olivine $\pm$ serpentine $\pm$ dolomite $\pm$ calcite	Ultramafic terrains	3.3
Fine-grained or microcrystalline matrix of carbonated ultramafic rock	magnesite $\pm$hydrommagnesite $\pm$ talc $\pm$ silica $\pm$ olivine $\pm$ serpentine $\pm$ brucite $\pm$ quartz $\pm$dolomite $\pm$ calcite	Ultramafic terrains	3.3

Nodules and bladed aggregates	magnesite $\pm$ hydromagnesite $\pm$ nesquehonite $\pm$ dypingite$\pm$ silica	Pedogenic soils	3.3
Fine-grained or microcrystalline mounds	magnesite $\pm$ hydromagnesite $\pm$ nesquehonite $\pm$ dypingite $\pm$ aragonite $\pm$ sulfates $\pm$ halite	Hypersaline lakes and playas	3.4
Thrombolites, nodules, stromatolites/laminated lithified mats, botryoids	magnesite $\pm$ hydromagnesite $\pm$ Mg-silicates	Alkaline lakes	3.4
Spherulites/coccoids	magnesite $\pm$ hydromagnesite $\pm$ dolomite	Alkaline lakes	3.4
Coatings on filaments and detrital grains	magnesite $\pm$ hydromagnesite	Alkaline lakes	3.4
Microcrystalline	magnesite $\pm$ calcite $\pm$ dolomite	Diagenetic replacement	3.5
Spar	magnesite $\pm$ tremolite, quartz $\pm$ calcite $\pm$ talc $\pm$ diopside	Metasomatic replacement	3.5
Spar	magnesite $\pm$ garnet $\pm$diopside in peridotite or eclogite assemblages	Ultra-high pressure (UHP) terrains	3.5

Laminated fabrics of primarily hydromagnesite makes up thrombolites and stromatolites in well-studied modern alkaline lake environments within the Las Eras lake, Spain (Sanz-Montero, Cabestrero and Sánchez-Román, 2019), Lake Salda, Turkey (Braithwaite and Zedef, 1994), and Lake Alchichica, Mexico (Kaźmierczak et al., 2011). In Las Eras lake, hydromagnesite, magnesite, and dolomite thrombolites are associated with cyanobacterial mats enriched in extrapolymeric substances (EPS), sometimes in association with sulfate salts (Sanz-Montero, Cabestrero and Sánchez-Román, 2019). Hydromagnesite aggregates nucleate EPS-encased microorganisms, in association with nesquehonite crystals to form coatings (Sanz-Montero, Cabestrero and Sánchez-Román, 2019). Dolomite and magnesite also form aggregates of nanoparticles that rest on the hydromagnesite-coated EPS (Sanz-Montero, Cabestrero and Sánchez-Román, 2019). In Lake Salda, stromatolites form in sizes ranging from a few cm in height in shallow water to 1-2 meters at depths of 6-8 meters below present lake level (Fig. 3.4) (Braithwaite and Zedef, 1996). The stromatolites contain laminae up to a few centimeters thick with distinct regions of ~5 μm spherical or bladed hydromagnesite-coated filaments and diatoms (Fig. 3.4) (Braithwaite and Zedef, 1996). Mg-silicates have been reported in modern Lake Salda stromatolites both as authigenic minerals and as trapped detrital grains (Balci et al., 2020), which is a common mineralogical component in highly alkaline systems (e.g. Darragi & Tardy, 1987). Lake Salda stromatolites are dominated by cyanobacteria and gamma and alpha-proteobacteria (Balci et al., 2020). In Lake Alchichica, Mexico, stromatolites, massive domes and crusts are covered by a cyanobacteria-hosted biofilm that
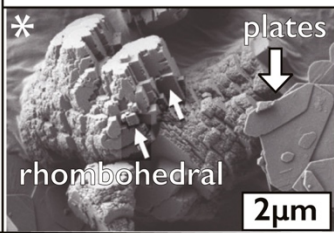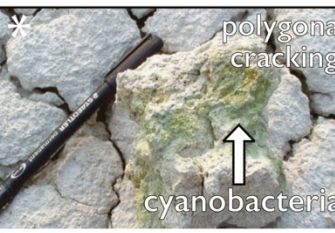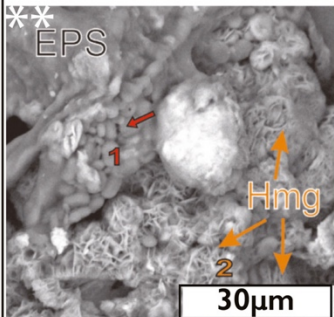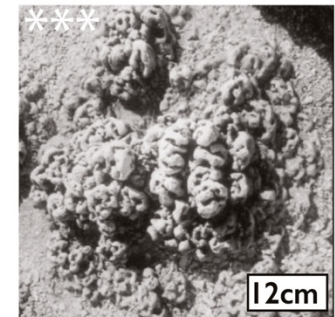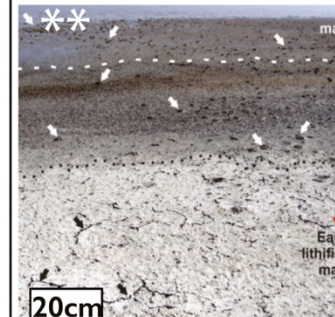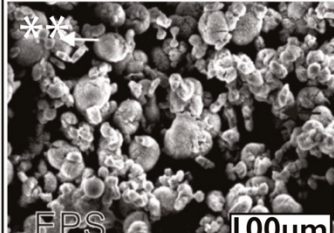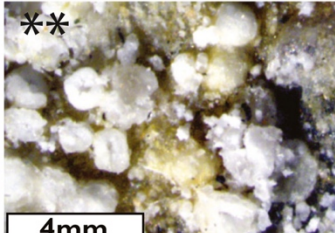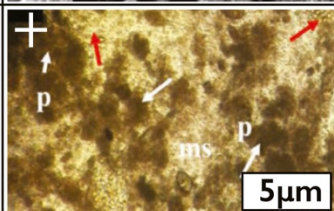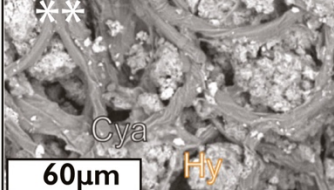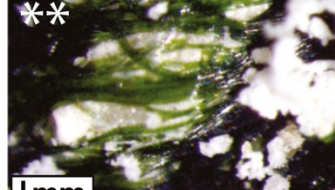
contains trapped hydromagnesite and aragonite inside an EPS matrix (Kaźmierczak et al., 2011; Gérard et al., 2013). In these systems, research is still needed in order to understand whether magnesium carbonates are precipitated authigenically within biofilms or if biofilms trap and bind the magnesium carbonates (see section 3.6.3).

Microbial mat associated textures can be retained within ancient magnesium carbonate deposits, like those expected on Mars. However, magnesium carbonates, especially magnesite, may not be authigenic and could represent instead diagenetic recrystallization of Ca-carbonates or hydrated magnesium carbonates. Magnesite in ancient Paleoproterozoic basin deposits in the Liaodong Peninsula, China forms stromatolitic structures as well as thinly laminated beds that are preserved in for example the Dashinqiao Fm, interpreted to have formed in shallow marine settings (Zhang, 1988; Dong et al., 2016). These stromatolites and laminated beds reveal complex associations between primary sedimentary magnesite with dark, microcrystalline microtextures and later coarse, sparry diagenetic magnesite replacement fabrics (Zhang, 1988; Dong et al., 2016). Similarly, in the Paleoproterozoic Tulomozerkskaya Fm, Russia, magnesite in stromatolitic structures and laminated beds, but are not interpreted to be primary precipitants and represent instead early diagenetic replacements of associated dolomite (see section 3.5.3).

3.5.3 Diagenetic, metasomatic, and metamorphic replacement

Sedimentary deposits, or *strata-bound* deposits, of limestone and dolostone formed in lacustrine and marine environments can be replaced by later magnesite when exposed to diagenetic or burial fluids that have migrated through ultramafic terrain (Fig. 3.5). Magnesite replacement can either preserve the original bedding and associated textures or form massive, fabric-destructive microcrystalline textures (Fig. 3.5) (Abu-Jaber and Kimberley, 1992).

Microcrystalline replacement magnesite with occasional neomorphic coarse crystals represents synsedimentary or early diagenetic replacement and forms with diagenetic sulfates and quartz (Abu-Jaber and Kimberley, 1992; Melezhik et al., 2001; Keeling et al, 2019) (Fig. 3.5.A, 5.D). Under relatively low-pressure burial conditions with temperatures at 100 to 400°C, metasomatism of primary dolostone by hydrothermal Mg-rich fluids leads to the formation of sparry magnesite (Fig. 3.5.A-C) (Aharon, 1988; Lugli, Morteani, and Blamart, 2002). This metasomatic magnesite spar is characterized by a medium (1-9 mm) to coarse (1-15 cm) crystal size, and can occur as massive deposits (Fig. 3.5.A), fracture fillings, or with porphyroblastic (scattered lens-shaped crystals in dolostones and sulfate rocks) (Fig. 3.5.B-C), rosette, banded, and palisade (Fig. 3.5.D) textures (Lugli, Morteani, and Blamart, 2002; Ronchi et al., 2008). At higher temperatures and pressures, metasedimentary, sparry magnesite has been found in

	Micro-scale	Meso-scale	Macro-scale
microcrystalline mounds in playa	* plates rhombohedral 2μm	* polygonal cracking cyanobacteria	* magnesite mounds wetlands
thrombolite/stromatolite/ nodules/botryoids alkaline lakes	** EPS 1 Hmg 2 30μm	*** 12cm	** mats Early lithified mats 20cm
spherulites/ spheroids alkaline lakes	** EPS 100μm	** 4mm	
peloids alkaline lakes	+ p ms p 5μm		
filament coatings alkaline lakes	** Cya Hy 60μm	** 1mm	+ 4cm

*Playa in Atlin, British Columbia from Power et al. (2014)
**Lake Las Eras, Central Spain from Sanz-Montero et al. (2019)
***Lake Salda Gölü, Turkey from Zedef et al. (2000)
+Lake Salda Gölü, Turkey from Balci et al. (2020)

Fig. 3.4: Key textures at micro-, meso-, and macro-scale in hypersaline and alkaline lake environments. White arrows in alkaline lake macroscale indicate location of mat mounds. Playa mounds macroscale image is an aerial photograph and hence missing scale. The symbols denote the source of images from publications or contributed by individuals as listed in the bottom. Hmg = hydromagnesite, EPS = extrapolymeric substances, Cya = cyanobacteria, Hy = hydromagnesite, p = peloid, ms = microsparitic.
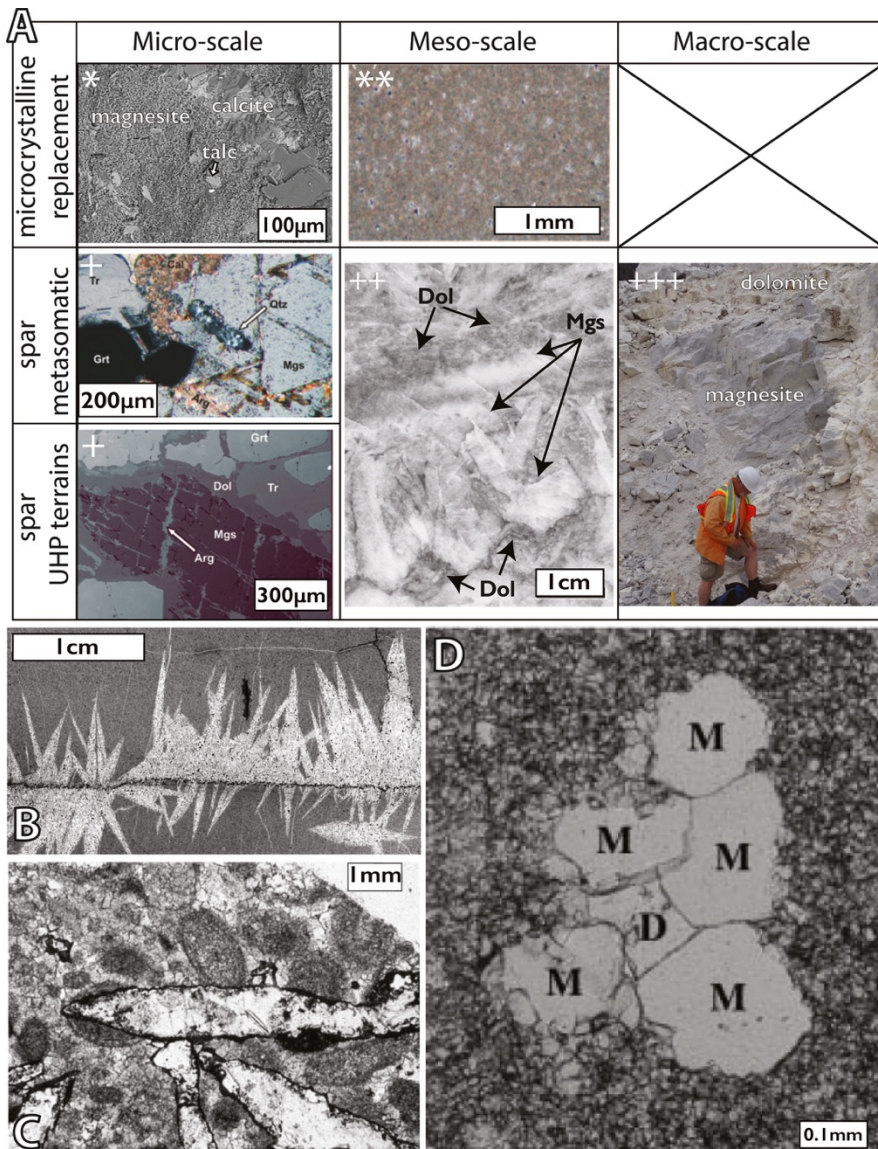
*Myrtle Springs Formation, South Australia from Keeling et al. (2019)
**Torshak magnesite deposit, ophiolite belt of Eastern Iran from Mirnejad et al. (2008)
+Jæren nappe, SW Norway from Smit et al. (2008)
++South Ural province from Krupenin & Kol'tsov (2017)
+++Jubilee Fm, British Columbia from Paradis & Simandi (2018)

Fig. 3.5: Key textures from diagenetic replacements. (A) Key textures at micro-, meso-, and macro-scale in diagenetic replacement environments (upper row) and metasomatic replacement as well as ultrahigh-pressure (UHP) environments (lower row). (B–D) Additional thin section micrographs show the diversity of magnesite replacement textures. (B) Lenticular sparry magnesite crystals growing from a stylolite and replacing dolomite in a metasomatic environment from Eugui-Asturreta magnesite deposit, Western Pyrenees, Spain (Lugli et al., 2000). (C) Lenticular sparry magnesite replacing oolitic dolomite rock from Burrano Fm, Northern Apennines, Italy (Lugli, Morteani & Blamart, 2002). (D) Neomorphic crystals of magnesite (M) and dolomite (D) and surrounding microcrystalline magnesite diagenetically replacing Paleoproterozoic dolostone from Tulomozerskaya Fm, Russian Karelia (Melezhik et al., 2001). The symbols denote the source of images from publications or contributed by individuals as listed in the bottom (Paradis & Simandl, 2018; Smit et al., 2008). Grt = garnet, Qtz = quartz, Mgs = magnesite, Dol = dolomite, Tr = tremolite, Arg = aragonite.

association with tremolite-quartz-calcite ± talc ± diopside (Ronchi et al., 2008; Krupenin and Kol'tsov, 2017). In ultrahigh-pressure (UHP) metamorphic terrains, magnesite occurs as sub-mm grains with diopside in assemblages of garnet websterites, peridotites and eclogites (Fig. 3.5) (Yang et al., 1993; Zhang and Liou, 1994).

3.6 Thermodynamics and kinetics of magnesium carbonate precipitation

As with other carbonates, thermodynamic and kinetic factors regulate precipitation of magnesium carbonates. Direct precipitation of terrestrial magnesite is not fully understood but can be favored by high temperatures, dehydration of preexisting hydrated magnesium carbonates, or perhaps microbially-mediated processes. In a Martian context, it will therefore be important to make careful observations of pseudomorphic textures, small-scale chemistry and crystal structure, or other evidence to differentiate processes.

3.6.1 Thermodynamics

Magnesite forms in aqueous solution by the addition of magnesium and carbonate ions (eq. 1). Equilibrium between magnesite and its constituent ions in solution is dictated by the solubility constant, K_{sp}, for a given temperature and pressure. K_{sp} is defined by the product of the activity of the magnesium ($a_{Mg^{2+}}$) and carbonate ($a_{CO_3^{2-}}$) ions in solution at equilibrium, divided by the activity of solid magnesite (a_{MgCO_3}). As pure solids are generally assumed to have an activity of unity, K_{sp} may be simplified to the product of the magnesium and carbonate ion activities (eq. 2). Experimental determination of K_{sp} at 25°C is complicated by long equilibration times between magnesite and solution at low temperatures. As a result, determination of K_{sp} values at ambient temperature rely on extrapolation of high temperature experimental data where magnesite precipitates readily. Reported K_{sp} values and other thermodynamic constraints on the precipitation and dissolution of magnesite vary (Bar, 1932; Langmuir, 1965; Halla and Van Taddel, 1966; Christ and Hosteltler, 1970; Sayles and Fyfe, 1973; Allison et al., 1991); generally accepted K_{sp} values are between $10^{-8.2}$ to $10^{-7.8}$ (Benezeth et al., 2011; Rossini et al, 1961; Robie and Waldbaum, 1968).

$$MgCO_3 \text{ (s)} \rightleftharpoons Mg^{2+} + CO_3^{2-} \tag{1}$$

$$K_{sp}^{mgs} = \frac{a_{Mg^{2+}} \times a_{CO_3^{2-}}}{a_{MgCO_3}} \cong a_{Mg^{2+}(eq)} \times a_{CO_3^{2-}(eq)} \tag{2}$$

The thermodynamic driving force for magnesite precipitation from aqueous solution can be defined by the saturation state (Ω), the ratio between the ion activity product (IAP) of reactive species and the solubility product (eq. 3).

$$\Omega = \frac{IAP}{K_{sp}} = \frac{a_{Mg^{2+}} \times a_{CO_3^{2-}}}{K_{sp}^{mgs}} \tag{3}$$

Precipitation is favored when $\Omega > 1$ and dissolution is favored when $\Omega < 1$. Magnesite is more soluble than other naturally occurring metal-carbonate phases: $K_{sp}^{magnesite} > K_{sp}^{calcite} > K_{sp}^{strontanite} > K_{sp}^{siderite} > K_{sp}^{rhodochrosite} > K_{sp}^{dolomite}$ (Stumm and Morgan, 1996). Even when conditions of supersaturation are reached ($\Omega > 1$), magnesite is rarely observed to nucleate and form as a primary precipitate in aqueous solution under ambient conditions, indicating that kinetic factors likely prevent direct magnesite precipitation from solution. Direct precipitation from supersaturated solutions in experiments has only been observed above 100°C (Hänchen et al., 2008), or at lower temperatures when aided by microbial materials and metabolism (see section 3.6.3).

Magnesite formation at ambient temperatures and atmospheric pressures has been observed via recrystallization of hydrated magnesium carbonates (Deelman, 1999; Konigsberger et al., 1999; Giammar et al., 2005; Hänchen et al., 2007; Hopkinson et al., 2012). The relative thermodynamic stabilities of the common phases in this system are magnesite > hydromagnesite > nesquehonite, above 8.5 °C, or lansfordite, below 8.5°C (Marion, 2001). Despite the inferior energetics, the hydrated phases appear to be less inhibited kinetically, may therefore precipitate before magnesite and then recrystallize to form the more thermodynamically stable magnesite. In Jezero crater and its watershed, infrared spectroscopic data is compatible with hydrous carbonates as a component with magnesite. Hence, we may find either magnesite, hydromagnesite, or a combination of these and other carbonate minerals within the landing site (see section 3.3).

3.6.2 Kinetics

Kinetic factors also impact magnesite precipitation and dissolution rates. Like calculation of the K_{sp}, kinetic data are experimentally determined at elevated temperatures and pressures and extrapolated to ambient conditions (Sayles and Fyfe, 1973; Saldi et al., 2009). Alternatively, kinetic data are obtained for the transformation of metastable phases to magnesite and can more aptly be defined as a "recrystallization" rate (Zhang et al., 2000). For solutions at $\Omega = 10$ and 25°C, the rate of magnesite precipitation was calculated to be on the order of 10^{-18} mol cm^{-2}s^{-1}, a rate six orders of magnitude slower than calcite formation at 25°C and similar oversaturation (Saldi et al., 2009). Power et al. (2019) calculated a slightly higher magnesite precipitation rate of 10^{-17} to 10^{-16} mol cm^{-2}s^{-1} within playas in Atlin, British Columbia.

Sayles and Fyfe (1973) observed an increase in the rate of magnesite precipitation with increasing pCO$_2$ and ionic strength and decreasing magnesium ion concentration (in contrast to thermodynamic predictions). Other phases in the MgO-CO$_2$-H$_2$O system do not experience kinetic sluggishness to the same extent as magnesite, and thus can facilitate magnesite formation (via recrystallization of hydrated precursors) on the order of hours (Sayles and Fyfe, 1973; Zhang et al., 2000; Schaef et al., 2011; Felmy et al., 2012).

The slow precipitation kinetics of magnesite are thought to originate from effects between the magnesite surface and magnesium ions. In most environmental waters, magnesium ions are strongly complexed with six to twelve water molecules that exchange slowly (Jiao et al., 2006; Di Tommaso and de Leeuw, 2010). The slow desolvation of magnesium ions at the magnesite surface effectively retards magnesium incorporation into and attachment of carbonate ions onto the crystal surface (Lippmann, 1973; Saldi et al., 2009). The relationship between magnesium ions and kinetic inhibition of mineral growth has been extensively studied in calcite (e.g. Bischoff, 1968). Solvated magnesium ions inhibit calcite growth by acting as "kink blockers" (Wasylenki et al., 2005; Mavromatis et al., 2013; Davis et al., 2000). Magnesium ions will adsorb to high energy surface sites (kinks) with waters of hydration still complexed. This effectively blocks the attachment of additional monomers to the surface until the complex dehydrates and incorporates into the crystal or the complex desorbs and returns to solution (Wasylenki et al., 2005; Mavromatis et al., 2013; Davis et al., 2000). At higher temperatures, magnesium ions exchange H_2O more rapidly, resulting in the observed trend of quicker rates at higher temperatures (Di Tommaso and deLeew, 2010). This concept was confirmed experimentally by Xu et al. (2013), although there may be an unknown additional inhibiting barrier to magnesium carbonate growth that is still the subject of study.

3.6.3 Studies of microbial influences on precipitation

Laboratory experiments have demonstrated the ability of microorganisms to influence precipitation of magnesium carbonates. Biotic processes is a viable way to overcome the thermodynamic and kinetic barriers outlined above. However, further research is still needed in order to fully confirm these biotic models for magnesium carbonate precipitation. Cultures of cyanobacteria isolated from Fayetteville Green Lake, New York, (Thompson and Ferris, 1990), playas within Atlin, British Columbia (Power et al., 2007), and Lake Salda (Shirokava et al., 2012) were found to promote magnesium carbonate precipitation through either increasing pH or providing cell surfaces that can induce the dehydration, concentration, and/or binding of Mg^{2+} ions (Renaut,, 1993; Moore et al., 2020). However, precipitation rates of hydrous magnesium carbonates were not found to be affected by the presence of cyanobacteria as compared to an abiotic control within Mavromatis et al. (2012).

In other studies, EPS has been found to play a large role in magnesium carbonate precipitation. In comparisons between laboratory experiments and Las Eras microbial mats, hydromagnesites were proposed to form early on by nucleating on EPS, while anhydrous magnesite and dolomite formed at later mat decay stages by nucleating on bacterial nanoglobules and/or collapsed cells (Sanz-Montero, Cabestrero and Sánchez-Román, 2019). The study proposed that as organic substrate declined, heterotrophs such as Firmicutes reduced metabolic activity and started to produce nanoglobules, causing a change in available substrates and the nucleation of dolomite and magnesite instead of hydrous magnesium carbonates (Sanz-Montero, Cabestrero and Sánchez-Román, 2019). Hydromagnesite within

Lake Salda microbial mats were similarly proposed to nucleate on degraded EPS caused by heterotrophic nanoglobule formation (Balci et al., 2020). Alternatively, the degradation of EPS itself has been proposed to release Mg^{2+}, thereby directly promoting saturation of magnesium carbonates (Kaźmierczak et al., 2011).

3.7 Isotopic and elemental constraints on magnesium carbonate formation

Stable and clumped isotope data derived from magnesite and/or hydrated magnesium carbonates can be used to place constraints on mechanisms of their formation and past environmental conditions. The carbon isotopic composition may record the composition of the magnesite carbon source, and $\delta^{18}O$ and Δ_{47} may provide constraints on the composition and temperature of magnesite-forming waters, both of which provide critical information related to the setting and processes of magnesite formation. For Mars, knowledge of the carbon and oxygen stable isotopic evolution of its atmosphere is limited to analysis of meteorites and measurements by the Mars Science Laboratory (MSL) rover, Phoenix lander, and Viking landers (Nier et al., 1977; Carr et al., 1985; Wright et al., 1992; Niles et al., 2010; Webster et al., 2013). Assuming that organic matter was not a dominant carbon source on Mars, the $\delta^{13}C$ of Martian magnesites from Jezero crater may provide insight into atmospheric CO_2 values from ancient Mars and constrain the evolution of the Martian atmosphere (Hu et al., 2015; Franz et al., 2020). This assumption is supported by a study of siderite-magnesite carbonate globules in the Martian meteorite ALH84001, indicating that these formed at low temperature from subsurface water with CO_2 derived from the Martian atmosphere (Halevy et al., 2011). Therefore, $\delta^{18}O$ measurements of Jezero magnesium carbonates may further contextualize the evolution of the oxygen isotopic budget throughout Mars' history and potentially identify the aqueous environment of magnesite formation in Jezero crater (Jakosky et al., 2018; Heard & Kite, 2020).

Carbon sources, fluid sources, and temperature of formation as well as diagenetic overprints have been identified using isotopic and elemental chemistry techniques on terrestrial samples and would be similarly applicable to magnesium carbonate samples returned from Mars. At the same time, continued studies on the application and interpretation of these techniques on terrestrial magnesium carbonates will help us better understand magnesium carbonate formation conditions in general and help us interpret these chemical signals within returned Martian samples.

3.7.1 Carbon sources

There is evidence that the processes involved in fractionating $\delta^{13}C$ within carbon in the precipitating system in terrestrial sedimentary and ultramafic systems differ, and thus can be used to distinguish different environmental conditions of magnesite formation. On Mars, we expect carbon to be primarily sourced from the atmosphere and mantle with minor contributions from meteoritic and potentially endogenous organic matter. The $\delta^{13}C$ of carbonates can be used to track changes in atmospheric

composition and input of volcanic gases. Detailed analyses of $\delta^{13}C$ can be used to identify other potential sources of carbon, mixing of these endmembers, and track processes such as evaporation These are particularly important measurements to be made not only for interpreting carbonate formation processes, but also for understanding why the CO_2-dominant atmosphere on Mars did not form abundant carbonate on the Martian surface (e.g., Hu et al., 2015; Franz et al., 2020).

Magnesite veins in ultramafic complexes record $\delta^{13}C$ values (-4 to -20 ‰ VPDB) lower than carbonates that precipitate from the typical range of Earth surface dissolved inorganic carbon (DIC) $\delta^{13}C$ values (Fig. 3.6) (Kralik et al., 1989; Schroll et al., 2002). Low $\delta^{13}C$ values have been interpreted as the result of either decarboxylation of organic matter within ocean sediments in hydrothermal systems or incorporation of inorganic carbon derived from organic matter remineralization in the soils and regolith through meteoric infiltration (Schroll et al., 2002; Quesnel et al., 2013; 2016; Zedef et al., 2000; Kelemen et al., 2011). The higher vein magnesite $\delta^{13}C$ values typically are interpreted to record mixing with an atmospheric carbon component as values are closer to those expected for carbonates precipitated from DIC (Schroll et al., 2002; Quesnel et al., 2013; 2016; Oskierski et al., 2013; Zedef et al., 2000). For veins and listvenites specifically in the Semail Ophiolite, Oman, the source of carbon may be local sediments as $\delta^{13}C$ is similar to that of local calcite-bearing metasediments (Kelemen et al., 2011; Falk and Kelemen, 2015).

Magnesite that forms in soil and sedimentary environments records higher $\delta^{13}C$ values of 0-10 ‰ VPDB (Fig. 3.6) representing atmospheric CO_2 (Power et al., 2019; Schroll et al., 2002; Melehzik et al., 2001; Zedef et al., 2000; Fallick et al., 1991; Kralik et al., 1989). Magnesite with enriched ^{13}C (> 0 ‰) has been interpreted to record the influence of evaporation and CO_2 degassing during precipitation (Fig. 3.6) (Melezhik et al., 2001; Power et al., 2014; 2019). Playa and lacustrine magnesite deposits can record fluctuations in lake levels and temperatures driven by climate change (via temperature and hydrology) in their carbon isotope compositions (Li & Ku, 1997; Andrews, 2006). Such measurements of magnesium carbonates from within the Jezero lake system may provide valuable constraints on any climatic fluctuations on ancient Mars that controlled the isotopic composition of the lake water.

3.7.2 Fluid sources

Detailed measurements of oxygen isotopes within Martian magnesium carbonates are important because they may allow us to determine the fluid sources that precipitated carbonates on Mars. The oxygen isotopic composition of carbonate ($\delta^{18}O$) is a function of both the $\delta^{18}O$ of the fluid source from which the carbonate precipitated and the temperature of carbonate formation (McCrea, 1950; Epstein, 1953). Water
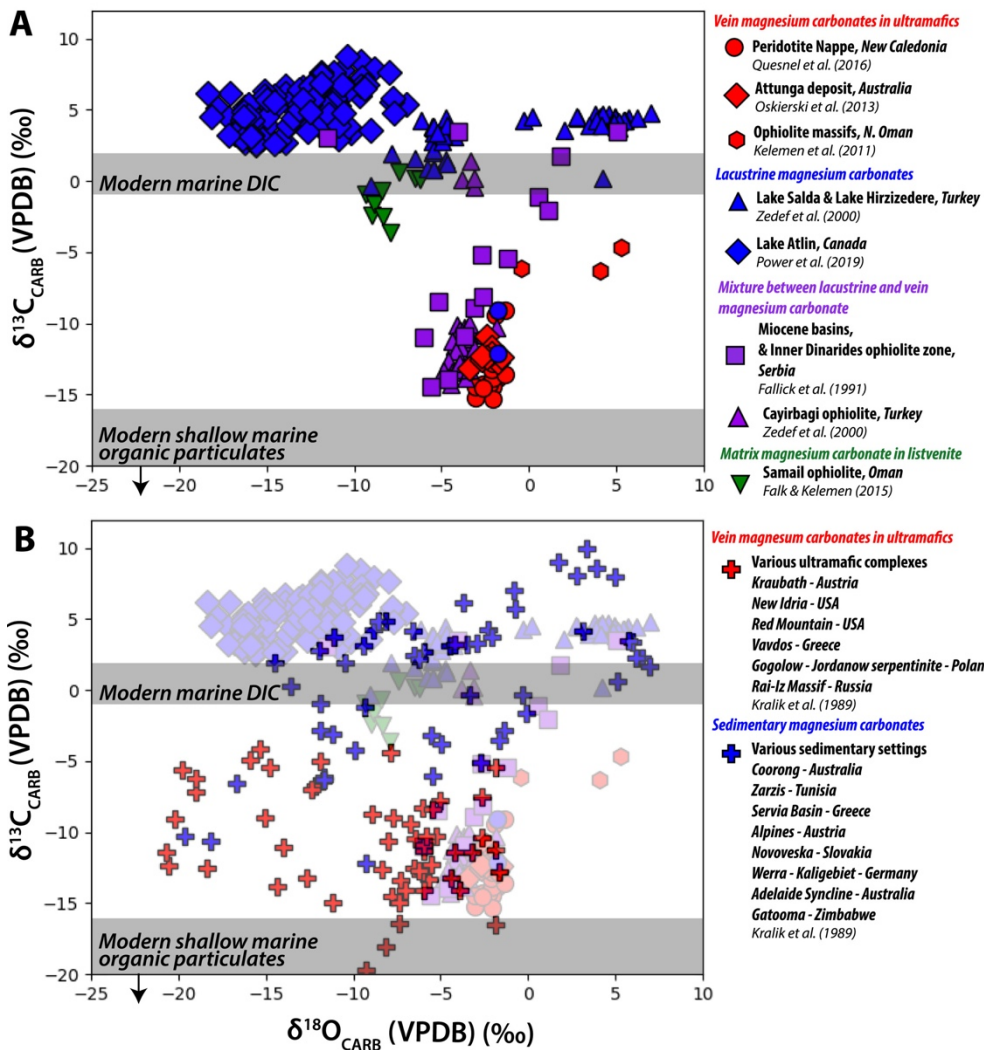
Fig. 3.6: Compilation of isotopic compositions of magnesium carbonates. (A) Recently published isotopic compositions of major magnesium carbonate deposits from veins in ultramafic complexes (red symbols) and lacustrine settings (blue symbols). Vein and lacustrine magnesium carbonates occupy two different endmember fields within the $\delta^{13}C$-$\delta^{18}O$ space. Certain samples reflect mixing between endmembers, e.g., mixing between vein and lacustrine magnesium carbonate or mixing between an organic and atmospheric carbon source (purple squares). The large $\delta^{18}O$ variation between sedimentary systems is driven by the local lake water composition as related to precipitation patterns, while $\delta^{18}O$ variation within a single lake system is attributed to evaporation effects enriching $\delta^{18}O$. Green triangles show the isotopic composition of matrix magnesites within listvenite from the Samail ophiolite, Oman (Falk & Kelemen, 2015). The $\delta^{13}C$ composition of vein and listvenite magnesite from Oman are higher compared with other vein magnesite and are thought to be derived from local calcite-bearing metasediments. (B) Comparison of data from panel A with a compilation by Kralik et al. (1989) of isotopic compositions of major deposits of vein (red plusses) and sedimentary (blue plusses) magnesium carbonate from around the world. Note that vein and sedimentary magnesium carbonate still appear to occupy separate fields in the $\delta^{13}C$-$\delta^{18}O$ space, but the boundaries between endmembers are no longer clear-cut. Example, ranges of modern marine DIC (Kroopnick, 1985) and the upper range of modern shallow marine organic particulates (Freeman, 2001) are shown as gray bars for comparison with data. Arrow shown to note that $\delta^{13}C$ of organic particulates can reach down to −36‰ but full range is not shown here.

$\delta^{18}O$ can be directly calculated if the temperature can be independently assessed, for example, by using clumped isotope temperature ($T(\Delta_{47})$) (e.g. Kim & O'Neil, 1997). Currently, hypotheses for Martian carbonate formation include hydrothermal alteration processes, weathering processes, or precipitation within a sedimentary system (see section 3.3 and 3.4). Determining the $\delta^{18}O$ composition of carbonates will allow us to directly test between these three different fluid sources. At the same time, we must also work towards a better understanding of these isotopic systems on Earth in order to apply robust interpretations to the Martian returned samples.

Very low magnesite $\delta^{18}O$ compositions (-20 to 0 ‰ VPDB; Fig. 3.6) in combination with $T(\Delta_{47})$ values approximating plausible Earth surface temperatures (20-60°C; Quesnel et al., 2016; Kelemen et al., 2011) are interpreted to record magnesite formation from meteoric fluids that exchanged with ultramafic rock during downward infiltration (Quesnel et al., 2013; 2016; Oskierski et al., 2013; Kelemen et al., 2011). Alternatively, some interpretations of $\delta^{18}O$ and clumped isotope values from magnesite in ultramafic complexes have led researchers to believe that magnesite formed hydrothermally and/or during burial at 70-100°C (Fallick et al., 1991; Falk & Kelemen, 2015). In summary, better understanding of the source fluids that form ultramafic rock-hosted magnesium carbonates is an ongoing pursuit and the sources of oxygen in the magnesium carbonates in ultramafic veins remain somewhat mysterious requiring further study (Zedef et al., 2000; Quesnel et al., 2013; 2016; Oskierski et al., 2013; Kelemen et al., 2011; Falk et al., 2016).

By contrast, sedimentary magnesite typically clearly records the water composition of their depositional environments (Fig. 3.6) (Kralik et al., 1989; Fallick et al., 1991; Zedef et al., 2000; Power et al., 2014; 2019). In evaporative lacustrine settings, magnesite may retain both low $\delta^{18}O$ reflective of meteoric fluids and high $\delta^{18}O$ resulting from progressive evaporation within samples from a single lake system (Fig. 3.6) (Zedef et al., 2000; Power et al., 2019). Similar to $\delta^{13}C$, the oxygen isotopic composition of sedimentary carbonates can record climatic flunctuations that control lake water composition (Li & Ku, 1997; Andrews, 2006). Combined $\delta^{13}C$ and $\delta^{18}O$ data of systems that include both vein and lacustrine magnesite reveal an isotopic mixing line with two endmembers: (1) a lacustrine, low-T endmember with variable $\delta^{18}O$ due to evaporative effects and high $\delta^{13}C$ where carbon was sourced from atmosphere, and (2) a hydrothermal endmember and low $\delta^{13}C$ environment where carbon was sourced from oxidation of organic matter (Fig. 3.6) (Fallick et al., 1991; Zedef et al., 2000).

Finally, it is important to consider possible diagenetic overprinting of isotopic compositions, which is common in many carbonates. Magnesium carbonates are highly soluble and thus prone to dissolution and recrystallization. In addition, primary magnesite and hydromagnesite isotopic signatures may be changed during dehydration of more hydrated magnesium carbonate phases (Power et al., 2019). Understanding whether or not a given sample may have experienced such post-deposition diagenetic

overprints of isotopic compositions is particularly important to Mars, as colder surface temperatures on Earth favor the formation of hydrated magnesium carbonates as precursors to magnesite (see section 3.6). Studies of dehydration processes of hydrated Ca-carbonate conversion to calcite/aragonite show that $\delta^{18}O$ can re-equilibrate due to exchange between CO_3- and H_2O-associated oxygen as water is lost during heating (Scheller et al., 2020). As such, it is critical to understand the isotopic effects of dehydration and diagenesis in Martian samples in order to make inferences about the carbon and fluid source of the precursor mineral.

3.7.3 Mg sources

The Mg-isotope systematics of magnesite have the potential to trace Mg sources and aqueous processes such as weathering and carbonation, that lead to magnesite formation on Earth and by extension on Mars. Mg has three stable isotopes of ^{24}Mg, ^{25}Mg, and ^{26}Mg. In general, magnesite minerals are depleted in ^{26}Mg compared to their source fluid, with the offset determined by a temperature-dependent fractionation factor (Pearce et al., 2012; Oskierski et al., 2019; de Obeso, 2020). As such, the Mg isotope composition of carbonates can be used to trace the fluid/rock source of Mg (Tipper et al., 2006). However, this interpretive framework is complicated by Mg isotope fractionations related to aqueous reactions (Blättler et al., 2015). Magnesite in ultramafic rocks appears to be ^{24}Mg-enriched by a few permil compared to their expected equilibrium value (Oskierski et al., 2019), which may result from carbonation reactions (Beinlich et al., 2014). Oskierski et al. (2019) demonstrated that nodular magnesite, formed through chemical weathering, may record a greater enrichment in ^{24}Mg compared to vein magnesite in the same system due to inter-species Mg isotope fractionations during dissolution/reprecipitation. While it has been proposed that Mg isotopes may record biological fractionations, initial natural and experimental magnesite formed in biotic and abiotic conditions appear to record the same Mg isotope fractionation (Mavromatis et al., 2012; Shirokova et al., 2013).

3.7.4 Temperature of precipitation and tracking disequilibrium conditions

In cases where fluid inclusions are preserved, fluid inclusion thermometry can be utilized to measure the temperature of the captured fluid. Fluid inclusion thermometry has been successfully applied to magnesium carbonates in listvenites and veins within ultramafic rock-hosted deposits, yielding 210-250 °C (Schandl & Wicks, 1993; Hansen et al., 2005). Alternatively, carbonate clumped isotope thermometry is a technique used to determine the temperature of formation of carbonate minerals by measuring the abundance of the mass-47 isotopologue (Δ_{47}) of CO_2 ($^{13}C^{18}O^{16}O$, "clumped species") released after digestion of a carbonate mineral. Clumped isotope thermometry also allows for the calculation of oxygen isotopic composition of the precipitating fluid (e.g., Daeron et al., 2011; Eiler, 2011, 2007; Fernandez et al., 2014; Huntington et al., 2011; Huntington and Lechler, 2015; Lloyd et al., 2017; Ryb et al., 2017). The basis for this measurement is the fact that the abundance of $^{13}C–^{18}O$ bonds within the solid is

temperature-dependent (Ghosh et al., 2006). Therefore, clumped isotope thermometry is a highly valuable technique applicable to Martian returned samples that can aid in determining fluid sources and carbonate formation environments on ancient Mars (see section 3.7.2). However, this thermometer is well established for calcite and dolomite, but is currently being developed for siderite and magnesite (e.g. Kelemen et al., 2011; Van Dijk et al., 2019).

Initial clumped isotope studies have been used to interpret conditions of magnesite genesis and the isotopic composition of the precipitating fluid (eg., García del Real et al., 2016; Kelemen et al., 2011; Quesnel et al., 2016). Most ultramafic rock-hosted vein magnesite generally yield low temperatures of 15-50 °C from clumped isotope thermometry indicative of formation through meteoric fluids (Kelemen et al., 2011; Streit et al., 2012; Quesnel et al., 2016; García del Real et al., 2016). Falk and Kelemen (2015) found higher clumped isotope temperatures (37-114 °C) of dolomite and magnesite formed through carbonation processes. Quartz-magnesite and talc-magnesite mineral pair oxygen isotope measurements were instead used to constrain vein and listvenite formation temperatures of 249-287 °C within the Linnajavri ultramafic complex, Norway (Beinlich et al., 2012). Lake magnesite yields low clumped isotope temperatures of 6-14 °C for Altin Playa, Canada (Power et al., 2019). Last, clumped isotopes of coarse crystals of magnesite within metamorphic rocks can record very high temperatures of 300-650 °C (García del Real et al., 2016).

The present state of the literature reveals some discrepancies between calculated clumped isotopes temperatures and other data, indicating that more work is needed for reliable magnesium carbonate paleothermometry. There are a number of methodological challenges with regards to measuring and analyzing magnesite clumped isotopes that require further study, including (1) ensuring complete liberation of CO_2 from magnesite during acid digestion, (2) determining the correct acid digestion fraction factor for magnesite, (3) determining the appropriate calibration curve for deriving temperatures from clumped isotope values, and (4) determining the temperature dependent magnesite-fluid and magnesite-CO_2 fractionation factors for oxygen and carbon isotopes. Furthermore, clumped isotope thermometry is only applicable when carbonates formed under equilibrium conditions. Disequilibrium-degassing, thermal perturbation, kinetic effects, shock effects, biological effects, and later heating events above the equilibrium blocking temperature (~145-235 °C for calcites; Stolper and Eiler, 2015; Lloyd et al., 2018) can also affect the clumped isotopic signatures and require further study. In fact, a second important use of measuring Δ_{47} is to identify carbonate formation under disequilibrium conditions. Ca-carbonate formation at disequilibrium has been confirmed using clumped isotopes (e.g. Falk et al., 2016). In these cases, disequilibrium and kinetic effects can result in large ranges of Δ_{47} and associated $\delta^{13}C$ and $\delta^{18}O$ that otherwise would have been falsely interpreted as a primary signal (e.g. Falk et al., 2016). Hence, application of clumped isotope techniques on returned Martian samples would be highly important in

order to interpret both the temperature of carbonate formation and the origin of δ^{13}C and δ^{18}O isotopic compositions.

3.8 Elemental constraints

Major, minor, and trace element concentrations in magnesite are diagnostic tools that have been used to detect detrital contamination, source rocks influence, diagenetic overprints, and redox conditions. Magnesites found in ultramafic environments typically have a very restricted range of trace elements (i.e., those that substitute for Mg mostly). Kuscu et al. (2017) measured trace element concentrations in vein magnesite from the Madenli area of the Sarkikaraagac Ophiolite, sedimentary hunite-magnesite deposits in Miocene-Pliocene lacustrine rocks in the Asagitirtar area, and hydromagnesite near Lake Salda in the lacustrine basin on the Yesilova ophiolites. They attributed that variations in trace element content between the sites was likely due to fluid percolation through local volcanic basement rock rather than processes related to variability in temperature or pressure. Lugli et al. (2000) observed positive correlations between trace elements and Al and K and attributed this to detrital silicate grains within samples.

Rare Earth Elements (REEs) can be used as chemical fingerprints that constrain formation environments and conditions. While most REEs are well-incorporated in Ca-carbonates, Light REEs (LREE) are rejected more effectively than Heavy REEs (HREE) by magnesite (and siderite) (Bau, M., & Möller, 1992). This is due to differences in bonding environments, charge, and ionic radii of Ca^{2+}, Mg^{2+}, and REE^{3+}. This is explained in part by lanthanide contraction and the fact that the ionic radius of Ca^{2+} is greater than that of Mg^{2+} in carbonates. Importantly for geochronological considerations, this implies that Sm will be more easily incorporated in to magnesite than Nd motivating the use of a ^{147}Sm-^{143}Nd isotope chronometer (see section 3.8). REE abundances in sedimentary magnesite may signal formation via diagenetic alteration of dolomite rather than direct precipitation prior to burial (eg. Fernandez-Nieto et al., 2003; Ellmies et al, 1999; Lugli et al., 2002; Morteani et al., 1982). For example, Fernandez-Nieto et al. (2003) demonstrated that magnesites intermixed with dolomites have lower LREE but similar HREE when compared to the dolomite. Using mass vs concentration REE profiles, they inferred that alteration processes led to the removal of the LREEs while simultaneously exhibiting little influence on the HREEs of the carbonate.

3.9 Absolute age dating of magnesium carbonate formation

Given the importance of magnesium carbonates to deciphering ancient aqueous, atmospheric, geologic, and potentially microbial processes in Jezero crater, determining their age and exposure history will help place Jezero within the context of the larger history of Mars. Techniques previously employed on Earth include those with the ability to assess the formation age of magnesite precipitated on the order of millions to billions of years ago (the ^{147}Sm-^{143}Nd, U-Pb concordia, and ^{207}Pb-^{206}Pb isochron methods) and

within tens of thousands to the last million years (^{14}C and U-series disequilibrium dating). There are also technique that have not been applied to magnesite on Earth but may have the ability to interrogate the surface exposure history of magnesite outcrops (^{3}He, ^{21}Ne, ^{22}Ne, and possibly ^{36}Ar).

3.9.1 Techniques for age dating ancient magnesite

U-Pb and Pb-Pb methods were successfully used to date sparry magnesite to ~1370-1380 Ma (Ovchinnikova et al., 2014) and 3043±59 Ma (Toulkeridis et al., 2010) within the Satka Fm, Russia, and Barberton Greenstone Belt, South Africa, respectively. Sm-Nd isochron ages of between 236±16 Ma and 193.5±8.6 Ma (Henjes-Kunst et al., 2014) were found for sparry magnesite within the Breitenau deposit, Eastern alps.

Magnesite dating using these methods may be challenging due to low parent isotope abundances and/or low parent/daughter isotope ratios. For example, Sm and Nd concentrations in the Breitenau deposit range between one ppm and a few hundred ppm, with ^{147}Sm/^{144}Nd ratios spanning 0.1 to 0.5 (Henjes-Kunst et al., 2014). It is unknown whether magnesites formed in other environments could be successfully leached to obtain such a favorably large range in Sm/Nd ratio or if they generally host Sm and Nd concentrations adequate for precise geochronology. Sm and Nd concentrations in magnesite samples from the Budd ultramafic complex are at sub-ppm levels (Toulkeridis et al. 2010); similar Sm and Nd concentrations in Martian Mg-rich carbonates would likely preclude successful application of the Sm-Nd method. While sedimentary crystalline magnesite from the Satka Formation exhibits relatively high U concentrations (0.94-2.1 ppm; Ovchinnikova et al., 2014), U concentrations in Mg-rich carbonate veins from the Semail Ophiolite are orders of magnitude lower (0.03-14.8 ppb; Mervine et al., 2015). If U concentrations in magnesium carbonates from Jezero crater are similar to those of the Semail Ophiolite, the application of the isochron technique (e.g., Toulkeridis et al., 2010; Ovchinnikova et al., 2014) may not be feasible for Martian samples. Additionally, mixing of two homogenous sources can lead to the appearance of a ^{207}Pb/^{204}Pb - ^{206}Pb/^{204}Pb diagram as an isochron. Caution must therefore be taken when employing such a technique; the U-Pb concordia technique is less susceptible to such issues.

The optimal situation for age dating of ancient Jezero carbonates would be lake- or ground-water precipitated carbonates that formed in a single episode with no signs of resetting by post-formation events. Post-formation events such as heating associated with meteorite impacts or fluid interactions could affect isotopic systems such that a date would be a recrystallization age. Samples should be examined both texturally and geochemically for evidence of impact events or post-formation fluid interactions that have the potential to induce isotopic contamination or entirely reset the U-Pb and Sm-Nd isotope systems. Application of clumped isotope thermometry can shed light on temperatures reached during crystallization or post-formation heating. Care must be taken to determine whether a formation or

partial/full recrystallization age is recorded, each of which can constrain the age of magnesium carbonate-forming environments and subsequent geological processes.

3.9.2 Young veins in old ultramafic rocks

Radiocarbon dating is commonly employed on Earth for systems with carbon-bearing materials with <50Ka ages. Due to their short half-life, radiocarbon techniques are not likely to be applicable to Martian magnesium carbonates samples. However, continued studies on radiocarbon dating of terrestrial magnesium carbonates could aid in further understanding magnesium carbonate formation in general. Before young radiocarbon dates were reported by Kelemen and Matter (2008), magnesium carbonate veins associated with the Semail Ophiolite were thought to have formed >60 Ma during its emplacement in the Late Cretaceous to Early Tertiary (e.g. Nasir et al., 2005). Such putative antiquity was contradicted by the discovery of magnesite containing live ^{14}C and dates spanning ~8-45 Ka (e.g., Kelemen and Matter, 2008; Kelemen et al., 2011; Mervine et al., 2014, Mervine et al., 2015). Mervine et al. (2015) confirmed these quaternary formation ages with U-series disequilibrium dating. Radiocarbon in magnesium carbonates can also be used to calculate carbonation rates (Oskierski et al., 2013) and tracing atmospheric carbon sources (Power et al., 2019). Hence continued studies of radiocarbon within terrestrial magnesium carbonates are warranted in order to understand the degree to which atmospheric carbon and weathering processes play a role in magnesium carbonate formation on Earth. This is an important consideration for Mars because we hope to measure ancient Martian atmospheric conditions through returned magnesium carbonates.

Care must be taken when performing radiocarbon dating of magnesium carbonate because of the many potential sources of carbon in its formation (e.g., Kelemen and Matter, 2008; Kelemen et al., 2011; Mervine et al., 2014; Oskierski et al., 2013; Power et al., 2019). Any ^{14}C dates in magnesite must be based on the assumption that carbon incorporated during crystallization retained atmospheric carbon isotope abundances. However, partial exchange of carbon between modern ^{14}C-rich fluids and ancient ^{14}C-dead carbonate can occur (Mervine et al., 2014). Resolving the extent of C exchangeability between magnesite and fluids is particularly important for porous microcrystalline magnesite.

3.9.3 Surface exposure ages

Measurements of cosmogenic isotopes could complement traditional geochronologic measurements focused on the formation age of magnesite. These isotopes are produced via the interaction of galactic cosmic rays with the nuclei that comprise the rocks within the upper 2-3 meters of the surface of a planetary body (generally through spallation or neutron capture; Lal, 1988). Based on the chemistry of a sample of interest, the production rate of a given cosmogenic isotope may be derived and a length of exposure calculated (Lal, 1988).

On Earth, measurement of radioactive ^{10}Be, ^{26}Al, and/or ^{36}Cl for this purpose is common (e.g.,

Kubik et al., 1984; Nishiizumi et al., 1986; Phillips et al., 1986; Yiou et al., 1984). On Mars, the duration of exposure is likely to be many millions of years (Farley et al., 2014; Vasconcelos et al., 2016; Martin et al., 2021), such that these radioactive nuclides will be in equilibrium (i.e., produced at the same rate that they decay). As a result, the daughter products of these nuclides must instead be measured to calculate exposure age, if they are uniquely identifiable. Of these, magnesium carbonates lack a target element for production of ^{26}Al, precluding its use. ^{10}Be decays to ^{10}B, which is the common isotope of boron and therefore cannot reliably be measured above background levels. The main daughter product of ^{36}Cl (produced by neutron capture on ^{35}Cl) is ^{36}Ar, a noble gas which is otherwise unlikely to be present in the crystal structure, making this a potentially useful exposure chronometer if it is produced in measurable quantities (discussed further below).

The spallogenic noble gases ^{3}He, ^{21}Ne, and ^{22}Ne are stable and likely to be produced at relatively high rates due to the large proportion of target Mg and (for ^{3}He) O in magnesium carbonate (Wieler, 2002). Noble gases are highly insoluble in crystalline material and will therefore be lost by diffusion if permitted by the thermal history and kinetic parameters of the material of interest. This low solubility also means that the noble gas contents of a given sample will be reset if recrystallization occurs. For cosmogenic dating of Martian magnesite, the primary determination is therefore whether a given noble gas is effectively trapped in the magnesite crystal structure at Martian surface temperatures, and whether evidence for recrystallization is present. No formal studies of the diffusion kinetics of magnesite have been performed with any of ^{3}He, ^{21}Ne, ^{22}Ne, and ^{36}Ar. Therefore, we turn to studies that have been performed on other carbonate minerals as a proxy for noble gas behavior in magnesite, recognizing that these crystal systems are not identical.

A study of ^{4}He diffusion in calcite and dolomite found that below ~50°C, helium is likely to be retained in these carbonate minerals (Copeland et al., 2007). However, attempts at applying (U-Th)/He dating in natural calcite samples have been met with mixed success (Copeland et al., 2007; Cros et al., 2014), likely due to complex multi-domain diffusion kinetics inherent to calcite (Amidon et al., 2015; Copeland et al., 2007). A subsequent study attempted calcite ^{3}He exposure measurements directly and similarly found reliable results in only some cases (Amidon et al., 2015). Promisingly, calcite minerals with a higher Mg wt% demonstrated more robust He retention in this study (Amidon et al., 2015), suggesting that magnesite may function more reliably as a He geochronometer than calcite.

Neon diffusivity in carbonate minerals has not been assessed. However, an empirical anticorrelation between atomic radius and diffusivity has been observed in a range of minerals (Baxter, 2010), suggesting that as an extremely rough approximation, the diffusivity of Ne in carbonates should lie somewhere between that of He and Ar. Given the closure temperatures of ~50°C for He (Copeland et al., 2007) and ~385°C for Ar (Cassata and Renne, 2013), this approximation hints that ^{21}Ne and ^{22}Ne may be

suitable for cosmogenic dating applications in Martian magnesium carbonates. [21]Ne and [22]Ne are likely to be produced at relatively high rates in magnesium carbonates, in this case because Mg is a major target element for the production of [21]Ne and [22]Ne via spallation (Wieler, 2002). We therefore assess [21]Ne and [22]Ne exposure dating to be a promising method of determining the length of magnesite exposure on Mars.

The lone study of argon diffusivity in calcite suggests a closure temperature of 385±2°C (Cassata and Renne, 2013), indicating that this noble gas could be quantitatively retained in magnesium carbonate minerals at Martian surface temperatures. However, it is uncertain whether significant amounts of [36]Ar would be produced in such minerals. The major component elements of magnesium carbonates (Mg, C, O) are all below that of [36]Ar, precluding spallogenic production. The sole mechanism of [36]Ar production in magnesium carbonates is therefore through decay of [36]Cl, which is produced via neutron capture of [35]Cl, so inclusion of trace chlorine or chloride contaminants is key for the success of a [36]Ar approach. Elevated Cl concentrations are observed in rocks of Meridiani planum and Gale crater where evaporative processes were involved (Tosca et al., 2005; Clark et al., 2005; Thomas et al., 2019). However, chlorine does not partition readily into calcite, aragonite, or dolomite (natural and synthetic samples generally contain <0.01 wt% Cl; Kitano et al., 1975; Staudt et al., 1993), casting doubt on the viability of this method unless abnormally high Cl concentrations or inclusions of minerals such as halite are observed in Martian magnesium carbonates.

3.10 Summary and implications for the 2020 rover mission

Based on understanding from current orbital data, the Mars 2020 Perseverance rover will encounter magnesite or its hydrous relatives at the Jezero landing site on Mars, associated with olivine-enriched units. By comparison with examples on the Earth, we expect to observe magnesium carbonate in at least one of five distinct expressions that include: (1) Precipitation in veins hosted in ultramafic-rocks formed by circulation of meteoric fluids or deeper hydrothermal fluids through fracture networks; (2) within the matrix of carbonated ultramafic rocks from hydrothermal alteration; (3) Nodule formation as an evaporative soil process; (4) Precipitation as authigenic sediment in alkaline lakes and playas; and, (5) Diagenetic replacement of precursor carbonates such as dolomite, calcite, and hydrous magnesium carbonates. The formation environments of the first four magnesium carbonate types span a spatial hydrologic gradient from uplifted ultramafic rocks to down-gradient sedimentary basin and may provide a close analogue for the magnesium carbonates in the Jezero crater region.

The most commonly preserved magnesium carbonate in terrestrial environments is magnesite. Hydrous magnesium carbonates typically co-occur with magnesite in alkaline lakes, playa, and soil environments. This observation and the pathways to formation of magnesite in general remains an enigma from a thermodynamic and kinetics perspective. Magnesite is more soluble than its Ca-rich counterparts and precipitation occurs slowly due to kinetic inhibition by solvated Mg ions. Hydrous magnesium

carbonates are less kinetically inhibited and may subsequently transform to magnesite. Understanding the thermodynamic stability of magnesite as a primary precipitate and as a recrystallization product will therefore be important for constraining physical conditions for magnesite and potentially hydrous magnesium carbonate formation on Mars.

Diagnostic textures and mineral assemblages can be directly analyzed with the Perseverance rover and record processes of formation and may also preserve biologic fabrics, assuming that life appeared or originated and was widely dispersed on Mars. Textures and phases associated with mineral precipitation include: (1) Fine-grained or microcrystalline vein- or matrix-forming magnesium carbonates associated with ultramafic terrains and carbonation products; (2) Nodules and bladed aggregates found in soils situated near ultramafic terrains; (3) Microcrystalline magnesium carbonates precipitated as primary crusts in playas and alkaline lakes; (4) Microcrystalline carbonates that replace limestones and dolostones; (5) Sparry calcite that form from metasomatic and metamorphic replacement. Thrombolites, stromatolites, crinkly and pustular laminites, botryoidal or spherulitic textures, and microscale filament, spheroids, and peloids may yield insight into whether or not biologic processes operated on the surface of ancient Mars if returned to Earth and studied in the laboratory. If life never originated on Mars, sampling these textures and fabrics could still provide significant insight into past environments and the history of water. The rover contains a suite of instruments that can detect and discriminate magnesium carbonate phases and then once confirmed move to more detailed analyses of these textures and mineral assemblages to determine their relation to ultramafic terrains, sedimentary, or diagenetic environments, providing insights into the evolution of ancient Mars and informing carbonate sampling strategies.

Establishing the $\delta^{13}C$ and $\delta^{18}O$ compositions of the surface-atmospheric environment at the time of magnesium carbonate formation will significantly aid in further understanding the carbon cycle on ancient Mars. This is due to the limited record of previous isotopic measurements of Martian surface materials. Aside from measurements of carbonate globules within the ALH84001 meteorite, the Jezero carbonates will yield the first insight into the $\delta^{13}C$ and $\delta^{18}O$ composition of the ancient Martian surface-atmospheric environment, providing invaluable new data points for the isotopic evolution of the Martian atmosphere, surface, and potentially the subsurface. Furthermore, stable isotope ratios of carbon, oxygen, and magnesium in magnesium carbonate minerals have proven highly valuable proxies of conditions (climate, fluid and atmospheric chemistry, surface or subsurface alteration processes, and biospheric evolution) in Earth's past and can be applied similarly for Martian samples (e.g. Zachos et al., 2001). Clumped isotope methodologies and fluid inclusion thermometry for magnesium carbonates are promising for establishing temperature and equilibrium/disequilibrium conditions of formation but are still in development. A number of radiometric dating techniques, including ^{147}Sm-^{143}Nd isochron dating, U-Pb concordia, and ^{207}Pb-^{206}Pb isochron dating have yielded promising results for magnesites on Earth

and could potentially be utilized for dating Martian magnesium carbonate samples. In addition, cosmogenic exposure dating utilizing the noble gases [3]He, [21]Ne, [22]Ne or [36]Ar could potentially be applied to returned Martian magnesium carbonate samples but it has not yet been attempted for terrestrial samples. Continued radiocarbon and U-series disequilibrium dating of young terrestrial samples may yield further insight into weathering processes and the role of atmospheric carbon in magnesium carbonate formation.

As we prepare for analyzing magnesium carbonates returned by the Mars 2020 mission, there are several notable areas in laboratory experiments that we can work to improve: (1) Understanding of the ability of magnesium carbonates to preserve biosignatures. (2) Understanding of the thermodynamic, kinetic, or metabolic conditions needed to induce precipitation, transformation, and replacement of various magnesium carbonates. (3) Understanding of tracking sources and transport of carbon, magnesium and fluids through isotope systematics, specifically focusing on understanding the origin of the large range in δ^{13}C and δ^{18}O signatures and how these reflect sources, aqueous conditions, and/or disequilibrium conditions in different environmental settings; (4) Methodology for performing clumped isotope and fluid inclusion thermometry of magnesium carbonates; (5) Focus on performing more radiogenic and cosmogenic dating experiments on magnesium carbonates to narrow down the most appropriate techniques applicable to ancient Martian magnesium carbonates.

References

Abu-Jaber, N. S. and Kimberley, M. M. (1992), Origin of ultramafic-hosted vein magnesite deposits, *Ore Geology Reviews, 7*(3),155–191. doi: 10.1016/0169-1368(92)90004-5

Aharon, P. (1988), A stable-isotope study of magnesites from the Rum Jungle Uranium Field, Australia: Implications for the origin of strata-bound massive magnesites, *Chemical Geology, 69*(1–2), pp. 127–145. doi: 10.1016/0009-2541(88)90164-7

Alçiçek, H. (2009), Late Miocene nonmarine sedimentation and formation of magnesites in the Acıgöl Basin, southwestern Anatolia, Turkey. *Sedimentary Geology*, *219*(1-4), 115-135. doi: 10.1016/j.sedgeo.2009.05.002

Alderman, A. R., & Von der Borch, C. C. (1961), Occurrence of magnesite–dolomite sediments in South Australia. *Nature*, *192*(4805), 861-861.

Allison, J. D., Brown, D. S., and Novo-Gradac, K. J. (1991), MINTEQA2/PRODEFA2, a geochemical assessment model for environmental systems: Version 3.0 user's manual. Environmental Research Laboratory, Office of Research and Development, US Environmental Protection Agency.

Amidon, W. H., Hobbs, D., Hynek, S. A., (2015), Retention of cosmogenic 3He in calcite. *Quaternary Geochronology, 27*, 172–184. https://doi.org/10.1016/j.quageo.2015.03.004

Andrews, J. E. (2006), Palaeoclimatic records from stable isotopes in riverine tufas: Synthesis and review. *Earth Science Reviews, 75*(1-4), 85-104. doi: 10.1016/j.earscirev.2005.08.002

Archer, P. D., et al., (2020), Detection of siderite (FeCO3) in Glen Torridon samples by the Mars Science Laboratory Rover. *LPSC 51*, abstract# 2709.

Ashley, P. M. (1997), Silica-carbonate alteration zones and gold mineralisation in the Great Serpentinite Belt, New England orogen, New South Wales. In *Tectonics and Metallogenesis of the New England Orogen* (Vol. 19, pp. 212-225). Geological Society of Australia Special Publication.

Balci, N., Gunes, Y., Kaiser, J., On, S. A., Eris, K., Garczynski, B., & Horgan, B. H. (2020), Biotic and Abiotic Imprints on Mg-Rich Stromatolites: Lessons from Lake Salda, SW Turkey. *Geomicrobiology Journal, 37*(5), 401-425.

Bandfield, J. L. (2003), Spectroscopic identification of carbonate minerals in the martian dust. *Science, 301*, 1084–1087. doi: 10.1126/science.1088054

Bär, O. (1932), Beitrag zum Thema Dolomitentstehung. Zentralblatt für Mineralogie und Paläontologie, 46-62.

Barnes, I., & O'Neil, J. R. (1969), The relationship between fluids in some fresh alpine-type ultramafics and possible modern serpentinization, western United States. *Geological Society of America Bulletin*, *80*(10), 1947-1960. doi: 10.1130/0016-7606(1969)80[1947:TRBFIS]2.0.CO;2

Bau, M., & Möller, P. (1992). Rare earth element fractionation in metamorphogenic hydrothermal calcite, magnesite and siderite. *Mineralogy and Petrology*, *45*(3-4), 231-246.

Baxter, E. F., (2010), Diffusion of noble gases in minerals. *Reviews in Mineralogy and Geochemistry, 72*, 509–557. https://doi.org/10.2138/rmg.2010.72.11

Beinlich, A., Plümper, O., Hövelmann, J., Austrheim, H., & Jamtveit, B. (2012). Massive serpentinite carbonation at Linnajavri, N–Norway. *Terra Nova*, *24*(6), 446-455. doi: 10.1111/j.1365 3121.2012.01083.x

Beinlich, A., Mavromatis, V., Austrheim, H. and Oelkers, E.H. (2014), Inter-mineral Mg isotope fractionation during hydrothermal ultramafic rock alteration–Implications for the global Mg cycle. *Earth and Planetary Science Letters, 392*, 166-176. doi: 10.1016/j.epsl.2014.02.028

Bell, M. S. (2016), CO2 release due to impact devolatilization of carbonate: Results of shock experiments. *Meteoritics & Planetary Science*, *51*(4), 619-646. doi: 10.1111/maps.12613

Bénézeth, P., Saldi, G. D., Dandurand, J.-L., and Schott, J. (2011), Experimental determination of the solubility product of magnesite at 50 to 200 C. *Chemical Geology, 286*(1-2), 21-31. doi: 10.1016/j.chemgeo.2011.04.016

Benson, L. V., Currey, D. R., Dorn, R. I., Lajoie, K. R., Oviatt, C. G., Robinson, S. W., Smith, G. I., and Stine, S. (1990). Chronology of expansion and contraction of four Great Basin lake systems

during the past 35,000 years. *Palaeogeography, Palaeoclimatology, Palaeoecology, 78*(3-4), 241-286. doi: 10.1016/0031-0182(90)90217-U

Bhattacharjee, S., Ryb, U., Eiler, J.M., Asimow, P.D., (2020), Structural and isotopic reordering in Magnesite: Insights from heating experiments. Goldschmidt 2020 Abstract. Doi: 10.46427/gold2020.184

Bibring, J.P., Langevin, Y., Mustard, J.F., Poulet, F., Arvidson, R., Gendrin, A., Gondet, B., Mangold, N., Pinet, P., Forget, F., team, O. (2006), Global mineralogical and aqueous Mars history derived from OMEGA/Mars express data. *Science, 312*, 400–404. doi: 10.1126/science.1122659

Bishop, J. L., et al. (2013), Mineralogy and morphology of geologic units at Libya Montes, Mars: Ancient aqueously derived outcrops, mafic flows, fluvial features, and impacts, *Journal of Geophysical Research Planets, 118*, 487–513, doi:10.1029/2012JE004151.

Blättler, C. L., Miller, N. R., & Higgins, J. A. (2015), Mg and Ca isotope signatures of authigenic dolomite in siliceous deep-sea sediments. *Earth and Planetary Science Letters*, *419*, 32-42.

Bonifacie, M., Calmels, D., Eiler, J.M., Horita, J., Chaduteau, C., Vasconcelos, C., Agrinier, P., Katz, A., Passey, B.H., Ferry, J.M., (2017), Calibration of the dolomite clumped isotope thermometer from 25 to 350 C, and implications for a universal calibration for all (Ca, Mg, Fe) CO3 carbonates. *Geochimica et Cosmochimica Acta, 200*, 255–279. doi: 10.1016/j.gca.2016.11.028

Bosak, T., Moore, K. R., Gong, J., Grotzinger, J. P. (2021). Searching for biosignatures in sedimentary rocks from early Earth and Mars. *Nature Reviews Earth & Environment, 2*(7), 490-506.

Boskabadi, A. et al. (2020), Carbonation of ophiolitic ultramafic rocks: Listvenite formation in the Late Cretaceous ophiolites of eastern Iran. *Lithos*, *352*, 105307.

Braithwaite, C. J. R. and Zedef, V. (1994), Living hydromagnesite stromatolites from Turkey, *Sedimentary Geology, 92*(1–2), 1–5. doi: 10.1016/0037-0738(94)90051-5.

Braithwaite, J. R. and Zedef, V. (1996), Hydromagnesite stromatolites and sediments in an alkaline Lake, Salda Golu, Turkey, *Journal of Sedimentary Research, 66*. doi: 10.1306/d426845f-2b26 11d7-8648000102c1865d.

Bramble, M. S., Mustard, J. F., & Salvatore, M. R. (2017), The geological history of northeast Syrtis Major, Mars. *Icarus, 293*, 66-93.

Brown, A. J., Viviano, C. E., & Goudge, T. A. (2020). Olivine-carbonate mineralogy of the Jezero crater region. *Journal of Geophysical Research: Planets*, *125*(3), e2019JE006011.

Buckley, H. A., & Woolley, A. R. (1990), Carbonates of the magnesite–siderite series from four carbonatite complexes. *Mineralogical Magazine*, *54*(376), 413-418.

Cabestrero, Ó. and Sanz-Montero, M. E. (2018), Brine evolution in two inland evaporative environments:

influence of microbial mats in mineral precipitation, *Journal of Paleolimnology, 59*(2), 139–157. doi: 10.1007/s10933-016-9908-0.

Carlos de Obeso, J., Santiago Ramos, D. P., Higgins, J. A., & Kelemen, P. B. A Mg isotopic perspective on the mobility of magnesium during serpentinization and carbonation of the Oman ophiolite. *Journal of Geophysical Research: Solid Earth*, e2020JB020237.

Carr, R. H., Grady, M. M., Wright, I. P. & Pillinger, C. T. (1985), Martian atmospheric carbon dioxide and weathering products in SNC meteorites. *Nature, 314*, 248–250, doi: 10.1038/314248a0

Carr, M. H. (1987), Water on Mars. *Nature, 326*, 30–35. doi: 10.1038/326030a0

Cassata, W. S., Renne, P. R., (2013), Kinetics of argon diffusion in calcite. *Geochemistry, 73*, 113–115. https://doi.org/10.1016/j.chemer.2012.10.001

Chai, L., & Navrotsky, A. (1996), Synthesis, characterization, and enthalpy of mixing of the (Fe, Mg) CO3 solid solution. *Geochimica et Cosmochimica Acta, 60*(22), 4377-4383.

Chernov, A. A. (2012), Modern crystallography III: Crystal growth. Vol. 36. Springer Science & Business Media.

Christ, C. L. and Hostetler, P. B. (1970), Studies in the system MgO-SiO 2 -CO 2 -H 2 O (II); tTe activity-product constant of magnesite, *American Journal of Science*, *268*(5), 439–453. doi: 10.2475/ajs.268.5.439.

Clark, I. D., & Fontes, J. C. (1990). Paleoclimatic reconstruction in northern Oman based on carbonates from hyperalkaline groundwaters. *Quaternary Research*, *33*(3), 320-336.

Clark, B. C. et al. (2005), Chemistry and mineralogy of outcrops at Meridiani Planum. *Earth and Planetary Science Letters*, *240*(1), 73-94. doi: 10.1016/j.epsl.2005.09.040

Cooperdock, E. H. G., Stockli, D. F., Kelemen, P. B., & de Obeso, J. C. (2020), Timing of magnetite growth associated with peridotite-hosted carbonate veins in the SE Samail ophiolite, Wadi Fins, Oman. *Journal of Geophysical Research: Solid Earth*, *125*(5), e2019JB018632.

Copeland, P., Watson, E. B., Urizar, S. C., Patterson, D., Lapen, T. J., (2007), Alpha thermochronology of carbonates. *Geochimica et Cosmochimica Acta, 71*, 4488–4511. https://doi.org/10.1016/j.gca.2007.07.004

Cros, A., Gautheron, C., Pagel, M., Berthet, P., Tassan-Got, L., Douville, E., Pinna-Jamme, R., Sarda, P., (2014), 4He behavior in calcite filling viewed by (U–Th)/He dating, 4He diffusion and crystallographic studies. *Geochimica et Cosmochimica Acta, 125*, 414–432. https://doi.org/10.1016/j.gca.2013.09.038

Curtis, C. D. (1978), Possible links between sandstone diagenesis and depth related geochemical reactions occurring in enclosing mudstones, *Geological Society of London Journal, 135*, 107–117. doi:

10.1144/gsjgs.135.1.0107

Daeron, M., Guo, W., Eiler, J., Genty, D., Blamart, D., Boch, R., Drysdale, R., Maire, R., Wainer, K., Zanchetta, G., (2011), 13C18O clumping in speleothems: Observations from natural caves and+ precipitation experiments. *Geochim. Cosmochim. Acta, 75,* 3303–3317. doi: 10.1016/j.gca.2010.10.032

Darragi, F., & Tardy, Y. (1987). Authigenic trioctahedral smectites controlling pH, alkalinity, silica and magnesium concentrations in alkaline lakes. *Chemical Geology*, *63*(1-2), 59-72.

Deelman, J. C. (1999), Low-temperature nucleation of magnesite and dolomite. *Neues Jahrbuch Fur Mineralogie Monatshefte*, 289-302.

Dence, M. R. (1971), Impact melts. *Journal of Geophysical Research*, *76*(23), 5552-5565. doi: 10.1029/JB076i023p05552

Di Tommaso, D. and de Leeuw, N.H. (2010), Structure and dynamics of the hydrated magnesium ion and of the solvated magnesium carbonates: Insights from first principles simulations. *Physical Chemistry Chemical Physics, 12*(4), 894-901. doi: 10.1039/B915329B

Dong, A., Zhu, X. K., Li, S. Z., Kendall, B., Wang, Y., & Gao, Z. (2016), Genesis of a giant Paleoproterozoic strata-bound magnesite deposit: Constraints from Mg isotopes. *Precambrian Research*, *281*, 673-683.

Duan, Z., & Sun, R. (2003). An improved model calculating CO2 solubility in pure water and aqueous NaCl solutions from 273 to 533 K and from 0 to 2000 bar. *Chemical Geology*, *193*(3-4), 257-271.

Dunn, J. R. (1953), The origin of the deposits of tufa in Mono Lake [California]. *Journal of Sedimentary Research*, *23*(1), 18-23. doi: 10.1306/D4269530-2B26-11D7-8648000102C1865D

Ece, Ö. I., & Matsubaya, O. (2005), Genesis of hydrothermal stockwork-type magnesite deposits associated with ophiolite complexes in the Kütahya-Eskişehir region, Turkey. *Neues Jahrbuch für Mineralogie-Abhandlungen: Journal of Mineralogy and Geochemistry*, *181*(2), 191-205. doi: 10.1127/0077-7757/2005/0014

Edwards, C. S., Ehlmann, B. L. (2015), Carbon sequestration on Mars. *Geology, 43*, 863–866. doi: 10.1130/g36983.1

Ehlmann, B. L., Mustard, J. F., Murchie, S. L., Poulet, F., Bishop, J. L., Brown, A. J., Calvin, W. M., Clark, R. N., Marais, D. J. D., Milliken, R. E., Roach, L. H., Roush, T. L., Swayze, G. A., Wray, J. J. (2008), Orbital identification of carbonate-bearing rocks on Mars. *Science, 322*, 1828 1832. doi: 10.1126/science.1164759

Ehlmann, B. L., et al. (2009), Identification of hydrated silicate minerals on Mars using MRO-CRISM: Geologic context near Nili Fossae and implications for aqueous alteration, *Journal of Geophysical. Research, 114*, E00D08, doi:10.1029/2009JE003339.

Eiler, J. M., (2011), Paleoclimate reconstruction using carbonate clumped isotope thermometry. *Quaternary Science Reviews, 30*, 3575–3588. doi: 10.1016/j.quascirev.2011.09.001

Eiler, J. M., (2007), "Clumped-isotope" geochemistry—The study of naturally-occurring, multiply substituted isotopologues. *Earth and Planetary Science Letters, 262*, 309–327. 10.1016/j.epsl.2007.08.020

Ellmies, R., Voigtländer, G., Germann, K., Krupenin, M. T., & Moeller, P. (1999), Origin of giant stratabound deposits of magnesite and siderite in Riphean carbonate rocks of the Bashkir mega anticline, western Urals. *Geologische Rundschau*, *87*(4), 589-602. doi: 10.1007/s005310050233

Emery, D., & Robinson, A. (1993), Inorganic geochemistry: Applications to petroleum geology: London, Blackwell, 254 p.

Falk, E. S., Guo, W., Paukert, A. N., Matter, J. M., Mervine, E. M., Kelemen, P. B., (2016), Controls on the stable isotope compositions of travertine from hyperalkaline springs in Oman: Insights from clumped isotope measurements. *Geochimica et Cosmochimica Acta, 192*, 1–28. doi: 10.1016/j.gca.2016.06.026

Falk, E. S., & Kelemen, P. B. (2015), Geochemistry and petrology of listvenite in the Samail ophiolite, Sultanate of Oman: Complete carbonation of peridotite during ophiolite emplacement. *Geochimica et Cosmochimica Acta, 160*, 70-90, doi: 10.1016/j.gca.2015.03.014

Falk, E.S., 2014. Carbonation of peridotite in the Oman Ophiolite. Columbia University.

Fallick, A. E., Ilich, M., & Russell, M. J. (1991), A stable isotope study of the magnesite deposits associated with| the Alpine-type ultramafic rocks of Yugoslavia. *Economic Geology, 86*(4), 847 861. doi: 10.2113/gsecongeo.86.4.847

Farley, K. A., (2000), Helium diffusion from apatite: General behavior as illustrated by Durango fluorapatite. *Journal of Geophysical Research: Solid Earth, 105*, 2903–2914. https://doi.org/10.1029/1999JB900348

Farley, K., Malespin, C., Mahaffy, P., Grotzinger, J., Vasconcelos, P., Milliken, R., Malin, M., Edgett, K., Pavlov, A., Hurowitz, J., (2014), In situ radiometric and exposure age dating of the Martian surface. *Science, 343*, 1247166. doi: 10.1126/science.1247166

Felmy, A, R., Qafoku, O., Arey, B. W., Hu, J. Z., Hu, M., Schaef, H. T., Ilton, E. S., et al. (2012), Reaction of water-saturated supercritical CO2 with forsterite: Evidence for magnesite formation at low temperatures. *Geochimica et Cosmochimica Acta,* 91, 271-282.

Fernandez, A., Tang, J., Rosenheim, B.E., (2014), Siderite 'clumped' isotope thermometry: a new paleoclimate proxy for humid continental environments. *Geochimica et Cosmochimica Acta, 126*, 411-421. doi: 10.1016/j.gca.2013.11.006

Fernández-Nieto, C., Torres-Ruiz, J., Subías Pérez, I., Fanlo González, I., & González López, J. M.

(2003), Genesis of Mg-Fe carbonates from the Sierra Menera magnesite-siderite deposits, Northeast Spain: Evidence from fluid inclusions, trace elements, rare earth elements, and stable isotope data. *Economic Geology*, *98*(7), 1413-1426. doi: 10.2113/gsecongeo.98.7.1413

Ferry, J. M., Rumble III, D., Wing, B. A., Penniston-Dorland, S. C., (2005), A new interpretation of centimetre-scale variations in the progress of infiltration-driven metamorphic reactions: Case study of carbonated metaperidotite, Val d'Efra, Central Alps, Switzerland. *Journal of Petrology, 46,* 1725-1746. doi: 10.1093/petrology/egi034

Frank, T. D. and Fielding, C. R. (2003), Marine origin for Precambrian, carbonate-hosted magnesite?, *Geology, 31*(12), 1101–1104. doi: 10.1130/G20101.1.

Franz, H. B et al. (2020). Indigenous and exogenous organics and surface–atmosphere cycling inferred from carbon and oxygen isotopes at Gale crater. *Nature Astronomy*, *4*(5), 526-532.

Freeman, K. H. (2001). Isotopic biogeochemistry of marine organic carbon. *Reviews in Mineralogy and Geochemistry*, *43*(1), 579-605.

Freestone, I. C., and Hamilton, D. L., (1980), The role of liquid immiscibility in the genesis of carbonatites—An experimental study. *Contributions to Mineralogy and Petrology, 73,* 105 117, https:// doi .org /10.1007 /BF00371385.

Gaffey, S. J. (1987), Spectral reflectance of carbonate minerals in the visible and near infrared (0.35 – 2.55 um): Anhydrous carbonate minerals, *J. Geophys. Res., 92*, 1429–1440, doi:10.1029/JB092iB02p01429.

Gaffey, S. J. (1985). Reflectance spectroscopy in the visible and near-infrared (0.35–2.55 µm): Applications in carbonate petrology. *Geology*, *13*(4), 270-273.

García del Real, P. et al. (2016), Clumped-isotope thermometry of magnesium carbonates in ultramafic rocks, *Geochimica et Cosmochimica Acta, 193*, 222–250. doi: 10.1016/j.gca.2016.08.003.

García del Real, P., Maher, K., Kluge, T., Bird, D. K., Brown Jr, G. E., John, C. M., (2016), Clumped isotope thermometry of magnesium carbonates in ultramafic rocks. *Geochimica et Cosmochimica Acta, 193*, 222–250. doi: 10.1016/j.gca.2016.08.003

García del Real, P. and Vishal, V. (2016) 'Mineral Carbonation in Ultramafic and Basaltic Rocks', In Vishal, V. and Singh, T. N. (eds) Geologic Carbon Sequestration: Understanding Reservoir Behavior. Cham: Springer International Publishing, pp. 213–229. doi: 10.1007/978-3-319-27019 7_11.

Gérard, E. et al. (2013), Specific carbonate-microbe interactions in the modern microbialites of Lake Alchichica (Mexico), *ISME Journal, 7*(10), 1997–2009. doi: 10.1038/ismej.2013.81.

Ghosh, P., Adkins, J., Affek, H., Balta, B., Guo, W., Schauble, E.A., Schrag, D., Eiler, J.M., (2006), 13C 18O bonds in carbonate minerals: a new kind of paleothermometer. *Geochim. Cosmochim. Acta,*

70, 1439–1456. doi: 10.1016/j.gca.2005.11.014

Giampouras, M., Garrido, C. J., Bach, W., Los, C., Fussmann, D., Monien, P., & García-Ruiz, J. M.
(2020), On the controls of mineral assemblages and textures in alkaline springs, Samail Ophiolite,
Oman. *Chemical Geology*, *533*, 119435. doi: 10.1016/j.chemgeo.2019.119435

Giammar, D. E., Bruant Jr, R. G., and Peters, C. A. (2005), Forsterite dissolution and
magnesite precipitation at conditions relevant for deep saline aquifer storage and sequestration of
carbon dioxide. *Chemical Geology, 217*(3-4), 257-276. doi: 10.1016/j.chemgeo.2004.12.013

Glennie, K. W., Boeuf, M. G. A., Clarke, M. H., Moody-Stuart, M., Pilaar, W. F. H., & Reinhardt, B. M.
(1973), Late Cretaceous nappes in Oman Mountains and their geologic evolution. *AAPG Bulletin*,
57(1), 5-27. doi: 10.1306/819A4240-16C5-11D7-8645000102C1865D

Grant, J. A., Golombek, M. P., Wilson, S. A., Farley, K. A., Williford, K. H., Chen, A. (2018), The
science process for selecting the landing site for the 2020 Mars rover. *Planetary Space Science,
164*, 106–126. doi: 10.1016/j.pss.2018.07.001

Graup, G. (1999), Carbonate-silicate liquid immiscibility upon impact melting: Ries Crater, Germany.
Meteoritics & Planetary Science, *34*(3), 425-438. doi: 10.1111/j.1945-5100.1999.tb01351.x

Grieve, R. A., Dence, M. R., & Robertson, P. B. (1977), Cratering processes – As interpreted from the
occurrence of impact melts. In *Impact and explosion cratering: Planetary and terrestrial
implications,* Pergamon Press (New York) (pp. 791-814).

Grotzinger, J. P., & James, N. P. (2000), Precambrian carbonates: evolution of understanding. *SEPM
Special Publications, 66.*

Grotzinger, J. P., & Kasting, J. F., (1993), New constraints on Precambrian ocean composition. *The
Journal of Geology*, *101*(2), 235-243. doi: 10.1086/648218

Grotzinger, J. P. (1989). Facies and evolution of Precambrian carbonate depositional systems: emergence
of the modern platform archetype. *SEPM Special Publications, 44.* doi: 10.2110/pec.89.44.0079

Grozeva N. G., Klein F., Seewald J. S. and Sylva S. P. (2017) Experimental study of carbonate formation
in oceanic peridotite. *Geochimica et Cosmochimica Acta, 199*, 264-286, doi: 10.1111/j.1365
3121.2012.01083.x.

Halevy, I., Fischer, W.W., Eiler, J.M., (2011), Carbonates in the Martian meteorite Allan Hills 84001
formed at 18$\pm$4 C in a near-surface aqueous environment. *Proceedings National Acadacemy
of Science, 108,* 16895–16899. doi: 10.1073/pnas.1109444108

Halla, F., and R. Van Tassel. (1966), Dissolution phenomena of alkaline earth carbonates. III. Magnesite,
MgCO3. *Redex Rundschau*, 356-362.

Halls, C., & Zhao, R. (1995), Listvenite and related rocks: Perspectives on terminology and mineralogy
with reference to an occurrence at Cregganbaun, Co. Mayo, Republic of Ireland. *Mineralium*

Deposita, *30*(3-4), 303-313. doi: 10.1007/BF00196366

Hamilton, V. E., and P. R. Christensen (2005), Evidence for extensive, olivine-rich bedrock on Mars, *Geology, 33*, 433–436, doi:10.1130/G21258.1.

Hänchen, M., Prigiobbe, V., Baciocchi, R., and Mazzotti, M. (2008), Precipitation in the magnesium carbonate system—effects of temperature and CO2 pressure. *Chemical Engineering Science, 63*(4), 1012-1028. doi: 10.1016/j.ces.2007.09.052

Hansen L. D., Dipple G. M., Gordon T. M. and Kellett D. A. (2005) Carbonated serpentinite (listwanite) at Atlin, British Columbia: a geological analogue to carbon dioxide sequestration. *The Canadian Mineralogist*, 43, 225-239.

Heard, A. W., & Kite, E. S. (2020), A probabilistic case for a large missing carbon sink on Mars after 3.5 billion years ago. *Earth and Planetary Science Letters*, *531*, 116001.

Hoefen, T. M., R. N. Clark, J. L. Bandfield, M. D. Smith, J. C. Pearl, and P. R. Christensen (2003), Discovery of olivine in the Nili Fossae region of Mars. *Science, 302*, 627– 630, doi:10.1126/science.1089647.

Hopkinson, L., Kristova, P., Rutt, K., and Cressey, G. (2012), Phase transitions in the system MgO–CO2–H2O during CO2 degassing of Mg-bearing solutions. *Geochimica et Cosmochimica Acta, 76*, 1-13. doi: 10.1016/j.gca.2011.10.023

Horgan, B. H. N., Anderson, R. B., Dromart, G., Amador, E. S., Rice, M. S. (2020), The mineral diversity of Jezero Crater: Evidence for possible lacustrine carbonates on Mars. *Icarus, 339*, 113526. doi: 10.1016/j.icarus.2019.113526

Hu, R., Kass, D. M., Ehlmann, B. L., & Yung, Y. L. (2015). Tracing the fate of carbon and the atmospheric evolution of Mars. *Nature Communications*, *6*(1), 1-9.

Huntington, K. W., Budd, D. A., Wernicke, B. P., Eiler, J. M., (2011), Use of clumped-isotope thermometry to constrain the crystallization temperature of diagenetic calcite. *J. Sediment. Res., 81*, 656–669. doi: 10.2110/jsr.2011.51

Huntington, K.W., Lechler, A.R., (2015), Carbonate clumped isotope thermometry in continental tectonics. *Tectonophysics, 647*, 1–20. doi: 10.1016/j.tecto.2015.02.019

Hynek, B. M., Beach, M., Hoke, M. R. T. (2010), Updated global map of Martian valley networks and implications for climate and hydrologic processes. *Journal of Geophysical Research, 115*. doi: 10.1029/2009je003548

Irving, A. J., & Wyllie, P. J. (1975), Subsolidus and melting relationships for calcite, magnesite and the join CaCO3-MgCO3 36 kb. *Geochimica et Cosmochimica Acta*, *39*(1), 35-53.

Isshiki, M., Irifune, T., Hirose, K., Ono, S., Ohishi, Y., Watanuki, T., Nishibori, E., Takata, M. and Sakata, M., 2004. Stability of magnesite and its high-pressure form in the lowermost mantle.

Nature, *427*(6969), 60-63. doi: 10.1038/nature02181

Jakosky, B. M., et al. (2018), Loss of the Martian atmosphere to space: Present-day loss rates determined from MAVEN observations and integrated loss through time. *Icarus*, *315*, 146-157.

Jiao, D., King, C., Grossfield, A., Darden, T. A., and Ren, P. (2006), Simulation of Ca2+ and Mg2+ solvation using polarizable atomic multipole potential. *The Journal of Physical Chemistry B, 110*(37): 18553-18559. doi: 10.1021/jp062230r

Jones, A. P., Wunemann, K., & Price, G. D. (2005), Modeling impact volcanism as a possible origin for the Ontong Java Plateau. *Special papers – Geological Society of America*, *388*, 711.

Jull, A. T., Cheng, S., Gooding, J. L., & Velbel, M. A. (1988). Rapid growth of magnesium-carbonate weathering products in a stony meteorite from Antarctica. *Science*, *242*(4877), 417-419.

Jurković, I., Palinkaš, L. A., Garašić, V., & Palinkaš, S. S. (2012), Genesis of vein-stockwork cryptocrystalline magnesite from the Dinaride ophiolites. *Ofioliti*, *37*(1), 13-26.

Kaźmierczak, J. et al. (2011), Hydrochemistry and microbialites of the alkaline crater lake Alchichica, Mexico, *Facies, 57*(4), 543–570. doi: 10.1007/s10347-010-0255-8.

Keeling, J., Horn, R. and Wilson, I. (2019), New kiln technology expands market opportunities for cryptocrystalline magnesite, *MESA Journal, 89*(1), pp. 22–38.

Kitano, Y., Okumura, M., & Idogaki, M. (1975), Incorporation of sodium, chloride, and sulfate with calcium carbonate. *Geochemical Journal*, *9*(2), 75-84.

Kremer, C. H., Mustard, J. F., Bramble, M. S. (2019), A widespread olivine-rich ash deposit on Mars. *Geology, 47*, 677–681. doi: 10.1130/g45563.1

Kelemen, P. B., & Manning, C. E. (2015), Reevaluating carbon fluxes in subduction zones, what goes down, mostly comes up. *Proceedings of the National Academy of Sciences*, *112*(30), E3997 E4006. doi: 10.1073/pnas.1507889112

Kelemen, P. B., Matter, J., Streit, E. E., Rudge, J. F., Curry, W. B., & Blusztajn, J. (2011), Rates and mechanisms of mineral carbonation in peridotite: natural processes and recipes for enhanced, in situ CO2 capture and storage. *Annual Review of Earth and Planetary Sciences, 39*, 545-576, doi: 10.1146/annurev-earth-092010-152509

Kelemen, P. B., & Matter, J. (2008), In situ carbonation of peridotite for CO2 storage. *Proceedings of the National Academy of Sciences*, *105*(45), 17295-17300. doi: 10.1073/pnas.0805794105

Kieffer, S. W. (1971), Shock metamorphism of the Coconino sandstone at Meteor Crater, Arizona. *Journal of Geophysical Research*, *76*(23), 5449-5473. doi: 10.1029/JB076i023p05449

Klein, F. and Garrido ,C. J. (2011) Thermodynamic constraints on mineral carbonation of serpentinized peridotite. Lithos 126, 147-160.

Klein, F. and McCollom, T. M. (2013) From serpentinization to carbonation: New insights from a CO2

injection experiment. *Earth and Planetary Science Letters, 379,* 137-145.

Kluge, T., John, C.M., Jourdan, A.-L., Davis, S., Crawshaw, J., (2015), Laboratory calibration of the calcium carbonate clumped isotope thermometer in the 25–250 C temperature range. *Geochimica et Cosmochimica Acta, 157*, 213–227. doi: 10.1016/j.gca.2015.02.028

Königsberger, E., Königsberger, L.-C., and Gamsjäger, H. (1999), Low-temperature thermodynamic model for the system Na2CO3− MgCO3− CaCO3− H2O. *Geochimica et Cosmochimica Acta, 63*(19-20), 3105-3119. doi: 10.1016/S0016-7037(99)00238-0

Kroopnick, P. M. (1985). The distribution of 13C of ΣCO2 in the world oceans. *Deep Sea Research Part A. Oceanographic Research Papers*, *32*(1), 57-84.

Kralik, M., Ahron, P., Schroll, E., & Zachmann, V. (1989), Carbon and oxygen isotope systematics of magnesites in magnesite formation. In "Magnesite. Geology, Mineralogy, Geochemistry, Formation of Mg Carbonates, P. Möller, *ed. Monograph Series on Mineral Deposits, 28*, 207 224.

Krupenin, M. T. and Kol'tsov, A. B. (2017), Geology, composition, and physicochemical model of sparry magnesite deposits of the Southern Urals, *Geology of Ore Deposits, 59*(1), pp. 14–35. doi: 10.1134/S1075701517010044.

Kubik, P. W., Korschinek, G., Nolte, E., Ratzinger, U., Ernst, H., Teichmann, S., Morinaga, H., Wild, E., Hille, P., (1984), Accelerator mass spectrometry of 36Cl in limestone and some paleontological samples using completely stripped ions. *Nuclear Instruments and Methods in Physics Research Section B: Beam Interactions with Materials and Atoms, 5*, 326–330. doi: 10.1016/0168 583X(84)90537-8

Kuşcu, M., Cengiz, O., & Kahya, A. (2017), Trace element contents and CO isotope geochemistry of the different originated magnesite deposits in Lake District (Southwestern Anatolia), Turkey. *Arabian Journal of Geosciences, 10*(15), 339. doi: 10.1007/s12517-017-3102-1

Lal, D., (1988), In situ-produced cosmogenic isotopes in terrestrial rocks. *Annual Review of Earth and Planetary Sciences, 16*, 355–388. doi: 10.1146/annurev.ea.16.050188.002035

Langmuir, D. (1965), Stability of carbonates in the system MgO-CO2-H2O. *The Journal of Geology, 73*(5), 730-754.

Lasaga, A. C. (2014), Kinetic theory in the earth sciences. Princeton University Press.

Leask, E. K. (2020), Investigating the Evolution of Surface Water on Mars through Spectroscopy of Secondary Minerals. Doctoral dissertation, California Institute of Technology.

Lee, W. J., & Wyllie, P. J. (2000). The system CaO-MgO-SiO 2-CO 2 at 1 GPa, metasomatic wehrlites, and primary carbonatite magmas. *Contributions to Mineralogy and Petrology*, *138*(3), 214-228.

Leshin, L. A., et al. (2013), Volatile, isotope, and organic analysis of martian fines with the Mars

Curiosity rover. *Science, 341*(6153). doi: 10.1126/science.1238937

Li, H. C., & Ku, T. L. (1997), δ13C–δ18C covariance as a paleohydrological indicator for closed-basin lakes. *Palaeogeography, Palaeoclimatology, Palaeoecology, 133*(1-2), 69-80. doi: 10.1016/S0031-0182(96)00153-8

Lippmann, Friedrich. (2012), Sedimentary carbonate minerals. Vol. 6. Springer Science & Business Media.

Lloyd, M. K., Eiler, J. M., Nabelek, P. I., (2017), Clumped isotope thermometry of calcite and dolomite in a contact metamorphic environment. *Geochimica et Cosmochimica Acta, 197*, 323–344. doi: 10.1016/j.gca.2016.10.037

Lloyd, M. K., Ryb, U., Eiler, J. M., (2018), Experimental calibration of clumped isotope reordering in dolomite. *Geochimica et Cosmochimica Acta, 242*, 1–20. doi: 10.1016/j.gca.2018.08.036

Lugli, S., Torres-Ruiz, J., Garuti, G., & Olmedo, F. (2000), Petrography and geochemistry of the Eugui magnesite deposit (Western Pyrenees, Spain): Evidence for the development of a peculiar zebra banding by dolomite replacement. *Economic Geology*, *95*(8), 1775-1791. doi: 10.2113/gsecongeo.95.8.1775

Lugli, S., Morteani, G. and Blamart, D. (2002), Petrographic, REE, fluid inclusion and stable isotope study of magnesite from the Upper Triassic Burano Evaporites (Secchia Valley, northern Apennines): Contributions from sedimentary, hydrothermal and metasomatic sources, *Mineralium Deposita, 37*(5), 480–494. doi: 10.1007/s00126-001-0251-6.

Malkin, A. I., A. A. Chernov, and I. V. Alexeev. (1989), Growth of dipyramidal face of dislocation-free ADP crystals: Free energy of steps. *Journal of Crystal Growth, 97*(3-4), 765-769. doi: 10.1016/0022-0248(89)90580-0

Mandon, L., Quantin-Nataf, C., Thollot, P., Mangold, N., Lozac'H, L., Dromart, G., Beck, P., Dehouck, E., Breton, S., Millot, C., Volat, M. (2020), Refining the age, emplacement and alteration scenarios of the olivine-rich unit in the Nili Fossae region, Mars. *Icarus, 336*, 113436. doi: 10.1016/j.icarus.2019.113436

Marion, G. M. (2001), Carbonate mineral solubility at low temperatures in the Na-K-Mg-Ca-H-Cl SO4-OH-HCO3-CO3-CO2-H2O system. *Geochimica et Cosmochimica Acta, 65*(12), 1883-1896. doi: 10.1016/S0016-7037(00)00588-3

Martin, P. E., Farley, K. A., Malespin, C. A., Mahaffy, P. R., Edgett, K. S., Gupta, S., et al. (2021). Billion-year exposure ages in Gale crater (Mars) indicate Mount Sharp formed before the Amazonian period. *Earth and Planetary Science Letters*, *554*, 116667. doi: 10.1016/j.epsl.2020.116667

Mavromatis, V., Pearce, C. R., Shirokova, L. S., Bundeleva, I. A., Pokrovsky, O. S., Benezeth, P. and Oelkers, E. H. (2012), Magnesium isotope fractionation during hydrous magnesium carbonate precipitation with and without cyanobacteria. *Geochimica et Cosmochimica Acta*, *76*, 161-174, 10.1016/j.gca.2011.10.019

Mavromatis, V., Gautier, Q., Bosc, O., & Schott, J. (2013). Kinetics of Mg partition and Mg stable isotope fractionation during its incorporation in calcite. *Geochimica et Cosmochimica Acta*, *114*, 188-203.

McCrea, J. M., (1950), On the isotopic chemistry of carbonates and a paleotemperature scale. *Journal of Chemical Physics, 18*, 849–857. doi: 10.1063/1.1747785

McSween Jr, H. Y., Labotka, T. C., & Viviano-Beck, C. E. (2015), Metamorphism in the martian crust. *Meteoritics & Planetary Science*, *50*(4), 590-603.

Mees, F. and Keppens, E. (2013), Stable isotope geochemistry of magnesite from Holocene salt lake deposits, Taoudenni, Mali, *Geological Journal, 48*(6), 620–627. doi: 10.1002/gj.2476.

Melezhik, V. A., Fallick, A. E., Medvedev, P. V., & Makarikhin, V. V. (2001), Palaeoproterozoic magnesite: Lithological and isotopic evidence for playa/sabkha environments. *Sedimentology, 48*(2), 379-397.

Menzel, M. D., Garrido, C. J., Sánchez-Vizcaíno, V. L., Marchesi, C., Hidas, K., Escayola, M. P., & Huertas, A. D. (2018), Carbonation of mantle peridotite by CO2-rich fluids: The formation of listvenites in the Advocate ophiolite complex (Newfoundland, Canada). *Lithos*, *323*, 238-261.

Mervine, E. M., Humphris, S. E., Sims, K. W., Kelemen, P. B., & Jenkins, W. J. (2014), Carbonation rates of peridotite in the Samail Ophiolite, Sultanate of Oman, constrained through 14C dating and stable isotopes. *Geochimica et Cosmochimica Acta*, *126*, 371-397. doi: 10.1016/j.gca.2013.11.007

Metzler, A., Ostertag, R., Redeker, H. J., & Stöffler, D. (1988), Composition of the crystalline basement and shock metamorphism of crystalline and sedimentary target rocks at the Haughton impact crater, Devon Island, Canada. *Meteoritics*, *23*(3), 197-207. doi: 10.1111/j.1945 5100.1988.tb01282.x

Mirnejad, H. et al. (2008), Mineralogy, stable isotope geochemistry, and paragenesis of magnesite deposits from the ophiolite belt of Eastern Iran, *Economic Geology, 103*(8), 1703–1713. doi:10.2113/gsecongeo.103.8.1703.

Mirnejad, H., Aminzadeh, M., Ebner, F., & Unterweissacher, T. (2015), Geochemistry and origin of the ophiolite hosted magnesite deposit at Derakht-Senjed, NE Iran. *Mineralogy and Petrology*, *109*(6), 693-704. doi: 10.1007/s00710-015-0408-0

Moore, K. R., Pajusalu, M., Gong, J., Sojo, V., Matreux, T., Braun, D., & Bosak, T. (2020). Biologically

mediated silicification of marine cyanobacteria and implications for the Proterozoic fossil record. *Geology*, *48*(9), 862-866.

Morteani, G., Möller, P., & Schley, F. (1982), The rare earth element contents and the origin of the sparry magnesite mineralizations of Tux-Lanersbach, Entachen Alm, Spiessnaegel, and Hochfilzen, Austria, and the lacustrine magnesite deposits of Aiani-Kozani, Greece, and Bela Stena, Yugoslavia. *Economic Geology*, *77*(3), 617-631. doi: 10.2113/gsecongeo.77.3.617

Morris, R. V., Ruff, S. W., Gellert, R., Ming, D. W., Arvidson, R. E., Clark, B. C., Golden, D. C., Siebach, K., Klingelhofer, G., Schroder, C., Fleischer, I., Yen, A. S., Squyres, S. W. (2010), Identification of carbonate-rich outcrops on Mars by the Spirit Rover. *Science, 329*, 421–424. doi: 10.1126/science.1189667

Mur, J. J. O., and Urpinell, M. I. (1987), Magnesite formation in recent playa lakes, Los Monegros, Spain. *Geological Society, London, Special Publications, 36*(1), 119-122. doi: 10.1144/GSL.SP.1987.036.01.10

Mustard, J. F., Ehlmann, B. L., Murchie, S. L., Poulet, F., Mangold, N., Head, J. W., Bibring, J.-P., Roach, L. H. (2009), Composition, Morphology, and Stratigraphy of Noachian Crust around the Isidis basin. *Journal of Geophysical. Research, 114*. doi: 10.1029/2009je003349

Mustard, J. F., et al. (2007), Mineralogy of the Nili Fossae region with OMEGA/Mars Express data: 1. Ancient impact melt in the Isidis basin and implications for the transition from the Noachian to Hesperian, *Journal of Geophysical. Research, 112*, E08S03, doi:10.1029/2006JE002834.

Mustard, J. F., Murchie, S. L., Pelkey, S. M., Ehlmann, B. L., Milliken, R. E., Grant, J. A., Bibring, J.-P., Poulet, F., Bishop, J., Dobrea, E. N., Roach, L., Seelos, F., Arvidson, R. E., Wiseman, S., Green, R., Hash, C., Humm, D., Malaret, E., Mcgovern, J. A., Seelos, K., Clancy, T., Clark, R., Marais, D. D., Izenberg, N., Knudson, A., Langevin, Y., Martin, T., Mcguire, P., Morris, R., Robinson, M., Roush, T., Smith, M., Swayze, G., Taylor, H., Titus, T., Wolff, M. (2008), Hydrated silicate minerals on Mars observed by the Mars Reconnaissance Orbiter CRISM instrument. *Nature, 454*, 305–309. doi: 10.1038/nature07097

Nasir, S., et al. (2007), Mineralogical and geochemical characterization of listwaenite from the Semail Ophiolite, Oman. *Geochemistry*, *67*(3), 213-228. doi: 10.1016/j.chemer.2005.01.003

Neal, C., & Stanger, G. (1985), Past and present serpentinisation of ultramafic rocks: An example from the Semail Ophiolite Nappe of Northern Oman. In *The Chemistry of Weathering* (pp. 249-275). Springer, Dordrecht.

Nier, A. O. & McElroy, M. B. (1977), Composition and structure of Mars' upper atmosphere: results from the neutral mass spectrometers on Viking 1 and 2. *Journal of Geophysical Research, 82*, 4341–4349. doi: 10.1029/JS082i028p04341

Niles, P. B., Boynton, W. V., Hoffman, J. H., Ming, D. W. & Hamara, D. (2010), Stable isotope measurements of Martian atmospheric CO2 at the Phoenix landing site. *Science, 329*, 1334–1337. doi: 10.1126/science.1192863

Niles, P. B., D. C. Catling, G. Berger, E. Chassefière, B. L. Ehlmann, J. R. Michalski, R. Morris, S. W. Ruff, and B. Sutter (2013), Geochemistry of carbonates on Mars: Implications for climate history and nature of aqueous environments, *Space Science Reviews, 174*, 301–328.

Nimmo, F., & Stevenson, D. J., (2000), Influence of early plate tectonics on the thermal evolution and magnetic field of Mars. *Journal of Geophysical Research: Planets*, *105*(E5), 11969-11979. doi: 10.1029/1999JE001216

Nishiizumi, K., Lal, D., Klein, J., Middleton, R., Arnold, J. R., (1986), Production of 10 Be and 26 Al by cosmic rays in terrestrial quartz in situ and implications for erosion rates. *Nature, 319*, 134–136. doi: 10.1038/319134a0

O'Neil, J. R. and Barnes, I. (1971), C13 and O18 compositions in some fresh-water carbonates associated with ultramafic rocks and serpentinites: Western United States, *Geochimica et Cosmochimica Acta, 35*(7), 687–697. doi: 10.1016/0016-7037(71)90067-6.

Osinski, G. R., Spray, J. G., & Lee, P. (2005), Impactites of the Haughton impact structure, Devon island, Canadian high Arctic. *Meteoritics & Planetary Science*, *40*(12), 1789-1812. doi: 10.1111/j.1945 5100.2005.tb00147.x

Osinski, G. R., & Spray, J. G. (2001), Impact-generated carbonate melts: Evidence from the Haughton structure, Canada. *Earth and Planetary Science Letters*, *194*(1-2), 17-29. doi: 10.1111/j.1945 5100.2001.tb01910.x

Oskierski, H. C., Dlugogorski, B. Z., & Jacobsen, G. (2013), Sequestration of atmospheric CO2 in a weathering derived, serpentinite-hosted magnesite deposit: 14C tracing of carbon sources and age constraints for a refined genetic model. *Geochimica et Cosmochimica Acta, 122*, 226-246, doi: 10.1016/j.gca.2013.08.029

Oskierski, H.C., Beinlich, A., Mavromatis, V., Altarawneh, M. and Dlugogorski, B. Z., (2019), Mg isotope fractionation during continental weathering and low temperature carbonation of ultramafic rocks. *Geochimica et Cosmochimica Acta, 262*, 60-77. doi: 10.1016/j.gca.2019.07.019

Paradis, S. and Simandl, G. J. (2018), Are there genetic links between carbonate - hosted barite - zinc - lead sulphide deposits and magnesite mineralization in southeast British Columbia ?, in Rogers, N. (ed.) Targeted Geoscience Initiative: 2017 report of activities, volume 1. Geological Survey of Canada, Open File, pp. 217–227.

Pearce, C. R., Saldi, G. D., Schott, J. and Oelkers, E. H. (2012), Isotopic fractionation during congruent dissolution, precipitation and at equilibrium: Evidence from Mg isotopes. *Geochimica et*

Cosmochimica Acta, 92, 170-183. doi: 10.1016/j.gca.2012.05.045

Phillips, F. M., Leavy, B. D., Jannik, N. O., Elmore, D., Kubik, P. W., (1986), The accumulation of cosmogenic chlorine-36 in rocks: A method for surface exposure dating. *Science, 231*, 41–43. doi: 10.1126/science.231.4733.41

Pohl, J., Stoeffler, D. I. E. T. E. R., Gall, H. V., & Ernstson, K. (1977), The Ries impact crater. In *Impact and explosion cratering: Planetary and terrestrial implications* (pp. 343-404).

Power, I. M. et al. (2007), Biologically induced mineralization of dypingite by cyanobacteria from an alkaline wetland near Atlin, British Columbia, Canada, *Geochemical Transactions, 8*, 1–16. doi: 10.1186/1467-4866-8-13.

Power, I. M. et al. (2014), A depositional model for hydromagnesite-magnesite playas near Atlin, British Columbia, Canada, *Sedimentology, 61*(6), 1701–1733. doi: 10.1111/sed.12124.

Power, I. M., Harrison, A. L., Dipple, G. M., Wilson, S. A., Barker, S. L., & Fallon, S. J. (2019), Magnesite formation in playa environments near Atlin, British Columbia, Canada. *Geochimica et Cosmochimica Acta, 255*, 1-24, 10.1016/j.gca.2019.04.008

Renaut, R. W. (1993), Morphology, distribution, and preservation potential of microbial mats in the hydromagnesite-magnesite playas of the Cariboo Plateau, British Columbia, Canada, *Hydrobiologia, 267*(1–3), 75–98. doi: 10.1007/BF00018792.

Rioux, M., Bowring, S., Kelemen, P., Gordon, S., Dudás, F., & Miller, R. (2012), Rapid crustal accretion and magma assimilation in the Oman-UAE ophiolite: High precision U-Pb zircon geochronology of the gabbroic crust. *Journal of Geophysical Research: Solid Earth*, *117*(B7). doi: 10.1029/2012JB009273

Rioux, M., Bowring, S., Kelemen, P., Gordon, S., Miller, R., & Dudás, F. (2013), Tectonic development of the Samail ophiolite: High-precision U-Pb zircon geochronology and Sm-Nd isotopic constraints on crustal growth and emplacement. *Journal of Geophysical Research: Solid Earth*, *118*(5), 2085-2101. doi: 10.1002/jgrb.50139

Rioux, M., Garber, J., Bauer, A., Bowring, S., Searle, M., Kelemen, P., & Hacker, B. (2016), Synchronous formation of the metamorphic sole and igneous crust of the Semail ophiolite: New constraints on the tectonic evolution during ophiolite formation from high-precision U–Pb zircon geochronology. *Earth and Planetary Science Letters*, *451*, 185-195. doi: 10.1016/j.epsl.2016.06.051

Robie, R. A., and D. R. Waldbaum. (1968), Thermodynamic properties of minerals and related substances at 298.15 0K and one atmosphere pressure and at higher temperatures. *US Geological Survey Bulletin 1259*.

Ronchi, L. H. et al. (2008), Genetic and metamorphic conditions constrained by fluid inclusions from

Paleoproterozoic (c. 1.8 Ga) magnesite ore deposits, NE Brazil, *Journal of South American Earth Sciences, 25*(4), 492–500. doi: 10.1016/j.jsames.2007.10.005.

Rosen, M. R., Miser, D. E., & Warren, J. K. (1988), Sedimentology, mineralogy and isotopic analysis of Pellet Lake, Coorong region, South Australia. *Sedimentology, 35*(1), 105-122.

Rosenbaum, J., Sheppard, S.M.F., (1986), An isotopic study of siderites, dolomites and ankerites at high temperatures. *Geochimica et Cosmochimica Acta, 50*, 1147–1150. doi: 10.1016/0016 7037(86)90396-0

Rossini, Frederick Dominic. (1961), Selected values of chemical thermodynamic properties. Vol. 500. US Government Printing Office.

Russell, M. J. et al. (1999), Search for signs of ancient life on Mars: Expectations from hydromagnesite microbialites, Salda Lake, Turkey, *Journal of the Geological Society, 156*(5), 869–888. doi: 10.1144/gsjgs.156.5.0869.

Ryb, U., Lloyd, M. K., Stolper, D. A., Eiler, J. M., (2017), The clumped-isotope geochemistry of exhumed marbles from Naxos, Greece. *Earth Planetary Science Letters, 470*, 1–12. doi: 10.1016/j.epsl.2017.04.026

Quesnel, B., Gautier, P., Boulvais, P., Cathelineau, M., Maurizot, P., Cluzel, D., Ulrich, M., Guillot, S., Lesimple, S., & Couteau, C. (2013), Syn-tectonic, meteoric water–derived carbonation of the New Caledonia peridotite nappe. *Geology, 41*(10), 1063-1066. doi: 10.1130/G34531.1

Quesnel, B., Boulvais, P., Gautier, P., Cathelineau, M., John, C. M., Dierick, M., Aginier, P. & Drouillet, M. (2016), Paired stable isotopes (O, C) and clumped isotope thermometry of magnesite and silica veins in the New Caledonia Peridotite Nappe. *Geochimica et Cosmochimica Acta, 183*, 234-249, 10.1016/j.gca.2016.03.021

Saldi, G. D., Jordan, G., Schott, J., and Oelkers, E. H. (2009), Magnesite growth rates as a function of temperature and saturation state. *Geochimica et Cosmochimica Acta, 73*(19): 5646-5657. doi: 10.1016/j.gca.2009.06.035

Saldi, G. D., Schott, J., Pokrovsky, O. S., Gautier, Q., and Oelkers, E. H. (2012), An experimental study of magnesite precipitation rates at neutral to alkaline conditions and 100–200 C as a function of pH, aqueous solution composition and chemical affinity. *Geochimica et Cosmochimica Acta, 83*, 93-109. doi: 10.1016/j.gca.2011.12.005

Salvatore, M. R. et al. (2018), Bulk mineralogy of the NE Syrtis and Jezero Crater regions of Mars derived through thermal infrared spectral analyses. *Icarus, 301*, 76-96.

Sanz-Montero, M. E., Cabestrero, Ó. and Sánchez-Román, M. (2019), Microbial Mg-rich carbonates in an extreme alkaline lake (Las Eras, Central Spain). *Frontiers in Microbiology, 10*(FEB), 1–15. doi: 10.3389/fmicb.2019.00148.

Sanz-Montero, M. E. and Rodríguez-Aranda, J. P. (2012), Magnesite formation by microbial activity: Evidence from a Miocene hypersaline lake, *Sedimentary Geology, 263*, 6–15. doi: 10.1016/j.sedgeo.2011.08.004.

Sasselov, D. D., Grotzinger, J. P., & Sutherland, J. D. (2020), The origin of life as a planetary phenomenon. *Science Advances*, *6*(6), eaax3419. doi: 10.1126/sciadv.aax3419

Sayles, F. L., and W. S. Fyfe. (1973), The crystallization of magnesite from aqueous solution. *Geochimica et Cosmochimica Acta, 37*(1), 87-99. doi: 10.1016/0016-7037(73)90246-9

Schaef, H. T., Windisch Jr, C. F., McGrail, B. P., Martin, P. F., and Rosso, K. M. (2011), Brucite [Mg (OH2)] carbonation in wet supercritical CO2: An in situ high pressure X-ray diffraction study. *Geochimica et Cosmochimica Acta, 75*(23), 7458-7471.

Schandl E. S. and Wicks F. J. (1993) Carbonate and associated alteration of ultramafic and rhyolitic rocks at the Hemingway Property, Kidd Creek volcanic complex, Timmins, Ontario. *Economic Geology, 88*, 1615-1635.

Scheller, E. L., & Ehlmann, B. L. (2020), Composition, Stratigraphy, and Geological History of the Noachian Basement Surrounding the Isidis Impact Basin. *Journal of Geophysical Research: Planets,* e2019JE006190.

Scheller, E. L. (2022). A multi-disciplinary approach: How aqueous minerals hold the key to understanding the climate and habitability of terrestrial planets. Chapter 4. PhD thesis. Caltech.

Schroll, E. (2002), Genesis of magnesite deposits in the view of isotope geochemistry. *Boletim Paranaense de Geociencias, 50*.

Searle, M., & Cox, J. (1999), Tectonic setting, origin, and obduction of the Oman ophiolite. *Geological Society of America Bulletin*, *111*(1), 104-122. doi: 10.1130/0016 7606(1999)111<0104:TSOAOO>2.3.CO;2

Sharma, S. D., Patil, D. J., Gopalan, K., (2002), Temperature dependence of oxygen isotope fractionation of CO2 from magnesite-phosphoric acid reaction. *Geochimica et Cosmochimica Acta, 66*, 589-593. doi: 10.1016/S0016-7037(01)00833-X

Shirokova, L. S., Mavromatis, V., Bundeleva, I. A., Pokrovsky, O. S., Bénézeth, P., Gérard, E., Pearce, C. R. and Oelkers, E. H. (2013), Using Mg isotopes to trace cyanobacterially mediated magnesium carbonate precipitation in alkaline lakes. *Aquatic Geochemistry, 19*(1), 1-24. doi: 10.1007/s10498-012-9174-3

Śliwiński, M. G., Kitajima, K., Spicuzza, M. J., Orland, I. J., Ishida, A., Fournelle, J. H., Valley, J. W., (2018), SIMS bias on isotope ratios in Ca-Mg-Fe carbonates (part III): δ18O and δ13C matrix effects along the magnesite–siderite solid-solution series. *Geostandards and Geoanalytical Research, 42*, 49–76. doi: 10.1111/ggr.12194

Smit, M. A., Bröcker, M. and Scherer, E. E. (2008), Aragonite and magnesite in eclogites from the Jæren nappe, SW Norway: Disequilibrium in the system CaCO3-MgCO3 and petrological implications, *Journal of Metamorphic Geology, 26*(9), 959–979. doi: 10.1111/j.1525-1314.2008.00795.x.

Stack, K. M. et al. (2020), Photogeologic Map of the Perseverance Rover Field Site in Jezero Crater Constructed by the Mars 2020 Science Team. *Space Science Reviews*, *216*(8), 1-47.

Staudt, W. J., Oswald, E. J., & Schoonen, M. A. (1993). Determination of sodium, chloride and sulfate in dolomites: A new technique to constrain the composition of dolomitizing fluids. *Chemical Geology*, *107*(1-2), 97-109.

Stolper, D. A., Eiler, J. M., (2015), The kinetics of solid-state isotope-exchange reactions for clumped isotopes: A study of inorganic calcites and apatites from natural and experimental samples. *American Journal of Science, 315,* 363–411. doi: 10.2475/05.2015.01

Streit, E., Kelemen, P., Eiler, J., (2012), Coexisting serpentine and quartz from carbonate-bearing serpentinized peridotite in the Samail Ophiolite, Oman. *Contributions to Mineralogy and Petrology, 164*, 821–837. doi: 10.1007/s00410-012-0775-z

Stumm, W. and James, M. (1996). Aquatic chemistry: Chemical equilibria and rates in natural waters. New York: Wiley.

Thomas, N. H., Ehlmann, B. L., Meslin, P. Y., Rapin, W., Anderson, D. E., Rivera-Hernández, F., Forni, O., Schroder, S., Cousin, A., Mangold, N., Gellert, R., Gasnault, O., Wiens, R. C. (2019). Mars Science Laboratory observations of chloride salts in Gale crater, Mars. *Geophysical Research Letters*, *46*(19), 10754-10763. doi: 10.1029/2019GL082764

Thompson, J. B. and Ferris, F. G. (1990), Cyanobacterial precipitation of gypsum, calcite, and magnesite from natural alkaline lake water. *Geology, 18*, 995–998. doi: 10.1016/j.cossms.2010.07.001.

Tipper, E. T., Galy, A., Gaillardet, J., Bickle, M. J., Elderfield, H. and Carder, E. A. (2006), The magnesium isotope budget of the modern ocean: Constraints from riverine magnesium isotope ratios. *Earth and Planetary Science Letters*, *250*(1-2), 241-253. doi: 10.1016/j.epsl.2006.07.037

Tornabene, L. L., Moersch, J. E., Mcsween, H. Y., Hamilton, V. E., Piatek, J. L., Christensen, P. R. (2008), Surface and crater-exposed lithologic units of the Isidis Basin as mapped by coanalysis of THEMIS and TES derived data products. *Journal of Geophysical Research, 113*. doi: 10.1029/2007je002988

Tosca, N. J. et al. (2005), Geochemical modeling of evaporation processes on Mars: Insight from the sedimentary record at Meridiani Planum. *Earth and Planetary Science Letters*, *240*(1), 122 148. doi: 10.1016/j.epsl.2005.09.042

Toulkeridis, T., Peucker-Ehrenbrink, B., Clauer, N., Kröner, A., Schidlowski, M., & Todt, W. (2010), Pb–Pb age, stable isotope and chemical composition of Archaean magnesite, Barberton

Greenstone Belt, South Africa. *Journal of the Geological Society*, *167*(5), 943-952. doi: 10.1144/0016-76492009-140

Treiman A. H., Amundsen. H. E. F., Blake D. F., and Bunch T. (2002), Hydrothermal origin for carbonate globules in Martian meteorite ALH84001: A terrestrial analogue from Spitsbergen (Norway). *Earth and Planetary Science Letters, 204*, 323-332.

Ulrich, M. et al. (2014), Dissolution–precipitation processes governing the carbonation and silicification of the serpentinite sole of the New Caledonia ophiolite. *Contributions to Mineralogy and Petrology*, *167*(1), 952.

Valley, J. W. (1997), Low-temperature carbonate concretions in the Martian meteorite ALH84001: evidence from stable isotopes and mineralogy. *Science, 275*, 1633–1638. doi: 10.1126/science.275.5306.1633

van Dijk, J., Fernandez, A., Storck, J. C., White, T. S., Lever, M., Müller, I. A., Bishop, S., Seifert, R. F., Driese, S. G., Krylov, A., Ludvigson, G. A., Turchyn, A. V., Lin, C. Y., Wittkop, C., Bernasconi, S. M., (2019), Experimental calibration of clumped isotopes in siderite between 8.5 and 62 °C and its application as paleo-thermometer in paleosols. *Geochimica et Cosmochimica Acta, 254*, 1–20. doi: 10.1016/j.gca.2019.03.018

Vasconcelos, P., Farley, K., Malespin, C., Mahaffy, P., Ming, D., McLennan, S., Hurowitz, J., Rice, M. S., (2016), Discordant K-Ar and young exposure dates for the Windjana sandstone, Kimberley, Gale Crater, Mars. *Journal of Geophysical Research: Planets, 121*, 2176–2192. doi: 10.1002/2016JE005017

Walker, J. C., Hays, P. B., & Kasting, J. F., (1981), A negative feedback mechanism for the long-term stabilization of Earth's surface temperature. *Journal of Geophysical Research: Oceans*, *86*(C10), 9776-9782. doi: 10.1029/JC086iC10p09776

Walter, M. R., Golubic, S., & Preiss, W. V. (1973), Recent stromatolites from hydromagnesite and aragonite depositing lakes near the Coorong Lagoon, South Australia. *Journal of Sedimentary Research*, *43*(4), 1021-1030.

Warren, J. K. (1990), Sedimentology and mineralogy of dolomitic Coorong lakes, South Australia. *Journal of Sedimentary Research*, *60*(6), 843-858.

Wasylenki, L. E., Dove, P. M. and De Yoreo, J. J., (2005). Effects of temperature and transport conditions on calcite growth in the presence of Mg2+: Implications for paleothermometry. *Geochimica et Cosmochimica Acta, 69*(17), 4227-4236. doi: 10.1016/j.gca.2005.04.006

Webster, C. R., Mahaffy, P. R., Flesch, G. J., Niles, P. B., Jones, J. H., Leshin, L. A., Atreya, S. K., Stern, J. C., Christensen, L. E., Owen, T., Franz, H., Pepin, R. O., Steele, A., & the SAM Science Team, (2013), Isotope ratios of H, C, and O in CO2 and H2O of the Martian atmosphere. *Science,*

341(6143), 260-263. doi: 10.1126/science.1237961

Westall, F., Foucher, F., Bost, N., Bertrand, M., Loizeau, D., Vago, J. L., Kminek, G., Gaboyer, F., Campbell, K.A., Bréhéret, J.-G., Gautret, P. and Cockell C. S. (2015), Biosignatures on Mars: What, where, and how? Implications for the search for martian life. *Astrobiology*, *15*(11), 998 1029. doi: 10.1089/ast.2015.1374

Wieler, R., (2002), Cosmic-ray-produced noble gases in meteorites. *Reviews in Mineralogy and Geochemistry, 47*, 125–170. doi: 10.2138/rmg.2002.47.5

Williford, K. H., Farley, K. A., Stack, K. M., Allwood, A. C., Beaty, D., Beegle, L. W., Bhartia, R., Brown, A. J., Juarez, M. de la T., Hamran, S.-E., Hecht, M. H., Hurowitz, J. A., Rodriguez Manfredi, J. A., Maurice, S., Milkovich, S., Wiens, R. C., 2018. The NASA Mars 2020 Rover Mission and the Search for Extraterrestrial Life. *Habitability Life Mars*, doi: 10.1016/B978-0-12-8099353.00010-4

Wright, I., Grady, M. M. & Pillinger, C (1992), Chassigny and the nakhlites: carbon-bearing components and their relationship to Martian environmental conditions. *Geochimica et Cosmochimica Acta 56*, 817-826. doi: 10.1016/0016-7037(92)90100-W

Xu, Jie, Chao Yan, Fangfu Zhang, Hiromi Konishi, Huifang Xu, and H. Henry Teng. (2013), Testing the cation-hydration effect on the crystallization of Ca–Mg–CO3 systems. *Proceedings of the National Academy of Sciences, 110*(44), 17750-17755. doi: 10.1073/pnas.1307612110

Yang, J., Godard, G., Kienast, J. R., Lu, Y., & Sun, J. (1993). Ultrahigh-pressure (60 Kbar) magnesite bearing garnet peridotites from northeastern Jiangsu, China. *The Journal of Geology, 101*(5), 541-554. doi: 10.1086/648248

Yiou, F., Raisbeck, G.M., Klein, J., Middleton, R., (1984), 26Al/10Be in terrestrial impact glasses. *Journal of Non-Crystalline Solids, Proceedings of the International Conference on Glass in Planetary and Geological Phenomena, 67*, 503–509. doi: 10.1016/0022-3093(84)90172-8

Zachmann, D. W., & Johannes, W. (1989), Cryptocrystalline magnesite. *Magnesite, Monograph Series on Mineral Deposits*, *28*, 15-28.

Zachos, J., Pagani, M., Sloan, L., Thomas, E., & Billups, K. (2001), Trends, rhythms, and aberrations in global climate 65 Ma to present. *Science*, *292*(5517), 686-693.

Zaitsev, A. N., Sitnikova, M. A., Subbotin, V. V., Fernández-Suárez, J., Jeffries, T. E., & Wall, F. (2004), Sallanlatvi complex—a rare example of magnesite and siderite carbonatites. *Phoscorites and carbonatites from mantle to mine: the key example of the Kola Alkaline Province. Mineralogical Society, London*, 201-245.

Zedef, V. et al. (2000), Genesis of vein stockwork and sedimentary magnesite and hydromagnesite deposits in the ultramafic terranes of southwestern Turkey: A stable isotope study, *Economic Geology, 95*(2), 429–445. doi: 10.2113/gsecongeo.95.2.429.

Zhang, R. Y. and Liou, J. G. (1994), Significance of magnesite paragenesis in ultrahigh-pressure metamorphic rocks. *American Mineralogist, 79*, 397–400. doi: 10.1016/j.cossms.2010.07.001.

Zhang, P., Anderson, H. L., Kelly, J. W., Krumhansl, J. L., and Papenguth, H. W.. (2000), Kinetics and mechanisms of formation of magnesite from hydromagnesite in brine. No. SAND99-1946J. Sandia National Labs., Albuquerque, NM (US); Sandia National Labs., Livermore, CA (US).

Zhang, Q. (1988). Early Proterozoic tectonic styles and associated mineral deposits of the North China platform. *Precambrian Research*, *39*(1-2), 1-29.

Zheng, Y.-F., (1999), Oxygen isotope fractionation in carbonate and sulfate minerals. *Geochemical Journal, 33,* 109–126. doi: 10.2343/geochemj.33.109

Guttulatic calcite: A carbonate microtexture that reveals frigid formation conditions

Eva L. Scheller[1], John Grotzinger[1], and Miquela Ingalls[1,2]

[1] Division of Geological and Planetary Sciences, California Institute of Technology, Pasadena, CA 91106, US

[2] Department of Geosciences, Pennsylvania State University, State College, PA 16801, US

4.1 Abstract

The paragenesis of carbonate pseudomorphic textures in the rock record inferred to represent replaced metastable ikaite ($CaCO_3 \cdot 6H_2O$), which forms at frigid temperatures, is uncertain. Petrographic analysis of Mono Lake Pleistocene tufas allowed recognition of a distinctive calcite microtexture, termed guttulatic calcite, that forms during carbonate dehydration and is diagnostic for precursor ikaite. The texture is characterized by pseudo-hexagonal or spherical low-Mg cores, likely formed initially by vaterite, with an ellipsoidal overgrowth, and a secondary high-Mg sparry or micritic cement. Observations of Mono Lake ikaite pseudomorphs, combined with a review of more ancient examples, indicate that guttulatic texture records carbonate dehydration of precursor ikaite and can be used to infer frigid paleotemperatures.

4.2 Introduction

Accurate reconstructions of past oscillations in seawater composition requires correctly identifying primary mineralogy and diagenetic overprints in the marine carbonate record based on carbonate textures (e.g., Stanley & Hardie, 1998; Grotzinger and Read, 1986). Ikaite ($CaCO_3 \cdot 6H_2O$) is a hydrated carbonate that was initially discovered in Ikka Fjord, Greenland (Buchardt et al., 2001) and subsequently reported from Antarctic and Arctic marine environments (Suess et al., 1982), and alkaline lakes of Patagonia and western North America, including Mono Lake, California (Bischoff et al., 1993b; Council & Bennett, 1993). Although experimental results show that high concentrations of Mg^{2+} and PO_4^{3-} or high pH may enable ikaite nucleation at up to 12 to 35°C (Stockmann et al., 2017; Purgstaller et al., 2017; Tollefsen et al., 2020), ikaite is metastable at these temperatures due to an increase in solubility with temperature (Bischoff et al., 1993a). Ikaite crystals have been observed to form naturally only at <9°C (Huggett et al., 2005; Field et al., 2017), even in highly alkaline and P-rich water (e.g. Mono Lake, pH~10; Bischoff et al., 1993b; Council & Bennett, 1993). When heated, ikaite loses its structural waters and transforms into a variety of Ca-carbonate polymorphs, including intermediate products of monohydrocalcite, vaterite and, ultimately, calcite (Tang et al., 2009; Sanchez-Pastor et al., 2016; Purgstaller et al., 2017; Stockmann et al., 2018; Tollefsen et al., 2020).

Putative ikaite pseudomorphs of predominantly low-Mg calcite, known as "glendonite," are argued to be a proxy for past cold depositional water environments (De Lurio & Frakes, 1999; Selleck et al., 2007; Swainson & Hammond, 2001). For example, Neoproterozoic glendonite has been used as evidence for near-freezing marine temperatures during, between, and after global glaciations (Dempster & Jess, 2015; James et al., 2005; Wang et al., 2020). "Glendonite" texture has no formal definition, although it is typically inferred to be an ikaite pseudomorph sometimes marked by cm-scale stellate crystals (e.g. Selleck et al., 2007). Some of these may be pseudomorphs after evaporite minerals that also form stellate or bipyramidal crystals (e.g. Jafarzadeh & Burnham, 1992). Modern ikaite forms a broad range of
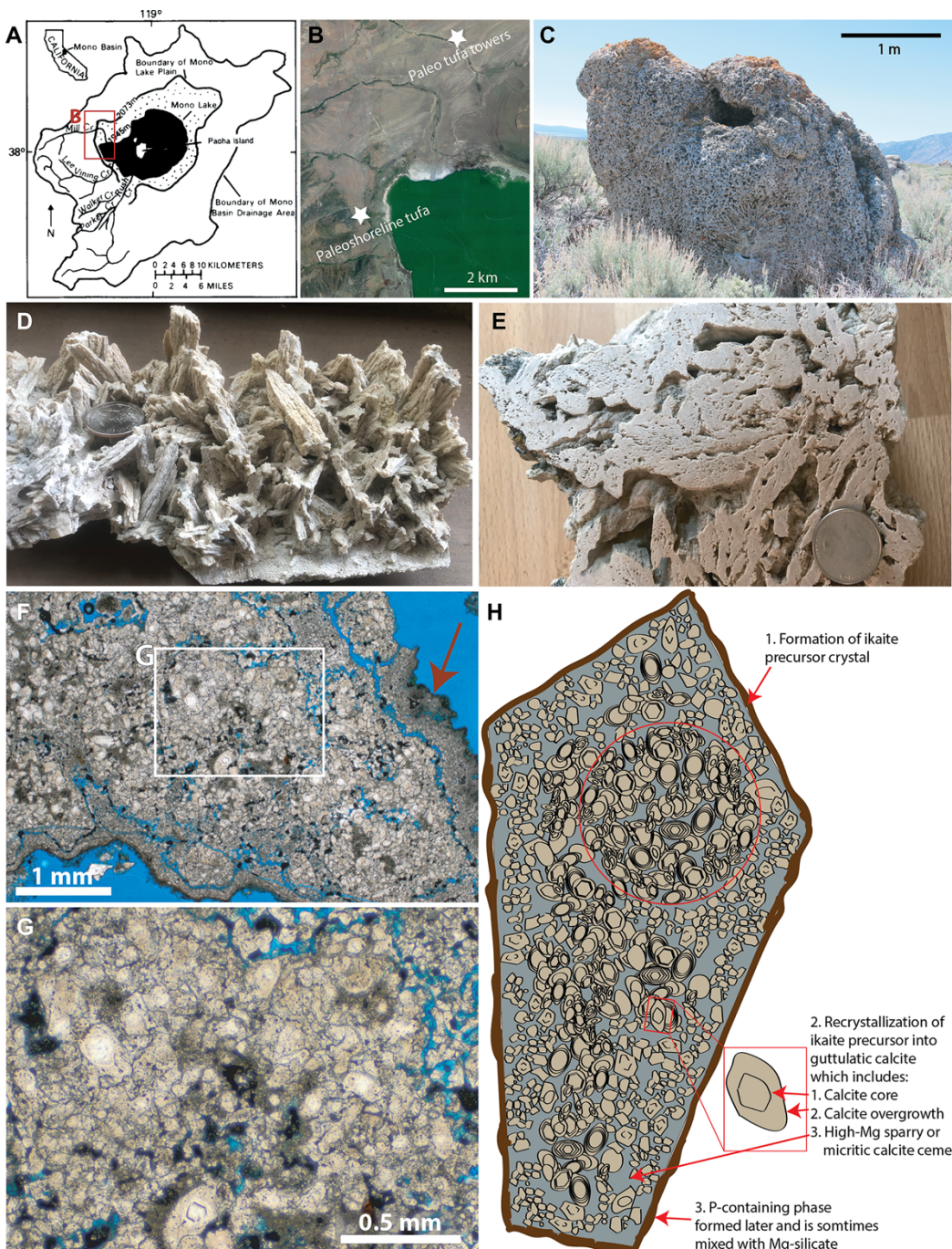
Fig. 4.1: Study area and ikaite pseudomorph textures. (A) Map of the Mono Lake study area (California, USA) adapted from Benson et al. (1990). Red box indicates location of (B) Google Earth™ map; stars depict sampling locations. (C) Field image of paleo tufa tower with thinolite tufas. (D) Example of intact thinolite tufas from paleo shoreline deposits. (E) Slab of thinolite tufa (sample N6) sampled from the location in C. Note the absence of stellate crystal morphology despite being reported as ikaite pseudomorphs. For scale in D–C, coin is 24.26 mm in diameter. (F) Thin section image of thinolite pseudomorphs with guttulatic calcite microtexture in plane-polarized light from sample in panel E. Dark phosphorus-bearing microcrystalline phase is coating the crystal (red arrow). White box indicates area shown in (G), where close-up shows calcite cores with overgrowths in a mosaic cemented by sparry or micritic calcite. (H) Drawing depicting the representative relationships between three calcite fabrics, Mg-silicate, and phosphorus-bearing phase. Red circle depicts position of final texture in Figure 4B.

123

morphologies including stellate, bi-pyramidal, prismatic, radial bladed, or "thinolite" crystals, in addition to massive microcrystalline textures in porous tufas, and speleothem crusts. Many of these macrotextures are undifferentiable from anhydrous carbonate tufa (see later sections). Therefore, a refined understanding of pseudomorphic microtextural paragenesis from ikaite dehydration is required to confidently identify former ikaite and infer primary cold-water temperatures. In this study, we show that calcite pseudomorphs of former ikaite display a characteristic microtexture – here termed "guttulatic"– making it a stronger proxy for recognizing ikaite dehydration within the carbonate record that relies neither on preservation of primary mineralogy or on precursor ikaite having formed cm-scale stellate crystals.

4.3 Geological setting and methods

Water column carbonate precipitation is negligible in hyperalkaline Mono Lake due to depletion of Ca (~ 4 ppm) (Fig. 4.1; Dunn, 1953). However, carbonates precipitate rapidly as either shoreline deposits or tufa towers where Ca-rich streams or groundwater mix with lake waters (Bischoff et al., 1993b; Dunn, 1953). Tufas are classified based on macroscopic textures: 1) thinolite tufa comprises radiating cm-scale crystals regarded as ikaite pseudomorphs (Shearman et al., 1989; Whiticar & Suess, 1998), 2) dendritic tufa forms branching structures that have colloform or shrubby appearance, and 3) lithoid tufa has a massive appearance (Dunn, 1953). Notably, fine-grained ikaite forms along the shoreline of Mono Lake during winter months and subsequently decomposes to anhydrous Ca-carbonate during seasonal warming (Bischoff et al., 1993b; Council & Bennett, 1993).

The three tufa textures characterize shoreline and tufa tower deposits that formed during high-stands of Pleistocene Lake Russell above present-day lake level (Benson et al., 1990). We studied thinolite tufa, dendritic tufa, and fabrics of thinolite-dendritic mixtures (Fig. 4.1) from both Pleistocene high-stand shorelines (n=19) and towers (n=5; Fig. 4.1). The described carbonates were confirmed to be calcite via X-ray powder diffraction. In addition, the carbonate samples were prepared as polished thin sections and studied by optical microscopy and field emission scanning electron microscopy (SEM).

Seven thin sections were studied using ZEISS 1550VP Field Emission SEM facility at Caltech. These included 2 thinolite tufa samples, 3 dendrite tufa samples, and 2 transition samples in which both thinolite and dendrite tufas are recorded. The 7 thin sections were carbon coated prior to analysis. We analyzed all of these 7 samples by a combination of BSE images and SEM-EDS elemental maps. Additionally, we collected point spectra in different phases of each BSE and SEM-EDS elemental map scene. The AZtec software was used to convert the EDS spectra into elemental wt%. These results are considered semi-quantitative as for example light elements, such as carbon, cannot be measured with EDS at the SEM facility at Caltech. Elemental ratios are considered more precise than absolute abundances as these will be the same regardless of the amount of any elements that were not measured. Therefore, we

converted elemental wt% into relative molar abundances of each element in order to calculate molar ratios and mole fractionations/percentages. Mg mole% were calculated as:

$$Mg \ mole\% = \frac{n_{Mg}}{n_{Mg} + n_{Ca}} * 100$$

Here n_{Mg} and n_{Ca} are the molar abundances of Mg and Ca, respectively. A total number of 46 point spectra and 27 point spectra were collected for type 1-2 calcite and type 3 calcite, respectively, within the
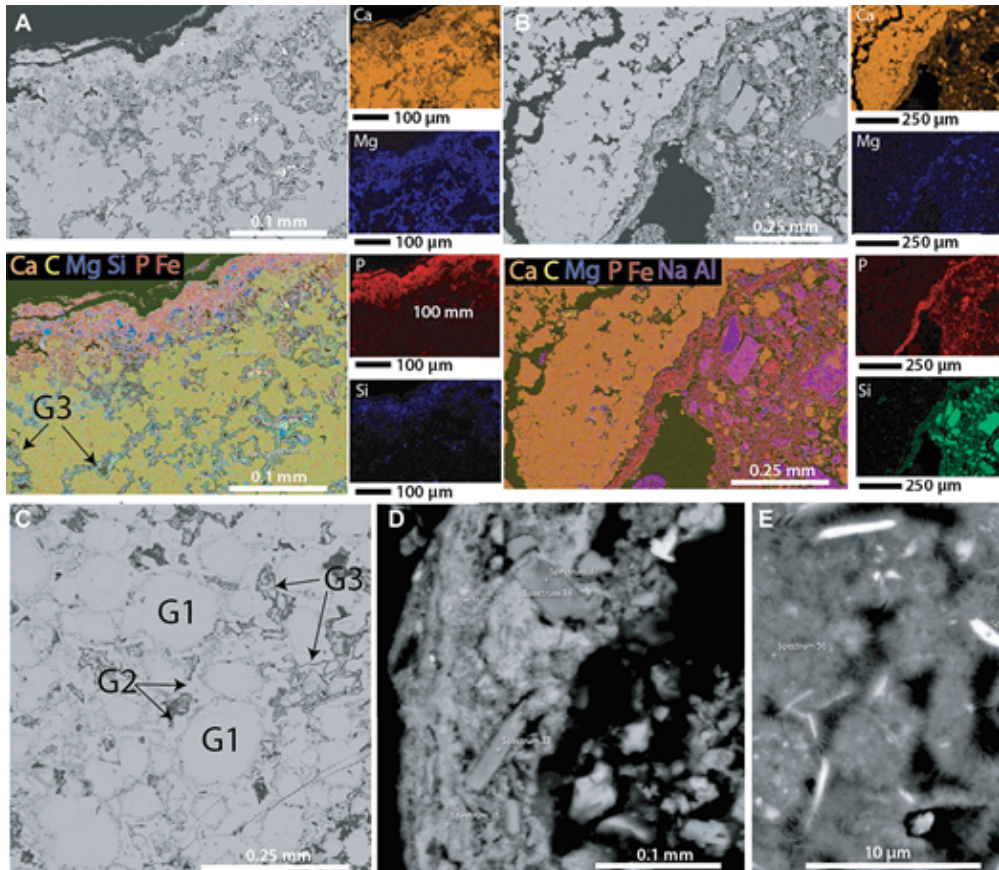
Fig. 4.2: BSE and SEM-EDS analysis of ikaite pseudomorphs. (A) Back-scattered electron (BSE) images and scanning electron microscope-energy-dispersive spectroscopy (SEM-EDS) elemental maps for sample N6 of thinolitic tufa from Mono Lake, California, USA (Fig. 1E). Consolidated EDS map shows the presence of three major chemical phases: low-Mg calcite (yellow), high-Mg calcite (green-blue), and a phosphorus-bearing phase that also contains Fe, Ca, and Si (red). (B) BSE images and SEM-EDS elemental maps for a different part of N6 (shown in Fig. 1E). The consolidated, layered EDS map shows the presence of calcite (orange) without the presence of surrounding high-Mg calcite. Here, the P-bearing phase (red) has formed around and/or entrained lithic fragments that are rich in Si, Na, and Al and presumably related to the surrounding bedrock. (C) BSE image of guttulatic texture shows low-Mg calcite cores (G1), overgrowths (G2), and high-Mg calcite cements (G3). (D) Close up BSE image of the P-bearing phase. Notice the microcrystalline texture and heterogeneity of the P-bearing phase that coats lithic fragments. (E) Close up BSE image of microcrystalline Mg-silicates that encloses bright lithic fragments occasionally found within P-bearing phase (e.g., dark blue in panel A).

4 thinolite-containing samples (summarized in Appendix A, Table S1). A total of 19 point spectra and a total of 28 point spectra were collected for the Mg-silicate and the phosphorous-bearing phase within the 4 thinolite-containing samples. Last, a total of 33 point spectra were collected from dendritic tufa calcite (summarized in Appendix A, Table S1).

SEM-EDS of dendritic tufas are included in Appendix A, Fig. S1 for comparison with Fig. 4.3 in the main manuscript that shows SEM-EDS images of thinolite tufas. Porosity between calcite fans and spherulites is filled by micritic calcite of the same composition as fans and spherulites (Appendix A, Fig. S1). High-Mg calcite is only very rarely observed within pore spaces of dendritic calcite (Appendix A, Fig. S1). Instead, the edges of fans and spherulites are often coated by microcrystalline Mg-silicates similar to the ones observed in the thinolitic tufa (Appendix A, Fig. S1). The stoichiometry of the Mg-silicates are generally consistent with Mg-clays, including stevensite/saponite, sepiolite, and kerolite, that are expected to have Mg/Si ratios of 0.75, 0.75, and 0.67, respectively. Substitutions of Fe and Ca in the Mg-site and Al in both the Mg- and Si-sites complicates the calculations of clay mineral stoichiometry. Variations of $(Mg + Fe)/(Si + Al)$ ratios in Appendix A, Table S2 yield approximate ranges of 0.6-0.9 (n=19), consistent with expected ratios for the Mg-clay suite.

4.4 Textures and composition

Thinolite tufas from Mono Lake consist of elongate crystals of 1 to 20 cm in length and a few mm to cm in width. Each cm-scale crystal is pseudomorphed by a mosaic of beige or brown calcite crystals (Fig. 4.1F). These calcite pseudomorphs have a ~10-100 μm pseudo-hexagonal or spherical core with a spherical, ellipsoidal, or anhedral shaped syntaxial calcite overgrowth (Fig. 4.1-3). Rhombohedral cores are rarely present. The syntaxial overgrowth records zones that express hexagonal crystal morphology close to the core and progressively evolve to ellipsoidal morphology further away from the core, often with accumulation of fluid and solid inclusions at the growth zone boundaries (Fig. 4.3). No chemical difference was identified between cores and overgrowth through SEM backscatter electron (BSE) imaging and energy dispersive spectroscopy (EDS) analyses (Fig. 4.2). Core and overgrowth calcite generally have low Mg mole% of ≤17.6% with an average of 3.5±4.0% (n=46) based on semi-quantitative calculations from EDS-spectra (Appendix A). In between overgrowth calcite, thinolite crystals are filled with high-Mg micritic or sparry calcite cements that have a Mg mole% of 10.6% to 50.0% with an average of 29.2±9.6% (n=27; Fig. 4.2-3).

The edges of the cm-scale thinolite crystals are coated with a μm-thick, dark, texturally heterogenous, optically opaque, microcrystalline or possibly amorphous layer that is enriched in phosphorus (Fig. 4.2). This yet undetermined P-bearing phase appears to be partly composed of silicates with P/Si of 1.0±0.5 (n=28). The P-bearing phase contains significant Ca with Ca/Si ratios of 2.5±1.2 (n=28) and Ca/P ratios of 2.7±1.4 (n=28) but only minor Mg. Furthermore, these intercrystalline spaces

may be filled with micritic low-Mg calcite and/or microcrystalline Mg-silicates (Fig. 4.2). The Mg-silicates measured with SEM-EDS are consistent with Mg-clays (Appendix A).

4.5 Discussion

4.5.1 Paragenetic sequences

Ancient and sub-recent ikaite pseudomorphic textures identified in published photomicrographs show a similar microtexture as observed in Mono Lake thinolite, including cores, overgrowth, and cement in a calcite mosaic (Fig. 4.3). Petrographic analysis revealed that cores are predominantly pseudo-hexagonal and overgrowths have pseudo-hexagonal to spherical/ellipsoidal zones (Fig. 4.3). We propose a detailed

Reference	Guttulatic?	Location and age
*Jansen et al. (1987)	Yes	Zaire deep-sea fan, Africa, modern
Panel H - Larsen (1994)	Yes	Creede Fm, Colorado, US, Oligocene
*Whiticar & Suess (1998)	Yes	Mono Lake tufas, California, US, modern
*McLachlan et al. (2001)	Yes	Dwyka beds, South Africa, Permian
*Greinert & Derkachev (2004)	Yes	Sea of Okhotsk, East Siberia, modern
Panel E - Huggett et al. (2004)	Yes	Review compilation
James et al. (2005)	No	Twitya Fm, Canada, Neoproterozoic
Panel G - Selleck et al. (2007)	Yes	Wandrawandian siltstone, Sydney Basin, Permian
Panel F - Frank et al. (2008)	Yes	Marine strata, East Australia, Permian
*Geptner et al. (2013)	Yes	Marine strata, White Sea Basin, Holocene
*Teichert & Luppold (2013)	Yes	NE Gremlingen, Germany, Early Jurassic
Dempster & Jess (2015)	No	Dalradian slates, Scotland, Neoproterozoic
*Rogov et al. (2016)	Yes	Lower Cretaceous strata, NE Siberia
*Grasby et al. (2017)	Yes	Upper Deer Bay Fm and Christopher Fm, Canada, Cretaceous
*Qu et al. (2017)	Yes	Marine strata, Washington, US, Paleogene
Field et al. (2017)	No	Railway tunnel, Peak Dale, UK, modern
*Morales et al. (2017)	Yes	Five sections across Siberia, Mesozoic
Vickers et al. (2018)	Yes	Rurikfjellet Fm and Caroline Fjellet Fm, Svalbard, Lower Cretaceous
*Vasileva et al. (2019)	Yes	Marine strata, Siberia, Jurassic
Panel I - Popov et al. (2019)	Yes	Turisalu Fm and Koporiye Fm, Estonia & Russia, Ordovician
Wang et al. (2020)	No	Doushantou Fm, China, Neoproterozoic

Full references are only found in supplement

Fig. 4.3: Thin section images of ikaite pseudomorphs. (A–D) Thin section images from four samples showing typical hexagonal core with syntaxial, zoned overgrowth (white arrows) and rare examples of rhombohedral (black arrows) and spherical (green arrows) cores. (E–I) Compilation of published thin section images reported as glendonite that also show guttulatic calcite microtexture. Panel images are used with permissions from the original authors; citations are provided in the table. (E,F) Notice the characteristic pattern of a hexagonal (white arrows) or spherical (green arrows) calcite core and a semi-spherical overgrowth. (G–I) Zoomed-out views allow recognition of the characteristic tight-knit calcite mosaic (red arrows) of hexagonal and rounded cores with overgrowths. The presence of guttulatic calcite in all previously published thin sections is shown in the table.

paragenetic model for this uncommon but distinctive microtexture by comparison to recent experimental results (Fig. 4.4B). We provide two likely mechanistic transformation pathways that support models

proposed in previous studies (e.g. Vickers et al., 2018).

Ikaite heating (at 5 °C to 35°C) experiments have shown that dehydration and transformation of ikaite into spherical and rhombohedral crystals of vaterite and calcite, respectively, occurs within minutes (Tang et al., 2009; Sanchez-Pastor et al., 2016; Purgstaller et al., 2017; Tollefsen et al., 2020). Vaterite is a highly unstable, hexagonal, anhydrous Ca-carbonate polymorph that forms nano- to micron-scale spherical and hexagonal crystals in experiments and natural cold spring environments (Tang et al., 2009; Konopacka-Lyskawa et al., 2019). Vaterite transforms to calcite within minutes to days (Tang et al., 2009; Sanchez-Pastor et al., 2016; Purgstaller et al., 2017; Konopacka-Lyskawa et al., 2019). The unique pseudo-hexagonal and spherical cores within ikaite pseudomorphs are most consistent with former
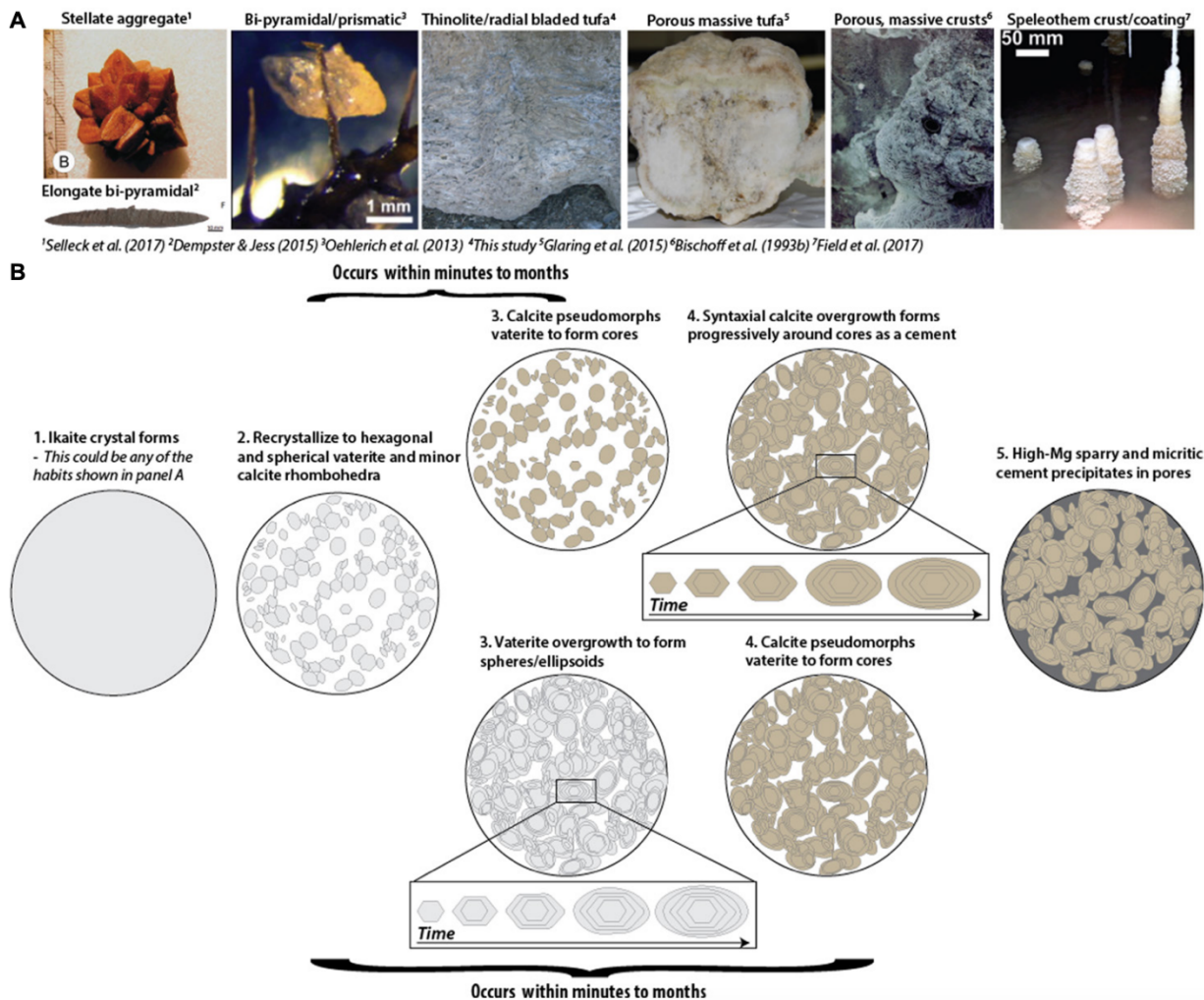
Fig. 4.4: Ikaite crystal habits and schematic of ikaite pseudomorph paragenesis. (A) Overview of natural macrohabits of ikaite crystals. Note that many are not "glendonite" stellate crystals. Images are used with permissions from the original authors; citations are provided in the figure. (B) Proposed formation model for guttulatic calcite in two different scenarios. The syntaxial overgrowth is either part of the initial spherical vaterite formation that is then recrystallized to a single crystal of calcite, or a later cement that forms around calcite pseudomorphs of vaterite cores.

vaterite pseudomorphs that are subsequently replaced by calcite (Fig. 4.4B). Rare rhombohedral cores would represent transformation to calcite directly from ikaite. The syntaxial overgrowth could form originally as vaterite growing by ostwald ripening of amorphous calcium carbonate into spherical/ellipsoidal structures (Konopacka-Lyskawa et al., 2019) with subsequent single-crystal replacement into calcite. Alternatively, the syntaxial overgrowth may be later calcite cement growing in stages. The former scenario is consistent with low-Mg calcite composition of cores and overgrowth in this study as both would be sourced from the low-Mg ikaite precursor. In other studies, overgrowths and cores differ in chemical composition, suggesting overgrowths could be products of later cementation (Vickers et al., 2018). Mg- and Fe-rich sparry calcite cements were observed more broadly within Mono Lake tufa facies and in several previous studies. These sparry cements have a later diagenetic origin that likely plays an important role in preserving the initially porous and friable pseudomorph crystal (Huggett et al., 2005; Vickers et al., 2018).

The association between ikaite pseudomorphs and microcrystalline Mg-silicates in Mono Lake tufas has not been previously observed, while the P-bearing phases have only recently been studied (Huggett et al., 2005; Ingalls et al., 2020). These phases postdate ikaite crystal growth as they coat the sides of the original ikaite crystals (Fig. 4.1F) and are not regarded as significant in the context of early ikaite transformation to calcite. Mg-silicates commonly are associated with carbonates that rapidly precipitate from high alkalinity water (e.g. Gomes et al., 2020), while the P-bearing phase is interesting due to phosphate's proposed role in promoting ikaite formation (Bischoff et al., 1993a).

4.5.2 Guttulatic calcite: A distinctive microtexture

We propose the term *guttulatic calcite* to capture the characteristic pseudomorphic ~10 to 100 μm pseudo-hexagonal or spherical calcite core, hexagonal and ellipsoidal zoned syntaxial overgrowth, and cement paragenetic sequence associated with neomorphic inversion of ikaite to vaterite and subsequently to calcite (Fig. 4.2-3). The term guttulatic is adapted after *guttula*, the Latin word for *very small droplet*, and is an appropriate descriptor for the droplet-like shape of calcite cores with overgrowth. A review of petrographic images or descriptions of microtextures associated with reported ikaite pseudomorphs shows that many examples do contain guttulatic calcite, originally described as a "microgranular mosaic," "oolitic and sparry," or "type 1-3 calcite" (Fig. 4.3). Here, we establish a correlation and distinction between guttulatic calcite and glendonite fabrics for many reported examples. We propose that guttulatic calcite is diagnostic specifically for carbonate dehydration, and that its recognition helps confidently establish former frigid conditions of primary mineral precipitation.

Significantly, several proposed Neoproterozoic ikaite pseudomorphs do not exhibit guttulatic microtexture (e.g. Dempster & Jess, 2015; James et al., 2005; Wang et al., 2020). Extensive recrystallization may have erased the guttulatic texture given that guttulatic calcite is an early diagenetic

feature which may not always be preserved. Other studies that report glendonite stellate crystal macrotextures and infer frigid paleotemperatures could also be substantiated through the petrographic search for guttalactic texture (e.g. De Lurio & Frakes, 1999; Price & Nunn, 2010). The guttulatic microtexture is unique in the context of carbonate mineral paragenesis and can be used to identify precursor ikaite and vaterite precursor in the many cases where precursor minerals did not form stellate or bipyramidal crystals (Fig. 4.4A).

4.6 Conclusion

Thinolite tufas at Mono Lake preserve a characteristic microtexture – guttulatic calcite –composed of ~10 to 100 μm sized pseudo-hexagonal or spherical cores, ellipsoidal zoned syntaxial overgrowth, and a secondary high-Mg sparry or micritic cement. These crystal pseudomorphs were later coated with Mg-silicates associated with alkaline lake conditions and a P-bearing amorphous phase; this later step may be particular to alkaline, lacustrine carbonates such as Mono Lake. Guttulatic microtexture is recognized in many, but not all, rocks described with ikaite pseudomorph macrotextures. We propose that guttulatic calcite forms during dehydration diagenesis through warming. Within minutes to months, the low-Mg calcite hexagonal and rounded cores are formed through transformation of the precursor hydrated carbonate into metastable vaterite that is subsequently transformed to calcite. Ellipsoidal calcite overgrowths form as part of initial vaterite recrystallization or as a later cement. Subsequently, high-Mg calcite cement precipitates in pores from pore waters of different chemistry. Recognition of guttulatic calcite provides evidence that hydrated carbonate precursors underwent dehydration diagenesis induced by heating after forming at frigid conditions regardless of whether the precursor formed stellate macrocrystals.

References

Benson, L. V., Currey, D. R., Dorn, R. I., Lajoie, K. R., Oviatt, C. G., Robinson, S. W., … Stine, S., 1990, Chronology of expansion and contraction of four great Basin lake systems during the past 35,000 years. *Palaeogeography, Palaeoclimatology, Palaeoecology, 78,* 241-286, https://doi.org/10.1016/0031-0182(90)90217-U.

Bischoff, J. L., Fitzpatrick, J. A., & Rosenbauer, R. J., (1993a), The solubility and stabilization of ikaite (CaCO3.6H2O) from 0° to 25°C: Environmental and paleoclimatic implications for thinolite tufa: *Journal of Geology, 101*, 21-33, https://doi.org/10.1086/648194.

Bischoff, J. L., Stine, S., Rosenbauer, R. J., Fitzpatrick, J. A., & Stafford, T. W., (1993b), Ikaite precipitation by mixing of shoreline springs and lake water, Mono Lake, California, USA. *Geochimica et Cosmochimica Acta, 57,* 3855-3865, https://doi.org/10.1016/0016-7037(93)90339-X.

Buchardt, B., Israelson, C., Seaman, P., & Stockmann, G., (2001), Ikaite tufa towers in Ikka Fjord, Southwest Greenland: Their formation by mixing of seawater and alkaline spring water. *Journal of*

Sedimentary Research, 71, 176-189, https://doi.org/10.1306/042800710176.

Council, T. C., & Bennett, P. C., (1993), Geochemistry of ikaite formation at Mono Lake, California: implications for the origin of tufa mounds. *Geology, 21,* 971-974, https://doi.org/10.1130/0091-7613(1993)021<0971:GOIFAM>2.3.CO;2.

De Lurio, J. L., & Frakes, L. A., (1999), Glendonites as a paleoenvironmental tool: Implications for early Cretaceous high latitude climates in Australia. *Geochimica et Cosmochimica Acta, 63,* 1039-1048, https://doi.org/10.1016/S0016-7037(99)00019-8.

Dempster, T., & Jess, S. A., (2015), Ikaite pseudomorphs in Neoproterozoic Dalradian slates record Earth's coldest metamorphism. *Journal of the Geological Society, 172,* 459-464, https://doi.org/10.1144/jgs2015-018.

Dunn, J. R., (1953), The origin of the deposits of tufa in Mono Lake [California]. J*ournal of Sedimentary Research, 23,* 18-23, https://doi.org/10.1306/d4269530-2b26-11d7-8648000102c1865d.

Field, L. P. et al. (2017), Unusual morphologies and the occurrence of pseudomorphs after ikaite ($CaCO_3 \cdot 6H_2O$) in fast growing, hyperalkaline speleothems. *Mineralogical Magazine, 81,* 565-589, https://doi.org/10.1180/minmag.2016.080.111.

Frank, T. D., Thomas, S. G., & Fielding, C. R., (2008), On using carbon and oxygen isotope data from glendonites as paleoenvironmental proxies: a case study from the Permian system of eastern Australia. *Journal of Sedimentary Research, 78,* 713-723.

Geptner, A. R., Vetoshkina, O. S., & Petrova, V. V., (2014), New data on the composition of stable isotopes in glendonites of the White Sea and their genesis. *Lithology and Mineral Resources, 49*, 473-490.

Glaring, M. A., Vester, J. K., Lylloff, J. E., Al-Soud, W. A., Sørensen, S. J., & Stougaard, P. (2015). Microbial diversity in a permanently cold and alkaline environment in Greenland. *PloS one*, 10(4), e0124863.

Gomes, J. P., Bunevich, R. B., Tedeschi, L. R., Tucker, M. E., & Whitaker, F. F., (2020), Facies classification and patterns of lacustrine carbonate deposition of the Barra Velha Formation, Santos Basin, Brazilian Pre-salt. *Marine and Petroleum Geology, 113,* 104176.

Greinert, J., & Derkachev, A., (2004), Glendonites and methane-derived Mg-calcites in the Sea of Okhotsk, Eastern Siberia: implications of a venting-related ikaite/glendonite formation. *Marine Geology, 204,* 129-144.

Huggett, J. M., Schultz, B. P., Shearman, D. J., & Smith, A. J., (2005), The petrology of ikaite pseudomorphs and their diagenesis. *Proceedings of the Geologists' Association, 116,* 207-220, https://doi.org/10.1016/S0016-7878(05)80042-2.

Ingalls, M., Blättler, C. L., Higgins, J. A., Magyar, J. S., Eiler, J. M., & Fischer, W. W. (2020). P/Ca in

carbonates as a proxy for alkalinity and phosphate levels. *Geophysical Research Letters*, *47*(21), e2020GL088804.

Jafarzadeh, A. A., & Burnham, C. P. (1992). Gypsum crystals in soils. *Journal of Soil Science, 43*(3), 409-420.

Jansen, J. H. F., Woensdregt, C. F., Kooistra, M. J., & Van der Gaast, S. J., (1987), Ikaite pseudomorphs in the Zaire deep-sea fan: An intermediate between calcite and porous calcite. *Geology, 15,* 245-248.

James, N. P., Narbonne, G. M., Dalrymple, R. W., & Kyser, T. K., (2005), Glendonites in Neoproterozoic low-latitude, interglacial sedimentary rocks, northwest Canada: Insights into the Cryogenian ocean and Precambrian cold-water carbonates. *Geology, 33,* 9-12, https://doi.org/10.1130/G20938.1.

Konopacka-Łyskawa, D. (2019). Synthesis methods and favorable conditions for spherical vaterite precipitation: A review. *Crystals*, *9*(4), 223.

Larsen, D., (1994), Origin and paleoenvironmental significance of calcite pseudomorphs after ikaite in the Oligocene Creede Formation, Colorado. *Journal of Sedimentary Research, 64,* 593-603.

McLachlan, I. R., Tsikos, H., & Cairncross, B., (2001), Glendonites (pseudomorphs after ikaite) in late carboniferous Marine Dwyka beds in Southern Africa. *South African Journal of Geology, 104,* 265-272.

Morales, C. et al. (2017), Glendonites track methane seepage in Mesozoic polar seas. *Geology, 45,* 503-506.

Oehlerich, M., Mayr, C., Griesshaber, E., Lücke, A., Oeckler, O. M., Ohlendorf, C., Schmahl, W. W. & Zolitschka, B. (2013). Ikaite precipitation in a lacustrine environment–implications for palaeoclimatic studies using carbonates from Laguna Potrok Aike (Patagonia, Argentina). *Quaternary Science Reviews, 71,* 46-53.

Popov, L. E., Álvaro, J. J., Holmer, L. E., Bauert, H., Ghobadi Pour, M., Dronov, A. V., … Zhang, Z., (2019), Glendonite occurrences in the Tremadocian of Baltica: first Early Palaeozoic evidence of massive ikaite precipitation at temperate latitudes. *Scientific Reports. 9,* 1-10, https://doi.org/10.1038/s41598-019-43707-4.

Price, G. D., & Nunn, E. V., (2010), Valanginian isotope variation in glendonites and belemnites from Arctic Svalbard: Transient glacial temperatures during the Cretaceous greenhouse. *Geology, 38,* 251-254, https://doi.org/10.1130/G30593.1.

Purgstaller, B., Dietzel, M., Baldermann, A., & Mavromatis, V., (2017), Control of temperature and aqueous Mg2+/Ca2+ ratio on the (trans-)formation of ikaite. *Geochimica et Cosmochimica Acta, 217,* 128-143, https://doi.org/10.1016/j.gca.2017.08.016.

Qu, Y., Teichert, B. M. A., Birgel, D., Goedert, J. L., & Peckmann, J., (2017), The prominent role of bacterial sulfate reduction in the formation of glendonite: A case study from Paleogene marine strata

of western Washington State. *Facies, 63*, 10.

Read, J. F., Grotzinger, J. P., Bova, J. A., & Koerschner, W. F. (1986). Models for generation of carbonate cycles. *Geology*, *14*(2), 107-110.

Rogov, M. A., Ershova, V. B., Shchepetova, E. V., Zakharov, V. A., Pokrovsky, B. G., & Khudoley, A. K., (2017), Earliest Cretaceous (late Berriasian) glendonites from Northeast Siberia revise the timing of initiation of transient Early Cretaceous cooling in the high latitudes. *Cretaceous Research, 71,* 102-112.

Sánchez-Pastor, N., Oehlerich, M., Astilleros, J. M., Kaliwoda, M., Mayr, C. C., Fernández-Díaz, L., & Schmahl, W. W. (2016). Crystallization of ikaite and its pseudomorphic transformation into calcite: Raman spectroscopy evidence. *Geochimica et Cosmochimica Acta*, *175*, 271-281.

Selleck, B. W., Carr, P. F., & Jones, B. G., (2007), A Review and Synthesis of Glendonites (Pseudomorphs after Ikaite) with New Data: Assessing Applicability as Recorders of Ancient Coldwater Conditions. *Journal of Sedimentary Research, 77,* 980-991, https://doi.org/10.2110/jsr.2007.087.

Shearman, D. J., McGugan, A., Stein, C., & Smith, A. J., (1989), Ikaite, CaCO 3 . 6H 2 O, precursor of the thinolites in the Quaternary tufas and tufa mounds of the Lahontan and Mono Lake Basins, western United States: *Geological Society of America Bulletin, 101,* 913-917, https://doi.org/10.1130/0016-7606(1989)101<0913:ICOPOT>2.3.CO;2.

Stanley, S. M., & Hardie, L. A., (1998), Secular oscillations in the carbonate mineralogy of reef-building and sediment-producing organisms driven by tectonically forced shifts in seawater chemistry. *Palaeogeography, Palaeoclimatology, Palaeoecology, 144,* 3-19.

Stockmann, G. et al. (2018), Control of a calcite inhibitor (phosphate) and temperature on ikaite precipitation in Ikka Fjord, southwest Greenland. *Applied Geochemistry, 89,* 11-22, https://doi.org/10.1016/j.apgeochem.2017.11.005.

Suess, E., Balzer, W., Hesse, K. F., Müller, P. J., Ungerer, C. A., Wefer, G., 1982. Calcium carbonate hexahydrate from organic-rich sediments of the Antarctic shelf: Precursors of glendonites. *Science, 216,* 1128-1131.

Swainson, I. P., & Hammond, R. P., (2001), Ikaite, CaCO3·6H2O: Cold comfort for glendonites as paleothermometers. *American Mineralogist, 86,* 1530-1533, https://doi.org/10.2138/am-2001-11-1223.

Tang, C. C., Thompson, S. P., Parker, J. E., Lennie, A. R., Azough, F., & Kato, K. (2009). The ikaite-to-vaterite transformation: new evidence from diffraction and imaging. *Journal of Applied Crystallography*, *42*(2), 225-233.

Teichert, B. M. A., & Luppold, F. W., (2013), Glendonites from an Early Jurassic methane seep—

Climate or methane indicators? *Palaeogeography, Palaeoclimatology, Palaeoecology, 390*, 81-93.

Tollefsen, E., Balic-Zunic, T., Mörth, C. M., Brüchert, V., Lee, C. C., & Skelton, A., (2020), Ikaite nucleation at 35 C challenges the use of glendonite as a paleotemperature indicator. *Scientific Reports*, *10,* 1-10.

Vasileva, K. Y., Rogov, M. A., Ershova, V. B., & Pokrovsky, B. G., (2019), New results of stable isotope and petrographic studies of Jurassic glendonites from Siberia. *Geologiska Föreningens i Stockholm Förhandlingar, 141*, 225-232.

Vickers, M., Watkinson, M., Price, G. D., & Jerrett, R., (2018), An improved model for the ikaite-glendonite transformation: Evidence from the lower cretaceous of spitsbergen, Svalbard. *Norsk Geologisk Tidsskrift*, https://doi.org/10.17850/njg98-1-01.

Wang, Z. et al. (2020), Wide but not ubiquitous distribution of glendonite in the Doushantuo Formation, South China: Implications for Ediacaran climate. *Precambrian Research, 338*, https://doi.org/10.1016/j.precamres.2019.105586.

Whiticar, M. J., & Suess, E. (1998). The Cold Carbonate Connection Between Mono Lake, California and the Bransfield Strait, Antarctica. *Aquatic Geochemistry*, *4*(3), 429-454.

Chapter 5

The mechanisms and stable-isotope effects of transforming hydrated carbonate into calcite pseudomorphs

Eva L. Scheller[1], Miquela Ingalls[2], John Eiler[1], John Grotzinger[1], and Uri Ryb[3]

[1]Division of Geological and Planetary Sciences, California Institute of Technology, Pasadena

[2]Department of Geosciences, Pennsylvania State University

[3]Institute of Earth Sciences, The Hebrew University of Jerusalem

5.1 Abstract

Ikaite ($CaCO_3 \cdot 6H_2O$) and monohydrocalcite ($CaCO_3 \cdot H_2O$; MHC) are hydrated carbonates that form at frigid (<9°C) temperatures. During gradual heating and dehydration, the more thermodynamically stable anhydrous calcite commonly replaces and pseudomorphs ikaite and MHC. Previously, ikaite pseudomorphs have been identified in the sedimentary record by characteristic replacive macro- and microtextures and interpreted as evidence for near-freezing marine paleotemperatures. Specifically, ikaite pseudomorphs have been used as geological evidence of global cold intervals in Earth history, but prior to this study, we lacked an understanding of isotopic behavior during mineral dehydration necessary to interpret isotopic compositions of such fabrics. Do the stable isotopic compositions of ikaite pseudomorphs preserve the primary environmental signal or are they altered during mineral transformation? Here, we propose a new isotopic framework for using oxygen ($\delta^{18}O_{CARB}$), carbon ($\delta^{13}C_{CARB}$), and clumped (Δ_{47}) isotope values of ikaite pseudomorphs as a paleoclimate proxy.

Isotopic analyses of carbonates from a sample of MHC yields compositions consistent with known growth conditions and parental waters. Through heating experiments of MHC from Ikka Fjord, we find that $\delta^{18}O_{CARB}$ and Δ_{47} decreased while $\delta^{13}C_{CARB}$ remained nearly unchanged during progressive dehydration. Model fits to experimental data suggest that the isotopic changes reflected partial re-equilibration of $\delta^{18}O_{CARB}$ and Δ_{47} towards the new diagenetic conditions due to oxygen equilibrium exchange between CO_3^{2-} and H_2O within the MHC lattice. However, this process is limited in our experiments (i.e., never reaches full equilibrium), an effect we argue reflects the fact that structural H_2O escapes the solid carbonate structure faster than isotopic exchange can reach equilibrium. In addition, labelled water experiments demonstrated that oxygen isotopic exchange also occurs with secondary external waters during dehydration, with $\delta^{18}O_{CARB}$ partially modified by labelled water $\delta^{18}O_{fluid}$. We apply this new framework to interpret the isotopic compositions of Pleistocene ikaite pseudomorphs from Mono Lake (CA, USA), high stand deposits which have undergone subaerial dehydration but not burial heating. Specifically, dehydration diagenetic overprinting of Δ_{47} can explain the warm temperatures 6-26°C recorded by ikaite pseudomorphs. In addition, precursor ikaite precipitation at low temperatures explains the higher $\delta^{18}O_{CARB}$ recorded by ikaite pseudomorph tufas compared to other calcite tufas in Pleistocene Mono Lake deposits. We consider the results of our controlled heating experiments to correct for the alteration of isotope signals during the dehydration of Mono Lake ikaite, and show that approximately coeval precursor ikaite and other calcite tufas in Pleistocene Mono Lake formed from similar fluid compositions but at different water temperatures. These characteristics suggest that primary ikaite formed during the winter and transformed through warming, while calcite tufas formed during warmer seasons. In summary, we show that the isotopic composition of ikaite and MHC pseudomorphs can be used for quantitative paleoclimate reconstruction of water temperature, $\delta^{18}O_{CARB}$, $\delta^{18}O_{fluid}$, and $\delta^{13}C_{CARB}$.

5.2. Introduction

Ikaite (CaCO$_3 \cdot$ 6H$_2$O) and monohydrocalcite (CaCO$_3 \cdot$H$_2$O; MHC) are hydrated carbonates that form at low temperatures close to the freezing point of water and are metastable under Earth surface conditions. When heated, ikaite and MHC transform into stable calcium carbonate phases (i.e. calcite, aragonite, and vaterite) (Tang et al., 2009; Sanchez-Pastor et al., 2016; Purgstaller et al., 2017; Stockmann et al., 2018; Tollefsen et al., 2020; Scheller et al., 2021). Ikaite and MHC were first identified in Ikka Fjord, Greenland (Buchardt et al., 2001; Pauly, 1963). Ikaite has subsequently been found to form in modern environments in the Antarctic (Dieckmann et al., 2008; Lu et al., 2012; Suess et al., 1982; Whiticar & Suess, 1998), Arctic (Dieckmann et al., 2010; Nomura et al., 2013), Patagonian high-altitude lakes (Oehlerich et al., 2013; Sánchez-Pastor et al., 2016), and alkaline lakes of western North America, such as Mono Lake, California (Bischoff et al., 1993; Council & Bennett, 1993).

   In certain cases, calcite pseudomorphs after ikaite can be identified in the sedimentary record (reviewed in Selleck et al., 2007; Scheller et al., 2021) through preservation of characteristic stellate or quasi bi-pyramidal ikaite macrohabits, often referred to as "glendonite" (e.g. Selleck et al., 2007). Recently, a characteristic microtexture, referred to as "guttulatic calcite," was proposed to record the paragenetic stages of dehydrating ikaite, which also can be used to recognize ikaite pseudomorphs (Scheller et al., 2021). The presence of glendonite or guttulatic calcite has been recorded within marine sedimentary deposits from Neoproterozoic to modern environments, suggesting these are common carbonate deposits (Selleck et al., 2007; Scheller et al., 2021). Ikaite becomes more soluble with increasing temperature (Bischoff et al., 1993; Papadimitriou et al., 2013), and thus, has only been observed at <9°C in natural experiments (Huggett et al., 2005; Field et al., 2017), even in highly alkaline and phosphorous-rich water (e.g. Mono Lake, pH~10; Bischoff et al., 1993b; Council & Bennett, 1993). Therefore, ikaite pseudomorph fabrics have been proposed to function as proxies for cold paleoclimate conditions and cold-water depositional environments in the past (De Lurio & Frakes, 1999; Selleck et al., 2007; Swainson & Hammond, 2001).

   Much interest has been given to observations of ikaite pseudomorphs within Neoproterozoic marine deposits that have been used as evidence for global glaciation or near-freezing marine conditions (Dempster & Jess, 2015; James et al., 2005; Wang et al., 2020). Ikaite pseudomorphs have also been used to reconstruct oxygen isotopic compositions of seawater by assuming carbonate precipitation at near-freezing conditions during the Ordovician (Popov et al., 2019), Permian (Selleck et al., 2007; Popov et al., 2019; Frank et al., 2008; McLachlan et al., 2001), Mesozoic (De Lurio & Frakes, 1999; Teichert & Luppold, 2013; Vasileva et al., 2019; Morales et al., 2017; Rogov et al., 2016; Price & Nunn, 2010), and Cenozoic (Larsen et al., 1994; Qu et al., 2017). Recently, however, ikaite has been precipitated under laboratory conditions at higher temperatures complicating inferences of past global cold periods

(Stockmann et al., 2017; Purgstaller et al., 2017; Tollefsen et al., 2020). In addition, it is difficult to interpret the isotopic composition of ikaite pseudomorphs due to the unknown isotopic effects of dehydrating hydrated carbonates. Taken together, this has cast doubt on the utility of ikaite pseudomorphs as proxy for seawater temperatures and compositions (Frank et al., 2008). There is a need to tie the textural evidence for conditions of ikaite formation to isotopic properties of ikaite pseudomorphs, in order to use these materials more confidently as proxies for past environmental conditions.

Here we present a new framework for interpreting the carbon ($\delta^{13}C_{CARB}$), oxygen ($\delta^{18}O_{CARB}$), and clumped isotope (Δ_{47}) composition of ikaite pseudomorphs in the carbonate record. The carbonate clumped isotope thermometer is based on the thermodynamic stability of "clumping," or bonding, of the rare, heavy isotopes of carbon and oxygen (^{13}C and ^{18}O) within CO_2, and is reported in units of Δ_{47} (Eiler, 2007). The Δ_{47} value of carbonate that precipitated in thermodynamic equilibrium with dissolved CO_2 is solely dependent on the temperature of carbonate formation and therefore can be used to reconstruct precipitation temperatures independent of knowledge of the oxygen isotopic composition of precipitating fluid (Eiler, 2007). Hence, measurements of Δ_{47} provide critical independent constraints on both formation temperature and calculation of the oxygen isotope composition of the precipitating fluid ($\delta^{18}O_{fluid}$) from $\delta^{18}O_{CARB}$ (Eiler, 2007). We report for the first time ikaite pseudomorph apparent formation temperatures by carbonate clumped isotope thermometry as measured in Pleistocene tufas from Mono Lake. Through heating experiments, we show also for the first time that $\delta^{18}O_{CARB}$ and Δ_{47} values alter while $\delta^{13}C_{CARB}$ remains unchanged during heating and dehydration of hydrated carbonates (specifically MHC). We propose a mechanistic model of H_2O and CO_3^{2-} equilibrium exchange within the hydrated carbonate lattice (particularly during the transformation of MHC intermediate to final product calcite and aragonite) that explains our observed isotopic fractionations. We apply this model to reconstruct the isotopic signatures of Pleistocene precursor ikaites, and to infer the lake water temperatures and $\delta^{18}O_{fluid}$ at the time of precursor ikaite formation. Hence, we provide the first model for reconstructing primary stable isotopic compositions and formation temperature of precursor ikaite from ikaite pseudomorphs within the sedimentary record.

5.3. Geological setting

Mono Lake is a hyperalkaline (pH ~ 10, calcium-to-alkalinity ratio (Ca:ALK) ~ 10^{-4}; Ingalls et al., 2020) lake in the Mono Basin, California with an abundance of tufa deposits (Dunn, 1953; Bischoff et al., 1993b; Council and Bennett, 1993) (Fig. 5.1). The modern and Pleistocene tufas occur either as shoreline deposits where river inlets meet the lake waters or as tufa towers that are thought to form around spring outlets (Bischoff et al., 1993; Dunn, 1953). Today, Mono Lake water $\delta^{18}O_{VSMOW}$ is ~ –0.1 ‰ (Li et al., 1997) and lake water dissolved inorganic carbon (DIC) $\delta^{13}C_{VPDB}$ is ~2 ‰ (Broecker & Peng, 1984). In comparison, river inlets from the high Sierras feeding into Mono Lake are comparatively ^{18}O- and ^{13}C-

depleted ($\delta^{18}O_{VSMOW}$ = -14 to -17.5‰ and DIC $\delta^{13}C_{VPDB}$ = -14‰; Li et al., 1997). Lake water ^{18}O- and ^{13}C-enrichment is due to strong evaporative controls on the closed-basin hydrology of Mono Lake (Li et al., 1997; Broecker & Peng, 1984).

Surrounding modern Mono Lake, we find Pleistocene high-stand (i.e. highest lake level) paleoshoreline and paleotower deposits from Lake Russell, a much larger and deeper Pleistocene lake system within Mono Basin (Benson et al., 1990; Benson et al., 1998). Pleistocene and Holocene lake-level fluctuations due to changing precipitation/evaporation balance caused co-variance and ranges in lake sediment $\delta^{18}O$ and $\delta^{13}C$ values of ~12‰ (Li & Ku, 1997; Li et al., 1997).

Both the modern and Pleistocene shoreline and tufa tower deposits have been divided previously into three categories based on macroscopic textures: 1) thinolite tufa include cm-scale pseudomorphs of calcite after ikaite, 2) dendritic tufa form branching structures that have a fan-like or shrubby appearance, and 3) lithoid tufa have a massive and porous appearance with no characteristic patterns (Dana, 1884;
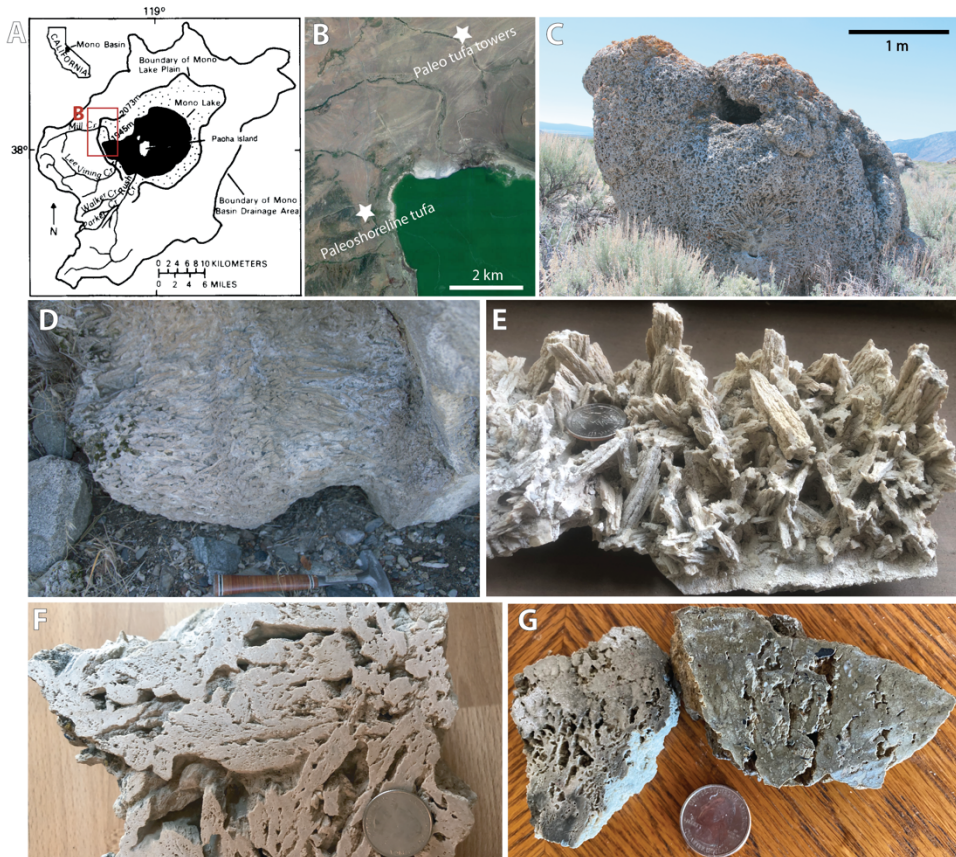
Fig. 5.1: Study area and samples. (A) Map of Mono Lake study area adapted after Benson et al. (1990). Panel B shown as red box. (B) Google Earth map depicting sampling locations. (C) Field image of paleo tufa tower with ikaite pseudomorph tufas. (D) Field image of paleo shoreline tufa with ikaite pseudomorphs. (E) Example of intact ikaite pseudomorph tufas from paleo shoreline deposits. (F) Slab of ikaite pseudomorph tufa (sample N6) sampled from the location in C. (G) Polished slabs of dendritic tufa samples from location in D (sample N2). Coin is 24.26 mm in diameter for scale in E-G.

Russell, 1889; Dunn, 1953). Here, we focus only on Pleistocene dendritic and thinolite tufas from Mono Lake high-stands that formed in Lake Russell (Fig. 5.1). The thinolite tufas of Mono Lake have been interpreted as calcite pseudomorphs after ikaite based on glendonite and guttulatic calcite texture (Fig. 5.1) (Shearman et al., 1989; Whiticar & Suess, 1998; Scheller et al., 2021). This interpretation was supported by the observation that ikaite forms on the southern shorelines of present-day Mono Lake during winter months and decomposes to anhydrous Ca-carbonate during seasonal warming (Bischoff et al., 1993; Council & Bennett, 1993). Other alkaline lakes compositionally and hydrologically similar to Mono Lake, such as Pyramid Lake, Nevada and Laguna Potrok Aike, Argentina, also precipitate ikaite, suggesting that ikaite could be a relatively common precipitate of cold, alkaline lake systems (Bischoff et al., 1993; Council & Bennett, 1993; Oehlerich et al., 2013; Sánchez-Pastor et al., 2016; Shearman et al., 1989; Whiticar & Suess, 1998).

5.4. Methods and materials

5.4.1 Mono Lake samples and preparation

This study includes measurements of 7 samples from a 2-m sequence of Pleistocene high-stand shoreline tufa, and 20 samples from 4 Pleistocene tufa towers (Fig. 5.1, Table 5.1). We include samples of thinolite, i.e., ikaite pseudomorph, tufa, dendritic tufa, and transitional fabrics that consisted of thinolite-dendritic tufa mixtures from the shoreline deposit and each tufa tower (Fig. 5.1). The described fabrics were drilled from each sample with a Dremel tool into a fine powder. All samples were confirmed to contain calcite through X-ray Powder diffraction (XRD) measurements measured with the PANalytical X'Pert Pro at the California Institute of Technology (Caltech) using a 2θ-range of 5-60°, step size of 0.0042°, and step measurement time of 80 seconds. Samples of Pleistocene high-stand shoreline tufa and tufa towers were made into thin sections and analyzed using visible-light microscopy and scanning electron microscopy, as reported in Scheller et al. (2021).

5.4.2 MHC dehydration experiments

Dehydration experiments were performed on a tufa tower sample from Ikka fjord that was transported from the University of Copenhagen to Caltech on dry ice. The sample was stored and prepared at Caltech in a -20°C freezer. We determined the mineral composition of the sample to be MHC by transporting the sample in dry ice to the PANalytical X'Pert Pro and using XRD methods from section 5.4.1 (Fig. 5.2). Mineralogy was also confirmed independently by analysis with a Renishaw inVia Qontor Raman spectrometer using a Linkham THMS600 stage where the sample was continuously flushed with liquid nitrogen during measurements. This sample was taken from tufa towers within Ikka Fjord that naturally contain both ikaite and MHC in its environment of -2 to 2°C submarine spring waters (Buchardt et al., 2001). Towers are predominantly ikaite, while seafloor debris is often MHC (Dahl & Buchardt, 2006). Although all parties involved originally thought that this sample would be ikaite and it was labelled as

such, it was measured as 100% MHC. This MHC sample formed under equilibrium conditions within its natural setting, as detailed in section 5.5.2.1, and therefore still represents a viable sample for experimental work on the behavior of dehydration of monohydrated carbonates.

Although it is possible that the sample transformed from ikaite to MHC during transport, we consider it unlikely. Numerous experiments that investigate ikaite transformation in experimental conditions have never observed MHC as a transformation product (Tang et al., 2009; Sanchez-Pastor et al., 2016; Purgstaller et al., 2017; Stockmann et al., 2018; Tollefsen et al., 2020). Furthermore, the ikaite dehydration process to form calcite occurs on such a fast time-scale (minutes to hours) that forming a long-term stable intermediate mineral product (such as MHC or vaterite) during partial dehydration has not been observed and is likely not possible. Metastable anhydrous carbonate phases, i.e. vaterite, can occur as a transformation product but only over a time-scale of minutes to hours (Tang et al., 2009; Sanchez-Pastor et al., 2016; Purgstaller et al., 2017; Stockmann et al., 2018; Tollefsen et al., 2020; Scheller et al., 2021). In the original observations by Dahl & Buchardt (2006), MHC was described to be a potential product of in-situ transformation of ikaite within the Ikka fjord. However, the MHC exhibits isotopic values in equilibrium with the ikaite-forming submarine spring waters and does not have a microtexture typical of ikaite replacement (Dahl & Buchardt, 2006; Scheller et al., 2021). Therefore, we find it most likely that the MHC grew independently of ikaite and possibly co-precipitated within the same submarine spring environment in Ikka fjord.

We performed two sets of experiments to simulate MHC dehydration in a dry environment where tufa dehydrates subaerially and in a wet environment where tufa dehydrates subaqueously:

5.4.2.1 Dry environment experiments

We filled two borosilicate tubes with ~ 0.5 to 1 cm diameter pieces of MHC (~ 15 g) within the -20°C freezer. Subsequently, we transported the samples on dry ice in borosilicate tubes sealed by a Swagelok connected to another flame-sealed borosilicate tube. In the lab, we connected the tubes to a vacuum line for ~5 minutes until pressure in the vacuum line was constant, removing most water vapor and atmospheric gases. The borosilicate tubes were then flame sealed and transferred to a 30°C water bath, where samples were heated for 24 hours. The sealed glass tubes were broken and the samples were retrieved, crushed, ground, and homogenized into fine powders with a mortar and pestle. One portion of the homogenized sample was set aside to be measured without any additional heating. As the 30°C experiment resulted in very little transformation of MHC to calcite (see section 5.5.2.1), the rest of the ground sample was placed in a Petri dish in an 80°C oven that was open to the atmosphere within the oven. Sample powder was removed from the 80°C oven at time steps ranging from 1.5 hours to 93 days (Table 5.2). After samples had been removed, they were measured on the XRD within a couple of hours using methods from section 5.4.1. Future researchers in this field are advised to measure XRD patterns

for MHC subjected to heating experiments immediately after removal from the heating device, as XRD peak ratios appear to be sensitive to changes during exposure to room temperature (we noted no evidence for comparable changes in isotopic compositions during room temperature storage).

The first attempt at this experiment was performed in 2018 and recorded the early part of transformation (Table 5.2). In order to include more time steps and investigate the variability of $\delta^{18}O$ within the MHC sample, we performed a second and third rendition of this experiment with new starting materials in 2020 (Table 5.2), broken up in two due to a period of laboratory COVID-19 lockdown. Some timesteps were measured for isotopic composition but not for reaction progress due to extended XRD laboratory lockdown (Table 5.2). Last, in order to investigate the importance of retaining and removing the released structural water, we performed a second dry experiment. Here, samples within two borosilicate tubes were heated in the 30°C bath for 24 hours while the tubes were connected to the vacuum line that would pump out any released water continuously throughout the heating experiment (i.e. no flame seal). Samples from this experiment were measured with no heating within the 80°C oven.

5.4.2.2 Wet environment experiments

We filled nine borosilicate tubes with ~0.5 cm diameter pieces of MHC (~ 1 g) within the -20°C freezer. We then added distilled water ($\delta^{18}O_{VSMOW}$ of -9.7 ‰) to the tubes in a 4˚C cooler. Subsequently, we transported sealed borosilicate tubes in dry ice to the laboratory as in 3.2.1, which froze the added water. Here, we connected the tubes to a vacuum line while submerged in an ethanol-dry ice slush for ~5 minutes until pressure in the vacuum line was constant, removing any incondensable atmospheric gasses while keeping water frozen. The borosilicate tubes were then flame sealed and transferred to the 80°C oven. Tubes were removed from the oven at time steps ranging from 30 min to 7 days (Table 5.2). At each time step, we cracked the tubes, and retrieved the submerged, wet carbonate pieces with a tweezer. The samples were then crushed, ground, and homogenized into fine powders with a mortar and pestle. This process evaporated any remaining water from the wet carbonate pieces. Mineralogy was immediately determined on the XRD using methods from section 5.4.1 and clumped isotope compositions with methods from section 5.4.3. We repeated this experiment twice using isotopically enriched water with 10% ^{18}O and removed the two tubes after 1 and 2 hours of heating.

5.4.2.3 XRD calibration

XRD patterns from the products of MHC dehydration experiments were converted to mol% MHC, calcite, and aragonite using peak height ratio calibrations. We weighed mixtures of pure, optical calcite and the Ikka Fjord MHC sample within a -20°C freezer. We transported the mixtures to the PANalytical X'Pert Pro while submerged in dry ice. We measured the 30° peak from calcite and the 31.5° from MHC using a 2θ-range of 27-33°, step size of 0.0042°, and step measurement time of 80 seconds for a total measurement duration of 15 minutes. This allowed us to create a calibration line for converting the peak

height ratios of the 30° and 31.5° peaks to mol% MHC and calcite (Appendix B, Fig. S1). The calibration function was found to follow a second-order polynomial in log-space, similar to what was observed for calcite and aragonite peak height ratios in Ingalls et al., (2020). Parameters were fitted using the Scipy module for python (Virtanen et al., 2020) (Appendix B, Fig. S1). The polynomial function was then used to convert XRD patterns for carbonate recovered from dry and wet experiments to mol% MHC and calcite. For wet experiments, we used both the MHC-calcite calibration function from this study and the calcite-aragonite calibration function from Ingalls et al. (2020) created for the same XRD instrument to convert to mol% MHC, calcite, and aragonite.
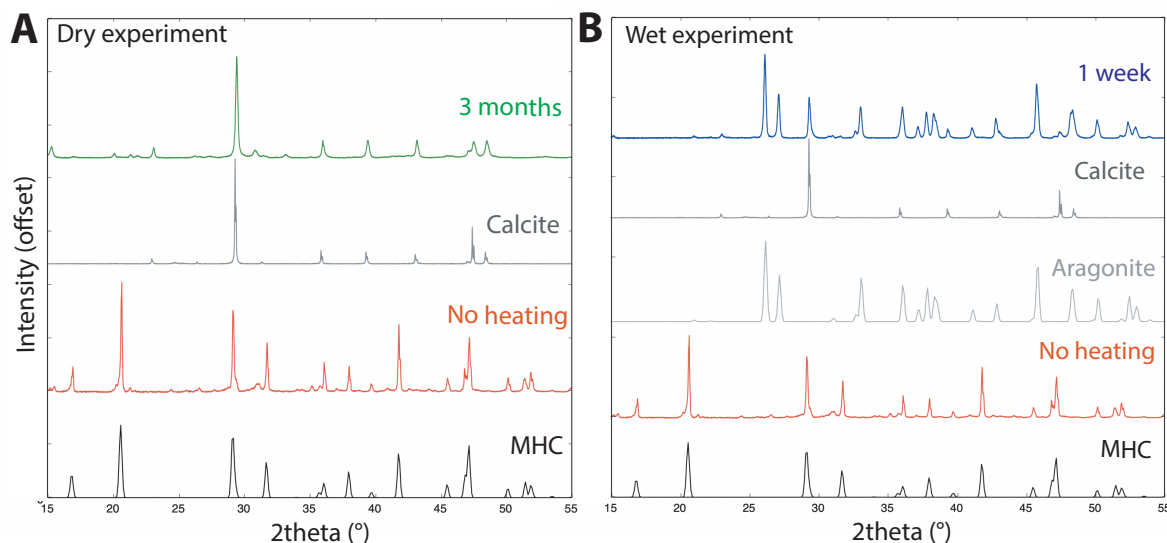
Fig. 5.2: XRD results from heating experiments. (A) XRD results before heating and after heating of the monohydrocalcite (MHC) sample from the dry experiment. Before heating, the sample has the MHC signature. After heating for 3 months, the sample contains only calcite. (B) XRD results before and after heating of MHC in the wet experiment. Before heating, the sample has a MHC signature. After heating for 1 week, the sample has changed into calcite and aragonite.

5.4.3 Clumped, oxygen, and carbon isotope measurements

We measured the clumped, oxygen, and carbon isotope compositions of Pleistocene shoreline tufa and tufa tower samples from Mono Lake as well as samples from dry and wet experiments. The quantitative clumped isotope geothermometer relies on the measurement of the mass-47 abundancy (Δ_{47}), which is defined as the enrichment of the $^{13}C^{18}O^{16}O$ isotopologue of CO_2 relative to a stochastic distribution of the heavy isotopes among all CO_2 molecules: $\Delta_{47} = \left(\frac{^{47}R}{^{47}R^*} - 1\right) \times 1000$ where

$^{47}R = [^{13}C^{16}O^{18}O + ^{12}C^{17}O^{18}O + ^{13}C^{17}O_2]/[^{12}C^{16}O_2]$ and * denotes a stochastic intramolecular distribution of isotopes. Clumped isotope measurements of Pleistocene shoreline samples were made over 3 analytical sessions from March 2017 to May 2018. Clumped isotope measurements of MHC dehydration experiments were replicated over several analytical sessions between 2018 and 2021 (Tables 5.1-2).

~10 mg aliquots of carbonate powders were digested in ~103% phosphoric acid in a common acid bath at 90°C, and the evolved CO_2 was passed through a custom-made automated sample preparation and purification system, the "Autoline," described in previous publications from the Caltech lab (e.g. Ryb et al., 2018; Hines et al., 2019). Water and non-condensable contaminants were removed by cryogenic purification steps, while contaminants that cause isobaric interferences (e.g. sulfur compounds, hydrocarbons) were removed from the evolved CO_2 via a gas chromatography column packed with Poropak and cooled to -20 °C. Purified CO_2 was then analyzed on a ThermoScientific MAT253 gas source mass spectrometer at Caltech, described using the acronym MSI in Huntington et al. (2009).

We assessed the impact of acid digestion temperature on the isotopic composition of hydrous carbonates by also performing acid digestion "off line" (in an evacuated split-tube device) at 25°C for three MHC samples that had not been subjected to heating and dehydration (Table 5.2). 20 mg of MHC sample was ground in the freezer and transferred to the laboratory in dry ice. The MHC sample was then placed in a split-tube glass reaction-vessel and dissolved in phosphoric acid at 25°C under vacuum for 1 hour. Evolved CO_2 was transferred from the split-tube vessel to a quartz tube using a water trap (ethanol-dry ice slurry) and liquid nitrogen cold trap, and transferred to the Caltech "Autoline" for automated purification and isotopic analysis.

The Δ_{47} values were projected from a working gas reference frame to the Carbon Dioxide Equilibrium Scale (CDES; Dennis *et al.*, 2011) to allow for interlaboratory comparison. To do so, standard CO_2 gases heated to 1000°C (HG) and CO_2 equilibrated through reaction with water at 25°C (EG) were measured. Following the procedures for the "primary" approach discussed in Dennis et al. (2011), for each analytical session we first fitted a line to the HG $\Delta_{47,SG-WG}$ values to project Δ_{47} to remove dependence on Δ_{47} values ($\Delta_{47,HGcorr}$). Second, we created an empirical transfer function from the HG and EG $\Delta_{47,HGcorr}$ values and their CDES reference frame accepted values, and used that transfer function to project Δ_{47} values into the CDES reference frame ($\Delta_{47,CDES}$).

Mass-48 is commonly used as a qualitative screening tool for sample gases that have contaminants such as hydrocarbons, halocarbons and/or sulfur compounds. The Δ_{48} screening tool is one of incrimination by association—it is assumed that contaminants with interferences on mass-48 may also add excess signal to any or all of masses 44-47. To identify "excess 48," we perform two York regressions on our heated gas δ_{48} vs. Δ_{48} data. The initial York regression is performed using the internal standard errors of δ_{48} and Δ_{48} values. Using the initial York regression, we estimate the external errors for these values, and perform a final York regression (following the approach in Huntington *et al.* (2009) for simulating external errors of heated gases). The 95% confidence interval of this δ_{48} vs. Δ_{48} regression is calculated, and this is referred to as our Δ_{48} line. Next, we calculate HG-corrected Δ_{48} values for sample and standard gases by calculating the deviation from the final Δ_{48} line, analogous to the early approaches

of determining Δ_{47} values. If the HG-corrected Δ_{48} value is $> 0.4 +$ the 95% predictive interval, the sample is labeled as "Δ_{48} excess". Only samples from the ^{18}O enriched water experiments had Δ_{48} excess, which was expected due to their highly enriched nature. Δ_{47} were therefore not meaningful for these samples and are not reported. All other samples did not have Δ_{48} excess.

Final "external" uncertainty ($\sigma_{external}$) for each analysis was calculated through two methods: 1) Calculating the standard error of the triplicate measurements, and 2) calculating an average of the internal standard error of the triplicate measurements, i.e. $\sigma_{external} = \frac{\sigma_{internal,1} + \sigma_{internal,2} + \sigma_{internal,3}}{3 * \sqrt{3}}$. The highest of the two calculated external uncertainties is reported in figures and tables. We leave all Δ_{47} values relative to the 90°C digestion temperature in tables, rather than correcting to a 25°C digestion, as is standard practice, to reduce the uncertainty associated with applying a commonly used acid digestion fractionation factor for calcite or dolomite to evolving MHC-calcite-aragonite mixtures. Last, we routinely measured in-house carbonate standards, specifically TV04 (travertine) and CIT Carrara marble, interspersed with experimental measurements as previously described by e.g. Ryb et al., (2018) and Hines et al., (2019). Experimental measurements are only reported from sessions in which standard residuals of Δ_{47} remained low (usually <0.01‰ to a maximum of 0.03‰) and stable in between experimental measurements (see Table 5.2). If these criteria were not fulfilled, measurements were repeated. We did not apply any extra corrections to Δ_{47} based on linear transfer functions with parameters calculated based on standard measurements.

Finally, temperatures were calculated for each sample using the T-Δ_{47} calibration of Bonifacie et al. (2017). T(Δ_{47}) thermometers calibrated explicitly for carbonates precipitating in very low temperature environments (e.g. Ghosh et al., 2006; Dennis et al., 2011; Thiagarajan *et al.*, 2011; Hines *et al.*, 2019) were considered due to the generally low annual temperatures of Mono Lake, but yielded T(Δ_{47}) values within error of the temperatures calculated using Bonifacie et al. (2017). Furthermore, Bonifacie et al. (2017) calibrations yielded a more realistic match for calculating the formation temperature of the pre-heated MHC sample than other calibrations (e.g. Ghosh et al., 2006; Dennis et al., 2011; Thiagarajan *et al.*, 2011; Hines *et al.*, 2019). Specifically, the Bonifacie et al. (2017) calibration yielded pre-heated MHC temperatures of -2 to 2°C, similar to those observed within the Ikka fjord (Buchardt et al., 2001), whereas the other calibrations yielded temperatures of ~5-10°C for pre-heated MHC. Temperature uncertainties are reported as 1σ by propagating 1 SE values of $\Delta_{47,CDES,90}$ through the Bonifacie et al. (2017) temperature calibration. Positive and negative temperature errors are reported, as the distribution is asymmetric about the mean because of the non-linear relationship of temperature to Δ_{47}: $\sigma_{T(\Delta 47)} =$

$$\sqrt{\frac{4.22 \times 10^4}{\Delta_{47,CDES,90} \pm \sigma_{\Delta_{47,CDES,90}} - 0.1262}} - T(\Delta_{47}).$$

5.5. Results

5.5.1 Isotopic compositions of Mono Lake samples

$\delta^{18}O_{VPDB}$ values of carbonate from thinolite/ikaite-pseudomorph tufas (Table 5.1) range from -4.4 to -2.0 ‰ and average -3.1 ± 0.7 ‰ (n=13), while the $\delta^{18}O_{VPDB}$ values for dendritic tufas range between -6.1 to -3.5 ‰ and average -4.9 ± 0.7 ‰ (n=12) (Fig. 5.3). Thus, the thinolite tufas record a higher $\delta^{18}O_{VPDB}$ value than dendritic tufas. The tufa samples with transition fabrics record intermediate $\delta^{18}O_{VPDB}$ values of -4.6 to -4.1 ‰ and average -4.4 ± 0.3 (n=4). The $\delta^{13}C_{VPDB}$ values of thinolite tufas are 3.9 to 4.5 ‰ and average 4.2 ± 0.1 ‰ (n=13), while the dendritic tufas have lower to similar values of 1.2 to 4.5 ‰ with an average value of 3.6 ± 1 ‰ (n=12) (Fig. 5.3). The general range of Δ_{47} for all samples is 0.60 to 0.68 ‰ (n = 29). The calculated $T(\Delta_{47})$ of dendritic tufas are 3.5 to 25.8°C with an average of 11.9 ± 6.0°C (n=13). Thinolite tufas record a similar to slightly higher $T(\Delta_{47})$ range of 6.2 to 26.2°C with an average of 14.7 ± 5.7°C (n=11) (Fig. 5.3). The tufa samples with transition fabrics record intermediate $T(\Delta_{47})$ of 7.7 to 19.7°C with an average of 13.5 ± 5.1°C.

5.5.2 Results of MHC heating experiments

5.5.2.1 Isotopic results

Isotopic analysis of the sample of MHC taken from Ikka fjord measured by 25 ˚C phosphoric acid digestion, yielded $\delta^{13}C_{CARB}$, $\delta^{18}O_{CARB}$, and Δ_{47} values consistent with equilibrium at the independently known environmental temperatures of the tufa tower from which it was taken. Specifically, the clumped
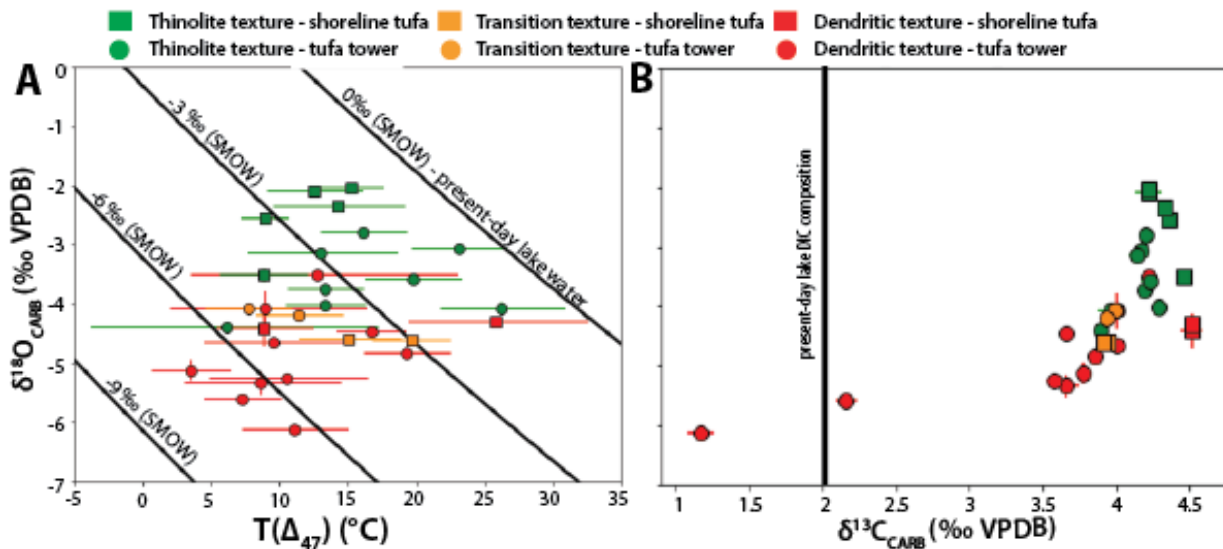
Fig. 5.3: Isotopic results of Mono Lake samples. (A) $\delta^{18}O_{CARB}$ values and calculated $T(\Delta_{47})$ of Pleistocene Mono Lake tufas from paleo shorelines (squares) and paleo tufa towers (circles). Tufa samples with thinolite (ikaite pseudormoph), dendritic, and transition texture are shown in green, red, and orange. Black lines denote the correlation between temperature of precipitation and recorded $\delta^{18}O_{VPDB}$ in the carbonate when assuming equilibrium fractionation from fluid compositions of 0 ‰, -3 ‰, -6 ‰, and -9 ‰. (B) $\delta^{18}O_{CARB}$ and $\delta^{13}C_{CARB}$ compositions for the same samples in panel A. Present-day Mono Lake DIC composition of 2 ‰ (VPDB) (Broecker et al., 1988) shown for comparison.

isotopes of the MHC tufa recorded a temperature of -1.9±0.8˚C, and Ikka fjord waters were measured to be -5 to 6 ˚C during sampling (Buchardt et al., 2001). Furthermore, the MHC recorded $\delta^{18}O$ of carbonate consistent with growth in waters with $\delta^{18}O_{VSMOW}$ of -12.4 to 11.6‰, and local ground water seeps in the Ikka fjord were measured to have $\delta^{18}O_{VSMOW}$ of ~ -15.5 to -11.7 ‰ at the time of sampling (Buchardt et al., 2001). This result suggests that MHC formed in isotopic equilibrium with the formation water, regardless of whether it grew independently from ikaite or was an early diagenetic dehydration product within the fjord (Dahl & Buchardt, 2006), though we suggest the former is more likely.
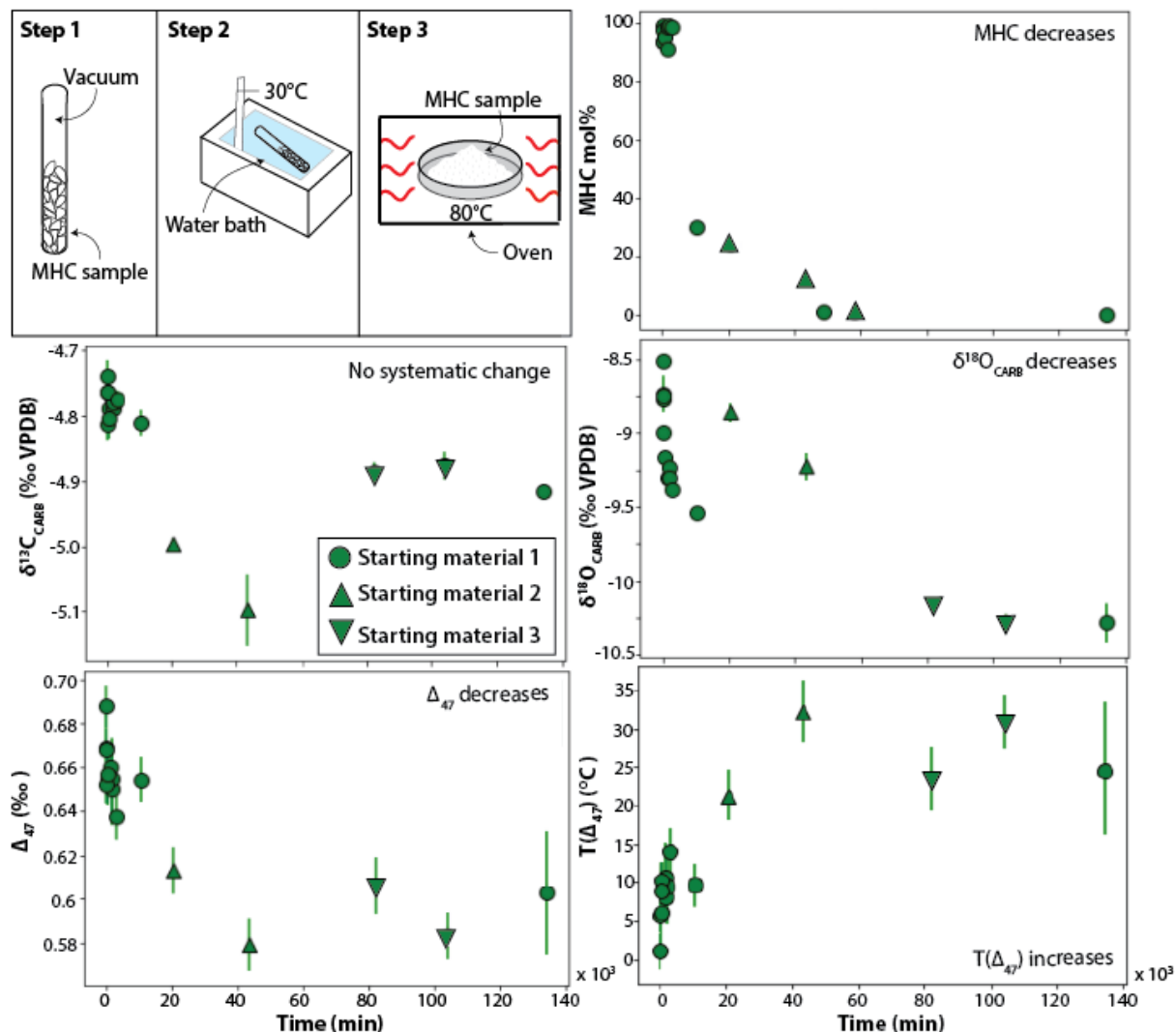
Fig. 5.4: Results from MHC heating experiments in dry environment. Borosilicate tubes with MHC are pumped to vacuum and sealed before being placed in 80°C oven. Measurements of reaction progress in MHC mol% calculated using XRD measurements shows that full conversion takes 140k min equivalent to ~3 months. $\delta^{18}O_{CARB}$ and Δ_{47} decreases, $T(\Delta_{47})$ increases, and $\delta^{13}C_{CARB}$ does not systematically change during progressive heating. Few off points to the overall trends in $\delta^{18}O_{CARB}$ are observed. These can be explained due to the fact that experiments were performed in 3 separate experimental batches with different starting $\delta^{18}O_{CARB}$ as discussed in text.

147

Table 5.1: Stable isotope dataset measured for Pleistocene Mono Lake paleo shoreline and paleo tower samples. All samples given in the table were measured with triplicates. Clumped isotope temperatures ($T(\Delta_{47})$) were calculated following methodology given in the methods section. Summary statistics are given for each texture type.

Name	Type	Texture	$\delta^{13}C_{CARB}$ (‰VPDB)	$\delta^{18}O_{CARB}$ (‰VPDB)	$\Delta_{47,CDES,90}$	$T(\Delta_{47})$
N2	Shoreline	Dendritic	4.51 ± 0.07	-4.41 ± 0.30	0.66 ± 0.01	$8.9 \pm^{3.6}_{3.5}$
N7	Shoreline	Dendritic	4.52 ± 0.03	-4.29 ± 0.07	0.60 ± 0.02	$25.8 \pm^{6.8}_{6.4}$
T1_SH_M	Tower	Dendritic	3.57 ± 0.05	-5.26 ± 0.06	0.65 ± 0.02	$10.5 \pm^{6.0}_{5.6}$
T1_SH_B	Tower	Dendritic	4.00 ± 0.01	-4.66 ± 0.02	0.65 ± 0.02	$9.6 \pm^{5.4}_{5.1}$
T4_SH_T	Tower	Dendritic	1.17 ± 0.09	-6.12 ± 0.07	0.65 ± 0.01	$11.1 \pm^{4.0}_{3.8}$
T4_SH_B	Tower	Dendritic	2.16 ± 0.07	-5.60 ± 0.05	0.66 ± 0.01	$7.2 \pm^{2.9}_{2.8}$
T4_SH_L	Tower	Dendritic	3.86 ± 0.04	$-4.84 \pm 0.0.2$	0.62 ± 0.01	$19.3 \pm^{3.2}_{3.1}$
T13_SH	Tower	Dendritic	3.66 ± 0.04	-4.46 ± 0.03	0.63 ± 0.01	$16.7 \pm^{2.6}_{2.5}$
T14_SH_T	Tower	Dendritic	3.77 ± 0.02	-5.12 ± 0.18	0.68 ± 0.01	$3.5 \pm^{3.0}_{2.9}$
T14_SH_B	Tower	Dendritic	3.66 ± 0.08	-5.33 ± 0.19	0.66 ± 0.02	$8.6 \pm^{5.9}_{5.6}$
T17_SH_T	Tower	Dendritic	4.22 ± 0.04	-3.51 ± 0.07	0.64 ± 0.04	$12.8 \pm^{10.3}_{9.3}$
T17_SH_B	Tower	Dendritic	4.00 ± 0.01	-4.66 ± 0.02	0.66 ± 0.02	$8.9 \pm^{7.5}_{6.9}$
Mean			3.59	-4.86		11.9
STD			0.98	0.69		6.0
Min			1.17	-6.12		3.5
Max			4.52	-3.51		25.8
N1	Shoreline	Transition	3.95 ± 0.07	-4.60 ± 0.08	0.63 ± 0.01	$15.1 \pm^{3.8}_{3.7}$
N4	Shoreline	Transition	3.91 ± 0.02	-4.61 ± 0.02	0.62 ± 0.01	$19.7 \pm^{2.9}_{2.8}$
T4_TR	Tower	Transition	3.99 ± 0.02	-4.07 ± 0.08	0.64 ± 0.01	$7.7 \pm^{3.6}_{3.5}$
T13_TR	Tower	Transition	3.94 ± 0.02	-4.19 ± 0.03	0.65 ± 0.01	$11.4 \pm^{6.8}_{6.4}$
Mean			3.94	-4.37		13.5
STD			0.04	0.28		5.1
Min			3.90	-4.61		7.7
Max			3.99	-4.07		19.7
N3	Shoreline	Pseudomorph/thinolite	4.46 ± 0.07	-3.51 ± 0.12	0.66 ± 0.01	$8.9 \pm^{3.3}_{3.2}$
N5	Shoreline	Pseudomorph/thinolite	4.36 ± 0.04	-2.56 ± 0.08	0.66 ± 0.01	$8.9 \pm^{1.8}_{1.8}$
N6_B	Shoreline	Pseudomorph/thinolite	4.33 ± 0.05	-2.35 ± 0.02	0.64 ± 0.02	$14.3 \pm^{4.9}_{4.7}$
N6_M	Shoreline	Pseudomorph/thinolite	4.22 ± 0.03	-2.10 ± 0.02	0.64 ± 0.01	$12.5 \pm^{3.5}_{3.4}$
N6_T	Shoreline	Pseudomorph/thinolite	4.22 ± 0.03	-2.04 ± 0.01	0.63 ± 0.01	$15.3 \pm^{2.3}_{2.3}$
T1_TH_T	Tower	Pseudomorph/thinolite	4.20 ± 0.02	-2.80 ± 0.05	0.63 ± 0.01	$16.1 \pm^{3.2}_{3.1}$
T1_TH_B	Tower	Pseudomorph/thinolite	4.23 ± 0.06	-3.57 ± 0.06	0.62 ± 0.01	$19.8 \pm^{3.6}_{3.5}$
T4_TH	Tower	Pseudomorph/thinolite	4.19 ± 0.04	-3.74 ± 0.06	0.64 ± 0.01	$13.4 \pm \pm^{2.8}_{2.7}$
T13_TH	Tower	Pseudomorph/thinolite	4.29 ± 0.02	-4.02 ± 0.04	0.64 ± 0.01	$13.4 \pm^{3.0}_{2.9}$
T14_TH_T	Tower	Pseudomorph/thinolite	3.89 ± 0.05	-4.39 ± 0.06	0.67 ± 0.04	$6.2 \pm^{11.1}_{10.0}$
T14_TH_B	Tower	Pseudomorph/thinolite	4.23 ± 0.06	-3.57 ± 0.06	0.60 ± 0.01	$26.2 \pm^{4.7}_{4.5}$
T17_TH_T	Tower	Pseudomorph/thinolite	4.17 ± 0.04	-3.06 ± 0.02	0.61 ± 0.01	$23.2 \pm^{3.6}_{3.5}$
T17_TH_B	Tower	Pseudomorph/thinolite	4.14 ± 0.06	-3.14 ± 0.03	0.64 ± 0.02	$13.0 \pm^{5.6}_{5.3}$
Mean			4.23	-3.14		14.7
STD			0.13	0.74		5.7
Min			3.89	-4.39		6.2
Max			4.46	-2.04		26.2

Table 5.2: Stable isotopes and reaction progress measured for all dry and wet experiments converting MHC to calcite and aragonite. All samples given in the table were measured with triplicates unless otherwise indicated, where n indicates number of repeated measurements. Clumped isotope temperatures $(T(\Delta_{47}))$ were calculated following methodology given in the methods section. Starting material numbers 1-5 indicate that 5 different starting materials with different starting $\delta^{18}O_{CARB}$ were used for 5 different dry heating experiments as discussed in the methods section. Table fields shaded as black means that analyses types were not applicable.

Exp. type	Time stamp (min)	MHC mol%	Calcite mol%	Arag. mol%	$\delta^{13}C_{CARB}$ (‰VPDB)	$\delta^{18}O_{CARB}$ (‰VPDB)	$\Delta_{47,CDES,90}$	$T(\Delta_{47})$
No heating, 25ºC digestion in two-legged man		100			-4.79 ± 0.06	-9.4 ± 0.11	0.70 ± 0.003	$-1.9 \pm {}^{0.8}_{0.8}$
Starting material 1 2018								
Dry	0	99	1		-4.76 ± 0.02	-8.74 ± 0.12	0.69 ± 0.01	$1.1 \pm {}^{2.4}_{2.4}$
Dry	98	99	1		-4.74 ± 0.02	-8.51 ± 0.05	0.67 ± 0.01	$5.8 \pm {}^{2.3}_{2.2}$
Dry	190	94	3		-4.81 ± 0.02	-8.77 ± 0.02	0.67 ± 0.02	$6.0 \pm {}^{4.2}_{4.0}$
Dry	280	94	6		-4.76 ± 0.03	-8.75 ± 0.05	0.65 ± 0.01	$10.2 \pm {}^{2.2}_{2.2}$
Dry	365	94	6		-4.80 ± 0.03	-9.00 ± 0.03	0.66 ± 0.01	$8.9 \pm {}^{3.7}_{3.6}$
Dry	614	95	5		-4.79 ± 0.01	-9.17 ± 0.04	0.65 ± 0.01	$9.6 \pm {}^{3.1}_{3.0}$
Dry	1530	99	1		-4.77 ± 0.01	-9.30 ± 0.05	0.66 ± 0.01	$8.1 \pm {}^{2.6}_{2.5}$
Dry	1782	91	9		-4.79 ± 0.02	-9.24 ± 0.06	0.65 ± 0.02	$10.7 \pm {}^{4.4}_{4.2}$
Dry	1970	99	1		-4.79 ± 0.02	-9.30 ± 0.05	0.65 ± 0.02	$9.5 \pm {}^{5.2}_{4.9}$
Dry	3022	99	1		-4.77 ± 0.01	-9.38 ± 0.03	0.64 ± 0.01	$14.1 \pm {}^{3.0}_{3.0}$
Dry	10510	30.0	70.0		-4.81 ± 0.02	-9.54 ± 0.04	0.65 ± 0.01	$9.6 \pm {}^{2.8}_{2.7}$
Dry	48960	1	99					
Dry	134293	0	100		-4.92 ± 0.01	-10.29 ± 0.13	0.60 ± 0.03	$24.4 \pm {}^{9.1}_{8.4}$
Starting material 2 2020 part 1								
Dry (n=2)	20460	24	76		-5.00 ± 0.01	-8.86 ± 0.06	0.61 ± 0.01	$21.3 \pm {}^{3.3}_{3.2}$
Dry (n=2)	43304	13	87		-5.10 ± 0.05	-9.23 ± 0.09	0.58 ± 0.01	$32.1 \pm {}^{4.0}_{3.9}$
Dry	57855	1	99					
Starting material 3 2020 part 2								
Dry (n=2)	82120				-4.89 ± 0.02	-10.17 ± 0.002	0.61 ± 0.01	$23.4 \pm {}^{4.2}_{4.0}$
Dry (n=2)	103860				-4.88 ± 0.02	-10.29 ± 0.06	0.58 ± 0.01	$30.8 \pm {}^{3.5}_{3.4}$
Starting material 4 2021 part 1								
Dry (n=1)	0				-5.01 ± 0.001	-9.22 ± 0.002	0.66 ± 0.03	$8.0 \pm {}^{8.3}_{7.6}$
Dry (n=1)	15360				-5.14 ± 0.002	-10.14 ± 0.004	0.60 ± 0.02	$25.3 \pm {}^{6.5}_{6.1}$
Starting material 5 2021 part 2								
Dry (n=1)	0				-5.48 ± 0.003	-9.53 ± 0.003	0.66 ± 0.01	$7.4 \pm {}^{2.7}_{2.6}$
Dry (n=1)	15360				-5.29 ± 0.005	-10.28 ± 0.01	0.60 ± 0.02	$25.3 \pm {}^{6.5}_{6.1}$
Wet distilled water								
Wet (n=2)	30	51	27	22	-5.98 ± 0.03	-10.32 ± 0.24	0.67 ± 0.02	$5.3 \pm {}^{5.2}_{4.9}$
Wet (n=2)	60	50	23	27	-5.56 ± 0.10	-8.99 ± 0.33	0.66 ± 0.01	$7.8 \pm {}^{2.8}_{2.7}$

	(min)				$\delta^{13}C$	$\delta^{18}O$	Δ_{47}	$T(\Delta_{47})$
Wet (n=2)	120	2	70	28	-4.88 ± 0.03	-9.62 ± 0.14	0.65 ± 0.01	$10.9\pm^{3.7}_{3.6}$
Wet (n=1)	180	62	17	21	-5.92 ± 0.002	-11.37 ± 0.002	0.60 ± 0.01	$23.7\pm^{4.4}_{4.2}$
Wet	270	3	74	23	-5.25 ± 0.01	-10.68 ± 0.05	0.65 ± 0.02	$10.5\pm^{4.3}_{4.1}$
Wet	1220	47	42	11	-5.21 ± 0.01	-11.33 ± 0.06	0.62 ± 0.01	$18.9\pm^{3.5}_{3.4}$
Wet	2880	44	38	18	-5.31 ± 0.01	-12.29 ± 0.04	0.61 ± 0.01	$23.4\pm^{3.3}_{3.2}$
Wet (n=1)	2886	■	■	■	-4.46 ± 0.01	-12.10 ± 0.002	0.61 ± 0.02	$21.2\pm^{5.3}_{5.1}$
Wet	10080	0	16	84	-5.41 ± 0.01	-11.28 ± 0.04	0.64 ± 0.02 (n=3)	$13.4\pm^{5.8}_{5.4}$ (n=3)
							0.62 ± 0.02 (n=2)	$19.8\pm^{5.3}_{5.0}$ (n=2)
Wet enriched water								
Wet (n=1)	60				-20.63 ± 0.003	718.04 ± 0.10		
Wet (n=1)	120				4.09 ± 0.06	1184.48 ± 2.54		

We found that dry powders of Ikka fjord MHC heated at 30°C for 24 hours in a water bath, within borosilicate tubes that were either flame-sealed or continuously connected to the vacuum line, did not differ significantly from each other or from unheated starting materials, in $\delta^{13}C_{CARB}$, $\delta^{18}O_{CARB}$, or Δ_{47}. Three renditions of these measurements showed that $\delta^{18}O_{VPDB}$ of the MHC sample was ~ -9.53 to -8.74‰ displaying a variability of at least 1‰ (Table 5.2) and recorded a $T(\Delta_{47})$ of 1 to 8°C. Thus, $\delta^{13}C_{CARB}$, $\delta^{18}O_{CARB}$, or Δ_{47} of MHC did not change significantly during 30°C vacuum heating for 24 hours. Furthermore, we found only very little transformation of MHC to calcite (~ 1 mol%) at this temperature (Table 5.2). This suggests that MHC transformation at 30°C is much slower than ikaite transformation, similar to previous results (Dahl & Buchardt, 2006)

The most striking result from the dry environment experiment (heating of MHC at 80 °C without added water) is the observation of a decrease in $\delta^{18}O_{VPDB}$ of 1.55‰ for the carbonates over a period of ~93 days, or 3 months (134293 min) (Fig. 5.4). The three separate renditions of the dry heating experiment had somewhat different starting $\delta^{18}O_{CARB}$ compositions ranging from -8.74‰ to -9.53‰ (Table 5.2). Starting material 1 and 3 seemed to be more similar in composition, whereas starting material 2 likely started out 1‰ higher than starting material 1 and 3 (Fig. 5.4). Regardless of this variability, in all renditions of the dry heating experiment using starting material 1-5, heating always results in a $\delta^{18}O_{CARB}$ decrease with time. In contrast, the wet environment experiment recorded a more dramatic and rapid decrease in $\delta^{18}O_{VPDB}$ of the carbonates of 2.6-3.6‰ relative to an average starting value of ~8.7‰, over 2 days (2880 min) to a week (10080 min) (Fig. 5.5).

The Δ_{47} values of MHC subjected to dry heating experiments decreased from an initial value corresponding to a $T(\Delta_{47})$ of ~1°C, evolving over ~14 days (20460 min) to ~93 days (134293 min) to Δ_{47} values corresponding to $T(\Delta_{47})$ of 24 to 32°C (Fig. 5.4). The wet experiment yielded a $T(\Delta_{47})$ value of 5°C after 30 min of heating. Wet heating for 2 days (2880 min) to a week (10080 min) yielded Δ_{47} values corresponding to $T(\Delta_{47})$ of 20 to 23°C. The wet and dry experiments recorded a statistically significant decrease in Δ_{47} of ~ 0.07-0.11‰, corresponding to an increase in $T(\Delta_{47})$ of 20 to 30°C even with the large uncertainties inherent to Δ_{47} measurements (Fig. 5.4-5). Heating under the dry or wet environment

experiment conditions led to subtle, erratic decreases in $\delta^{13}C_{VPDB}$ to ranges of -5.48 to -4.74 ‰ and -5.98 to -4.46 ‰ for dry and wet experiment carbonates, respectively (Fig. 5.4-5). Last, MHC submerged in water enriched with 10% ^{18}O showed a notable increase in $\delta^{18}O_{CARB}$ values. Heating of samples within ^{18}O enriched water for 60 and 120 min resulted in a $\delta^{18}O_{VPDB}$ value of 718.0 ‰ and 1184.5 ‰ of the carbonate, respectively. This finding indicates that environmental water can exchange O with structural carbonate during the transformation of MHC to calcite and aragonite, though this could be directly or indirectly, by way of any structural H_2O that has not yet left the structure.
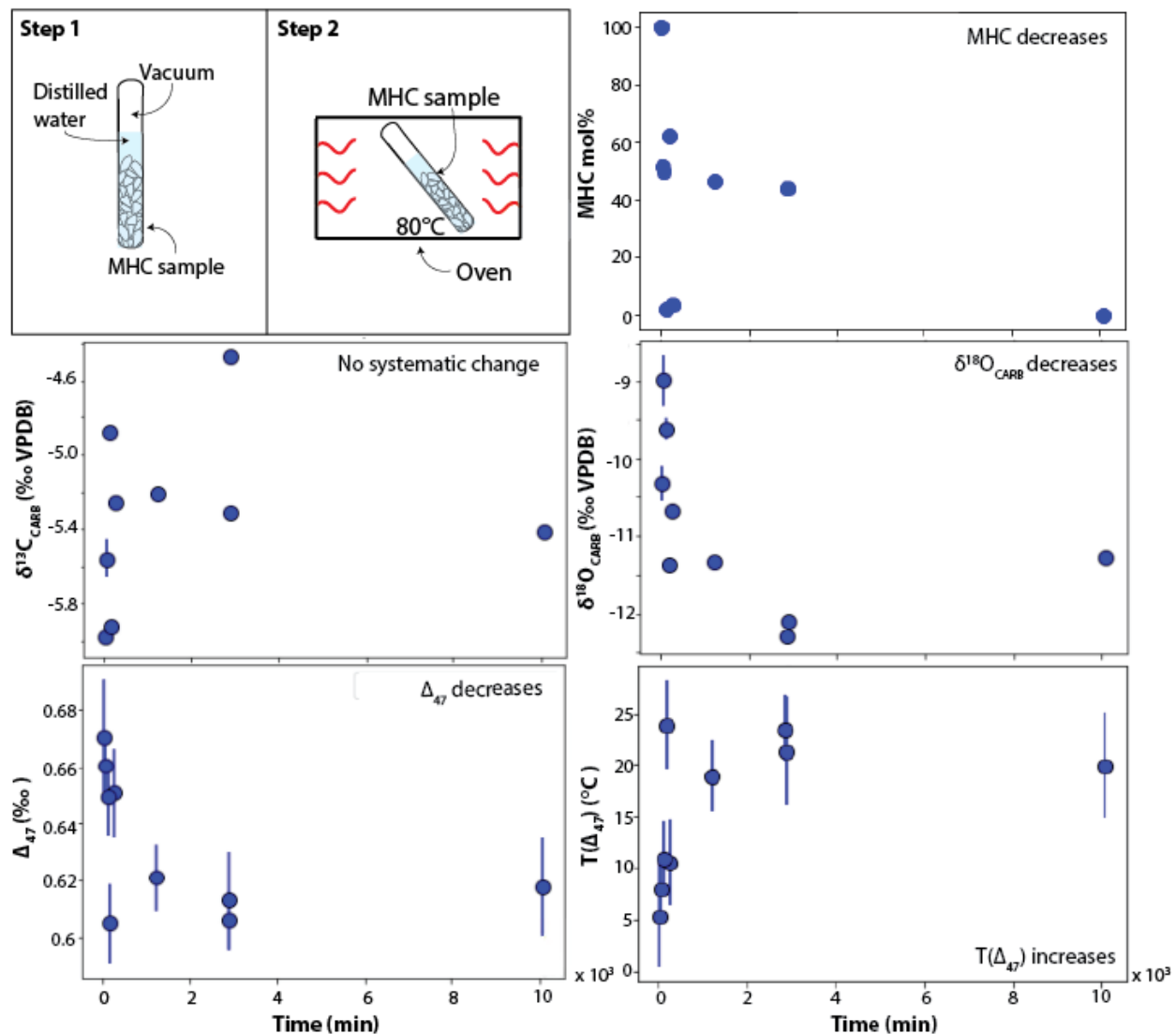
Fig. 5.5: Results from MHC heating experiments in wet environment. Borosilicate tubes with MHC and distilled or enriched water are pumped to vacuum and sealed before being placed in 80°C oven. Measurements of reaction progress in MHC mol% calculated using XRD measurements shows that full conversion takes 10k min equivalent to ~1 week. $\delta^{18}O_{CARB}$ and Δ_{47} decreases, $T(\Delta_{47})$ increases, and $\delta^{13}C_{CARB}$ does not systematically change during progressive heating. Few off points to the overall trends in reaction progress are observed as discussed in text.

5.5.2.2 Reaction progress results from XRD experiments

Prior to heating at 80˚C (but after an initial period stored at 30 ˚C), the samples yielded XRD patterns corresponding to 99 mol% MHC (Fig. 5.2). During the dry-environment experiments, each sample partially or completely transformed to calcite (as measured by proportions of diagnostic MHC and calcite XRD peaks, see Appendix B Fig. S1), with complete transformation occurring after 93 days, or ~3 months (Fig. 5.2). In contrast, during the wet-environment heating experiments, MHC gradually transformed to a mixture of calcite and aragonite (Fig. 5.2, Table 5.2), and completed this transformation after 1 week. Tracking the reaction progress through XRD peak height ratios suggests a systematic reaction progress for dry experiments that can be described by first-order reaction kinetics, as expected (Fig. 5.4). Note that the decrease in $\delta^{18}O_{CARB}$ occurs over approximately the same time scale as this conversion. The rate of progress of phase transformation during the wet experiment is more difficult to constrain because, unlike the dry experiment, each datum represents a separate sample of MHC rather than a homogenized mixture. Therefore, it is possible that the greater scatter of data in the plot of MHC fraction vs. time for wet experiments, reflects natural variability of properties of the sample that might influence phase transformation kinetics, such as impurities and/or different crystal shapes and sizes. Nevertheless, the wet experiments also generally follow a first-order rate law with a higher rate coefficient than the dry experiment (but recognizing that some data points are exceptions to this generalization; Fig. 5.5). We also note that data for both wet and dry experiments suffer from significant uncertainty to the calibration of proportions of MHC to calcite based on XRD line parameters (Appendix B Fig. S1).

5.6 Discussion

5.6.1 Isotopic fractionations caused by diagenetic carbonate dehydration

The experimental heating of MHC reveals that $\delta^{18}O_{CARB}$ and Δ_{47} both decrease during heating, approximately in synch with transformation of MHC to anhydrous solid carbonates, whereas $\delta^{13}C_{CARB}$ remains little changed. A noticeable feature of these changes is that the phase transformation is complete on the time-scales of our experiments, and both Δ_{47} and $\delta^{18}O_{CARB}$ reach steady-state (time invariant) values, but these values do not correspond to those expected for equilibrium at the temperatures of the experiment (80°C; Fig. 5.4-5). A carbonate formed in equilibrium at 80°C is expected to yield a Δ_{47} of 0.46 ‰ (Bonifacie et al., 2017). In contrast, the minimum Δ_{47} reached in the experiments was 0.58 ± 0.01‰ and 0.60 ± 0.01‰ for the dry and wet conditions, respectively. The difference between the temperature-dependent oxygen isotope fractionation between calcite and water at 0°C vs. 80°C is 15 ‰ (Kim & O'Neil, 1997). If the change in $\delta^{18}O_{CARB}$ during heating is facilitated by oxygen exchange between structural CO_3^{2-} and H_2O (as is suggested by the fact that this change occurs even in the 'dry' experiments where no other material besides the components of MHC was available for exchange), we

would expect that ¼ of this change in oxygen isotope fractionation, between the presumably large low-temperature fractionation established when the mineral grew and the 15 ‰ smaller fractionation that prevails at 80˚C, is expressed by the CO_3^{2-}-associated oxygen and ¾ is expressed by the H_2O-associated oxygen (e.g. equation 8-9). Thus, the $\delta^{18}O$ of carbonate in MHC should decrease by 3.8 ‰ and the $\delta^{18}O$ of structural H_2O in MHC should increase by 11.2 ‰, assuming full re-equilibration between the two. However, the $\delta^{18}O_{CARB}$ decreased by only 1.55‰ and 2.6-3.6‰ for the dry and wet experiment, respectively. Thus, our experiments present evidence that might appear contradictory: the systematic change in $\delta^{18}O$ of carbonate during heating and attainment of a steady state indicates exchange between structural carbonate and structural water, yet that steady state fails to reflect equilibrium, and this observation is accompanied by synchronous but also partial re-equilibration of clumped isotope composition. The larger shift in $\delta^{18}O$ of structural carbonate during the wet experiments may reflect exchange between structural carbonate and environmental water, or between structural water and environmental water accompanied by exchange between structural carbonate and structural water, and yet is also accompanied by synchronous changes in Δ_{47} that reflect partial re-equilibration, faster than but to an extent closely similar to dry experiments.

We have attempted to explain these findings by way of a model that tracks and explicitly links four concurrent processes: 1) transformation of MHC to calcite (and/or aragonite), associated with loss of structural water; 2) oxygen isotope exchange between structural carbonate and structural water; 3) resetting of clumped isotope composition of structural carbonate; and 4) oxygen isotope exchange between structural water and environmental water (when present, as in the wet experiments; Fig. 5.6).

The transformation of MHC to calcite can be described as:

$$CaCO_3 \cdot H_2O \rightarrow CaCO_3 + H_2O \ (1.)$$

We can approximate the reaction rate (R) of MHC-associated CO_3^{2-} expressed in mol% ($M_{MHC,CO3}$) into calcite as a first order reaction fitted to the reaction progress dataset calculated from XRD (Fig. 5.6):

$$R = -k_{MHC} * M_{MHC,CO3} \ (2.)$$

Here, k_{MHC} is the reaction coefficient governing the loss of H_2O from MHC. Through the integrated first order rate law, we calculated the expected mol% MHC at each time-step (t):

$$M_{MHC_t} = M_{MHC_0} * e^{-k_{MHC} * t} (3.)$$

Here, MHC_0 is the starting mol% of MHC which was determined to be ~100 mol% MHC (Table 5.2, Fig. 5.4-5). This also gives us the mol% of anhydrous carbonate as either calcite or aragonite (M_{CC}):

$$M_{CC_t} = 100 - M_{MHC_t} \ (4.)$$

From stoichiometry, we then calculate the mol% of oxygen within MHC-associated CO_3^{2-} ($M_{MHC,CO3}$), MHC-associated H_2O ($M_{MHC,H2O}$), and anhydrous carbonate-associated CO_3^{2-} ($M_{CC,CO3}$). Here, the important relationship is that:

$$M_{MHC,H2O_t} = \frac{1}{3} M_{MHC,CO3_t} \quad (5.)$$

We approximate the flux of oxygen exchange (F_{ex}) between MHC-associated H_2O and CO_3^{2-} via a fractional approach to equilibrium, described here as a first order reaction dependent on the difference between the expected equilibrium fractionation between H_2O and CO_3^{2-} at 80 °C ($\varepsilon_{eq,80°C}$) and the observed difference between the measured $\delta^{18}O$ of the CO_3^{2-} and an estimated $\delta^{18}O$ of H_2O within MHC (see below) at each time step shown in eq. 6.

$$F_{ex_{t+1}} = k_{ex} * \left[\varepsilon_{eq,80°C} - \left(\delta^{18}O_{MHC,CO3_t} - \delta^{18}O_{MHC,H2O_t} \right) \right] \quad (6.)$$

Here k_{ex} is the exchange coefficient governing the oxygen exchange between structural H_2O and structural CO_3^{2-}. For the wet experiment, we also include an additional term related to the flux of oxygen exchange between the structural H_2O of MHC and the external H_2O ($\delta^{18}O_{H2O,ext} = -9.7 \pm 0.2$ ‰ (SMOW), $measured; asssumed\ to\ be\ time\ invariant$) of the distilled water in which the MHC was submerged during heating ($F_{ex,w}$) as shown in eq. 7.

$$F_{ex,w_{t+1}} = k_{ex,w} * \left(\delta^{18}O_{H2O,ext_t} - \delta^{18}O_{MHC,H2O_t} \right) \quad (7.)$$

Here $k_{ex,w}$ is the exchange coefficient governing the oxygen exchange between structural and external H_2O. Eq. 7 relies on the assumption that there is no isotopic fractionation between the hydrated and free water. This is the mechanism by which our model explains the fact that the wet experiments that used enriched water yielded highly ^{18}O-enriched solid carbonate products (Table 5.2). The $\delta^{18}O$ value of MHC-associated CO_3^{2-} and H_2O can then be calculated as shown in eq. 8-9.

$$\delta^{18}O_{MHC,CO3_{t+1}} = \delta^{18}O_{MHC,CO3_t} + F_{ex_{t+1}} * \frac{M_{MHC,H2O_{t+1}}}{M_{MHC,CO3_{t+1}} + M_{MHC,H2O_{t+1}}} \quad (8.)$$

$$\delta^{18}O_{MHC,H2O_{t+1}} = \delta^{18}O_{MHC,H2O_t} - F_{ex_{t+1}} * \frac{M_{MHC,CO3_{t+1}}}{M_{MHC,CO3_{t+1}} + M_{MHC,H2O_{t+1}}} \quad (9.)$$

By mass balance, we can then calculate the $\delta^{18}O$ of calcite-associated CO_3^{2-} shown in eq. 10.

$$\delta^{18}O_{CC,CO3_{t+1}} = \frac{\delta^{18}O_{CC,CO3_t} * M_{CC,CO3_t} + \delta^{18}O_{MHC,CO3_t} * \left(M_{MHC,CO3_{t+1}} - M_{MHC,CO3_t} \right)}{M_{CC,CO3_{t+1}}} \quad (10.)$$

Note that eqns. 6-10 treat the $\delta^{18}O$ value as a conservative property that follows principles of mass balance; this is not strictly true but the systematic errors this simplification engenders are not significant compared to other errors and experimental variations in the data to which we fit this model.

We must also account for changes to Δ_{47} of MHC caused by re-equilibration to approach the equilibrium value of Δ_{47} at the experimental temperature of 80 °C. The MHC internal clumped isotope exchange flux (F_{in}) can be expressed via a fractional approach assuming a first order reaction dependency:

$$F_{in_{t+1}} = k_{in} * \left[\Delta_{47_{CO3,80°C}} - \Delta_{47_{MHC,CO3_t}} \right] (11.)$$

Here, we assume that exchange of oxygen between structural carbonate and structural water in MHC controls the rate at which carbonate ions in MHC are able to re-equilibrate (based on the fact that these experiments are being performed at a condition where solid carbonates generally undergo no changes in Δ_{47} through solid-state carbonate-ion—carbonate-ion exchange; Stolper and Eiler, 2015). Thus, k_{in} should be closely similar to k_{ex} (a testable prediction that we will examine in our fits of this model to the experimental data). Thus, the value of Δ_{47} of MHC at any time step (Δt) can then be calculated as:

$$\Delta_{47_{MHC,CO3_{t+1}}} = F_{in_{t+1}} * \Delta t + \Delta_{47_{MHC,CO3_t}} (12.)$$

The Δ_{47} value of calcite ($\Delta_{47_{CC,CO3}}$) can be expressed by a mass balance shown in eq. 13.

$$\Delta_{47_{CC,CO3_{t+1}}} = \frac{\Delta_{47_{CC,CO3_t}} * M_{CC,CO3_t} + \Delta_{47_{MHC,CO3_t}} * \left(M_{MHC,CO3_{t+1}} - M_{MHC,CO3_t} \right)}{M_{CC,CO3_{t+1}}} (13.)$$

The model-predicted isotopic compositions of the MHC-CC mixtures (i.e., what we measure in our experimental products) at each time step would then be expressed as an average weighted by the amount of MHC and CC as shown in eq. 14-15.

$$\delta^{18}O_{MIX_t} = \delta^{18}O_{MHC,CO3_t} * \frac{M_{MHC,CO3_t}}{M_{MHC,CO3_t} + M_{CC,CO3_t}} + \delta^{18}O_{CC,CO3_t} * \frac{M_{CC,CO3_t}}{M_{MHC,CO3_t} + M_{CC,CO3_t}} (14.)$$

$$\Delta_{47_{MIX_{t+1}}} = \Delta_{47_{MHC,CO3_{t+1}}} * \frac{M_{MHC,CO3_t}}{M_{MHC,CO3_t} + M_{CC,CO3_t}} + \Delta_{47_{CC,CO3_{t+1}}} * \frac{M_{CC,CO3_t}}{M_{MHC,CO3_t} + M_{CC,CO3_t}} (15.)$$

As given in eq. 15, we are assuming that Δ_{47} mix linearly, although this is not actually the case (Defliese & Lohmann, 2015). However, given the fact that $\delta^{13}C$ remains unchanged for MHC and calcite carbonate, the mixing will closely approximate a linear relationship. We, furthermore, demonstrated the close approximation of a linear relationship using representative model values within a non-linear mixing calculation. The simulations of this model can be fitted to data by varying the exchange coefficients governing the isotopic exchanges, $k_{ex,}$ $k_{ex,w}$, and k_{in}, as well as the reaction coefficient, k_{MHC} (Fig. 5.6). k_{ex} and k_{in} are expected to have the same value, and we fit these independently to test that this holds true for our experimental results. We perform a grid search of model parameters and fit to the experimental data using the following empirically defined criteria (Fig. 5.6). For dry experiments, simulations were fit to be within 2σ of $\delta^{18}O_{CARB}$ and 0.75σ for Δ_{47}. For wet experiments, simulations were fit to be within 3σ of $\delta^{18}O_{CARB}$ and 0.5σ for Δ_{47}. The difference in chosen simulation limits for the two experiments were arbitrarily set to produce the tightest simulation space that could explain all data points. The difference reflects that there was more spread in $\delta^{18}O_{CARB}$ and less spread in Δ_{47} for the wet experiment data compared to the dry experiment data. Exchange and reaction coefficient ranges for dry experiments that
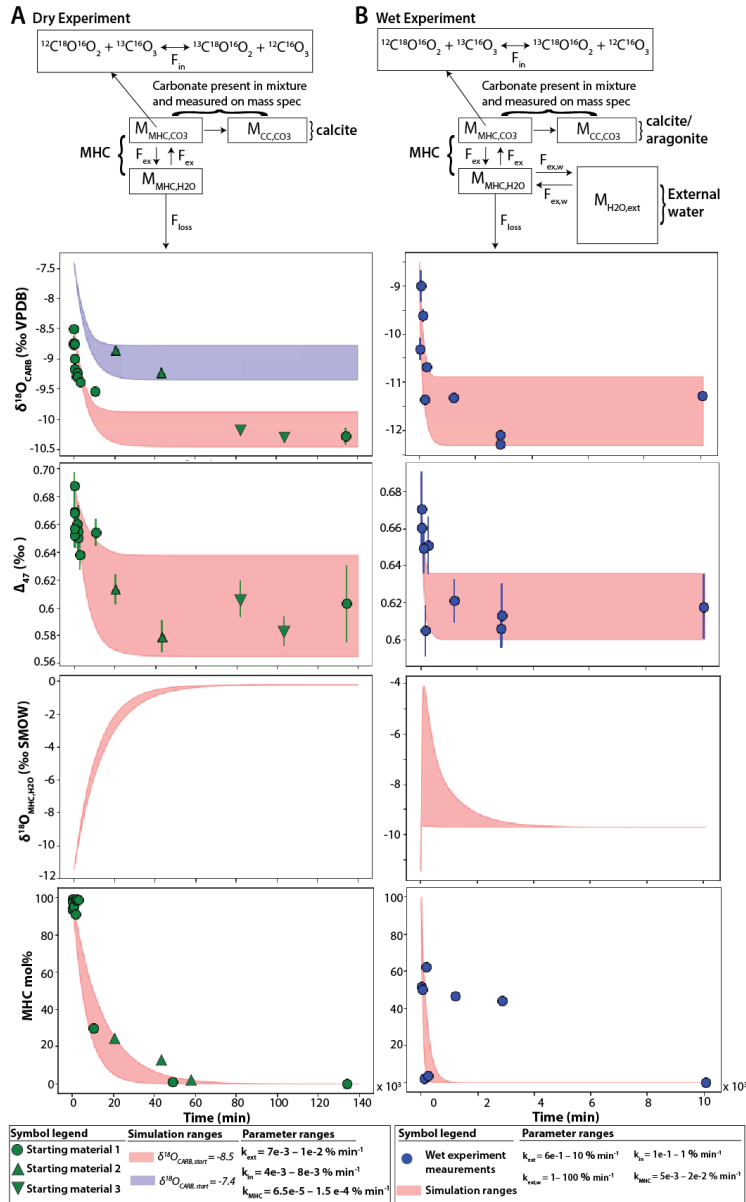
Fig. 5.6: Simulation results for MHC heating experiments. (A) Simulation results from proposed isotopic exchange model for dry (A) and wet (B) experiments. (A) Upper panel shows the box model set-up with three reservoirs of MHC (M_{MHC}), anhydrous carbonate (M_{CC}), and structural H_2O (M_{H2O}). The equilibrium exchange flux for oxygen isotopes (F_{ex}) and clumped isotopes (F_{in}) between structural CO_3^{2-} and H_2O-associated oxygen drives the decrease in $\delta^{18}O_{CARB}$ and Δ_{47} of the carbonate, and the oxygen isotope increase for structural H_2O within the MHC ($\delta^{18}O_{MHC,H2O}$). F_{loss} represents the loss of structural H_2O. Grid search simulation solution ranges are shown in pink and compared with experimental results from Fig. 5.4 (green symbols). Blue simulation ranges represent the same isotopic model but with a different starting $\delta^{18}O_{CARB}$ of materials. The range of first order reaction coefficients for oxygen isotope exchange (k_{ex}), clumped isotope exchange (k_{in}), and reaction progress (k_{MHC}) used for simulations are given in the legend. (B) Same as A except wet experiments also include oxygen isotope equilibrium exchange flux ($F_{ex,w}$) between an infinite external water reservoir ($M_{H2O,ext}$) and structural H_2O. Therefore, we constrain also the first order reaction coefficient for oxygen isotope exchange between external and structural H_2O ($k_{ex,w}$).

satisfied these criteria varied between 7e-3 to 1e-2 %min^{-1}, 4e-3 to 8e-3 %min^{-1}, and 6.5e-5 to 1.5e-4 mol% min^{-1} for k_{ex}, k_{in}, and k_{MHC} respectively. For wet experiments k_{ex}, $k_{ex,w}$, k_{in}, and k_{MHC} were found to have a larger possible range due to larger spread of data and an extra degree of freedom. It was also found that the exchange and reaction coefficients were 1 to 3 orders of magnitude faster compared to the dry experiment, suggesting that transformation and exchange happens faster in a subaqueous environmentthan in a subaerial environment. Specifically, model fits to the wet experiments yielded ranges of 6e-1 to 10 %min^{-1}, 1-100 %min^{-1}, 1e-1 to 1%min^{-1}, and 5e-3 to 2e-2 %min^{-1} for k_{ex}, $k_{ex,w}$, k_{in}, and k_{MHC}, respectively.

Two essential and possibly counter-intuitive features of the data that the preceding model explains are: 1) changes in isotopic composition of structural carbonate proceed rapidly during MHC dehydration, but effectively stop, well short of equilibrium compositions, once structural water has been removed and the conversion to calcite is complete; and 2) changes in $\delta^{18}O$ and Δ_{47} follow a closely similar rates. These two findings seem to require that isotopic change (in both properties) occurs only within MHC domains and effectively stops when a MHC domain dehydrates and converts to an anhydrous carbonate. This interpretation is consistent with prior findings that calcite is essentially inert to oxygen isotope or clumped isotope changes at the temperatures and timescales of our experiments (e.g. Henkes et al., 2014). It also makes a prediction that if one could heat MHC without transformation to calcite (something we were not able to observe, but that might imaginably be possible for some combination of temperature and water pressure) then our model predicts that one should observe rapid and eventually *complete* re-equilibration of $\delta^{18}O$ and Δ_{47}, rather than the cessation of isotopic change that we observed once transformation of MHC to calcite or aragonite was complete. Conversely, if one observed no change in isotopic composition in such an experiment, our proposed model would be disproven and one should instead conclude that isotopic change is somehow controlled by the micro-physical processes of the transformation reaction itself, yet somehow fails to achieve equilibrium when reaction is complete.

5.6.2 Correcting dehydration diagenetic overprint on $\delta^{18}O_{CARB}$ and Δ_{47} of ikaite

The MHC transformation model functions as a conceptual hypothesis for the isotopic dehydration diagenetic overprint of ikaite. However, the application of our model to isotopic data from ikaite pseudomorphs requires an assumption that ikaite dehydration follows the same isotopic exchange reactions as MHC dehydration. We must constrain the likely temperature-dependent reaction and exchange coefficients related to ikaite dehydration in future studies for fully validated quantitative reconstructions. Although we had originally preferred to perform this experiment on ikaite, MHC does present as a less complicated, more stable, and thus easier material to perform dehydration experiments on. A similar experimental framework applied to ikaite would have to accommodate the extremely rapid transformation process of ikaite (Tang et al., 2009; Sanchez-Pastor et al., 2016; Purgstaller et al., 2017; Stockmann et al., 2018; Tollefsen et al., 2020).

When investigating natural data, marine ikaite pseudomorphs often yield lower $\delta^{18}O_{VPDB}$ values than co-occurring calcites in the same strata. Permian ikaite pseudomorphs were depleted by up to 9 ‰ compared to co-occurring brachiopods (Selleck et al., 2007), Cretaceous ikaite pseudomorphs were depleted by 0.5 to 11 ‰ compared to co-occurring belemnites (Price & Nunn, 2010), and Jurassic ikaite pseudomorphs were depleted by up to 3‰ compared to co-occurring carbonate crusts (Teichert & Luppold, 2013). Other Permian (Frank et al., 2008) and Jurassic (Vasileva et al., 2019) ikaite pseudomorphs exhibited similar values as calcite brachiopods and concretions as well as cements. If ikaite is assumed to have precipitated at lower temperatures than co-occurring calcites, the expectation would be that ikaite $\delta^{18}O_{VPDB}$ would be higher than the calcite $\delta^{18}O_{VPDB}$. Therefore, the summarized data aligns with the expectations from our dehydration experiments: ikaite pseudomorph $\delta^{18}O_{VPDB}$ is lower than its precursor due to dehydration diagenetic overprint. However, it is also possible that the very low $\delta^{18}O_{VPDB}$ values of ikaite pseudomorph carbonate occur because the precursor was influenced by a fresh water component (Selleck et al., 2007; Price & Nunn, 2010), as is the case for modern ikaite growing in Ikka fjord. When examining the $\delta^{18}O_{VPDB}$ of modern transformed ikaite from marine deposits within the Sea of Othotsk, Zaire fan, Nankai Trough, Bransfield Strait, and Ikka fjord (Selleck et al., 2007), the $\delta^{18}O_{VPDB}$ values of ikaite pseudomorph carbonates do not appear to be significantly lower than their expected equilibrium values, rendering data inconclusive with regard to whether a dehydration diagenetic overprint on the isotopic compositions of ikaite pseudomorphs can be expected at all transformation conditions. Further examination of clumped isotope values of the above mentioned samples would be enlightening as to whether a dehydration diagenetic overprint of the temperature and $\delta^{18}O_{VPDB}$ is recorded or not.

As a proof of concept, the model proposed in eq. 1-15 can be adapted to different temperature conditions and hydrated carbonate stoichiometries. To demonstrate, we can apply the proposed oxygen exchange model to the case of ikaite pseudomorph formation in Pleistocene Mono Lake to solve for precursor ikaite formation temperature and $\delta^{18}O_{CARB}$ as an inverse modelling problem (Fig. 5.7). The reaction of ikaite transformation to calcite can be described as:

$$CaCO_3 \cdot 6H_2O \rightarrow CaCO_3 + 6H_2O \ (16.)$$

We must therefore change eq. 5 to the expression in eq. 17 to account for the molar relationship between oxygen associated with structural H_2O ($M_{ikaite,H2O}$) and CO_3^{2-} ($M_{ikaite,CO3}$) within ikaite:

$$M_{ikaite,H2O_t} = 2 * M_{ikaite,CO3_t} (17.)$$

Second, the temperature of transformation must be changed from 80°C. For the purposes of this demonstration, we assume that transformation occurred at room-temperature of 25°C (representing the highest temperatures recorded by ikaite pseudomophs from Mono Lake) although temperature of

transformation could be changed to any desired temperature. Therefore, we change eq. 6 and eq. 12 to the following:

$$F_{ex_{t+1}} = k_{ex} * \left[\varepsilon_{eq,25°C} - \left(\delta^{18}O_{MHC,CO3_t} - \delta^{18}O_{MHC,H2O_t} \right) \right] \quad (18.)$$

$$F_{in_{t+1}} = k_{in} * \left[\Delta_{47_{CO3,25°C}} - \Delta_{47_{MHC,CO3_t}} \right] \quad (19.)$$

The difference between the temperature-dependent oxygen isotope fractionation at 0°C and room temperature (~25°C) is 5.5‰ within calcite (Kim & O'Neil, 1997). Because of the 3:6 carbonate-water oxygen ratio within ikaite, oxygen within carbonate should express 2/3 of this fractionation equivalent to 3.67‰, while oxygen within structural H_2O should express 1/3 of this fractionation equivalent to 1.83‰. All other equations remain the same for the case of ikaite transformation. It is likely that the exchange coefficients as well as reaction coefficients for the case of ikaite transformation at 25°C are not the same as for MHC transformation at 80°C. These must be determined by future experiments. For the purposes of this demonstration, we adapt intermediary values for exchange and reaction coefficients from dry and wet experiments of MHC. Although, we cannot use these absolute values as representative for ikaite transformation and any such attempt would be meaningless, we can assume that the activation energy for the exchange coefficients (k_{ex}, k_{in}) and reaction coefficients (k_{MHC}) would be the same, and thereby their relative rates would be the same.

As a proof of concept, if we apply the adapted model to room-temperature transformation of ikaite assuming similar exchange and reaction coefficients as MHC transformation, we reconstruct ikaite pseudomorph $\delta^{18}O_{VPDB}$ ranges of -4.5 to -2‰ and an average T(Δ_{47}) of ~14°C in one possible scenario (Table 5.2, Fig. 5.7). We simulate both a subaerial dry environment and a subaqueous wet environment. Subaerial and subaqueous environments would give rise to differences in ikaite pseudomorph $\delta^{18}O_{CARB}$ values depending on the lake water $\delta^{18}O_{fluid}$ composition. However, the resulting difference in reconstructed Pleistocene Mono Lake water $\delta^{18}O$ assuming dry and wet conditions is only 0.5‰ (Fig. 5.7). In one possible scenario, simulations show that precursor ikaite precipitated at 0°C with a $\delta^{18}O_{VPDB}$ of -3 to 0‰ can explain the isotopic values of our ikaite pseudomorphs from Pleistocene Mono Lake. This $\delta^{18}O_{CARB}$ and temperature would correspond to precursor ikaite precipitation from $\delta^{18}O_{fluid}$ values of -6 to -3‰ (SMOW) assuming ikaite yields the same temperature-dependent oxygen fractionation between fluid and carbonate as calcite (Kim & O'Neil, 1997).

5.6.3 Preferred interpretation of the Pleistocene Mono Lake tufa isotopic record: a seasonal record

In this section, we interpret the paleoclimatic implications of our conceptual reconstruction of precursor ikaite $\delta^{13}C_{CARB}$, $\delta^{18}O_{CARB}$, and T(Δ_{47}) as compared to the isotopic values of dendritic tufas within the Pleistocene Mono Lake system. We suggest that ikaite formation, pseudomorphism, and dendritic textures represents a seasonal record within Pleistocene Mono Lake.
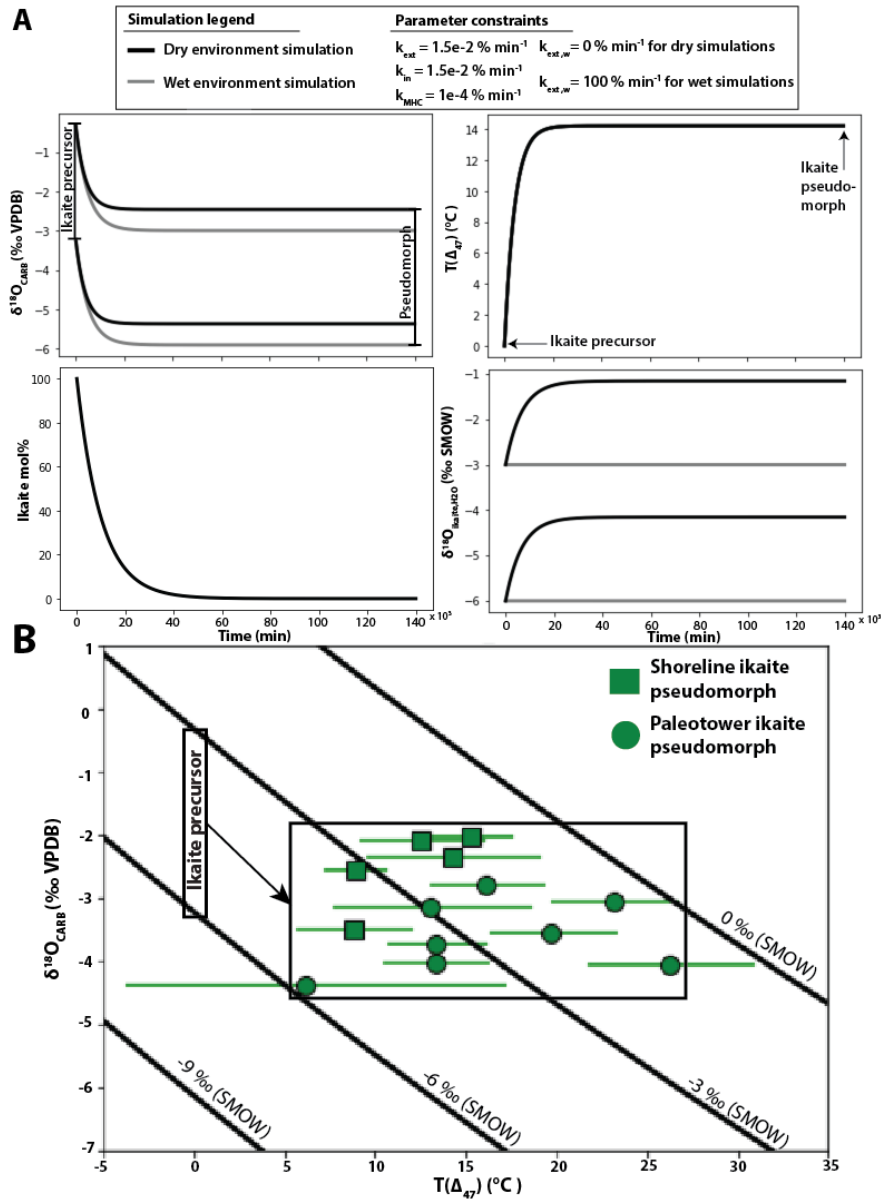
Fig. 5.7: Simulations of Mono Lake ikaite precursor. (A) Dry (black) and wet (grey) simulations of precursor ikaite conversion to pseudomorph from proposed model. The model simulates the expected change in ikaite carbonate oxygen isotopic composition ($\delta^{18}O_{CARB}$) and structural water ($\delta^{18}O_{ikaite,H2O}$), as well as carbonate clumped temperature (T(Δ_{47})) with reaction progress expressed as the change in ikaite mol% in exchange for calcite formation. Two starting conditions for $\delta^{18}O_{CARB}$ were considered corresponding to precipitation of carbonate from lake water $\delta^{18}O_{fluid}$ of -6 to -3‰ (SMOW) at 0°C. Intermediate parameter values for first order reaction coefficients for oxygen isotope exchange (k_{ex}), clumped isotope exchange (k_{in}), and reaction progress (k_{MHC}) were chosen for example simulations. For wet simulations the first order reaction coefficient for oxygen isotope exchange between external and structural H_2O ($k_{ex,w}$) is assumed to be 1, whereas dry simulations can be assumed to not exchange with external water. Note that these simulations closely approximate the measured $\delta^{18}O_{CARB}$ and T(Δ_{47}) of Pleistocene ikaite pseudomorphs from Mono Lake (Fig. 5.3). (B) Back-projection of $\delta^{18}O_{CARB}$ and T(Δ_{47}) of ikaite pseudomorphs (from Fig. 5.3) based on proposed model in Panel A. Black lines denote the correlation between temperature of precipitation and recorded $\delta^{18}O_{CARB}$ in the carbonate when assuming equilibrium fractionation from fluid compositions of 0 ‰, -3 ‰, -6 ‰, and -9 ‰.

5.6.3.1 Dendritic tufas and precursor ikaite formed at alternating seasons from the same fluid

The high $T(\Delta_{47})$ of ikaite pseudomorph most likely records a diagenetic overprint that occurred during equilibrium exchange of oxygen, as demonstrated in section 5.6.2 (Fig. 5.7). This would explain the warmer apparent temperatures recorded by the ikaite pseudomorphs compared to their natural occurrence at ~0°C with a maximum of 9°C in natural environments. This would also explain the systematically high $\delta^{18}O_{CARB}$ of ikaite pseudomorphs as compared to dendritic tufas. While the dehydration diagenetic overprint is expected and likely has driven $\delta^{18}O_{CARB}$ down, the high $\delta^{18}O_{CARB}$ values of ikaite pseudomorphs compared to dendritic tufa values are inherited from the precursor ikaite because carbonate precipitated at lower temperature will record higher $\delta^{18}O_{CARB}$ compared to carbonate precipitated at higher temperatures from the same fluid composition (Fig. 5.3, 5.7) (Kim & O'Neil, 1997). The recorded $T(\Delta_{47})$ range of 6.2-26.2°C would represent the minimum bound on the transformation temperature if assuming the dehydration diagenetic process occurs similar to that within MHC (section 5.6.1-5.6.2). The $\delta^{18}O_{CARB}$ compositions and $T(\Delta_{47})$ values of dendritic tufas were consistent with formation in fluids with $\delta^{18}O_{SMOW}$ compositions of -7.6 to -1.8‰ at a temperature of 3.5 to 25.8°C (Fig. 5.3, Table 5.2). The approximate reconstruction of precursor ikaite tufas ~0°C was consistent with formation in similar fluids to those that formed the dendritic tufas with $\delta^{18}O_{SMOW}$ compositions of -6 to -3‰ (section 5.6.2).

Bischoff et al. (1993) found that the formation of ikaite is seasonal in modern Mono Lake. Our interpretation of Pleistocene precursor ikaite tufas and dendritic tufas as having formed from lake water with similar oxygen isotope compositions but at distinct temperatures of ~ 0°C and 3.5 to 25.8°C would be consistent with the interpretation of Bischoff et al. (1993). In this interpretation of the paragenetic sequence, ikaite formed only in winter, while dendritic tufas formed in slightly warmer conditions/seasons. The ikaite transformed to stable calcium carbonate minerals during warmer seasons. Annual periods of ikaite forming conditions in Pleistocene Lake Russell were likely prolonged compared to present-day due to colder climate in the western US during the Pleistocene (Benson et al., 1990; Benson et al., 1998). Based other experimental observations, the dehydration and pseudomorph formation was fast and occurred in the order of days to months during the transition from winter to spring (Tang et al., 2009; Sanchez-Pastor et al., 2016; Purgstaller et al., 2017; Stockmann et al., 2018; Tollefsen et al., 2020; Scheller et al., 2021).

5.6.3.2 Reconstruction of Pleistocene Mono Lake $\delta^{13}C$ of DIC

We observed through our experiments that $\delta^{13}C_{CARB}$ does not change during dehydration diagenesis. Therefore, it can be assumed that the $\delta^{13}C_{CARB}$ of thinolite/ikaite pseudomorph tufas reflect their precursor environment. The ikaite pseudomorph $\delta^{13}C_{VPDB}$ (4.23±0.13‰) are also largely similar to the $\delta^{13}C_{VPDB}$ of dendritic tufas (3.59±0.98‰), indicating that lake DIC compositions were also similar during ikaite and dendritic tufa formation. The $\delta^{13}C_{VPDB}$ of all the tufas have an average of 3.92‰ (n=29), indicating that

DIC composition of the lake water-ground or spring water mixing zones during precipitation of the paleoshoreline and paleotower facies was ~2.9‰ (VPDB) when applying an ~1‰ fractionation factor between carbonate and DIC (Chacko et al., 2001), slightly higher than today (2 ‰ (VPDB); Broecker & Peng, 1984). Two measurements of dendritic tufas have the lowest $\delta^{13}C_{CARB}$, $\delta^{18}O_{CARB}$, and precipitated from the fluids with the lowest $\delta^{18}O_{fluid}$. Carbonates within Mono Lake sediments from the Pleistocene and Holocene have been observed to have covarying $\delta^{13}C_{CARB}$ and $\delta^{18}O_{CARB}$ interpreted to reflect changes to lake level within closed-basin evaporative system (Li & Ku, 1997; Li et al., 1997). Hence, these low $\delta^{13}C_{CARB}$ and low $\delta^{18}O_{CARB}$ dendritic tufas could reflect a higher lake stage compared to the rest of the samples related to warmer seasons with higher contributions of surface run-off, which are low in $\delta^{13}C_{DIC}$ and $\delta^{18}O_{fluid}$ compared to Mono Lake water (Li & Ku, 1997; Li et al., 1997).

5.7 Conclusions

In this study, we propose a conceptual model that facilitates reconstruction of precursor ikaite $\delta^{18}O_{CARB}$, Δ_{47}, $\delta^{13}C_{CARB}$ from ikaite pseudomorphs within the sedimentary record for use in paleoclimate studies. Monohydrocalcite (MHC) heating experiments reveal that hydrated carbonate dehydration diagenesis decreases $\delta^{18}O_{CARB}$ and Δ_{47}, while $\delta^{13}C_{CARB}$ remains unchanged. MHC transformed to calcite after three months during dry heating, while MHC transformed to calcite and aragonite during subaqueous heating after one week. While the $\delta^{18}O_{CARB}$ and Δ_{47} change within dry experiments is explained by oxygen equilibrium exchange between structural CO_3^{2-} and H_2O, the wet subaqueous experimental conditions caused also minor exchange between structural and external H_2O. Therefore, the change in $\delta^{18}O_{CARB}$ during heating in a subaerial environment is controlled only by the equilibrium conditions of the secondary temperature, while the $\delta^{18}O_{CARB}$ change within a subaqueous environment will also depend on the composition of the external water.

This phenomenon would explain the high $T(\Delta_{47})$ of 6-26°C recorded within ikaite pseudomorph tufas from Pleistocene Mono Lake high-stand deposits. Δ_{47} altered to lower values, towards the diagenetic conditions, during dehydration of the precursor ikaite. Likewise, the higher $\delta^{18}O_{CARB}$ of ikaite pseudomorphs in comparison to dendritic tufas can be explained by carbonate-water fractionation at colder temperatures but similar water isotopic composition. In a proof of concept for correcting the diagenetic overprint through the proposed oxygen equilibrium exchange model, Pleistocene precursor ikaite and dendritic tufas would have precipitated from the same fluid at ~0°C and 3.5 to 25.8°C, respectively. Thus, we propose that precursor ikaite precipitated during the winter and transformed to calcite during the spring through dehydration diagenesis, while dendritic tufas formed at slightly warmer conditions within the Pleistocene Mono Lake system. This study shows that it is possible to reconstruct precursor ikaite $\delta^{13}C_{CARB}$, $\delta^{18}O_{CARB}$ and Δ_{47} from ikaite pseudomorphs. This approach can now be applied to ikaite and other hydrated carbonate pseudomorphs within the sedimentary record for reconstruction of

frigid marine and lacustrine paleotemperature and isotopic compositions, while we look towards future experiments to determine the reaction and exchange coefficients of ikaite transformation.

References

Benson, L. V., Currey, D. R., Dorn, R. I., Lajoie, K. R., Oviatt, C. G., Robinson, S. W., Smith, G. I., Stine, S., 1990, Chronology of expansion and contraction of four great Basin lake systems during the past 35,000 years. *Palaeogeography, Palaeoclimatology, Palaeoecology, 78,* 241-286, https://doi.org/10.1016/0031-0182(90)90217-U.

Benson, L. V., Lund, S. P., Burdett, J. W., Kashgarian, M., Rose, T. P., Smoot, J. P., & Schwartz, M. (1998). Correlation of late-Pleistocene lake-level oscillations in Mono Lake, California, with North Atlantic climate events. *Quaternary Research*, *49*(1), 1-10.

Bischoff, J. L., Fitzpatrick, J. A., & Rosenbauer, R. J., (1993a), The solubility and stabilization of ikaite (CaCO3.6H2O) from 0° to 25°C: Environmental and paleoclimatic implications for thinolite tufa. *Journal of Geology, 101*, 21-33, https://doi.org/10.1086/648194.

Bischoff, James L., Stine, S., Rosenbauer, R. J., Fitzpatrick, J. A., & Stafford, T. W., (1993b), Ikaite precipitation by mixing of shoreline springs and lake water, Mono Lake, California, USA. *Geochimica et Cosmochimica Acta, 57*, 3855-3865, https://doi.org/10.1016/0016-7037(93)90339-X.

Bonifacie, M., Calmels, D., Eiler, J. M., Horita, J., Chaduteau, C., Vasconcelos, C., Agrinier, P., Katz, A., Passey, B. H., Ferry, J. M. & Bourrand, J. J. (2017). Calibration of the dolomite clumped isotope thermometer from 25 to 350 C, and implications for a universal calibration for all (Ca, Mg, Fe) CO3 carbonates. *Geochimica et Cosmochimica Acta*, *200*, 255-279.

Broecker, W. S., Wanninkhof, R., Mathieu, G., Peng, T. H., Stine, S., Robinson, S., Herczeg, A. & Stuiver, M. (1988). The radiocarbon budget for Mono Lake: An unsolved mystery. *Earth and Planetary Science Letters*, *88*(1-2), 16-26.

Buchardt, B., Israelson, C., Seaman, P., & Stockmann, G., (2001), Ikaite Tufa Towers in Ikka Fjord, Southwest Greenland: Their formation by mixing of seawater and alkaline spring water. *Journal of Sedimentary Research, 71,* 176-189, https://doi.org/10.1306/042800710176.

Chacko, T., Cole, D. R., & Horita, J. (2001). Equilibrium oxygen, hydrogen and carbon isotope fractionation factors applicable to geologic systems. *Reviews in Mineralogy and Geochemistry*, *43*(1), 1-81.

Council, T. C., & Bennett, P. C., (1993), Geochemistry of ikaite formation at Mono Lake, California: implications for the origin of tufa mounds. *Geology, 21,* 971-974, https://doi.org/10.1130/0091-7613(1993)021<0971:GOIFAM>2.3.CO;2.

Dahl, K., & Buchardt, B. (2006). Monohydrocalcite in the arctic Ikka fjord, SW Greenland: First reported marine occurrence. *Journal of Sedimentary Research*, *76*(3), 460-471.

Dana, E. S. (1884). *A crystallographic study of the thinolite of Lake Lahontan* (No. 12). US Government
      Printing Office.

De Lurio, J. L., & Frakes, L. A., (1999), Glendonites as a paleoenvironmental tool: Implications for early
      Cretaceous high latitude climates in Australia. *Geochimica et Cosmochimica Acta, 63,* 1039-1048,
      https://doi.org/10.1016/S0016-7037(99)00019-8.

Dempster, T., & Jess, S. A., (2015), Ikaite pseudomorphs in Neoproterozoic Dalradian slates record
      Earth's coldest metamorphism. *Journal of the Geological Society, 172,* 459-464,
      https://doi.org/10.1144/jgs2015-018.

Dennis, K. J., Affek, H. P., Passey, B. H., Schrag, D. P., & Eiler, J. M. (2011). Defining an absolute
      reference frame for 'clumped'isotope studies of CO2. *Geochimica et Cosmochimica Acta*, *75*(22),
      7117-7131.

Dieckmann, G. S., Nehrke, G., Papadimitriou, S., Göttlicher, J., Steininger, R., Kennedy, H., Wolf
      Gladrow, D. & Thomas, D. N. (2008). Calcium carbonate as ikaite crystals in Antarctic sea ice.
      Geophysical Research Letters, *35*(8).

Dunn, J. R., (1953), The origin of the deposits of tufa in Mono Lake [California]: Journal of Sedimentary
      Research, v. 23, p. 18-23, https://doi.org/10.1306/d4269530-2b26-11d7-8648000102c1865d.

Eiler, J. M. (2007). "Clumped-isotope" geochemistry—The study of naturally-occurring, multiply
      substituted isotopologues. *Earth and planetary science letters*, *262*(3-4), 309-327.

Field, L. P., Milodowski, A. E., Shaw, R. P., Stevens, L. A., Hall, M. R., Kilpatrick, A., … Ellis, M. A.,
      (2017), Unusual morphologies and the occurrence of pseudomorphs after ikaite (CaCO 3 ·6H 2 O)
      in fast growing, hyperalkaline speleothems. *Mineralogical Magazine, 81,* 565-589,
      https://doi.org/10.1180/minmag.2016.080.111.

Frank, T. D., Thomas, S. G., & Fielding, C. R., (2008), On using carbon and oxygen isotope data from
      glendonites as paleoenvironmental proxies: a case study from the Permian system of eastern
      Australia. *Journal of Sedimentary Research, 78,* 713-723.

Geptner, A. R., Vetoshkina, O. S., & Petrova, V. V., (2014), New data on the composition of stable
      isotopes in glendonites of the White Sea and their genesis. *Lithology and Mineral Resources, 49,*
      473-490.

Ghosh, P., Adkins, J., Affek, H., Balta, B., Guo, W., Schauble, E. A., Schrag, D. & Eiler, J. M. (2006).
      13C–18O bonds in carbonate minerals: a new kind of paleothermometer. *Geochimica et*
      Cosmochimica Acta, *70*(6), 1439-1456.

Glaring, M. A., Vester, J. K., Lylloff, J. E., Al-Soud, W. A., Sørensen, S. J., & Stougaard, P. (2015).
      Microbial diversity in a permanently cold and alkaline environment in Greenland. *PloS one, 10*(4),
      e0124863.

Gomes, J. P., Bunevich, R. B., Tedeschi, L. R., Tucker, M. E., & Whitaker, F. F., (2020), Facies classification and patterns of lacustrine carbonate deposition of the Barra Velha Formation, Santos Basin, Brazilian Pre-salt. *Marine and Petroleum Geology, 113,* 104176.

Greinert, J., & Derkachev, A., (2004), Glendonites and methane-derived Mg-calcites in the Sea of Okhotsk, Eastern Siberia: implications of a venting-related ikaite/glendonite formation. *Marine Geology, 204,* 129-144.

Henkes, G. A., Passey, B. H., Grossman, E. L., Shenton, B. J., Pérez-Huerta, A., & Yancey, T. E. (2014). Temperature limits for preservation of primary calcite clumped isotope paleotemperatures. *Geochimica et cosmochimica acta*, *139*, 362-382.

Hines, S. K., Eiler, J. M., Southon, J. R., & Adkins, J. F. (2019). Dynamic intermediate waters across the late glacial revealed by paired radiocarbon and clumped isotope temperature records. *Paleoceanography and Paleoclimatology*, *34*(7), 1074-1091.

Huggett, J. M., Schultz, B. P., Shearman, D. J., & Smith, A. J., (2005), The petrology of ikaite pseudomorphs and their diagenesis. *Proceedings of the Geologists' Association, 116,* 207-220, https://doi.org/10.1016/S0016-7878(05)80042-2.

Ingalls, M., Blättler, C. L., Higgins, J. A., Magyar, J. S., Eiler, J. M., & Fischer, W. W. (2020). P/Ca in carbonates as a proxy for alkalinity and phosphate levels. *Geophysical Research Letters*, *47*(21), e2020GL088804.

Jafarzadeh, A. A., & Burnham, C. P. (1992). Gypsum crystals in soils. *Journal of Soil Science, 43*(3), 409-420.

Jansen, J. H. F., Woensdregt, C. F., Kooistra, M. J., & Van der Gaast, S. J., (1987), Ikaite pseudomorphs in the Zaire deep-sea fan: An intermediate between calcite and porous calcite. *Geology, 15,* 245-248.

James, N. P., Narbonne, G. M., Dalrymple, R. W., & Kyser, T. K., (2005), Glendonites in Neoproterozoic low-latitude, interglacial sedimentary rocks, northwest Canada: Insights into the Cryogenian ocean and Precambrian cold-water carbonates. *Geology, 33,* 9-12, https://doi.org/10.1130/G20938.1.

Kim, S. T., & O'Neil, J. R. (1997). Equilibrium and nonequilibrium oxygen isotope effects in synthetic carbonates. *Geochimica et cosmochimica acta*, *61*(16), 3461-3475.

Konopacka-Łyskawa, D. (2019). Synthesis methods and favorable conditions for spherical vaterite precipitation: A review. *Crystals*, *9*(4), 223.

Larsen, D., (1994), Origin and paleoenvironmental significance of calcite pseudomorphs after ikaite in the Oligocene Creede Formation, Colorado. *Journal of Sedimentary Research, 64,* 593-603.

Li, H. C., & Ku, T. L. (1997). δ13C–δ18C covariance as a paleohydrological indicator for closed-basin lakes. *Palaeogeography, Palaeoclimatology, Palaeoecology*, *133*(1-2), 69-80.

Li, H. C., Ku, T. L., Stott, L. D., & Anderson, R. F. (1997). Stable isotope studies on Mono Lake
(California). 1. d18 in lake sediments as proxy for climatic change during the last 150 years.
Limnology and Oceanography, *42*(2), 230-238.

Lu, Z., Rickaby, R. E., Kennedy, H., Kennedy, P., Pancost, R. D., Shaw, S., Lennie, A., Wellner, J. &
Anderson, J. B. (2012). An ikaite record of late Holocene climate at the Antarctic Peninsula.
Earth and Planetary Science Letters, *325*, 108-115.

McLachlan, I. R., Tsikos, H., & Cairncross, B., (2001), Glendonites (pseudomorphs after ikaite) in late
carboniferous Marine Dwyka beds in Southern Africa. *South African Journal of Geology, 104,* 265-
272.

Morales, C. et al. (2017), Glendonites track methane seepage in Mesozoic polar seas. *Geology, 45,* 503-
506.

Nomura, D., Assmy, P., Nehrke, G., Granskog, M. A., Fischer, M., Dieckmann, G. S., Hu, Y. &
Schnetger, B. (2013). Characterization of ikaite ($CaCO_3 \cdot 6H_2O$) crystals in first-year Arctic sea
ice north of Svalbard. *Annals of Glaciology*, *54*(62), 125-131.

Oehlerich, M., Mayr, C., Griesshaber, E., Lücke, A., Oeckler, O. M., Ohlendorf, C., Schmahl, W. W. &
Zolitschka, B. (2013). Ikaite precipitation in a lacustrine environment–implications for
palaeoclimatic studies using carbonates from Laguna Potrok Aike (Patagonia, Argentina).
Quaternary Science Reviews, 71, 46-53.

Papadimitriou, S., Kennedy, H., Kennedy, P., & Thomas, D. N. (2013). Ikaite solubility in seawater
derived brines at 1 atm and sub-zero temperatures to 265 K. *Geochimica et Cosmochimica Acta*,
109, 241-253.

Pauly, H. (1963). " Ikaite", a new mineral from Greenland. *Arctic*, *16*(4), 263-264.

Popov, L. E. et al. (2019), Glendonite occurrences in the Tremadocian of Baltica: first Early Palaeozoic
evidence of massive ikaite precipitation at temperate latitudes. *Scientific Reports, 9,* 1-10,
https://doi.org/10.1038/s41598-019-43707-4.

Price, G. D., & Nunn, E. V., (2010), Valanginian isotope variation in glendonites and belemnites from
Arctic Svalbard: Transient glacial temperatures during the Cretaceous greenhouse. *Geology, 38,*
251-254, https://doi.org/10.1130/G30593.1.

Purgstaller, B., Dietzel, M., Baldermann, A., & Mavromatis, V., (2017), Control of temperature and
aqueous Mg2+/Ca2+ ratio on the (trans-)formation of ikaite. *Geochimica et Cosmochimica Acta,
217,* 128-143, https://doi.org/10.1016/j.gca.2017.08.016.

Qu, Y., Teichert, B. M. A., Birgel, D., Goedert, J. L., & Peckmann, J., (2017), The prominent role of
bacterial sulfate reduction in the formation of glendonite: a case study from Paleogene marine strata
of western Washington State. *Facies, 63,* 10.

Read, J. F., Grotzinger, J. P., Bova, J. A., & Koerschner, W. F. (1986). Models for generation of carbonate cycles. *Geology*, *14*(2), 107-110.

Rogov, M. A., Ershova, V. B., Shchepetova, E. V., Zakharov, V. A., Pokrovsky, B. G., & Khudoley, A. K., (2017), Earliest Cretaceous (late Berriasian) glendonites from Northeast Siberia revise the timing of initiation of transient Early Cretaceous cooling in the high latitudes. *Cretaceous Research, 71,* 102-112.

Russell, I. C. (1889). *Quaternary history of Mono Valley, California*. US Government Printing Office.

Ryb, U., & Eiler, J. M. (2018). Oxygen isotope composition of the Phanerozoic ocean and a possible solution to the dolomite problem. *Proceedings of the National Academy of Sciences*, *115*(26), 6602-6607.

Sánchez-Pastor, N., Oehlerich, M., Astilleros, J. M., Kaliwoda, M., Mayr, C. C., Fernández-Díaz, L., & Schmahl, W. W. (2016). Crystallization of ikaite and its pseudomorphic transformation into calcite: Raman spectroscopy evidence. *Geochimica et Cosmochimica Acta*, *175*, 271-281.

Scheller, E. L., Grotzinger, J., & Ingalls, M. (2022). Guttulatic calcite: A carbonate microtexture that reveals frigid formation conditions. *Geology*, *50*(1), 48-53.

Selleck, B. W., Carr, P. F., & Jones, B. G., (2007), A Review and Synthesis of Glendonites (Pseudomorphs after Ikaite) with New Data: Assessing Applicability as Recorders of Ancient Coldwater Conditions. *Journal of Sedimentary Research, 77,* 980-991, https://doi.org/10.2110/jsr.2007.087.

Shearman, D. J., McGugan, A., Stein, C., & Smith, A. J., (1989), Ikaite, CaCO 3 . 6H 2 O, precursor of the thinolites in the Quaternary tufas and tufa mounds of the Lahontan and Mono Lake Basins, western United States. *Geological Society of America Bulletin, 101,* 913-917, https://doi.org/10.1130/0016-7606(1989)101<0913:ICOPOT>2.3.CO;2.

Stanley, S. M., & Hardie, L. A., (1998), Secular oscillations in the carbonate mineralogy of reef-building and sediment-producing organisms driven by tectonically forced shifts in seawater chemistry. *Palaeogeography, Palaeoclimatology, Palaeoecology, 144,* 3-19.

Stockmann, G. et a. (2018), Control of a calcite inhibitor (phosphate) and temperature on ikaite precipitation in Ikka Fjord, southwest Greenland. *Applied Geochemistry, 89,* 11-22, https://doi.org/10.1016/j.apgeochem.2017.11.005.

Stolper, D. A., & Eiler, J. M. (2015). The kinetics of solid-state isotope-exchange reactions for clumped isotopes: A study of inorganic calcites and apatites from natural and experimental samples. *American Journal of Science*, *315*(5), 363-411.

Suess, E., Balzer, W., Hesse, K.F., Müller, P.J., Ungerer, C.A., Wefer, G., 1982. Calcium carbonate hexahydrate from organic-rich sediments of the Antarctic shelf: Precursors of

glendonites. *Science, 216,* 1128-1131.

Swainson, I. P., & Hammond, R. P., (2001), Ikaite, CaCO3·6H2O: Cold comfort for glendonites as paleothermometers. *American Mineralogist, 86,* 1530-1533, https://doi.org/10.2138/am-2001-11-1223.

Tang, C. C., Thompson, S. P., Parker, J. E., Lennie, A. R., Azough, F., & Kato, K. (2009). The ikaite-to-vaterite transformation: new evidence from diffraction and imaging. *Journal of Applied Crystallography*, *42*(2), 225-233.

Teichert, B. M. A., & Luppold, F. W., (2013), Glendonites from an Early Jurassic methane seep—Climate or methane indicators? *Palaeogeography, Palaeoclimatology, Palaeoecology, 390,* 81-93.

Thiagarajan, N., Adkins, J., & Eiler, J. (2011). Carbonate clumped isotope thermometry of deep-sea corals and implications for vital effects. *Geochimica et Cosmochimica Acta*, *75*(16), 4416-4425.

Tollefsen, E., Balic-Zunic, T., Mörth, C. M., Brüchert, V., Lee, C. C., & Skelton, A., (2020), Ikaite nucleation at 35 C challenges the use of glendonite as a paleotemperature indicator. *Scientific Reports, 10,* 1-10.

Vasileva, K. Y., Rogov, M. A., Ershova, V. B., & Pokrovsky, B. G., (2019), New results of stable isotope and petrographic studies of Jurassic glendonites from Siberia. *Geologiska Föreningens i Stockholm Förhandlingar, 141,* 225-232.

Vickers, M., Watkinson, M., Price, G. D., & Jerrett, R., (2018), An improved model for the ikaite-glendonite transformation: Evidence from the lower cretaceous of spitsbergen, Svalbard. *Norsk Geologisk Tidsskrift,* https://doi.org/10.17850/njg98-1-01.

Virtanen, P., et al. (2020). SciPy 1.0: fundamental algorithms for scientific computing in Python. *Nature methods*, *17*(3), 261-272.

Wang, Z. et al. (2020), Wide but not ubiquitous distribution of glendonite in the Doushantuo Formation, South China: Implications for Ediacaran climate. *Precambrian Research, 338,* https://doi.org/10.1016/j.precamres.2019.105586.

Whiticar, M. J., & Suess, E. (1998). The Cold Carbonate Connection Between Mono Lake, California and the Bransfield Strait, Antarctica. *Aquatic Geochemistry*, *4*(3), 429-454.

Chapter 6

Aqueous alteration processes and implications for organic geochemistry in Jezero crater, Mars

Primary 10 authors: Eva L. Scheller[1][†] & Joseph Razzell Hollis[2,3][†], Emily L. Cardarelli[2], Andrew Steele[4], Luther W. Beegle[2], Rohit Bhartia[5], Pamela Conrad[4], Kyle Uckert[2], Sunanda Sharma[2], Bethany L. Ehlmann[1,2]

†These authors contributed equally to this work

[1] Division of Geological and Planetary Sciences, California Institute of Technology, Pasadena, CA 91106, US

[2] NASA Jet Propulsion Laboratory, California Institute of Technology,; Pasadena, CA, US

[3] Natural History Museum of London, London, UK

[4] Earth and Planets Laboratory, Carnegie Institution for Science;, Washington, DC, US

[5] Photon Systems Incorporated, Covina, CA, US

[full author list can be found as table in Appendix C]

6.1 Abstract:

The Perseverance rover's SHERLOC instrument used deep-UV Raman and fluorescence spectroscopy to discover evidence for two potentially habitable ancient aqueous environments that contain aromatic organic compounds. Spectral and textural observations of the olivine-carbonate assemblage within Jezero crater, Mars reveal carbonation of ultramafic protolith. A separate, probably later, brine formed sulfate-perchlorate mixtures in void spaces. Fluorescence signatures consistent with multiple types of aromatic organic compounds occur throughout these samples, preserved in minerals related to both aqueous processes. These organic-mineral associations indicate aqueous alteration processes led to the preservation and possibly formation of organic compounds on Mars.

6.2 Introduction

The Perseverance rover landed in Jezero crater, a site selected to fulfill the Mars-2020 mission goals: to determine whether life ever existed on Mars, to characterize the geology and climate of Mars, and to prepare for human exploration (Farley et al., 2020). Jezero hosted an open-basin lake during the Noachian (~3.7 Ga) (Farley et al., 2020; Goudge et al., 2015), has units associated with the largest carbonate deposit identified on Mars (Goudge et al., 2015; Ehlmann et al., 2008; Horgan et al., 2020), and has a well-preserved delta with clay and carbonate-bearing sediments, well-suited to preservation of organics (Farley et al., 2020). Organics have previously been detected on Mars (Navarro-González et al,. 2010; Eigenbrode et al., 2018), and here we resolve the spatial and mineralogical context of organics in Jezero crater with the rover's SHERLOC instrument (Scanning Habitable Environments with Raman and Luminescence for Organics and Chemicals), a deep-ultraviolet fluorescence and Raman spectrometer capable of mapping organic and mineral composition with a spatial resolution of 100 μm (Bhartia et al., 2021).

We report the presence of organics and aqueously formed minerals at Jezero crater in three rock targets (Appendix C) analyzed during the first 208 sols of the mission (Fig. 6.1) located in two different orbitally and rover-identified geological units within the floor of Jezero crater (Farley et al., submitted; Stack et al., 2020). The Garde target is from the altered ultramafic Séítah formation (Fm), orbitally mapped as the Crater Floor Fractured 1 unit (CF-f1) (Fig. 6.1) (Farley et al., submitted; Stack et al., 2020; Holm-Alwmark et al., 2021). The Guillaumes and Bellegarde targets are from the overlying and therefore younger basaltic Máaz Fm, orbitally mapped as the ~2.3-2.6 Ga (Holm-Alwamark et al., 2021) Crater Floor Fractured Rough unit (CF-fr) (Farley et al., submitted; Stack et al., 2020; Holm-Alwmark et al., 2021).
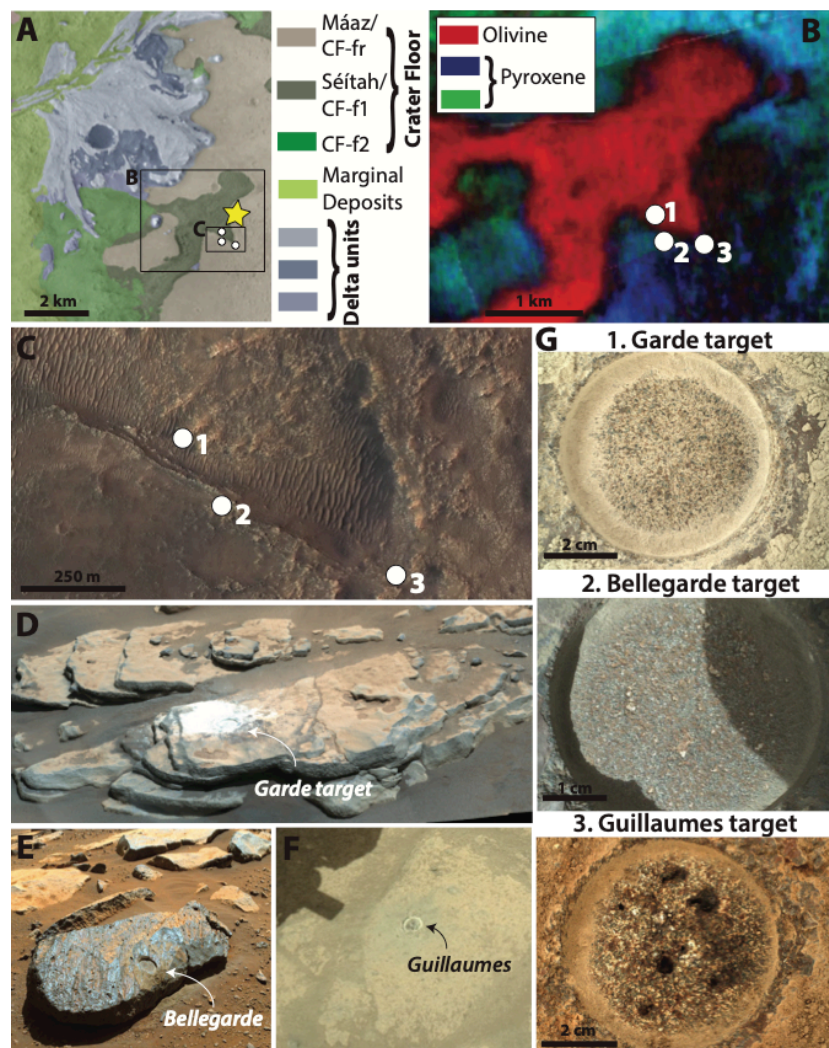
Fig. 6.1: Rover images of the three abraded targets and their orbital context. (A) Map of orbitally defined geological units within Jezero crater from (Stack et al., 2020), including the Crater Floor Fractured Rough unit (CF-fr) equivalent to the Máaz Fm, the Crater Floor Fractured 1 (CF-f1) unit equivalent to the Séítah Fm, and the Crater Floor Fractured 2 (CF-f2) unit. Star shows the Octavia E. Butler landing site, while white circles show the position of the three abraded targets. The locations of panels B and C are outlined in black rectangles. (B) Orbital infrared spectroscopy map showing the location of pyroxene- or olivine-bearing materials in the study area from (Horgan et al., 2020). Labels on white circles correspond to panel G. (C) HiRISE view of study area. (D) Mastcam-Z image showing the Garde patch on the Bastide outcrop. (E) Mastcam-Z image showing the Bellegarde patch on the Rochette rock. (F) Navcam image showing the Guillaumes patch on the Roubion outcrop. (G) WATSON images of abraded targets analyzed in this study.

6.3 Mineral and fluorescence detections in the Séítah Fm

All three Raman spectral scans (Appendix C) from Garde exhibit strong peaks that have a peak position range of 1080–1090 cm^{-1} (n=38) attributed to carbonate, and peaks with a peak position range of 820–840 cm^{-1} (n=60) attributed to olivine (Fig. 6.2) (Appendix C, Razzell Hollis et al., 2021ab). These spectral detections were overlaid on Wide-Angle Topographic Sensor for Operations and eNgineering

(WATSON) camera images to correlate spectral position with textures (Appendix C). Olivine and carbonate are found associated with μm- to mm-sized light-toned tan, reddish-brown, and dark-toned sub-angular grains as well as light-toned intergranular spaces (Fig. 6.2B,E). Spectral features of olivines and carbonates often co-occur in a single spectrum; however, there are also areas where either olivine or carbonate occur independently. Spectral observations of a weak, broad Raman peak centered ~1060 cm^{-1}
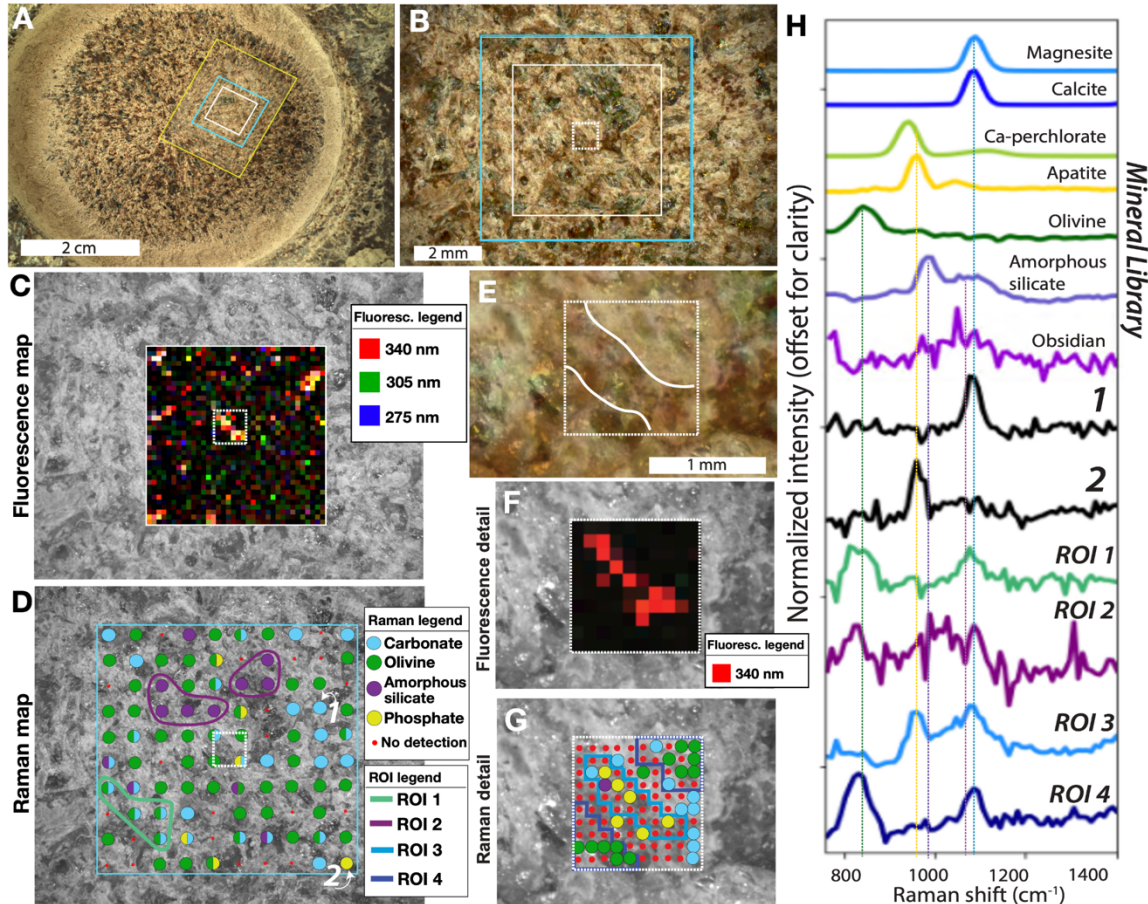
Fig. 6.2: SHERLOC Raman and fluorescence results for the Garde abraded patch. (A) WATSON image of abraded patch with SHERLOC context image superimposed. Blue and white squares show the outline of fluorescence and Raman maps, respectively. Yellow rectangle is outline of panel B. (B) Zoom in on panel A showing WATSON and context image merge image. White dotted outline in panel B-D indicates the location of the high-resolution detail scan (Appendix C) shown in panel E-G. (D-G) Grey-scale version of image in panel B with data superimposed. (C) Fluorescence map showing the intensity of three main features centralized at 340 nm, 305 nm, and 275 nm in red, green, and blue, respectively. (D) Raman mineral maps showing the location of detected olivine, carbonate, phosphate, and weak amorphous silicate features. Purple and green outlines are regions of interest (ROIs 1-2) used for spectra shown in panel H. (E) Zoom in on panel B shows that strong fluorescence signatures correlate with intergranular spaces between grain boundaries (outlined in white lines). (F) Fluorescence map from detail scan showing high-intensity 340 nm feature in red. (G) Raman map from detail scan and ROI 3-4 outlines intergranular and mineral domain textures (same legend as panel D). (H) Representative Raman spectra from SHERLOC (1-2) and average spectra from ROIs compared with laboratory measurements. Positions of representative spectra are indicated with numbers in panel D, while ROIs are indicated with colored outlines in panel D and G.

(FWHM ~200 cm^{-1}) may indicate a disordered phase consistent with amorphous silicates, often difficult to detect given their low intensity (Fig. 6.2). A peak at 965±5 cm^{-1} is likely phosphate, although perchlorate cannot be excluded at low signal to noise ratios (Fig. 6.2).

Garde detail scans (Appendix C) exhibit strong fluorescence signatures, centralized at ~340 nm, that spatially correlate with carbonate, phosphate, and amorphous silicate spectra localized within narrow intergranular spaces (Fig. 6.2E-F). Other areas exhibit less fluorescence (Fig. 6.2C). In a few grid points, an asymmetric fluorescence peak at ~330 nm can be found instead of the dominant ~340 nm symmetric feature. The carbonate peak positions observed within interstitial materials and surrounding grains are observed to be within ±5 cm^{-1} uncertainty of each other (Fig. 6.2H). Laboratory data show that Mg-rich carbonates, such as dolomite and magnesite, have peak positions of 1095-1100 cm^{-1}, while Ca-rich and Fe-rich carbonates have peak positions at 1080-1087 cm^{-1} (Razzell Hollis et al,. 2021ab). Although some of our carbonate measurements fall within the uncertainty of these ranges, wavenumber peak positions mostly between them suggest solid solutions of either Fe-Mg or Ca-Mg carbonate, similar to carbonates in Martian meteorites (Steele et al., 2007). Other Perseverance instrument observations found mixed Fe- and Mg-carbonates consistent with SHERLOC observations (Farley et al., submitted). The position of the olivine peak appears shifted compared to our reference spectra, which were acquired for Mg-rich olivines with Fo# 80-90 (Razzell Hollis et al., 2021); lower frequency indicates that the olivines present in Garde are relatively Fe-rich by comparison (Kuebler et al., 2006).

6.4 Mineral and fluorescence detections in the Máaz Fm

Guillaumes features white and reddish brown, anhedral patches, 1-2 mm across (Fig. 6.3A, S1). These are secondary materials within a basaltic igneous rock (Farley et al., 2021) interpreted as void fills and correlate with sulfate and perchlorate spectra. Spectra with high intensity 950-955 cm^{-1} peaks and minor 1090-1095 cm^{-1} and 1150-1155 cm^{-1} peaks match laboratory measurements of anhydrous Na-perchlorate (Fig. 6.3G, Appendix C). Two strong Na-perchlorate detections correlate with centers of the brightest material within the anhedral patches. Guillaumes spectra commonly contain a single low-intensity peak positioned at 950-955 cm^{-1}. We interpret these as low intensity Na-perchlorate, although the cation species is uncertain due to a lack of resolvable minor peaks (Fig. 6.3G, Appendix C). Other spectra exhibit a both 950-955 cm^{-1} peaks and equally strong 1010-1020 cm^{-1} peaks, with low intensity broad features at 1120±5 cm^{-1}, and occasional broad 3450±5 cm^{-1} hydration features, consistent with a mixture of sulfate and perchlorate that is minimally hydrated (Fig. 6.3A,G). A Ca-sulfate species best explains these spectra when coupled with elemental chemistry data (Appendix C).

Bellegarde contains white 0.5-1 mm anhedral to sub-euhedral secondary crystals that have a reddish brown semi-isopachous rim interpreted as void fills within a basaltic igneous rock (Appendix C Fig. S2). These crystals exhibit 1010-1020 cm^{-1} peaks, similarly attributed to Ca-sulfate when coupled

with elemental chemistry data (Appendix C). Several of the sulfate peaks are also associated with a narrow low-intensity hydration feature at 3560±5 cm⁻¹, consistent with hydrated Ca-sulfates (Appendix C Fig. S3). The Bellegarde target contains a single 1080±5 cm⁻¹ peak of possible Ca-carbonate (Fig. 6.4, Appendix C Fig. S2). Last, both targets contain materials with a single 965-975 cm⁻¹ peak that we attribute to phosphate minerals, though perchlorate cannot be excluded. These SHERLOC mineral detections within the Bellegarde and Guillaumes targets are consistent with the results from the other instruments (Farley et al., submitted) (Appendix C Fig. S5-S6).
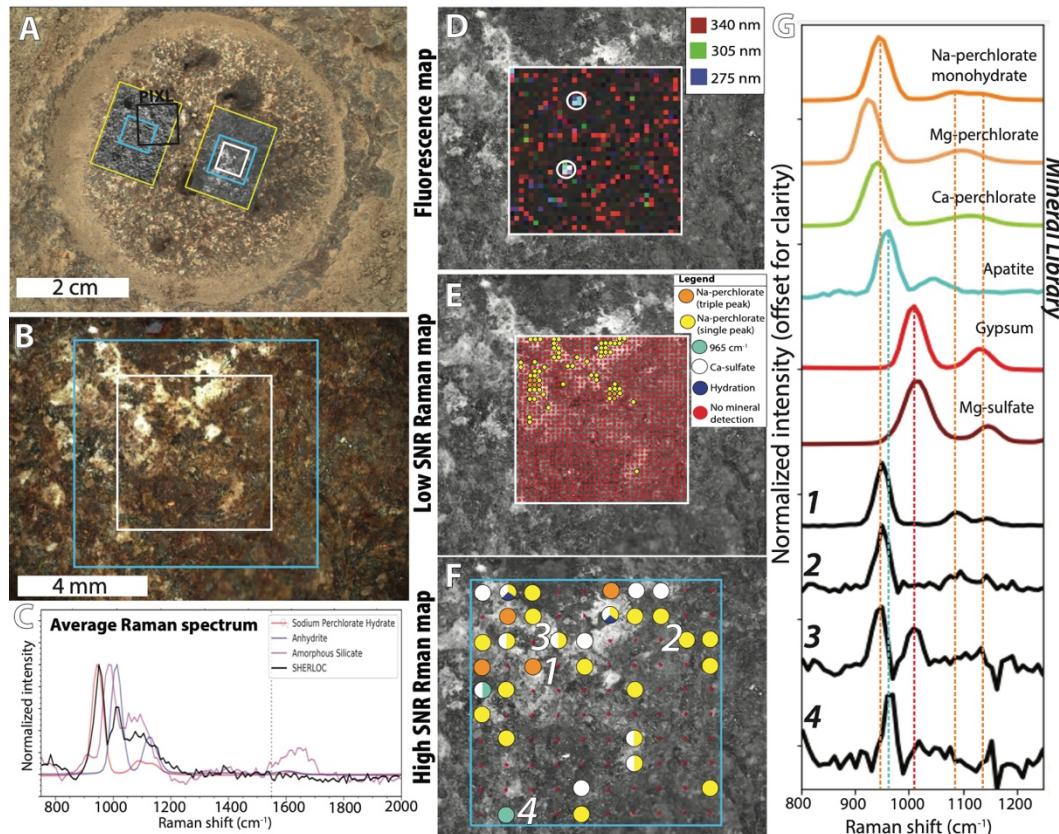
Fig. 6.3: SHERLOC Raman and fluorescence results for the Guillaumes abraded patch. (A) WATSON image of abraded patch with SHERLOC context image superposed inside yellow outline. White, blue, and black squares show the outline of fluorescence and low signal-to-noise ratio (SNR) Raman map (panel D-E), low SNR Raman map (panel F), and PIXL scan (Appendix C Fig. S5), respectively. (B) Zoom in on panel A showing WATSON and context image merge image. (C) Average Raman spectrum compared with laboratory measurements of amorphous silicate showing a possible match to the broad, low intensity feature, while peak features indicate match with Na-perchlorate and anhydrite sulfate. Note features in laboratory spectra at 1500-1600 cm⁻¹ are O₂ (vertical, dotted line) and trace organic contaminants. (D-F) Grey-scale version of image in panel B with data superposed. (D) Fluorescence map showing the intensity of three main features centralized at 340 nm, 305 nm, and 275 nm in red, green, and blue, respectively. White circles indicate locations exposed to LIBS shots (Appendix C). (E-F) Low and high SNR (Appendix C) Raman mineral maps showing the locations of detected perchlorate, Ca-sulfate with and without hydration, and 965 cm⁻¹ peaks. (G) Representative Raman spectra from SHERLOC (1-4) compared with laboratory measurements. Positions of representative spectra are indicated with numbers in panel E-F.
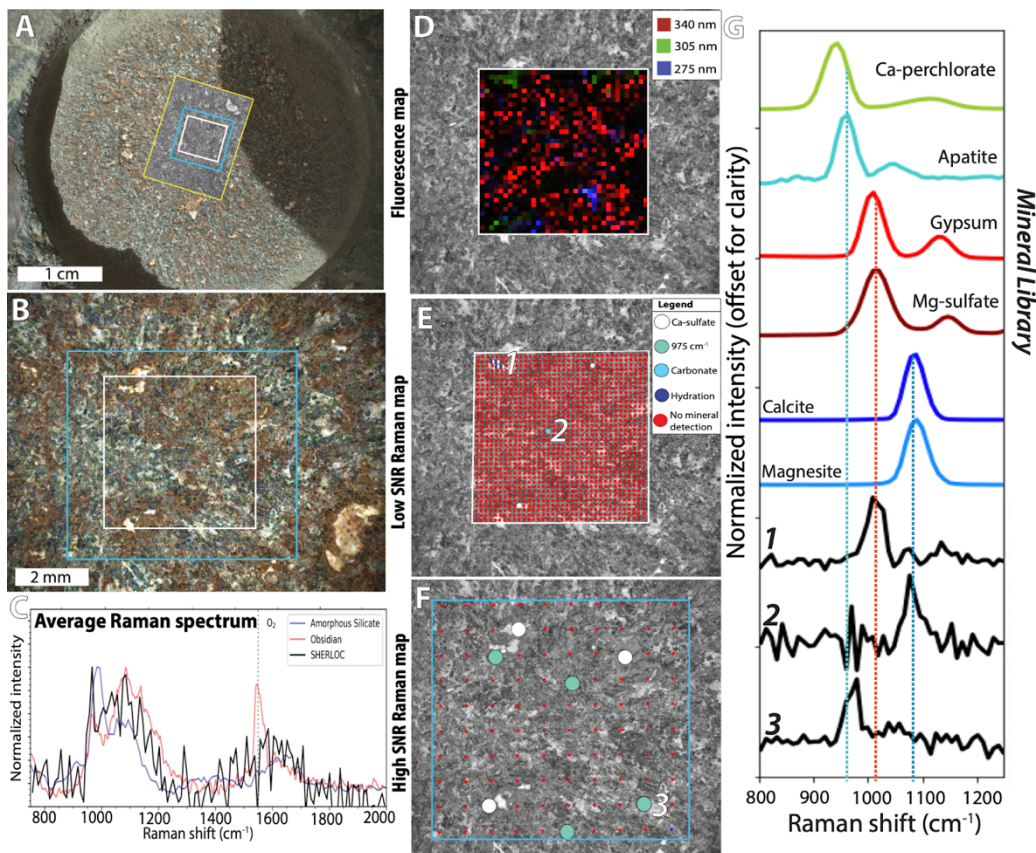
Fig. 6.4: SHERLOC Raman and fluorescence results for the Bellegarde abraded patch. (A) WATSON image of abraded patch with SHERLOC context image superimposed inside yellow outline. Blue and white squares show the outline of fluorescence and low signal-to-noise ratio (SNR) Raman map (panel D-E) and high SNR Raman map (panel F), respectively. (B) Zoom in on panel A showing WATSON and context image merge. (C) Average Raman spectrum compared with laboratory measurements of amorphous silicate and obsidian showing a possible match to the broad, low intensity feature. Note features in laboratory spectra at 1500-1600 cm^{-1} are O$_2$ (dotted line) and trace organic contaminants. (D-F) Grey-scale version of image in panel B with data superposed. (D) Fluorescence map showing the intensity of three main features centralized at 340 nm, 305 nm, and 275 nm in red, green, and blue, respectively. (E-F) Low and high SNR (Appendix C) Raman mineral maps showing the location of detected Ca-sulfate with and without hydration, carbonate, and 975 cm^{-1} peaks. (G) Representative Raman spectra from SHERLOC (1-3) compared with laboratory measurements (full hydrated sulfate spectrum in Appendix C Fig. S3). Positions of representative spectra are indicated with numbers in panel E-F.

Guillaumes and Bellegarde targets commonly exhibit a weak, broad fluorescence feature with a maximum at ~340 nm (Fig. 6.3D, 6.4D) that appears to be widely distributed across each surface and is occasionally correlated with reddish-brown materials. Bellegarde has two other signatures at ~275 and ~305 nm (blue and green, respectively, in Fig. 6.4D), which are strong and localized on specific, light-toned features. The ~305 nm signature is associated with detected sulfate (Fig. 6.4, Appendix C Fig. S2). In Guillaumes, a second fluorescence signature at ~275 nm (Fig. 6.3D) is observed in two locations, approximately 300 μm in diameter, coincident with previous SuperCam (a different Perseverance rover

175

instrument) laser spots (Appendix C).

6.5 Carbonation of ultramafic protolith recorded within Jezero crater

Observation of olivine and carbonate mixtures within the Garde target of the Séítah Fm is consistent with orbital infrared observations (Goudge et al., 2015; Ehlmann et al., 2008; Horgan et al., 2020) and substantiated by multiple lines of evidence (Farley et al., submitted). Previously proposed hypotheses for the formation of these carbonates include low-temperature and high-temperature aqueous alteration of an olivine-rich protolith (Ehlmann et al., 2008; Tarnas et al., 2021; Scheller et al., 2021) or authigenic precipitation from lake or groundwater causing cement or tufa formation (Horgan et al., 2020; Tarnas et al., 2021; Scheller et al., 2021). Our 10-100 μm-scale textural and spectroscopic evidence supports carbonate formation through aqueous alteration of an ultramafic protolith, known as carbonation. The supporting evidence includes: (1) Carbonate cation compositions consistent with those of olivines, suggesting mixed Fe- and Mg-olivine gave rise to mixed Fe- and Mg-carbonates, similar to observations of ultramafic systems on Earth and within Martian meteorites (Steele et al., 2007; Scheller et al., 2021; Kelemen et al., 2011). (2) The observed carbonates co-occur with hydrated materials (Farley et al., submitted) and potentially aqueously formed amorphous silicates and phosphate. (3) The spectral and textural variation of olivine and carbonate dominated zones within both primary grains and intergranular spaces are expected for carbonated ultramafic protoliths on Earth (reviewed in Scheller et al., 2021) and within Martian meteorites (Steele et al., 2007; 2016; 2022).

These observations suggest that the degree of aqueous alteration to the ultramafic protolith was relatively low since large olivine-rich domains remain intact, although the alteration is pervasive and occurs throughout the primary lithology rather than in specific spatial domains, e.g., fractures. In ultramafic alteration environments on Earth and in Martian meteorites, carbonation can be associated with the formation of oxides, hydroxides, and/or Mg-rich phyllosilicates replacing both olivine and orthopyroxene e.g., (Steele et al., 2007; 2016; 2022; Scheller et al., 2021; Kelemen et al., 2011), which have not been observed (Farley et al., submitted). Carbonation can occur in a wide range of temperatures from cold, ambient to hydrothermal/metamorphic (Scheller et al., 2021; Kelemen et al., 2011). High temperature minerals, such as serpentine, have not been definitively observed in the Séítah Fm to date, which may suggest time limited interactions short durations or colder fluid temperatures.

The similarity between the mineralogy of the Garde target in the Séítah Fm to the surrounding widespread, regional olivine-carbonate-bearing unit with a similar orbital spectroscopic signature and geomorphological texture (Ehmann et al., 2008; Horgan et al., 2020; Tarnas et al., 2021; Scheller et al., 2021) suggests that carbonation of olivine may have occurred throughout this extensive region on ancient Mars (~2.7-3.8 Ga). These observations parallel those made by the Spirit rover in Gusev Crater (Morris et al., 2010) and carbonation of olivine or pyroxene documented within (1.3-4 Ga) Martian meteorites

(Steele et al., 2007; 2016; 2022, Tomkinson et al., 2013), while the Curiosity rover found only trace amounts of carbonates within soils (Leshin et al., 2013). Previous modeling efforts have suggested that carbonate deposition could have played a role in the evolution of Mars' atmosphere (Ehlmann et al., 2008; Tomkinson et al., 2013; Edwards & Ehlmann, 2015; Hu et al., 2015), but the geological nature of such a depositional mechanism had remained unexplained. Taken together, micron-scale SHERLOC observations of this phenomenon bridges previous orbital and meteorite observations and demonstrates ultramafic alteration resulting in geological deposition of carbonates. SHERLOC observations also provide evidence that olivine carbonation was involved in either synthesis or preservation of organics (see below), which makes this environment potentially habitable as previously suggested (Farley et al,. 2020; Goudge et al,. 2015; Ehlmann et al., 2008; Horgan et al., 2020; Steele et al., 2016; 2022).

6.6 Later aqueous perchlorate and sulfate brines in Jezero crater

Jezero crater perchlorate detections, like the initial Phoenix observations (Hecht et al., 2009), are substantiated by three independent instruments observing at different spatial resolutions (Farley et al., submitted). Previous evidence for Martian perchlorates includes evolved gas analysis of samples by the Curiosity rover (Leshin et al., 2013; Martin et al., 2020), proposed but later disputed orbital detections within recurring slope lineae (Leask et al., 2018), and detection within the Tissint meteorite (Steele et al., 2018). This new finding substantiates the observation that perchlorates are a typical minor mineral species in the Martian environment. The SHERLOC perchlorate detections differ from previous mission observations because they are observed to be intimately related to aqueous processes including sulfate formation within voids, they occur within the interior of the rock and not on the surface, and they are likely Na-perchlorate.

Perchlorate detection within the Máaz Fm directly substantiates aqueous formation processes on Mars, occurring separately from the older (Farley et al., submitted) Séítah Fm carbonation environment. In PIXL-analyzed Séítah rocks, Mg-sulfates and Na-Cl phases were also observed as void fills that formed after carbonation (Liu et al., submitted). Previous hypotheses for perchlorate formation on Mars are (1) irradiation of chlorine-bearing parent minerals (Carrier & Kounaves, 2015), (2) atmospheric oxidation of chlorine species (Catling et al., 2010), (3) formation from brines (Steele et al., 2018; Bishop et al., 2021; Toner et al., 2014), and/or (4) mobilization in thin films of fluid (Martin et al., 2020). The Jezero perchlorates form white void-fills within rock interiors, and did not form directly on the surface as expected from materials formed by cosmic radiation or atmospheric oxidation, suggesting that either the hypotheses of mobilization through liquid briny water or direct formation in brines must explain their occurrence beneath the surface. The concomitant detection of sulfates and perchlorates within the Guillaumes target is another clue to their origin. It is possible that sulfate formed together with perchlorate or together with parent chlorine-bearing species, such as halite, within percolating briny

waters that were then subsequently oxidized to perchlorate (Steele et al., 2018; Bishop et al., 2021; Toner et al., 2014). Bellegarde exhibited mm-scale crystals of aqueously formed sulfate without detectable quantities of perchlorate, suggesting these brines were not evolved enough to precipitate chlorine-bearing parent species, that perchlorate formation was not pervasive within the Máaz Fm, or that perchlorates were since dissolved. Perchlorates are easily dissolved in liquid water, and therefore perchlorate formation establishes an upper bound on the last period these rocks were exposed to liquid water. The associated void fill texture indicates that these formed after the basaltic host rock crystallized. These observations suggest that sulfate-perchlorate formation occurred in a separate aqueous alteration event, potentially capable of retaining habitable conditions [9,31,35-36], subsequent to the aqueous episode

6.7 Evidence for organics in Jezero crater

DUV fluorescence is particularly sensitive to aromatic organic compounds and the fluorescence signatures observed in all three targets are consistent with emission from aromatic organic compounds containing 1 or 2 fused aromatic rings and/or aromatic heterocycles (Appendix C, Bhartia et al., 2008; 2021). Organics associated with low intensity ~340 nm fluorescence were widespread within Guillaumes and Bellegarde and showed no apparent association with particular minerals (Fig. 6.3-4), though in the Garde target some high intensity ~340 nm fluorescence was concomitant with carbonate, phosphate, and amorphous silicate mixtures (Fig. 6.2F-G). Organics associated with ~305 nm and ~275 nm fluorescence occurred with sulfates within the Bellegarde target (Fig. 6.4D-F). Although assignment of fluorescence signatures to specific organic compounds is non-specific, ~340 nm fluorescence is consistent with a base structure of 2-ring aromatic organics like naphthalene and ~275 nm fluorescence is more consistent with 1-ring aromatic organics like benzene (Bhartia et al., 2008). The ~305 nm fluorescence may be either 1- or 2-ring aromatics, depending on functional groups.

We did not detect Raman peaks consistent with aromatic organic compounds, such as the C=C stretching mode (or G band) around ~1600 cm^{-1}. However, Raman scattered light is several orders of magnitude weaker than fluorescence (Appendix C; Bhartia et al., 2008). Organic concentrations were likely insufficient to produce detectable Raman scattering. Conservative estimates of quantification suggest a range from 5 x 10^{-11} to 3 x 10^{-10} grams of aromatic organics in localized points in the scan (Appendix C). Estimates from the average fluorescence maps (Appendix C Fig. S7) suggest a bulk concentration of 0.1 to 10 ppm, with higher concentrations associated with more aqueously altered surfaces (Appendix C), consistent with known bulk concentrations of organics, containing one and two ring aromatic species, indigenous to Martian meteorites (11.2 ± 6.9 ppm (Steele et al., 2016)), Curiosity rover detections in Gale crater (ranging from ~70 ppbw to 10.6 ± 8.9 ppm (Eigenbrode et al., 2018; Freissinet et al., 2015)), and theoretical concentrations of organics in surface material (Benner et al., 2000).

Several formation mechanisms for Martian organics have been proposed, e.g., infall of meteoritic material (Eigenbrode et al., 2018), a putative relic Martian biosphere, or *in situ* synthesis mechanisms (Steele et al., 2016; 2022). The weak 340 nm fluorescence signature was ubiquitous across separate mineralogy and was also observed on the calibration targets after landing, suggesting it may be organic material within deposited dust. However, the strongest 275, 305, and 340 nm fluorescence signatures were found in materials associated with aqueous processes, i.e. sulfate- and carbonate-bearing materials. In-situ synthesized refractory macromolecular carbon phases (MMC), which are rich in aromatic organics, have been previously shown associated with perchlorate/sulfate formation in Tissint (Steele et al., 2018), and with serpentinization-carbonation processes in ALH8400 (Steele et al., 2022). In both examples, organics were proposed to have been synthesized abiotically and *in situ* at mineral grain boundaries by aqueous processes. Our observations cannot exclude the possibility that these organics were introduced by other abiotic processes, e.g. meteoritic infall, or may derive from putative biological processes. However, given the similarity in organic-mineral associations between Jezero samples and Martian meteorites, abiotic aqueous synthesis is a reasonable explanation for the origin of organic material detected by SHERLOC. Higher spatial resolution analyses upon return of these samples to Earth are necessary to conclusively establish the origins of the detected organics

SHERLOC characterizes mineral assemblages rich in olivine and carbonate indicative of carbonation of an ultramafic protolith. The observed formation of co-occurring Ca-sulfates and perchlorates within younger rocks indicates that subsequent aqueous alteration occurred in Jezero crater. Both of these environments could have been potentially habitable, and SHERLOC observed fluorescence signatures consistent with organics, suggesting that building blocks for life were also present, preserved, and potentially synthesized in these ancient environments. Upon return to Earth of the Montdenier and Montagnac rock samples obtained from the same rock as Bellegarde, and the Salette and Coulette rock samples obtained from the Séítah Fm, we will be able to examine products of two unique aqueous, potentially habitable environments, and their associated organics.

References:

Benner, S. A. et al., (2000), The missing organic molecules on Mars, *Proceedings of the National Academy of Sciences,* 97, 2425-2430.

Bhartia, R. et al., (2021), Perseverance's Scanning Habitable Environments with Raman and Luminescence for Organics and Chemicals (SHERLOC) Investigation. *Space Sciences Review* 217, 58.

Bhartia, R. et al., Explosives Detection and Analysis by Fusing Deep Ultraviolet Native Fluorescence and Resonance Raman Spectroscopy. In Laser-Based Optical Detection of Explosives (eds. Pellegrino, P. M., Holthoff, E. L. & Farrell, M. E.) 67–97 (Taylor & Francis Group, 2015).

Bhartia, R. et al., (2008), Classification of organic and biological materials with deep ultraviolet excitation. *Applied Spectroscopy,* 62, 1070–1077.

Bradski, G. (2000). The OpenCV Library. *Journal of Software Tools*. (2000).

Bishop, J. L. et al., (2021), Martian subsurface cryosalt expansion and collapse as trigger for landslides. *Science Advances, 7*, eabe4459.

Carrier, B. L. et al., (2019), Attenuation of Ultraviolet Radiation in Rocks and Minerals: Implications for Mars Science. *Journal of Geophysical Research Planets*, *124,* 2599–2612.

Carrier, B. L. & Kounaves, S. P., (2015), The origins of perchlorate in the Martian soil. *GRL, 42*, 3739 3745.

Catling, D. C. et al., (2010), Atmospheric origins of perchlorate on Mars and in the Atacama. *Journal of Geophysical Research Planets, 115*(E1).

Edwards, C. S. & Ehlmann, B. L., (2015), Carbon sequestration on Mars. *Geology, 43*, 863-866.

Edgett, K. S., (2021), Perseverance's SHERLOC WATSON – post-landing refinement of relations between focus, range, and image scale using images acquired on Mars, plus an update on particulates on the detector. *Zenodo.* 10.5281/zenodo.5555292.

Ehlmann, B. L. et al., (2008), Orbital identification of carbonate-bearing rocks on Mars. *Science, 322*, 1828-1832.

Eigenbrode, J. L. et al., (2018), Organic matter preserved in 3-billion-year-old mudstones at Gale crater, Mars. *Science, 360*, 1096–1101.

E. Eshelman et al., (2018), Detecting aromatic compounds on planetary surfaces using ultraviolet time-resolved fluorescence spectroscopy. *Planetary and Space Science, 151***,** 1-10.

Eshelman, E. et al., (2015), Time-resolved detection of aromatic compounds on planetary surfaces by ultraviolet laser induced fluorescence and Raman spectroscopy. *Planetary and Space Science, 119***,** 200-207.

Farley, K. et al., (in review), Aqueously-altered igneous and sedimentary rocks on the floor of Jezero crater, Mars, *Science.*

Farley, K. A. et al., (2020), Mars 2020 mission overview, *Space Science Review, 216*, 1-41.

Fischer, E. et al., (2021), Raman spectroscopy as a tool to identify brine formation. *LPSC 6051.*

Freissinet, C. et al., (2015), Organic molecules in the Sheepbed Mudstone, Gale Crater, Mars. *Journal of Geophysical Research, 120*, 495-514.

Fries, M. et al., (in review), The SHERLOC Calibration Target on the Mars 2020 Perseverance Rover:

Design, Operations, and Extended Outreach Functions.

Goudge, T. A. et al., (2015), Assessing the mineralogy of the watershed and fan deposits of the Jezero crater paleolake system, Mars. *Journal of Geophysical Research Planets, 120*, 775-808.

Hecht, M. H. et al., (2009), Detection of perchlorate and the soluble chemistry of martian soil at the Phoenix lander site. *Science, 325,* 64-67.

Holm-Alwmark, S. et al., (2021), Stratigraphic Relationships in Jezero Crater, Mars–Constraints on the Timing of Fluvial-Lacustrine Activity from Orbital Observations. *Journal of Geophysical Research Planets*, e2021JE006840.

Horgan, B. H. et al., (2020), The mineral diversity of Jezero crater: Evidence for possible lacustrine carbonates on Mars. *Icarus, 339*, 113526.

Hu, R. et al., (2015), Tracing the fate of carbon and the atmospheric evolution of Mars. *Nature Communications, 6*, 1-9.

Kelemen, P. B. et al., (2011), Rates and mechanisms of mineral carbonation in peridotite: natural processes and recipes for enhanced, in situ CO2 capture and storage. *Annual Review of Earth and Planetary Sciences, 39*, 545-576.

Kuebler, K. E. et al., (2006), Extracting olivine (Fo–Fa) compositions from Raman spectral peak positions. *Geochimica et Cosmochimica Acta*, *70*, 6201-6222.

Leask, E. K. et al., (2018), Challenges in the search for perchlorate and other hydrated minerals with 2.1 μm absorptions on Mars. *Geophysical Research Letters, 45*, 12-180.

Leshin, L. A. et al., (2013), Volatile, isotope, and organic analysis of martian fines with the Mars Curiosity rover. *Science, 341*.

Leutenegger, S. et al., (2011), BRISK: Binary Robust invariant scalable keypoints," *2011 International Conference on Computer Vision*, 2548-2555.

Martin, P. E et al., (2020), Reevaluation of perchlorate in Gale crater rocks suggests geologically recent perchlorate addition. *Journal of Geophysical Research Planets, 125*, e2019JE006156.

Mason, D. P. and Elwood Madden, M. E., (2021), Using Raman spectroscopy to detect and monitor freezing and melting processes in near-saturated water-salt mixtures at Mars-analogue temperatures. *LPSC, 6013.*

Minitti, M. E. et al., (2021), The Mars 2020 WATSON imaging subsystem of the SHERLOC investigation and anticipated early results. *LPSC, 2548***.**

Morris, R. V. et al., (2010), Identification of carbonate-rich outcrops on Mars by the Spirit rover. *Science*, *329*, 421-424.

Navarro-González, R. et al., (2010), Reanalysis of the Viking results suggests perchlorate and organics at midlatitudes on Mars. *Journal of Geophysical Research Planets, 115*(E12).

Newville, M. et al., (2014), LMFIT: Non-Linear Least-Square Minimization and Curve-Fitting for Python. *Zenodo,* 10.5281/zenodo.11813.

Oren, A. et al., (2014), Perchlorate and halophilic prokaryotes: implications for possible halophilic life on Mars. *Extremophiles, 18*, 75-80.

Razzell Hollis, J. et al., (2021a), A deep-ultraviolet Raman and Fluorescence spectral library of 62 minerals for the SHERLOC instrument onboard Mars 2020. *Planetary Space Science, 209*, 105356.

Razzell Hollis, J. et al., (2021b). Deep-ultraviolet Raman spectra of Mars-relevant evaporite minerals under 248.6 nm excitation. *Icarus, 357*, 114067.

Razzell Hollis, J., Rheingold, D., Bhartia, R., Beegle, L. W., (2020), An Optical Model for Quantitative Raman Microspectroscopy. *Applied Spectroscopy, 74*, 684–700.

Salvatore, M. R. et al., (2018), Bulk mineralogy of the NE Syrtis and Jezero crater regions of Mars derived through thermal infrared spectral analyses. *Icarus, 301*, 76-96.

Scheller, E. L. et al., (2021), Formation of Magnesium Carbonates on Earth and Implications for Mars. *Journal of Geophysical Research Planets, 126*, e2021JE006828.

Shkolyar, S., Eshelman, E. J., Farmer, J. D., Hamilton, D., Daly, M. G., & Youngbull, C. (2018). Detecting Kerogen as a Biosignature Using Colocated UV Time-Gated Raman and Fluorescence Spectroscopy. *Astrobiology*, *18*(4), 431–454. https://doi.org/10.1089/ast.2017.1716

Shkolyar, S. et al., (2021), Detecting Ce^{3+} as a biosignature mimicker using UV time-resolved laser induced fluorescence and Raman spectroscopy: Implications for planetary missions. *Icarus*, *354*, 114093.

Smith, R. J. et al., (2021), X-Ray Amorphous Components in Sedimentary Rocks of Gale Crater, Mars: Evidence for Ancient Formation and Long-Lived Aqueous Activity. *Journal of Geophysical Research Planets, 126*, e2020JE006782.

Steele, A. et al., (2022), Organic synthesis associated with serpentinization and carbonation on early Mars. *Science*, *375,* 172-177.

Steele, A. et al., (2018), Organic synthesis on Mars by electrochemical reduction of CO_2. *Science Advances, 4*, eaat5118.

Steele, A. et al., (2007), Comprehensive imaging and Raman spectroscopy of carbonate globules from Martian meteorite ALH 84001 and a terrestrial analogue from Svalbard. *Meteoritics & Planetary Science, 42*, 1549-1566.

Steele, A. et al., (2016), The provenance, formation, and implications of reduced carbon phases in Martian meteorites. *Meteoritics & Planetary Science, 51*, 2203–2225.

Stack, K. M. et al., (2020), Photogeologic map of the perseverance rover field site in Jezero Crater constructed by the Mars 2020 Science Team. *Space Science Review, 216*, 1-47.

Suto, M., Wang, X., Shan, J., & Lee, L. C. (1992). Quantitative photoabsorption and fluorescence spectroscopy of benzene, naphthalene, and some derivatives at 106–295 nm. *Journal of Quantitative Spectroscopy and Radiative Transfer*, *48*(1), 79–89. https://doi.org/https://doi.org/10.1016/0022-4073(92)90008-R.

Tarnas, J. D. et al., (2021), Characteristics, origins, and biosignature preservation potential of carbonate bearing rocks within and outside of Jezero crater. *Journal of Geophysical Research Planets*, e2021JE006898.

Tomkinson, T. et al., (2013), Sequestration of Martian CO_2 by mineral carbonation. *Nature Communications, 4*, 2662.

Toner, J. D. et al., (2014), The formation of supercooled brines, viscous liquids, and low-temperature perchlorate glasses in aqueous solutions relevant to Mars. *Icarus, 233*, 36-47.

Uckert, K. et al., (2019), A semi-autonomous method to detect cosmic rays in Raman hyperspectral data sets. *Applied Spectroscopy, 73*, 1019-1027.

Virtanen, P. et al., (2020), SciPy 1.0: Fundamental Algorithms for Scientific Computing in Python. *Nature Methods, 17*, 261-272.

Wu, Z. et al., (2016), Spectroscopic study of perchlorates and other oxygen chlorides in a Martian environmental chamber. *Earth and Planetary Science Letters, 452*, 123-132.

Chapter 7

Long-term drying of Mars by sequestration of ocean-scale volumes of water in the crust

E. L. Scheller[1*], B. L. Ehlmann[1,2], R. Hu[2], D. Adams[1], Yuk L. Yung[1,2]

[1]Division of Geological and Planetary Sciences, California Institute of Technology, Pasadena, CA, 91125, USA.

[2]Jet Propulsion Laboratory, California Institute of Technology, Pasadena, CA 91109, USA.

7.1 Abstract

Geological evidence shows that ancient Mars had large volumes of liquid water. Models of past hydrogen escape to space, calibrated with observations of the current escape rate, cannot explain the present-day deuterium-to-hydrogen isotope ratio (D/H). We simulated volcanic degassing, atmospheric escape, and crustal hydration on Mars, incorporating observational constraints from spacecraft, rovers, and meteorites. We found that ancient water volumes equivalent to a 100 to 1500 meter global layer are simultaneously compatible with the geological evidence, loss rate estimates, and D/H measurements. In our model, the volume of water participating in the hydrological cycle decreased by 40 to 95% over the Noachian period (~3.7 billion to 4.1 billion years ago), reaching present-day values by ~3.0 billion years ago. Between 30 and 99% of martian water was sequestered through crustal hydration, demonstrating that irreversible chemical weathering can increase the aridity of terrestrial planets.

7.2 Introduction

There is abundant geomorphological evidence for large volumes of surface liquid water early in martian history (Carr & Head, 2003), with estimated volumes equivalent to a ~100 to 1500 m global equivalent layer (GEL) (Carr & Head, 2003; Clifford & Parker, 2001; Di Achille & Hynek, 2010, Kurokawa et al., 2014). Liquid water on Mars decreased over geological time; presently, most water is stored in the polar ice caps or as subsurface ice. Estimates for the total modern water inventory, in the atmosphere and as ice, total a 20 to 40 m GEL (Appendix D, Zuber et al., 1998; Plaut et al., 2007; Christensen et al., 2006). The availability of water to participate in the hydrologic cycles of terrestrial planets is expected to influence their climate and habitability. However, the processes that caused the decline of available water on Mars are poorly constrained. Previous studies have suggested that Mars experienced substantial water loss from atmospheric escape, which is supported by the current atmospheric deuterium-to-hydrogen isotope ratio (D/H) of 5 to 10 × SMOW (standard mean ocean water on Earth; D/H at 1 SMOW is 155.76×10^{-6}) (Appendix D, Doneahue et al., 1995; Webster et al., 2013; Villanueva et al., 2015). The D/H value at ~4 billion years ago was 2 to 4 × SMOW, inferred from martian meteorites (Appendix D Fig. S1) (Boctor et al., 2015; Greenwood et al., 2008). Existing models used these observations, combined with assumed atmospheric escape fractionation factors (α_{escape}) of 0.016 to 0.32 during loss, to estimate integrated atmospheric escape of at least 10 to 200 m GEL (Appendix D Fig. S1) (Kurokawa et al., 2014; Villanueva et al., 2015, Lammer et al., 2003; Alsaeed et al., 2019; Jakosky et al., 2018). These estimates imply an initial 50 to 240 m GEL of water on ancient Mars, which is consistent only with the lower range of geological estimates (100 to 1500 m GEL) (Carr & Head, 2003; Clifford & Parker, 2001; Di Achille & Hynek, 2010; Kurokawa et al., 2014). This has been interpreted as implying a large, unknown reservoir of water on present-day Mars (Kurokawa et al., 2014). For present-day Mars, the rate of atmospheric water loss is measured from the H escape flux because water vapor dissociates in the atmosphere and its

hydrogen escapes. Spacecraft measurements of the current H escape flux, 10^{26} to 10^{27} H atoms s^{-1}, are equivalent to the escape of 3 to 25 m GEL water across 4.5 billion years (Jakosky et al., 2018; Chaffin et al., 2014) and cannot explain all the water loss. Another potential water loss mechanism is crustal hydration through irreversible chemical weathering, in which water and/or hydroxyl are incorporated into minerals. Orbital and in situ data show that widespread chemical weathering has produced a substantial reservoir of hydrous minerals on Mars, potentially totaling hundreds of meters of GEL in the crust (Appendix D, Mustard et al., 2019). We hypothesized that crustal hydration during the first 1 billion to 2 billion years decreased the volume of the hydrologically available water reservoir, followed by subsequent atmospheric loss that fractionated the martian atmosphere to its current observed D/H. We simulated water loss through geological time to constrain Mars' water history and to compare the simulations to D/H data from the Curiosity rover (5) and laboratory analyses of martian meteorites (Appendix D, Fig. S1).
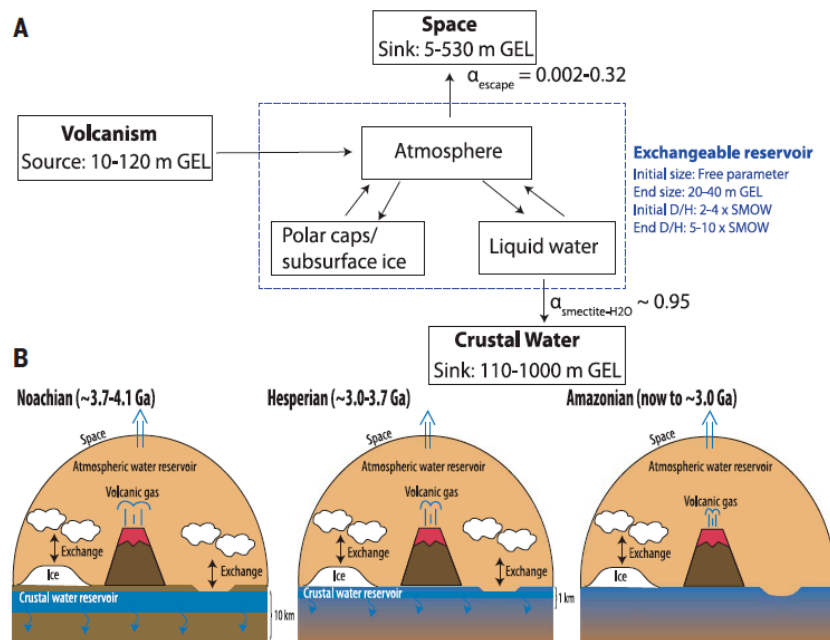
Fig. 7.1. Schematic illustration of water sink and source fluxes considered in our simulations. (A) Box model representation with ranges of integrated water sinks, sources, reservoir sizes, and fractionation factors adopted in our simulations. The crustal water reservoir is based on rover and remote sensing observations and represents all unexchangeable subsurface ice, liquid water, and structural water in minerals (5). The integrated amount of H escape to space is based on measurements of the current flux and KINETICS calculations of fluxes (Appendix D, Figs. S2 and S3). The integrated volcanic degassing is based on thermochemical models (Appendix D, Grott et al., 2011). The blue box indicates the exchangeable reservoir, with its properties in blue text. (B) Schematic representation of our assumptions for the Noachian, Hesperian, and Amazonian periods. During the Noachian, the fluxes associated with crustal hydration and volcanic degassing are high. These all reduce during the Hesperian. During the Amazonian, volcanic degassing falls further, and there is negligible crustal hydration because the water is predominantly solid ice. Ga, billion years ago.

7.3 A hydrogen isotope water reservoir model

We developed a water budget and D/H model that integrates water sinks and sources, including crustal hydration, volcanic degassing, and atmospheric escape (Fig. 7.1) (Appendix D). Most previous models included only atmospheric escape (Kurokawa et al., 2014, Villanueva et al., 2015, Lammer et al., 2003); one model (Alsaeed et al., 2019) also included volcanic degassing. We treat liquid water, ice, and atmospheric vapor as a single exchangeable reservoir, an isotopic modeling technique that was originally developed for carbon reservoir models (Hu et al., 2015). We assume that liquid and solid phases, not vapor, dominate the exchangeable reservoir and that fractionation between them is negligible [the fractionation factor is $\alpha_{ice\text{-}liquid} = 1.02$ (Chacko et al., 2001)]. Our simulations are constrained so that the exchangeable reservoir can never be negative and must reproduce 20 to 40 m GEL water today. The initial exchangeable reservoir size ($X_{ex,0}$)—the ancient hydrologically available water inventory—is a free parameter except during sensitivity analyses. We determined permitted ranges of source and sink fluxes for crustal hydration (F_{crust}), volcanic degassing ($F_{volcanic}$), and atmospheric escape (F_{esc}) during the Noachian (~4.0 billion to 3.7 billion years ago), Hesperian (~3.7 billion to 3.0 billion years ago), and Amazonian (~3.0 billion years ago to present) periods of martian geological history following observational and previous model constraints (Fig. 7.1 and Appendix D, Table S1). Models were evaluated by their ability to reproduce the D/H of the present-day exchangeable reservoir ($R_{ex,end}$) of 5 to 10 × SMOW. We also compared our simulation results with a compilation of Curiosity rover Sample Analysis at Mars (SAM) data sets that recorded a D/H composition range of 3 to 5 × SMOW for gas released from Hesperian samples during high-temperature (>374°C) combustion experiments (Appendix D). We calculated a permitted range of F_{crust} from measurements of water wt % in Mars surface materials and global remote sensing observations of hydrated minerals. The mass fraction of crustal water is based on rover measurements from Gale crater, orbital global infrared and neutron spectrometer data, and measurements of the NWA 7034 martian meteorite (0.5 to 3 wt % water) (Appendix D). The volume of the crustal reservoir is based on orbital measurements of clay exposure depths in the Valles Marineris canyon and craters 5 to 10 km in depth (Appendix D, Mustard et al., 2019). We adopted permitted ranges of 100 to 900 m GEL of water in Noachian aged crust and 10 to 100 m GEL of water in Hesperian-aged crust on the basis of this analysis (Appendix D, Table S1) (Mustard et al., 2019). Although F_{crust} is based on observations of hydrated minerals, we considered crustal water as a single reservoir representing any combination of ice, liquid, and structural water, formerly participating in the hydrologic cycle, that now no longer exchange isotopes with the exchangeable reservoir. We determined $F_{volcanic}$ using previous thermochemical models of the martian mantle (Grott et al., 2011). Different parameterizations of those models (Grott et al., 2011) predict outgassing of a 10 to 120 m GEL of water from volcanic processes
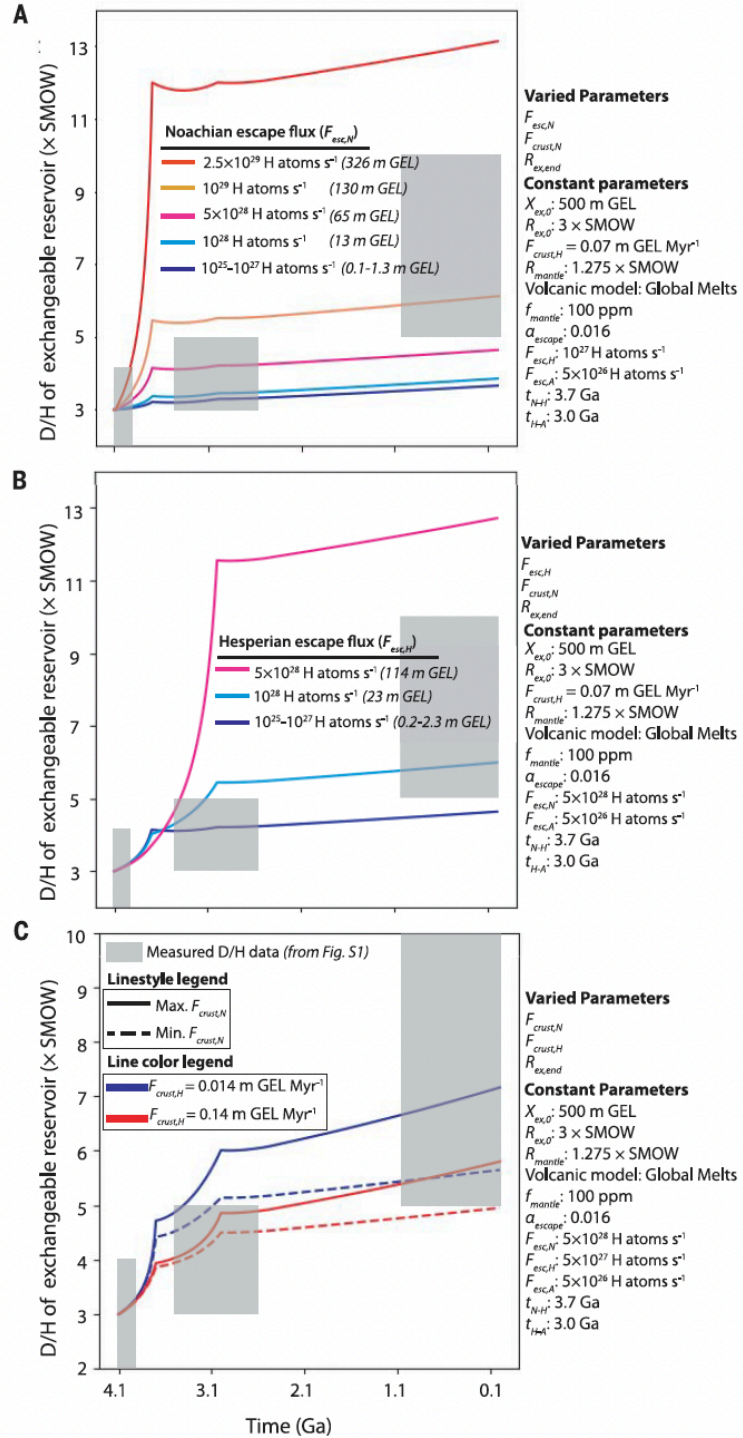
Fig. 7.2. Simulated D/H evolution for different assumptions of crustal hydration and atmospheric escape rates. (A to C) The evolution of the D/H of the exchangeable reservoir in our simulation. Most parameters, including $X_{ex,0}$, are fixed; $R_{ex,end}$ is a free parameter to visualize the model sensitivity. The colored lines show results for different assumptions of the flux rates. The large range of D/H measurements from meteorite, rover, and telescope observations are indicated with gray rectangles (Appendix D, Fig. S1). (A) Effects of increasing the Noachian escape flux ($F_{esc,N}$). (B) Effects of increasing the Hesperian escape flux ($F_{esc,H}$). (C) Effects of increasing the Noachian ($F_{crust,N}$) and Hesperian ($F_{crust,H}$) crustal hydration fluxes. When $F_{crust,N}$ increases, the exchangeable reservoir becomes smaller, inducing larger fractionations during the Noachian. When $F_{crust,H}$ increases, the allowed values of $F_{crust,N}$ decrease, causing less fractionation during the Noachian.

since 4.1 billion years ago (Grott et al., 2011). We considered Noachian and Hesperian F_{esc} values between 1025 and 1030 H atoms s^{-1} and adopted the measured current escape rate of 5×10^{26} H atoms s^{-1} for the Amazonian (Appendix D, Table S1). We compared these escape fluxes with simulations using the one-dimensional (1D) photochemical model KINETICS (Allen et al,. 1981; Nair et al., 1994) with adopted past solar extreme ultraviolet flux, variable atmospheric pressures, and mesospheric and surface temperatures (Appendix D, Table S2).

7.4 Controls on D/H and water loss

In our model, stepwise mixing between the exchangeable reservoir and the depleted volcanically outgassed water vapor (0.8 to $2 \times$ SMOW) (Appendix D, Fig. S1 and Table S1) (Leshin et al., 2000; Gillet et al., 2002) causes the D/H of the exchangeable reservoir to decrease (Appendix D).We do not include fractionation associated with degassing or its redox sensitivity because these are negligible compared with the large range of potential D/H compositions of the volcanic gas inferred from meteorites (Appendix D). Atmospheric escape causes D/H of the exchangeable reservoir to fractionate toward heavier values, which we modeled through stepwise Rayleigh distillation, a common isotopic reservoir modeling technique, at each 10-million-year time step with an α_{escape} of 0.002 to 0.32 (Cangi et al., 2020; Krasnopolsky et al., 2000; Yung et al., 1988). The fractionation factor between smectite, the most common hydrated mineral found on Mars, and water [$\alpha_{smectite-H2O}$=0.95 (Appendix D)] is used in the stepwise Rayleigh distillation model as a first-order approximation of fractionation through crustal hydration (Appendix D, Table S3) (5); we found that this fractionation is minor compared with that caused by atmospheric escape. The D/H of the exchangeable reservoir increases during the Noachian in all our simulations, and through the Hesperian in most of them, because of a combination of crustal hydration and atmospheric escape (Figs. 7.2 and 7.3). Higher $F_{esc,N}$ and $F_{esc,H}$ increase D/H fractionations of the exchangeable reservoirs (Fig. 7.2, A and B). We found that the Noachian and Hesperian H escape flux ranges that satisfy the model constraints (Appendix D, Fig. S2) have a wide allowable range, ~0.1 to 1000 times the current 5×10^{26} H atoms s^{-1} escape flux. Independently, our KINETICS photochemical simulations produced the same range (~10^{25} to 5×10^{29} H atoms s^{-1}) (Appendix D, Fig. S3). We considered multiple scenarios, including (i) a range of standard ancient Mars conditions, (ii) high-altitude water injection [60 parts per million (ppm) at 100 km], and (iii) fixing a surface H_2 mixing ratio of 10^{-3}, which is higher than present-day levels of 10^{-5} (Nair et al., 1994). The maximum KINETICS permitted escape flux (~5×10^{29} H atoms s^{-1}) and our D/H model maximum permitted flux (4×10^{29} H atoms s^{-1}) match the diffusion limited escape of 5×10^{29} H atoms s^{-1} that we calculated using equations from (Kasting & Pollack, 1983). The injection of high-altitude water and increased surface H_2 concentrations both increase the production of high-altitude H_2; one or both would be required for loss fluxes 100 to 1000 times higher than that of the present (Appendix D, Fig. S3). Crustal hydration during early Mars history also increases
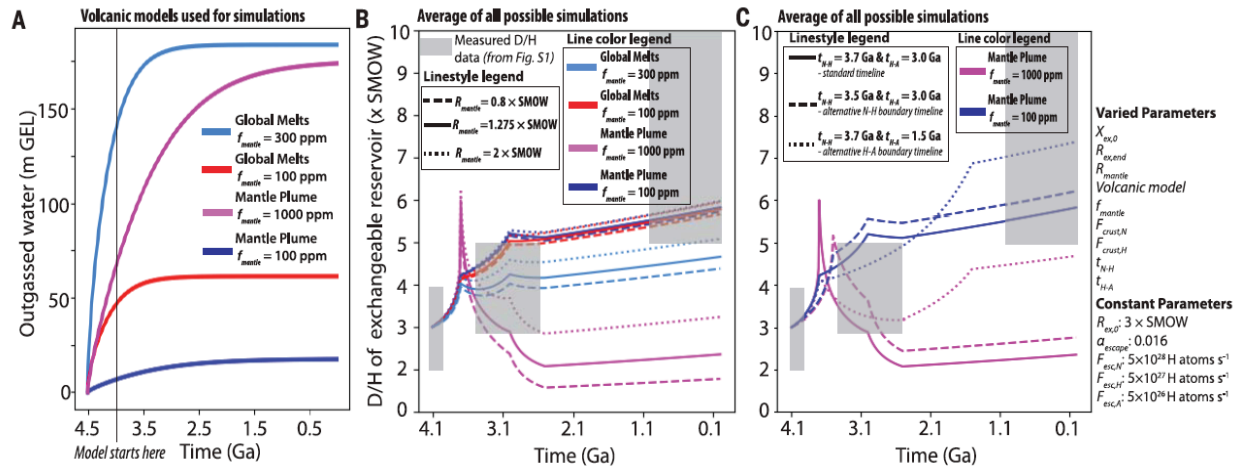
Fig. 7.3. Simulated D/H evolution for different assumptions of the volcanic outgassing as a function of time. (A) Adopted volcanic models (Appendix D, Grott et al., 2011). The Mantle Plume model (Grott et al., 2011) assumes an initial mantle water content (f_{mantle}) of 100 ppm (dark blue) or 1000 ppm (purple). The alternative Global Melts model (Grott et al., 2011) assumes f_{mantle} is 100 ppm (red) or 300 ppm (light blue). (B) The evolution of the D/H ratio in the exchangeable reservoir from an average of simulations with each assumed volcanic model. Line colors are the same as in (A), and gray boxes are the same as in Fig. 7.2. Line styles refer to assumed D/H composition of volcanic gas [dashed, 0.8×SMOW (Gillet et al., 2002); solid, 1.275×SMOW (Usui et al., 2012); and dotted, 2×SMOW (Leshin et al., 2000)]. (C) Evolution of the D/H in the exchangeable reservoir for average of simulations with different assumptions of volcanic model and age of the Noachian-Hesperian boundary (t_{N-H}) and the Hesperian-Amazonian boundary (t_{H-A}) (Appendix D). These transition ages control when F_{esc} and F_{crust} values change under our assumptions for the Noachian, Hesperian, and Amazonian periods (Appendix D). Line colors are the same as in (A). Line styles refer to the assumed timing of t_{N-H} and t_{H-A} (solid, standard boundary ages where t_{N-H} is 3.7 Ga and t_{H-A} is 3.0 Ga; dashed, t_{N-H} is moved to 3.5 Ga; dotted, t_{H-A} is moved to 1.5 Ga). In these simulations, $R_{ex,end}$ is allowed to vary.

D/H fractionation of the exchangeable reservoirs, with the permitted range of $F_{crust,N}$ depending on the assumed $F_{crust,H}$ (Fig. 7.2C). This is primarily because higher $F_{crust,N}$ decreases the exchangeable reservoir size, not because of the fractionation [$\alpha_{smectite-H2O} = 0.95$ (Appendix D)] associated with clay formation. Because the exchangeable reservoir is reduced through crustal hydration, less atmospheric escape is needed to produce the modern D/H of the atmosphere. During the Noachian, decreasing exchangeable reservoir size and increasing D/H are a feature of all of our simulations. Changes to the assumed timing of the boundary between the Noachian and Hesperian (t_{N-H}) and balance of $F_{crust,N}$ to $F_{crust,H}$ only slightly affect the Noachian D/H fractionation (Figs. 7.2C and 7.3C). During the Amazonian, the exchangeable reservoir size is low, and its D/H increases slightly in all our simulations because of the lack of crustal hydration, low H escape flux (assumed equal to the present rate), and a low volcanic degassing flux (Figs. 7.2 and 7.3). By contrast, the D/H evolution during the Hesperian is less well constrained because models with low total volcanic outgassing (10 to 20 m GEL) result in D/H increases, whereas models with high outgassing (60 to 120 m GEL) result in D/H decreasing or staying approximately constant (Fig. 7.3, A and B). The amount of volcanic degassing controls the required sizes of F_{crust} and F_{esc} for different $X_{ex,0}$ to

190

reproduce the present-day D/H ($R_{ex,end}$) (Appendix D, Figs. S4 to S6). Evolution of Hesperian D/H is also sensitive to the absolute timing of the debated (Appendix D) boundary between the Hesperian and Amazonian periods (t_{H-A}) because in our model, that boundary sets the hydration and volcanic flux magnitudes (Fig. 7.3C).

7.5 Crustal hydration as a water sink

Considering the simulations over our whole parameter space, we found that the amounts of water lost through crustal hydration and atmospheric escape vary in ratios ranging from 3:8 to 99:1 (Fig. 7.4 and Appendix D Figs. S4 to S6), which is equivalent to ~30 to 99% of initial water being lost through crustal hydration (Appendix D). The maximum proportional contribution of atmospheric escape occurs when the volume of the crustal water reservoir is minimum and vice versa. Any larger proportional escape would produce D/H heavier than the present day observed value (>10×SMOW). However, the absolute allowed volumes of integrated crustal hydration and atmospheric escape are dependent on the size of the initial exchangeable reservoir (Appendix D Figs. S4 to S6). For some of our atmospheric escape flux relative to the present day flux is required to account for the observed increase in D/H and decrease in the exchangeable water reservoir (Fig. 7.4 and Appendix D, Figs. S3 and S4). Both the maximum and minimum escape-to-space cases (Fig. 7.4 and Appendix D, Figs. S4 to S6) occur with intermediate assumed initial exchangeable reservoir volumes (~500 m GEL). Accounting for water loss through both crustal hydration and atmospheric escape (Appendix D, Figs. S4 to S6) resolves the apparent contradiction between the estimates of integrated H escape, the D/H of present-day Mars, and geological estimates of a large and ancient exchangeable reservoir (Carr & Head, 2003, Kurokawa et al., 2014). These can be reconciled because the amount of atmospheric escape needed for the atmosphere to reach the present-day D/H is reduced by the removal of large initial water volumes through crustal hydration. Our models require larger Noachian exchangeable reservoirs (100 to 1500 m GEL) than those of previous work (50 to 240 m GEL) because we include crustal hydration (Fig. 7.4F). The whole parameter space allows for initial exchangeable water reservoirs of 100 to 1500 m GEL at 4.1 billion years ago, 20 to 300 m GEL at the Noachian-Hesperian boundary, and a near-constant 20 to 40 m GEL throughout the Amazonian (Fig. 7.4F). We chose a preferred solution on the basis of observational constraints on the parameter space (Table 7.1 and Fig. 7.4F). In this preferred simulation, the Noachian and Hesperian H escape fluxes are twice that of today: $F_{esc,N} = F_{esc,H} \sim 10^{27}$ H atoms s^{-1}. The KINETICS simulations indicate that the most probable long-term H escape flux was similar to that of today, although there may have been enhancements of shorter duration, such as during dust storms or surface fluxes of H_2 from geologic processes (Appendix D, Figs. S2 and S3). In the preferred model, crustal hydration removes 500 m GEL and 50 m GEL during the Noachian and Hesperian, respectively, corresponding to roughly 3 wt % H_2O in Noachian crust of 5 km thickness and 1 wt % H_2O in Hesperian crust of 1 km thickness (Mustard et al.,

Table 7.1: Summary of parameters assumed or calculated in preferred simulation scenario. This is a summary table showing the assumed parameter values for our preferred simulation (Fig. 7.4.F) and our reasoning for the selection of these. Our preferred simulation reproduces a D/H composition ~5.3 × SMOW for the present-day atmosphere and an initial exchangeable reservoir size of ~570 m GEL.

Variable	Meaning	Value	Units	Reasoning
Calculated				
$R_{ex,end}$	D/H of present-day exchangeable reservoir	~5.3 × SMOW	N/A	Calculated result of our preferred model
$X_{ex,0}$	Initial size of exchangeable reservoir	~570	m GEL	Calculated result of our preferred model
Assumed				
$R_{ex,0}$	Initial D/H of exchangeable reservoir	4 × SMOW	N/A	D/H measurements of ALH84001 from (Greenwood et al., 2008)
R_{mantle}	D/H of mantle	1.275 × SMOW	N/A	D/H measurements of meteorites from (Usui et al., 2012)
$\alpha_{smectite-H2O}$	D/H fractionation factor between smectite and water	0.95	N/A	Literary review of geochemical experiments (Appendix D, Table S2)
α_{escape}	D/H fractionation factor of atmospheric escape	0.16	N/A	Photochemical model result from (Krasnopolsky, 2000)
$X_{ex,end}$	Present-day size of exchangeable reservoir	20-40	m GEL	A range of remote sensing evidence (Appendix D)
$F_{crust,N}$	Rate of water drawdown by crustal hydration during the Noachian	1.25	m GEL Myr^{-1}	Intermediate value based on remote sensing evidence (Appendix D)
$F_{crust,H}$	Rate of water drawdown by clay formation during the Hesperian	0.07	m GEL Myr^{-1}	Intermediate value based on remote sensing evidence (Appendix D)
f_{mantle}	Water content of mantle	100	ppm	Most commonly adopted meteorite measurements (Appendix D, Grott et al,. 2011)
$F_{volcanic}$	Rate of volcanic degassing of H_2O	Time-dependent fluxes, see text	m GEL Myr^{-1}	Compiling two thermal evolution models from (Grott et al,. 2011)
$F_{volcanic,A}$	Rate of volcanic production after 2.5 Ga	2×10^{-4}	m GEL Myr^{-1}	Geological remote sensing evidence (Appendix D)
$F_{esc,A}$	Present-day H escape flux	5×10^{26}	H atoms s^{-1}	Spacecraft measurements (Appendix D, Jakosky et al., 2018)
$F_{esc,N}$	H escape flux during the Noachian	10^{27}	H atoms s^{-1}	Modelled in this study (Appendix D, Fig. S2-S3)
$F_{esc,H}$	H escape flux during the Hesperian	10^{27}	H atoms s^{-1}	Modelled in this study (Appendix D, Fig. S2-S3)
t_{N-A}	End of deep, "Noachian" crustal alteration	3.7	Ga	Most commonly adopted age (Appendix D)
t_{H-A}	End of shallow , "Hesperian" crustal alteration	3.0	Ga	Most commonly adopted age (Appendix D)

2019). This is compatible with the range of present-day water contents and crustal reservoir depths measured from orbit and rovers (Appendix D). $F_{volcanic}$ is assumed on the basis of volcanic degassing simulations (Grott et al., 2011), which themselves assumed f_{mantle} = 100 ppm on the basis of meteorite measurements (Appendix D). This is compatible with observational constraints on crustal production rates and water contents of martian meteorites (Appendix D). Our preferred simulation is therefore similar to the minimum escape case shown in Fig. 7.4C. These simulations adopt $R_{ex,0}$ = 4×SMOW on the basis of meteorite measurements (Appendix D) and produce a present-day D/H of ~5.3×SMOW.

7.6 Consequences for Mars evolution

If the planet accreted with 0.1 to 0.2 wt % water (Brasser et al., 2013), the large Noachian exchangeable reservoirs predicted by the model are consistent with Mars primordial water volumes. A martian primordial volume of >1100 m GEL (potentially thousands of meters of GEL) could have been produced by catastrophic outgassing of the mantle (~500 to 6000 m GEL) (Elkins-Tanton, 2008; Erkaev et al.,

2014), delivery of water through impacts (600 to 2700 m GEL) (Lunine et al., 2003), and/or capture of gasses from the protoplanetary disc (Lammer et al., 2013). However, the high hydrogen loss rates indicated by the D/H at 4.1 billion years ago recorded within meteorites (Kurokawa et al., 2014, Boctor et al., 2003) and possible evidence for hydrodynamic escape in xenon isotopes (Jakosky & Jones, 1997) suggest that a large part of the primordial atmosphere and water were lost during the pre-Noachian period. Our proposed volumes of a 100 to 1500 m GEL during the early Noachian are within the lower end of these predicted primordial volumes and would therefore be compatible with the loss of a large part of the primordial atmosphere. After loss of the primordial atmosphere, isotope measurements of carbon and argon suggest that loss of a large fraction of these elements from the remaining martian atmosphere and the reservoirs that exchange with the atmosphere would have occurred after 4.1 billion years ago (Hu et al., 2015, Jakosky & Jones, 1997; Atreya et al., 2013; Jakosky et al., 2017;). This matches our proposed trajectory of water loss within the exchangeable reservoir, which is reduced by 80 to 99% after 4.1 billion years ago within our model simulations. Our modeled initial reservoirs are also consistent with geological estimates of Noachian and Hesperian surface water volumes. A 100 to 150-m GEL ocean during the Hesperian (Carr & Head, 2003; Carr & Head, 2019) has been suggested from geomorphological observations and is compatible with our preferred simulation. A larger 550 m GEL ocean that has been suggested at the Noachian-Hesperian boundary (Di Achille & Hynek, 2010) is possible in simulations in which F_{crust} and F_{esc} are both maximized in the Noachian and Hesperian, requiring the initial exchangeable water reservoir at 4.1 billion years ago to be a ~1500 m GEL (Fig. 7.4F). Even larger oceans of 1000 to 1500 m GEL have been proposed on the basis of geomorphology (Carr & head, 2003; Clifford & Parker, 2001); these would be permitted only in certain simulation scenarios during the early Noachian and not later epochs (Fig. 7.4F). Our models are compatible with the major observed trajectories of the martian climate. A high-volume Noachian exchangeable reservoir is consistent with geomorphological evidence for large volumes of Noachian surface waters and observed widespread hydrated mineral formation. Aqueous alteration of the crust could have produced periods of warmer and wetter climates (Appendix D) (Wordsworth et al., 2016; 2015; Tosca et al., 2018) through accumulation of H_2 in the atmosphere (Appendix D Figs. S4 to S6). In cases in which atmospheric escape dominates water loss over the crustal hydration sink, H loss could be balanced by atmospheric oxygen escape (18 to 58 m GEL) and crustal oxidation (~30 to 380 m GEL) (Appendix D). However, in cases in which crustal hydration dominates water loss, short-term accumulation of H_2 could have occurred (Appendix D). In our KINETICS simulations, the accumulation of H_2 in the atmosphere results in increased H escape flux (Appendix D Fig. S3). The permitted parameter space of our D/H model allows either (i) a Hesperian exchangeable reservoir that was initially large but smaller than the Noachian reservoir ($\leq$300-mGEL) and decreased or (ii) a Hesperian reservoir that was similar to present-day levels of a 20 to 40 m GEL (Fig. 7.4F). In case

(i), the Hesperian may have had sustained periods of warm and wet climate, which could have caused chemical weathering on a global scale and potentially formed an ocean (Carr & Head, 2003; Carr & Head, 2019). In case (ii), the Hesperian climate was likely similar to the Amazonian climate, with the exception of few local and short-lived instances of surface liquid water reservoirs (Grotzinger et al., 2015). During the Amazonian period, the low H escape flux and low volcanic degassing flux counter each other, producing low model water availability within the exchangeable reservoir that is consistent with geomorphological and mineralogical evidence of an arid climate (Fig. 7.4F) (Kasting & Pollack, 1983; Ehlmann et al,. 2011). Crustal hydration would produce a buried water reservoir with a composition reflecting that of the Noachian exchangeable reservoir of ~2 to 4 × SMOW. Martian meteorites that are 1.6 billion to 0.1 billion years old have D/H values of ~2 to 3 × SMOW (Usui et al., 2015; Liu et al., 2015). Previously proposed explanations include a distinct subsurface fluid reservoir, mixing between low–D/H igneous and high–D/H present-day atmospheric material, or terrestrial contamination (Usui et al., 2015; Liu et al., 2015). We suggest that exchange between younger igneous rocks and fluids derived from hydrated Noachian (~2 to 4 × SMOW) crust could account for the intermediate D/H in these meteorites.

7.7 Comparative planetary evolution

We conclude that the increasing aridity of Mars over its history was caused by the sink of chemical weathering of the crust (Fig. 7.4), which was recorded in the widespread Noachian hydrated minerals on the planet's surface (Mustard et al., 2019). On Earth, crustal hydration also occurs, but plate tectonics enables recycling of crustal water that is eventually outgassed to the atmosphere through volcanism (Lammer et al., 2009). This has facilitated sustained participation of water in the hydrologic cycle throughout geological history on Earth (Lammer et al., 2009). The ancient age of most hydrated minerals (Ehlmann et al., 2011) indicates that any such recycling did not persist on Mars. Irreversible chemical weathering therefore plays a role in regulating the habitability of terrestrial planets by controlling the time scales of sustained participation of water in the hydrologic cycle. Our model makes testable predictions for D/H measurements of the rock and ice record (Figs. 7.2 and 7.3): a substantial long-term secular increase in D/H over the Noachian and potentially Hesperian, with little change over the Amazonian. Under a variable climate, our model also indicates that the geological record might contain evidence of short-term D/H cyclicity: Transient warm periods with greater atmospheric H_2O (Wordsworth et al,. 2015) would periodically increase crustal hydration and escape flux, rapidly increasing D/H, whereas

during cold periods, the D/H would decrease or increase slowly, depending on the balance between volcanic degassing and atmospheric escape.
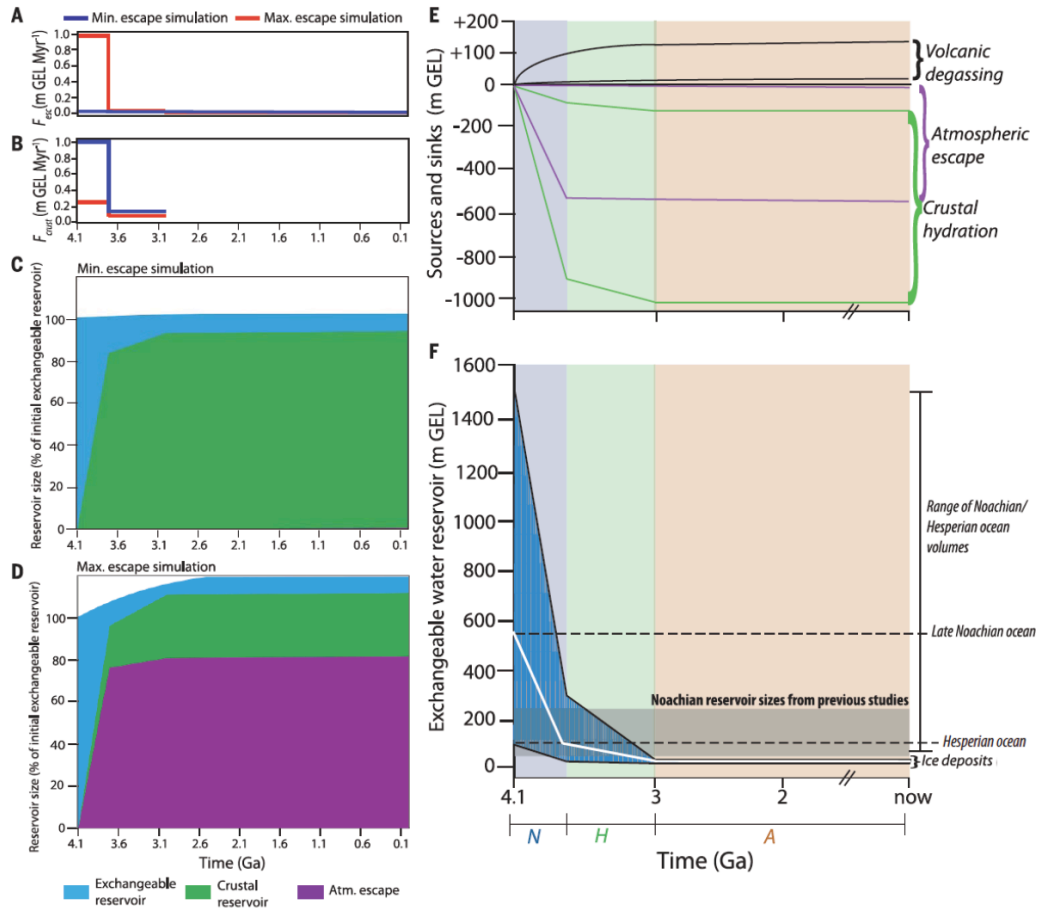
Fig. 7.4. Compilation of relative reservoir sizes through time from all our simulations. (A to D) Model simulations with minimum and maximum possible atmospheric escape fluxes (F_{esc}) and crustal hydration fluxes (F_{crust}) within allowed parameter space and simulation constraints, where the exchangeable reservoir D/H of 5 to 10×SMOW must be reproduced. (A) Evolution of minimum (blue line) and maximum (red line) F_{esc} within the constrained simulation space through geological time. (B) Evolution of minimum (red line) and maximum (blue line) F_{crust} within the constrained simulation space through geological time. [(C) and (D)] Size evolution of three simulated reservoirs through geological time shown as a cumulative percentage. Colored areas indicate the time evolution within the exchangeable reservoir (blue), crustal reservoir (green), and water escaped to the atmosphere (purple). (C) The scenario in which F_{esc} is minimized and F_{crust} is maximized. (D) The scenario in which F_{esc} is maximized and F_{crust} is minimized. (E) Upper and lower bounds on sources and sinks from Fig. 1 through time derived from our simulations (black, volcanic degassing source; green, crustal hydration sink; purple, atmospheric escape sink) (Appendix D). (F) The range of exchangeable reservoir sizes (teal) permitted by our simulations. For comparison, we show the reservoirs derived by previous studies (gray rectangle) (Kurokawa et al., 2014; Villanueva et al., 2015; Lammer et al., 2003; Alsaeed & Jakosky, 2019) and ocean sizes based on geomorphological evidence (dashed lines) (Carr & Head, 2003; Clifford & Parker, 2011; Di Achille & Hynek, 2010). Our preferred simulation scenario is shown as a solid white line. Noachian (N), Hesperian (H), and Amazonian (A) time intervals used in model are shaded in blue, green, and red, respectively.

195

References

Achille, G. Di. & Hynek, B. M., (2010), Ancient ocean on mars supported by global distribution of deltas and valleys. *Nature Geoscience, 3*, 459-463.

Ackerman, A. S., Marley, M. S., (2001), Precipitating condensation clouds in substellar atmosphere. *The Astrophysical Journal, 556*, 872.

Agee, C. B. et al., (2013), Unique meteorite from early Amazonian Mars: Water-rich basaltic breccia Northwest Africa 7034. *Science, 339*, 780-785.

Allen, M., Yung, Y. L., Waters, J. W., (1981), Vertical transport and photochemistry in the terrestrial mesosphere and lower thermosphere (50-120 km). *Journal of Geophysical Research Space Physics, 86*, 3617-3627.

Alsaeed, N. R. & Jakosky, B. M., (2019), Mars water and D/H from 3.3 Ga to present. *Journal Geophysical Research Planets,* DOI: 10.1029/2019JE006066.

Atreya, S. K. et al., (2013), Primordial argon isotope fractionation in the atmosphere of Mars measured by the SAM instrument on Curiosity and implications for atmospheric loss. *Geophysical Research Letters, 40,* 5605-5609.

Audouard, J. et al., (2014), Water in the Martian regolith from OMEGA/Mars Express. *Journal of Geophysical Research Planets, 119*, 1969-1989.

Bramson, A. M., Byrne, S., Bapst, J., (2017), Preservation of midlatitude ice sheets on Mars. *Journal of Geophysical Research Planets, 122*, 2250-2266.

Brasser, R., (2013), The formation of Mars: building blocks and accretion time scale. *Space Science Reviews, 174*, 11-25.

Boctor, N. Z. et al., (2003), The sources of water in Martian meteorites: Clues from hydrogen isotopes. *Geochimica et Cosmochimica Acta, 67*, 3971-3989.

Borg, L. E. et al., (1999), The age of the carbonates in Martian meteorite ALH84001. *Science, 286*, 90-94.

Cangi. E. et al., (2020), Higher Martian Atmospheric Temperatures at All Altitudes Increase the D/H Fractionation Factor and Water Loss. *Journal of Geophysical Research Planets, 125*.

Capuano, R. M. et al., (1993), Evidence of fluid flow in microfractures in geopressured shales. *American Association of Petroleum Geologists bulletin, 77*, 1303-1314.

Carr, M. H., Head, J., (2019), Mars: Formation and fate of a frozen Hesperian ocean. *Icarus, 319*, 433 443.

Carr, M. H., Head, J. W., (2010), Geologic history of Mars. *Earth & Planetary Science Letters, 294*, 185 203.

Carr, M. H. & Head, J. W., (2003), Oceans on Mars: An assessment of the observational evidence and possible fate. *Journal of Geophysical Research Planets, 108*, E5.

Carter, J. et al., (2013), Hydrous minerals on Mars as seen by the CRISM and OMEGA imaging
spectrometers: Updated global view. *Journal of Geophysical Research Planets, 118*, 831-858.

Chacko, T., Cole, D. R., Horita, J., (2001), Equilibrium oxygen, hydrogen, and carbon isotope
fractionation factors applicable to geologic systems. *Reviews in Mineralogy and Geochemistry*,
43, 1-81.

Chaffin, M. S. et al., (2017), Elevated atmospheric escape of atomic hydrogen from mars induced by
high-altitude water. *Nature Geoscience, 10*, 174-178.

Chaffin, M. A. et al., (2014), Unexpected variability of Martian hydrogen escape. *Geophysical Research
Letters*, *41*, 314-320.

Chassefière, E. et al., (2013), The fate of early Mars' lost water: the role of serpentinization. *Journal of
Geophysical Research Planets, 118*, 1123-1134.

Chassefiere, E., Leblanc, F., (2011), Constraining methane release due to serpentinization by the
observed D/H ratio on Mars. *Earth & Planetary Science Letters*, *310,* 262-271.

Christensen, P. R., (2006), Water at the poles and in permafrost regions of Mars. *Elements, 2,* 151-155.

Clancy, R. T. et al., (2000), An intercomparison of ground-based millimeter, MGS, TES, and Viking
atmospheric temperature measurements: Seasonal and interannual variability of
temperatures and dust loading in the global Mars atmosphere. *Journal of Geophysical Research,
105,* 9553-9571.

Claire, M. W. et al., (2012), The evolution of solar flux from 0.1 nm to 160 μm: quantitative estimates
for planetary studies. *The Astrophysical Journal, 757*, 95.

Clifford, S. M. & Parker, T. J., (2001), The evolution of the Martian hydrosphere: Implications for the
fate of a primordial ocean and the current state of the northern plains. *Icarus*, *154*, 40-79.

Baratoux, D. et al., (2013), The petrological expression of early Mars volcanism. *Journal of Geophysical
Research Planets, 118*, 59-64.

Barnes, J. et al*.,* (2020), Multiple early-formed water reservoirs in the interior of Mars. *Nature
Geoscience, 13*, 260-264.

Bhattacharyya, D. et al., (2015), A strong seasonal dependence in the Martian hydrogen exosphere.
Geophysiacl Research Letters, 42, 8678-8685.

Day, J. M. D. et al., (2018), Martian magmatism from plume metasomatized mantle. *Nature
communications, 9,* 1-8 (2018).

Dobson, P. F., Epstein S., Stolper, E. M., (1989), Hydrogen isotope fractionation between coexisting
vapor and, silicate glasses and melts at low pressure. *Geochimica et Cosmochimica Acta, 53*,
2723-2730.

Donahue, T. M., (1995), Evolution of water reservoirs on mars from D/H ratios in the atmosphere and crust. *Nature, 374*, 432-434.

Dundas, C. M. et al., (2018), Exposed subsurface ice sheets in the Martian mid-latitudes. *Science, 359,* 199-201.

Ehlmann, B. L. et al., (2017), Chemistry, mineralogy, and grain properties at Namib and High dunes, Bagnold dune field, Gale crater, Mars: A synthesis of Curiosity rover observations. *Journal of Geophysical Research Planets, 122*, 2510-2543.

Ehlmann, B. L. et al., (2011), Subsurface water and clay mineral formation during the early history of Mars. *Nature, 479*, 53-60.

Elkins-Tanton, L. T., (2008), Linked magma ocean solidification and atmospheric growth for Earth and Mars. *Earth & Planetary Science Letters, 271*, 181-191.

Erkaev, N. V. et al., (2014), Escape of the Martian protoatmosphere and initial water inventory. *Planetary and Space Science, 98*, 106-119.

Fischer, D. A., (2007), Mars' water isotope (D/H) history in the strata of the North Polar Cap: Inferences about the water cycle. *Icarus, 187*, 430-441.

Fraeman, A. A., Korenaga, J., (2010), The influence of mantle melting on the evolution of Mars. *Icarus, 210*, 43-57.

Gaillard, F., Scaillet, B., (2009), The sulfur content of volcanic gases on Mars. *Earth & Planetary Science Letters, 279*, 34-43.

Gillet, J. et al., (2002), Aqueous alteration in the Northwest Africa 817 (NWA 817) Martian meteorite. *Earth & Planetary Science Letters, 203*, 431-444.

Grant, J. A. et al., (2014), The timing of alluvial activity in Gale crater, Mars. *Geophysical Research Letters, 41*, 1142-1149.

Greeley, R., Schneid, R. D., (1991), Magma generation on Mars: Amounts, rates, and comparisons with Earth, Moon, and Venus. *Science, 254*, 996-998.

Greenwood, J. P. et al., (2008), Hydrogen isotope evidence for loss of water from Mars through time. *Geophysical Research Letters, 35*, 5.

Grimm, R. et al., (2017), On the secular retention of ground water and ice on Mars. *Journal of Geophysical Research Planets, 122*, 94-109.

Grott, M. et al., (2013), Long-term evolution of the Martian crust-mantle system. *Space Science Reviews, 174*, 49-111.

Grott, M. et al., (2011), Volcanic outgassing of CO_2 and H_2O on Mars. *Earth & Planetary Science Letters, 308*, 391-400.

Grotzinger, J. P. et al., (2015), Deposition, exhumation, and paleoclimate of an ancient lake deposit, Gale crater, Mars. *Science, 350*, 6257.

Haberle, R. M., "Solar system/syn, atmospheres, evolution of atmospheres | Planetary Atmospheres: Mars" in *Encyclopedia of Atmospheric Sciences* (Elsevier, Amsterdam, Netherlands ed. 2, 2015), pp. 168-177.

Hartmann, W. K., (2005), Martian cratering 8: Isochron refinement and the chronology of Mars. *Icarus, 174*, 294-320.

Hauck, S. A., Phillips, R. J., (2002), Thermal and crustal evolution of Mars. *Journal of Geophysical Research Planets, 107*, E7.

Heard, A. W., Kite, E. S., (2020), A probabilistic case for a large missing carbon sink on Mars after 3.5 billion years ago. *Earth & Planetary Science Letters, 531*, 116001.

Heavens, N. G. et al., (2018), Hydrogen escape from mars enhanced by deep convection in dust storms. *Nature Astronomy, 2*, 126-132.

Hu, S. et al., (2019), Ancient geologic events on Mars revealed by zircons and apatites from the Martian regolith breccia NWA 7034. *Meteoritics & Planetary Science, 54*, 850-879.

Hu, R. et al., (2015), Tracing the fate of carbon and the atmospheric evolution of Mars. *Nature communications, 61*, 1-9.

Hu, S. et al., (2014), NanoSIMS analyses of apatite and melt inclusions in the GRV 020090 Martian meteorite: Hydrogen isotope evidence for recent past underground hydrothermal activity on Mars. *Geochimica et Cosmochimica Acta, 140*, 321-333.

Humayun, M. et al., (2013), Origin and age of the earliest Martian crust from meteorite NWA 7533. *Nature, 503*, 513-516.

Hyeong, K., Capuano, R. M., (2004), Hydrogen isotope fractionation factor for mixed-layer illite/smectite at 60 to 150 C: new data from the northeast Texas Gulf Coast. *Geochimica et Cosmochimica Acta, 68*, 1529-1543.

Jakosky. B. M. et al., (2018), Loss of the Martian atmosphere to space: Present-day loss rates determined from MAVEN observations and integrated loss through time. *Icarus, 315*, 146-157.

Jakosky, B. M. et al., (2017), Mars' atmospheric history derived from upper-atmosphere measurements of 38Ar/36Ar. *Science, 355*, 1408-1410.

Jakosky, B. M., Jones, J. H., (1997), The history of Martian volatiles. *Review of Geophysics, 35*, 1-16.

Karlsson, N. B., Schmidt, L. S., Hvidberg, C. S., (2015), Volume of Martian midlatitude glaciers from radar observations and ice flow modeling. *Geophysical Research Letters, 42*, 2627-2633.

Kasting, J. F. & Pollack, J. B. (1983), Loss of water from Venus. I. Hydrodynamic escape of hydrogen. *Icarus, 53*, 479-508.

Krasnopolsky, V., (2000), On the deuterium abundance on Mars and some related problems. *Icarus, 148*, 597-602.

Kurokawa, H. et al., (2016), Interactive evolution of multiple water-ice reservoirs on Mars: Insights from hydrogen isotope compositions. *Geochemical Journal, 50*, 67-79.

Kurokawa, H. et al., (2014), Evolution of water reservoirs on Mars: Constraints from hydrogen isotopes in Martian meteorites. *Earth & Planetary Science Letters*, *394*, 179-185.

Lammer, H. et al., (2013), Outgassing history and escape of the Martian atmosphere and water inventory. *Space Science Review*, *174*, 113-154.

Lammer, H. et al., (2009), What makes a planet habitable? *The Astronomy and Astrophysics Review*, *17*, 181-249.

Lammer, H. et al., (2003), Estimation of the past and present Martian water-ice reservoirs by isotopic constraints on exchange between the atmosphere and the surface. *International Journal of Astrobiology*, *2*, 195-202.

Lapen, T. J. et al., (2010), A younger age for ALH84001 and its geochemical link to shergottite sources in Mars. *Science, 328*, 347-351.

Lawrence, J. R., Taylor, H. P., (1972), Hydrogen and oxygen isotope systematics in weathering profiles. *Geochimica et Cosmochimica Acta, 36*, 1377-1393.

Le Deit, L. et al., (2013), Sequence of infilling events in Gale Crater, Mars: Results from morphology, stratigraphy, and mineralogy. *Journal of Geophysical Research Planets, 118*, 2439-2473.

Leshin, L. A. et al., (2013), Volatile, isotope, and organic analysis of Martian fines with the Mars Curiosity rover. *Science, 341*, 6153.

Leshin, L. A., (2000). Insights into Martian water reservoirs from analyses of Martian meteorite QUE94201. *Geophysical Research Letters*, *27*, 2017-2020.

Liu, Y. et al., (2018), Impact-melt hygrometer for Mars: The case of shergottite Elephant Moraine (EETA) 79001. *Earth & Planetary Science Letters*, *490*, 206-215.

Lunine, J. et al., (2003), The origin of water on Mars. *Icarus, 165*, 1-8.

Mahaffy, P. R. et al., (2015), The imprint of atmospheric evolution in the D/H of Hesperian clay minerals on Mars. *Science, 347*, 412-414.

Mahaffy, P. R. et al., (2012), The sample analysis at Mars investigation and instrument suite. *Space Science Reviews, 170*, 401-478.

Mane, P. et al., (2016), Hydrogen isotopic composition of the Martian mantle inferred from the newest Martian meteorite fall, Tissint. *Meteoritics & Planetary Science, 51*, 2073-2091.

Martin, P. E. et al., (2017), A Two-Step K-Ar Experiment on Mars: Dating the Diagenetic Formation of
    Jarosite from Amazzonian Groundwaters. *Journal of Geophysical Research Planets, 122*, 2803
    2818.

Maurice, S. et al., (2011), Mars Odyssey neutron data: 1. Data processing and models of water
    equivalent-hydrogen distribution. *Journal of Geophysical Research Planets, 116*, E11.

McSween, H. Y. et al., (2006), Alkaline volcanic rocks from the Columbia Hills, Gusev crater, Mars.
    Journal of Geophysical Research Planets, 111, E9.

McSween, H. Y., Harvey, R. P., (1993), Outgassed water on Mars: Constraints from melt inclusions in
    SNC meteorites. *Science, 259*, 1890-1892.

Montmessin, F. et al., (2004), Origin and role of water ice clouds in the Martian water cycle as inferred
    from a general circulation model. *Journal of Geophysical Research Planets, 109*, E10.

Morris, R. V. et al., (2006), Mössbauer mineralogy of rock, soil, and dust at Gusev crater, Mars: Spirit's
    journey through weakly altered olivine basalt on the plains and pervasively altered basalt in the
    Columbia Hills. *Journal of Geophysical Research Planets, 111*, E2.

Morschhauser, A., Grott, M., Breuer, D., (2011), Crustal recycling, mantle dehydration, and the thermal
    evolution of Mars. *Icarus, 212*, 541-558.

Murchie, S. L. et al., (2009), A synthesis of Martian aqueous mineralogy after 1 Mars year of
    observations from the mars Reconnaissance Orbiter. *Journal of Geophysical Research Planets,
    114*, E2.

Mustard J. F., Sequestration of volatiles in the Martian crust through hydrated minerals: A
    significant planetary reservoir of water" in *Volatiles in the Martian Crust* (Elsevier,
    Amsterdam, Netherlands ed. 2, 2019), pp. 247-264.

Mustard, J. F., Cooper, C. D., Rifkin, M. K., Evidence for recent climate change on Mars from
    the identification of youthful near-surface ground ice. *Nature, 412*, 411-414 (2001).

Nair, H. et al., (1994), A photochemical model of the Martian atmosphere. *Icarus, 111*, 124-150.

Nerozzi, S., Holt, J. W., (2019), Buried ice and sand caps at the north pole of Mars: revealing a record of
    climate change in the cavi unit with SHARAD. *Geophysical Research Letters, 46,* 7278-7286.

Owen, T. et al., (1988), Deuterium on Mars: The abundance of HDO and the value of D/H. *Science, 240*,
    1767-1767.

Plaut, J. J. et al., (2007), Subsurface radar sounding of the South Polar Layered Deposits of Mars.
    Science, 316, 92-95.

Plesa, A. C. et al., (2014), Can a fractionally crystallized magma ocean explain the thermo-chemical
    evolution of Mars? *Earth & Planetary Science Letters, 403*, 225-235.

Sarafian, A. R. et al., (2017), Early accretion of water and volatile elements to the inner Solar System: evidence from angrites. *Philosophical Transactions of the Royal Society A: Mathematical, Physical and Engineering Sciences, 375*.

Savin, S. M., Epstein, S., (1970), The oxygen and hydrogen isotope geochemistry of clay minerals. *Geochimica et Cosmochimica Acta, 34*, 25-42.

Schaefer, L., Fegley Jr., B., (2017), Redox states of initial atmospheres outgassed on rocky planets and planetesimals. *The Astrophysical Journal, 842*, 120.

Seiff, A., (1987), Structure of the atmospheres of Mars and Venus below 100 kilometers, *Advanced Space Research, 7*, 5-16.

Sheppard, S. M. F., Gilg, H. A., (1996), Stable isotope geochemistry of clay minerals. *Clay minerals, 31*, 1-24.

Stone, S. et al. (2020), Hydrogen escape from Mars is driven by seasonal and dust storm transport of water. *Science, 370*, 824-831.

Sun, V. Z., Milliken, R. E., (2015), The geology of mineralogy of Ritchey crater, Mars: Evidence for post-Noachian clay formation. *Journal of Geophysical Research Planets, 119*, 810-836.

Sutter, B. et al., (2017), Evolved gas analyses of sedimentary rocks and eolian sediment in Gale Crater, Mars: Results of the Curiosity rover's sample analysis at Mars instrument from Yellowknife Bay to the Namib Dune. *Journal of Geophysical Research Planets, 122*, 2574-2609.

Tanaka, K. L. et al., (2014), The digital global geologic map of Mars: Chronostratigraphic ages, topographic and crater morphologic characteristics, and updated resurfacing history. *Planetary and Space Science, 95*, 11-24.

Taylor, G. J. et al., (2010), Mapping Mars geochemically. *Geology, 38*, 183-186.

Thomas, N. H. et al. (2020). Hydrogen Variability in the Murray Formation, Gale Crater, Mars. *Journal of Geophysical Research Planets, 125,* e2019JE006289.

Tosca, N. J. et al., (2018), Magnetite authigenesis and the warming of early Mars. *Nature Geoscience, 11*, 635-639.

Usui, T. et al., (2015), Meteoritic evidence for a previously unrecognized hydrogen reservoir on Mars. *Earth & Planetary Science Letters, 410*, 140-151.

Usui, T. et al., (2012), Origin of water and mantle-crust interactions on Mars inferred from hydrogen isotopes and volatile element abundances of olivine-hosted melt inclusions of primitive shergottites. *Earth & Planetary Science Letters, 357*, 119-129.

Vaniman, D. T. et al., (2014), Mineralogy of a mudstone at Yellowknife Bay, Gale crater, Mars. *Science, 343*, 6169.

Villanueva, G. L. et al., (2015), Strong water isotopic anomalies in the Martian atmosphere: Probing current and ancient reservoirs. *Science, 348*, 218-221.

Webster, C. R. et al., (2013), Isotope ratios of H, C, and O in CO_2 and H_2O of the Martian atmosphere. *Science, 341*, 6143.

Wernicke, L., Jakosky, B., (2019), Quantifying the Water Stored in Hydrated Minerals on Mars. *AGU Fall Meeting,* #P41C-3462.

Whitten, J. L., Campbell, B. A., (2018), Lateral continuity of layering in the Mars South Polar Layered Deposits from SHARAD sounding data. *Journal of Geophysical Research Planets, 123*, 1541 1554.

Wordsworth, R. et al., (2017), Transient reducing greenhouse warming on early Mars. *Geophysical Research Letters, 44*, 665-671.

Wordsworth, R. D., (2016), The climate of early Mars. *Annual Reviews in Earth & Planetary Science, 44*, 381-408.

Wordsworth, R. D. et al., (2015), Comparison of "warm and wet" and "cold and icy" scenarios for early Mars in a 3-D climate model. *Journal of Geophysical Research Planets*, *120*, 1201-1219.

Yeh, H. W., (1980), D/H ratios and late-stage dehydration of shales during burial. *Geochimica et Cosmochimica Acta, 44*, 341-352.

Y. L. Yung & W. B. DeMore, *Photochemistry of Planetary Atmospheres* (Oxford University Press, Oxford, UK, 1998).

Yung, Y. L. et al., (1988), HDO in the Martian atmosphere implications for the abundance of crustal water. *Icarus, 76*, 146-159.

Zuber, M. T. et al., (1998), Observations of the north polar region of Mars from the Mars Orbiter Laser Altimeter. *Science, 282*, 2053-2060.

Chapter 8

Summary, implications, and outstanding questions

In this thesis, I used a wide range of techniques at many different scales to characterize how minerals on both Earth and Mars are tied to ancient environments, climates, and habitability. In summary, I was able to advance the scientific field in three different areas by using an interdisciplinary approach, which involved remote sensing, rover operations, a wide range of spectroscopy, mass spectrometry, and modelling. (1) I provided a characterization of Mars' most ancient crustal materials, and I modelled how hydration of the ancient Martian crust would have played a role in drying out the planet. (2) During the Perseverance rover's prime mission, I observed and reported on uniquely identified organics-preserving aqueous environments by, in part, using prior work on terrestrial analogue studies on magnesium carbonate formation on Mars. (3) I developed new methodologies for both recognizing more ikaite pseudomorphs in the sedimentary record and using the clumped isotopic composition of these for reconstructing the temperature and isotopic composition of cold climate waters.

8.1 Understanding the most ancient geological processes on Mars

The ~4 Ga ancient crust on Mars provides a window into some of the earliest and most intriguing geological processes recorded within the entire solar system to understand how the surfaces of terrestrial planets are initially formed. There are few planetary bodies that preserve such old surfaces in existence within the solar system. For example, the crusts of Earth and Venus are young due to tectonic resurfacing. Therefore, Mars is an excellent case study for – in particular – how these preserved ancient geological processes shaped the habitability of the planet.

In Chapter 2, I put forward that there are primarily three processes that are observed to have shaped the ancient crust on Mars: yet- uncharacterized igneous activity, aqueous environments that led to extensive formation of hydrated minerals, and basin-scale impact events that brecciated large regions of the crust. In Chapter 7, I pose that, in particular, the aqueous environments, which caused hydrated mineral formation, had global consequences for the hydrological cycle of Mars. By compiling many decades of results from NASA and ESA missions to Mars, it is evident that the inventory of water on the Martian surface has decreased over time, ultimately drying out the planet to the arid desert we know today. Previous studies proposed that the loss of Mars' water was caused by atmospheric loss of hydrogen. However, it was difficult to reconcile observations of relatively low rates of atmospheric loss and the hydrogen isotope evolution with the large amounts of water volumes inferred to have been needed to create canyons, valleys, lakes, and possibly even oceans on ancient Mars. In Chapter 7, I propose and

demonstrate through modelling that taking into account hydrated mineral formation solves these discrepancies if we consider that 30-99% of Mars original water inventory is now residing within the crust as structural H_2O locked up in mineral lattices. I propose, furthermore, that this crustal hydration phenomenon would have sent Mars on a completely different evolutionary pathway compared to Earth.

So far, the only way that I and other scientists have been able to directly characterize these preserved signs of ancient ~4 Ga geological processes are through satellite infrared spectroscopy and imagery. Due to the limits of satellite remote sensing there are a number of outstanding questions (see below) that cannot yet be addressed. However, my mapping of the rover's landing site and extended mission traverse suggests that many of these questions can be addressed with the Perseverance rover in the near-future.

8.1.1 Further implications and outstanding questions

What was(were) the aqueous environment(s) and geological mechanism(s) that resulted in extensive clay formation on ancient ~4 Ga Mars and led to drying of the planet early in its history?

Because satellite remote sensing cannot provide us with field relationships, petrography, and detailed chemical compositions, it is still an open question what exact environment, or more probably environments, resulted in the extensive hydrated mineral formation on ancient Mars. Hypotheses for the geological mechanisms that enabled hydrated mineral formation, include sedimentary lacustrine and/or marine environments, surface weathering environments of basalts and/or ultramafic materials, subsurface liquid or ice reservoirs, and/or hydrothermal circulation due to heating by volcanic or impact activity. This is also why we cannot choose a specific geological mechanism/process to model in Chapter 7, because such specificity is not allowed with the current limits of the data that we have. However, as posed in Chapter 2 the Perseverance rover will for the first time characterize at least part of these aqueous environments within the ~4 Ga crust. The rover, with its ability to perform more detailed analyses of field relationships, textures, and 10-100 micron-scale chemical and mineralogical composition of rocks, will be able to address which one of these environments resulted in what types of hydrated minerals on ancient Mars.

Aside from drying the planet, what other climatic effects could the large-scale formation of hydrated minerals have had on the Martian climate?

Chapter 7 addresses primarily the role of hydrated minerals as part of the hydrological cycle of Mars. However, I also note that the sequestration of these minerals are quite likely to release important volatiles that affect the composition and structure of the Martian atmosphere. For example, the formation of clays

from a stand-point of both mass balance and redox reactions is actually likely to involve H_2-producing reactions. So far, there have been a number of hypotheses for what mechanism(s) could possibly have kept Mars' surface warm enough to sustain liquid water. Warming through H_2-CO_2 collision absorption heating is one of the primary hypotheses and makes understanding H_2-producing geological environments one of the most important questions to address in terms of understanding the Martian atmosphere. In turn, Chapter 7 shows that such H_2 production would have also affected the hydrogen escape rate from the atmosphere. I hypothesize that this could have resulted in a feedback loop in which H_2 could be produced while H_2O and OH is sequestered within the crust, causing increased atmospheric loss, thereby drying out the planet quickly while keeping it warm, suggesting that understanding these crustal hydration processes can also help us unlock the mysteries of ancient terrestrial planet climates.

What is the type of igneous activity that is recorded within seemingly igneous materials within the ancient Martian crust?

It is largely unknown how all of the ancient crust that primarily consists of igneous minerals, which we characterize in Chapter 2, came to be. We proposed that basin-scale impact melt processes could potentially have formed these materials, similar to how we think about mare formation and megaregolith on the Moon. However, the Martian case is enigmatic because the relationship of these materials in comparison the impact basins are not as straight-forward to interpret as on the Moon due to later aqueous environments, fluvial and lacustrine environments, weathering, and erosion. In Chapter 2, we furthermore observe that some of these materials preserved within megabreccia appear to have formed before the giant impacts occurred. One idea is that the most ancient crust was formed through the crystallization of a primordial magma ocean that solidified to the primordial Martian crust resulting in massive outgassing of volatiles into a steam atmosphere. Is that what we could be seeing remnants of within the crust, or is it a different igneous process that we have yet to understand? The Perseverance rover will have the unique ability to address this question by analyzing these ancient igneous materials within ~4 Ga megabreccia blocks and possibly surrounding crustal regions where these igneous materials appear to be preserved, as shown in Chapter 2.

Can we use field observations on Mars to test models of the physical mechanisms of deformation following extremely large impacts that occurred early in the history of terrestrial planets?

Another aspect of why it is difficult to understand the formation of these ancient terrestrial planet crusts is because we do not fully understand the geological processes involved during giant impacts. These types

of processes have largely been modelled because there is very few opportunities for studying them in the field. On Earth, the remnants of these impact basins are poorly preserved (i.e. Sudbury and Vredeford) or difficult to access (i.e. Chixulub). The best we have been able to do is through manned-mission, sample, and remote sensing studies of impact craters and basins on the Moon. The extended mission area of the Perseverance rover, which contains records of these giant impact transient cavity collapse processes poses an intriguing field site for answering questions of how giant impact basins have affected planetary bodies early in solar system history, as posed in Chapter 2.

8.2 Characterizing carbonate-forming, organics-preserving ancient aqueous environments on Mars

During the first year of Perseverance operations, I have started to address some of the questions posed above, specifically centered around carbonate-forming aqueous environments. In Chapter 3, I outlined how magnesium carbonates form on Earth as analogues for magnesium carbonate formation within the landing site of the Perseverance rover, Jezero crater, including via aqueous alteration of ultramafic igneous rocks (carbonation). In Chapter 6, the returned Perseverance data showed that indeed carbonation of an ultramafic protolith resulted in carbonate-deposition within the Jezero crater, confirming hypotheses which had previously been suggested by studies using orbital remote sensing and laboratory studies of meteorites. Furthermore, these carbonate-materials also preserve fluorescence signatures of Martian aromatic organic compounds, suggesting that these processes at least played a role in preserving the organic compounds and possibly in forming them. Hence, this ancient environment could potentially have been habitable, although this and other related questions for Martian astrobiological potential will need to be examined upon return of these laboratory samples to Earth as outlined in the below and summarized in Chapter 3.

8.2.1 Further implications and outstanding questions

As we enter the larger more extensive carbonate-containing regions around the Jezero crater, what were these carbonate-forming environments like?

So far, the extent of our rover analyses within the Jezero crater have been limited, and it has been proposed in many studies that the ultramafic carbonation environments or at least some – unknown – mineralogical combination of olivine and carbonate exists higher in the Jezero stratigraphy as well as in the entire region stretching ~1000 km in radius from the current position of the Perseverance rover. These units had a very similar satellite infrared spectroscopic signature compared to the Jezero crater's carbonated ultramafic materials. However, it is an open question whether this carbonation environment explains all of the satellite observations. There are also other hypotheses suggesting that this could have been geological units with the same approximate combination of minerals but different geological origins. For example, some of these units have been proposed to be lacustrine deposits and potentially a

redeposition of the carbonated ultramafics within the catchment area. Future measurements as the Perseverance rover drives towards these other areas of olivine and carbonate will be able to address that question. Ultimately, characterizing the carbonate formation in this area is particularly important for understanding the ancient Martian carbon cycle, which has major implications for the Martian climate considering that the Martian atmosphere is predominantly CO_2 (read below).

How were the Martian organics formed, and could they have supported life?

Our first measurements of the spatial distribution and organic-mineral associations on the Martian surface using the Perseverance rover's SHERLOC instrument are a huge step towards understanding the processes that controlled Martian organics preservation. However, it is not possible to address what processes formed them with these data alone, including any putative abiotic or even biological origins. At this point, we can really only guess that perhaps aqueous processes could have been involved in their synthesis as has been proposed for similar organic-mineral associations in Martian meteorites. These types of questions can be much better addressed when the organics-bearing samples are returned to Earth for future analysis of the molecular structure of the organics, their abundance, and their similarity or dissimilarity to organics found within terrestrial environments as well as carbonaceous chondrites.

What atmospheric records can be unlocked by analyzing the returned carbonates within the laboratory in future?

The carbonate isotopes recorded within the Jezero carbonates are either derived from or have very likely exchanged with the Martian CO_2 atmosphere at one point or another, similar to other carbonates that have been measured for isotopic compositions on Mars, as described in Chapter 3. Hence, measurements of these can help us fill in the wide gaps in our understanding of the evolution of Mars' atmosphere. The isotopic signature of the Martian atmosphere, which may at least to some degree be recorded within the Jezero carbonates, can be thought of as reflecting the sum of processes that affected the Martian carbon cycle through time in a similar way as we described how the hydrogen isotopic signature of the atmosphere reflects the hydrological cycle of Mars through time in Chapter 7. Hence, these laboratory measurements can help us understand processes that controlled the Martian atmosphere, such as loss of the atmosphere through atmospheric processes, loss of atmosphere through carbonate formation, or volcanic outgassing of CO_2 etc. That is why the carbonates themselves, aside from the organics preserved within these materials, are such a vital material to return to Earth for further study through the techniques that I outline in Chapter 3.

8.3 Developing methodology for using hydrated carbonates as tracers for cold climates

In Chapter 4, I define a new carbonate microtexture that allows us to recognize ikaite pseudomorphs within the sedimentary record. Based on natural observations of ikaite forming only in frigid conditions at temperatures <9ºC, and we can use the recognition of such ikaite pseudomorph fabrics to infer frigid formation conditions. Furthermore, in Chapter 5 we develop a concept for understanding how clumped isotope compositions measured of these ikaite pseudomorph or any other hydrated carbonate that has since dehydrated can be used to directly calculate formation temperatures and the isotopic composition of the ikaite. Chapter 5 demonstrates that there is a diagenetic overprint that affects both clumped isotope temperatures and oxygen isotope values when hydrated carbonates dehydrate. I found that this diagenetic overprint is caused by equilibrium exchange of oxygen between the water and carbonate within the hydrated carbonate lattice, and importantly it can therefore be modelled, characterized, and corrected for in order to reconstruct the isotopic signatures of the original hydrated carbonate precursor.

This is a useful technique that opens up many avenues for future exploration. Ikaite pseudomorphs have been recognized within the sedimentary records throughout geological history and have been used to for example infer "Snow Ball Earth" conditions, to infer polar latitudinal conditions, and to infer glaciated lacustrine conditions during the Pleistocene. With these two new techniques, one textural and one isotopic, we have a better compass for performing these reconstructions of glaciated climates in the future. We can set out to find new ikaite pseudomorphs and measure them for their isotopic composition to reconstruct formation temperatures and oxygen isotope compositions of the waters they formed in, or we can go back to old data and re-interpret these values when considering the diagenetic overprint. Understanding these dehydration textures and diagenetic isotopic overprints may even become important for Martian returned samples of magnesium carbonates, which could potentially be dehydration products of precursor hydrated magnesium carbonates, when we attempt to reconstruct their precipitation temperatures and isotopic compositions.

8.4 Concluding remarks

In summary, at a higher level than these specific scientific questions and implications derived from my work, what unites my research and the ultimate question that is derived from this thesis is:

What are the primary geological controls that shape the habitability and astrobiological potential of terrestrial planets within or near the habitable zone of the solar system and within exoplanetary systems?

Across the ancient creation myths that I grew up with, it is striking how a central principle re-occurs; that life arose from the rocks, the sand, and the planet itself.

Christianity: *"God formed man from the dust of the earth. He blew into his nostrils the breath of life"*

Norse religion: *"Da drog tre aser kærlige og kraftfulde langs havet; På stranden fandt de to træer, Ask*

og Embla, visne og våde – skæbneløse. Træet havde ikke ånd, kunne ikke tænke eller tale, koldt og vådt som det var; Odin gav det ånde. Høner gav det ånd, Lodur gav det lød og livets varme."
[English Translation: *"The three Norse gods fared lovingly and powerful along the ocean shoreline; In the beach sand they found two trees. Ash and Elm, withered and wet – without fates. The trees had no spirit, they could not think or talk, cold and wet as it was: Odin gave it breath, Høner gave it spirit. Lodur gave it glow and life's warmth."*]

Taoism: *"天地开辟之初.大地上并没有人类.是女娲抟捏黄土造了人.她干得又忙又累.竭尽全力干还赶不上供应.于是她就拿了绳子把它投入泥浆中.举起绳子一甩.泥浆洒落在地上 变成了一个人"*

[English Translation: *"At the beginning of the creation of the world, there were no human beings on the Earth. Nuwa kneaded yellow dirt to create human beings. Though she worked feverishly, she did not have enough strength to finish her task. So she took a rope and drew it across the mud. The mud spilled on the ground and turned into humans."*]

There has been a number of different ways – including studying planets' masses, physical structure, distance from the sun, and atmospheric composition – to address the planetary habitability question in many different fields. However, I think what we are collectively finding in – at least – the search for ancient microbial life in the solar system that equally important is understanding the implications of geological processes in shaping and evolving these planetary characteristics. In a way, we are circling back to these questions already asked by the ancients across the world: how we derive from the rocks and the planet itself.

Supporting information for Chapter 4: SEM-EDS map of dendritic tufas and all SEM-EDS point spectral data

Fig. S1: SEM analyses of dendritic tufas from Mono Lake. (A) BSE images and elemental maps produced by SEM-EDS for sample N2 of dendritic tufa from Mono Lake, shown as leftmost sample in Fig. 4.1.G. The consolidated layered EDS map shows the presence of 3 major chemical phases: calcite (yellow), Mg-silicates (blue), and high-Mg calcite (green). Mg-silicates and Mg-enriched calcite formed in zones around the primary calcite fabrics. (B) BSE images and elemental maps produced by SEM-EDS for a different sample of dendritic tufas, sample S1, from Mono Lake. The consolidated layered EDS map shows only 2 major chemical phases: calcite (yellow color) and Mg-silicates (blue color). Here, Mg-silicates have formed around the primary calcite fans and spherulites, and occurs between the primary calcite fans and spherulites and the massive (interpreted to probably be sparry) calcite filling a porosity in the middle. (C) BSE image of Mg-silicate aggregates that have formed within porosities. (D) Close up BSE image of Mg-silicates. Notice the microcrystalline, heterogeneous nature of the Mg-silicates. The stoichiometric compositions of bright crystals were found to be consistent with lithic fragments.
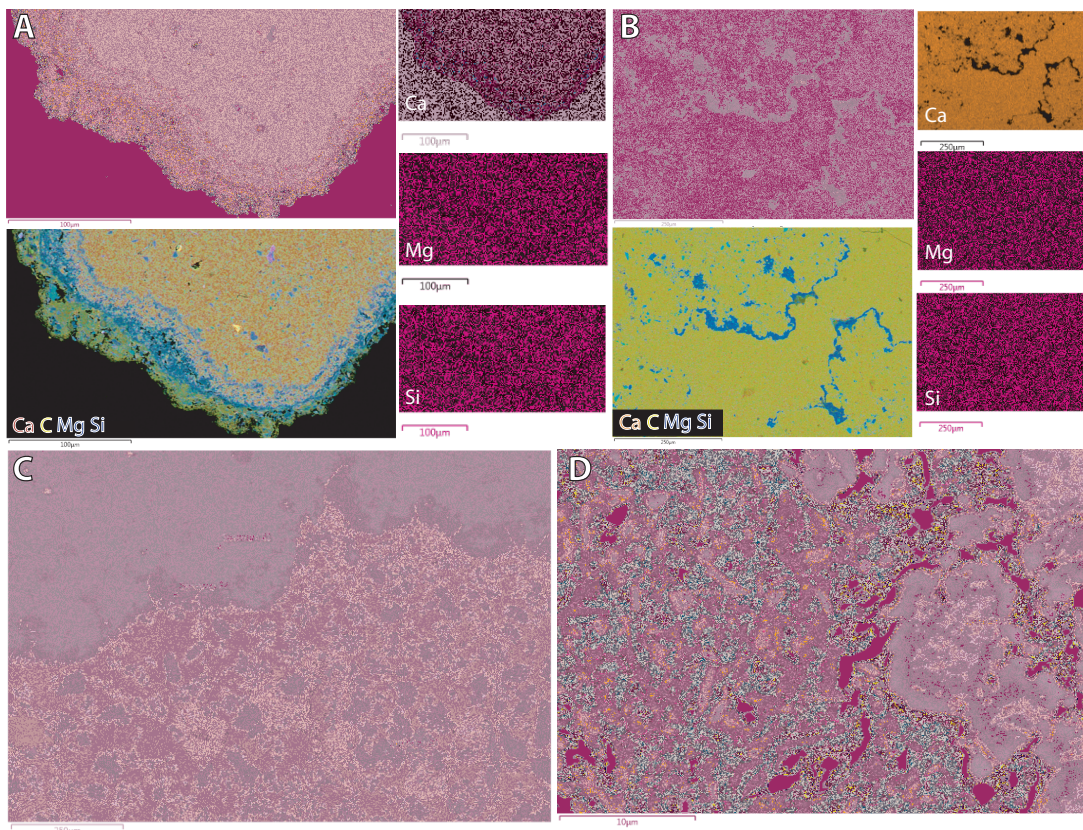
Table S1: Mg mole% from point spectra of thinolite tufa type 1-2 calcite, thinolite tufa type 3 calcite, and dendritic tufas. Summary statistics in orange fields at the bottom.

Thinolite tufa Core and overgrowth Mg mole%	Thinolite tufa Cement Mg mole%	Dendritic tufa Shrub/spherulite Mg mole%
1.38	38.86	13.73
3.81	38.69	12.40
1.43	30.45	17.51
3.69	31.72	13.43
3.74	11.91	10.73
1.48	10.63	12.15
4.19	26.73	20.82
4.22	38.97	7.71
4.28	31.06	12.12
0.00	19.58	11.84
3.61	34.98	11.35
1.09	32.08	17.38
3.74	35.18	15.81
0.45	13.98	11.04
0.00	34.16	6.13
9.59	29.83	5.79
0.00	34.61	7.11
9.05	12.36	7.16
17.57	10.90	25.80
5.83	32.14	10.53
7.05	33.53	5.20
0.28	39.71	5.23
0.17	40.99	5.10
6.49	38.00	4.46
6.42	28.49	5.00
1.87	30.64	3.06
9.34	27.06	0.97
7.11		3.96
0.33		2.56
1.46		4.30
3.64		2.42
0.00		0.99
3.84		
0.82		
1.85		

	0.33		
	0.29		
	4.98		
	0.00		
	0.00		
	15.88		
	2.34		
	6.95		
	0.32		
	0.80		
	0.96		
Mean	3.54	29.16	9.18
STD	3.98	9.56	5.98
Max	17.57	40.99	25.80
Min	0.00	10.63	0.97
Count	46	27	32

Table S2: (Mg+Fe)/(Si+Al) ratios from point spectra of Mg-silicate in thinolite tufa. Summary statistics in orange fields at the bottom.

|	**Thinolite Mg-silicate (Mg+Fe)/(Si+Al)**
	0.83
	0.84
	0.94
	0.86
	0.84
	0.86
	0.84
	0.80
	0.79
	0.84
	0.72
	0.68
	0.80
	0.64
	0.67
	0.63
	0.83
	0.74
	0.87
Mean	0.79
STD	0.09
Max	0.94
Min	0.63
Count	19

Table S3: P/Si, Ca/Si, and Ca/P ratios from point spectra of phosphorous-bearing amorphous/microcrystalline phase in thinolite tufa. Summary statistics in orange fields at the bottom.

	Thinolite tufa phosphorous-bearing phase		
	P/Si	**Ca/Si**	**Ca/P**
	1.09	1.90	1.74
	1.26	2.56	2.03
	0.86	2.17	2.51
	0.40	0.93	2.35
	0.98	2.61	2.66
	0.69	4.84	7.05
	0.57	1.22	2.13
	1.45	5.05	3.49
	1.18	3.00	2.56
	0.30	1.32	4.43
	0.39	1.75	4.49
	1.24	3.11	2.51
	1.58	2.96	1.87
	0.63	4.55	7.19
	0.94	1.92	2.04
	1.80	4.23	2.35
	1.56	3.88	2.50
	0.60	1.25	2.09
	0.77	1.49	1.94
	1.11	1.97	1.78
	0.87	1.71	1.97
	0.53	1.22	2.31
	1.61	2.99	1.86
	0.69	1.65	2.39
	1.82	3.66	2.00
	0.89	1.85	2.08
	1.91	3.96	2.07
	0.75	1.50	2.00
Mean	1.02	2.55	2.73
STD	0.46	1.21	1.42
Max	1.91	5.05	7.19
Min	0.30	0.93	1.74
Count	28	28	28

Supporting information for Chapter 5: XRD calibration and additional simulations

Figure S1: XRD calibration data and calibration curve fit used for calculating calcite mol% and MHC mol% for heating experiments. The calibration was performed by measuring the peak height (PH) ratio of the 30° and 31.5° peaks for calcite and MHC, respectively, within pre-measured mixtures of MHC and calcite. A polynomial was fitted to the logarithmically transformed PH ratios as described in methods. Best fit parameters and their standard deviation error are given in the plot.
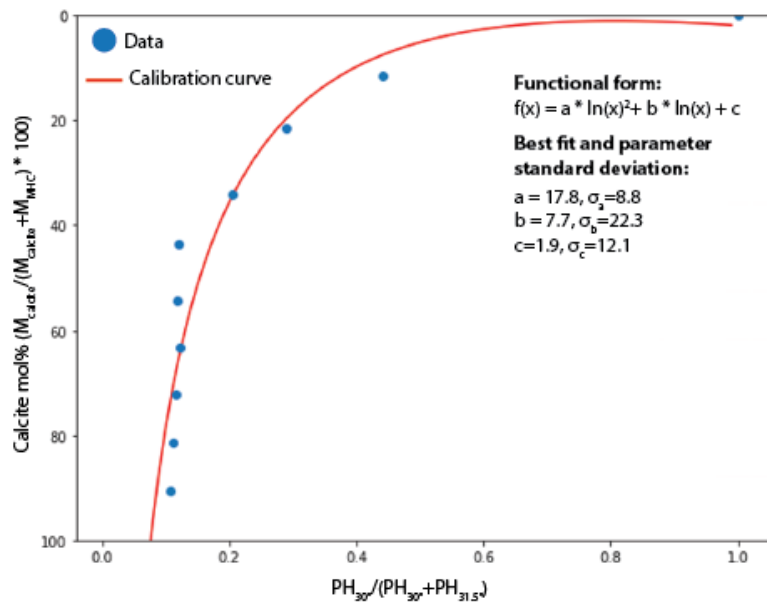
Fig. S2: Example simulations of dry experiment that shows separate simulations of $\delta^{18}O_{CARB}$, Δ_{47}, and $\delta^{18}O_{MHC,H2O}$ for calcite (CC), MHC, and MHC-CC-mixture with assumed intermediary reaction and exchange coefficients. MHC-CC mixture simulation curves is used to fit experimental data points in Fig. 5.6. We observe here that MHC carbonate and structural H_2O reaches equilibrium values for both $\delta^{18}O_{CARB}$ and Δ_{47}. The mixture values, however, is much higher because the calcite component inherits the isotopic signature of intermediate re-equilibration steps.
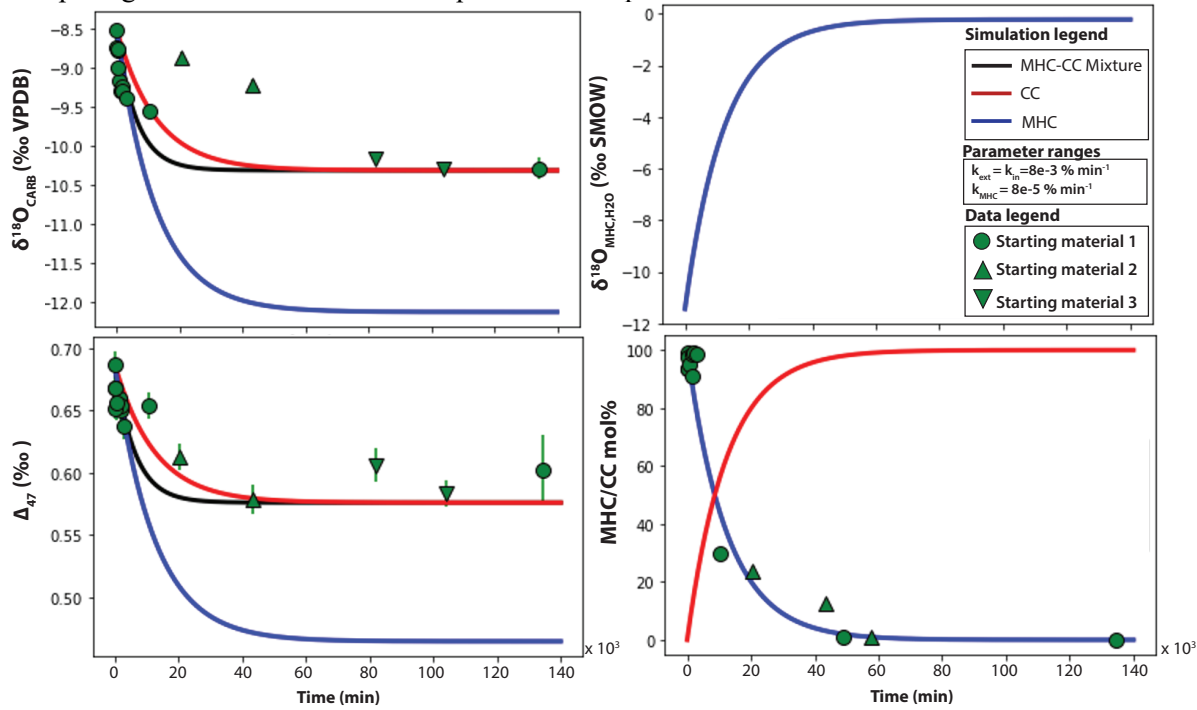
Appendix C

Supporting information for Chapter 6: Author list, materials and methods, and supplementary text and figures

Table S1: Full author list table.

Name	**Institution**	**Email**
Eva L. Scheller	Division of Geological and Planetary Sciences, California Institute of Technology, Pasadena, CA	eschelle@caltech.edu
Joseph Razzell Hollis	1) The Natural History Museum, London, United Kingdom, 2) NASA Jet Propulsion Laboratory, California Institute of Technology, Pasadena, CA	j.razzellhollis@gmail.com
Emily L. Cardarelli	NASA Jet Propulsion Laboratory, California Institute of Technology, Pasadena, CA	emily.cardarelli@jpl.nasa.gov
Andrew Steele	Earth and Planets Laboratory, Carnegie Institution for Science, Washington, DC	asteele@carnegiescience.edu
Luther W. Beegle	NASA Jet Propulsion Laboratory, California Institute of Technology, Pasadena, CA	luther.w.beegle@jpl.nasa.gov
Rohit Bhartia	Photon Systems Incorporated, Covina, CA	r.bhartia@photonsystems.com
Pamela Conrad	Earth and Planets Laboratory, Carnegie Institution for Science, Washington, DC.	pconrad@carnegiescience.edu
Kyle Uckert	NASA Jet Propulsion Laboratory, California Institute of Technology, Pasadena, CA	kyle.uckert@jpl.nasa.gov
Sunanda Sharma	NASA Jet Propulsion Laboratory, California Institute of Technology, Pasadena, CA	sunanda.sharma@jpl.nasa.gov
Bethany L. Ehlmann	Division of Geological and Planetary Sciences, California Institute of Technology, Pasadena, CA	ehlmann@caltech.edu
William J. Abbey	NASA Jet Propulsion Laboratory, California Institute of Technology, Pasadena, CA	william.j.abbey@jpl.nasa.gov
Sanford A. Asher	Department of Chemistry, University of Pittsburgh, Pittsburgh, PA.	asher@pitt.edu
Kathleen C. Benison	Department of Geology and Geography, West Virginia University, Morgantown, WV	kathleen.benison@mail.wvu.edu
Eve L. Berger	Texas State University - Jacobs JETS - NASA Johnson Space Center, Houston, TX.	eve.l.berger@nasa.gov
Olivier Beyssac	Sorbonne Université, Muséum National d'Histoire Naturelle, UMR CNRS 7590 IMPMC. 4 Place Jussieu, 75005 Paris, France	olivier.beyssac@upmc.fr
Benjamin L. Bleefeld	Malin Space Science Systems, San Diego, CA.	bleefeld@msss.com

Tanja Bosak	Department of Earth, Atmospheric, and Planetary Sciences, Massachusetts Institute of Technology, Cambridge, MA	tbosak@mit.edu
Adrian J. Brown	Plancus Research, Severna Park, MD, USA	adrian.j.brown@nasa.gov
Aaron S. Burton	NASA Johnson Space Center, Houston, TX.	aaron.burton@nasa.gov
Sergei V. Bykov	Department of Chemistry, University of Pittsburgh, Pittsburgh, PA.	bykov@pitt.edu
Ed Cloutis	Geography, The University of Winnipeg, Winnipeg, Canada	e.cloutis@uwinnipeg.ca
Alberto G. Fairén	1) Centro de Astrobiología (CSIC-INTA), Madrid, Spain, 2) Department of Astronomy, Cornell University, Ithaca, NY, USA	agfairen@cab.inta-csic.es
Lauren DeFlores	NASA Jet Propulsion Laboratory, California Institute of Technology, Pasadena, CA	lauren.p.deflores@jpl.nasa.gov
Kenneth A. Farley	Division of Geological and Planetary Sciences, California Institute of Technology, Pasadena, CA	farley@gps.caltech.edu
Deirdra M. Fey	Malin Space Science Systems, San Diego, CA.	dfey@msss.com
Teresa Fornaro	INAF-Astrophysical Observatory of Arcetri, Florence, Italy.	teresa.fornaro@inaf.it
Allison C. Fox	NASA Postdoctoral Program - NASA Johnson Space Center, Houston, TX.	allison.c.fox@nasa.gov
Marc Fries	NASA Johnson Space Center, Houston, TX.	marc.d.fries@nasa.gov
Keyron Hickman-Lewis	1) Department of Earth Sciences, The Natural History Museum, London, United Kingdom, 2) Dipartimento di Scienze Biologiche, Geologiche e Ambientali, Università di Bologna, Bologna, Italy	keyron.hickman-lewis@nhm.ac.uk
William F. Hug	Photon Systems, Inc.	w.hug@photonsystems.com
Joshua E. Huggett	Malin Space Science Systems, San Diego, CA.	jhuggett@msss.com
Samara Imbeah	Malin Space Science Systems, San Diego, CA.	samara@msss.com
Linda C. Kah	Department of Earth and Planetary Sciences, University of Tennesee, Knoxville, TN.	lckah@utk.edu
Peter Kelemen	Lamont Doherty Earth Observatory, Columbia University, Palisades, NY	peterk@ldeo.columbia.edu
Megan R. Kennedy	Malin Space Science Systems, San Diego, CA.	mkennedy@msss.com
Tanya Kizovski	Department of Earth Sciences, Brock University, St. Catharines, ON L2S 3A1, Canada	tkizovski@brocku.ca
Carina Lee	Lunar & Planetary Institute, Universities Space Research Association, Houston, TX	carina.h.lee@nasa.gov
Yang Liu	NASA Jet Propulsion Laboratory, California Institute of Technology, Pasadena, CA	yang,liu@jpl.nasa.gov
Francis M. McCubbin	NASA Johnson Space Center, Houston, TX	francis.m.mccubbin@nasa.gov
Kelsey R. Moore	Division of Geological and Planetary Sciences, California Institute of Technology, Pasadena, CA	krmoore@caltech.edu
Brian E. Nixon	Malin Space Science Systems, San Diego, CA.	nixon@msss.com

Jorge I. Núñez	Johns Hopkins University Applied Physics Laboratory, Laurel, MD 20723-6005	jorge.nunez@jhuapl.edu
Carolina Rodriguez Sanchez-Vahamonde	Malin Space Science Systems, San Diego, CA.	crodriguez@msss.com
Ryan D. Roppel	Department of Chemistry, University of Pittsburgh, Pittsburgh, PA.	rdr38@pitt.edu
Mark A. Sephton	Earth Science and Engineering, South Kensington Campus, Imperial College London, SW7 2AZ	m.a.sephton@imperial.ac.uk
Shiv K. Sharma	Hawaii Institute of Geophys and Planetology, University of Hawaii at Manoa, Honolulu, HI-96822	shiv@hawaii.edu
Sandra Siljeström	RISE Research Institutes of Sweden, Stockholm, Sweden	sandra.siljestrom@ri.se
Svetlana Shkolyar	1) University of Maryland, College Park, MD, 2) NASA Goddard Space Flight Center, Greenbelt, MD	svetlana.shkolyar@nasa.gov
David L. Shuster	Earth and Planetary Science, University of California Berkeley, Berkeley, CA	dshuster@berkeley.edu
Justin I. Simon	NASA Johnson Space Center, Houston, TX	justin.i.simon@nasa.gov
Rebecca J. Smith	Department of Geosciences, Stony Brook University, Stony Brook, NY	rebecca.j.smith@stonybrook.edu
Kathryn M. Stack	NASA Jet Propulsion Laboratory, California Institute of Technology, Pasadena, CA	kathryn.m.stack@jpl.nasa.gov
Kim Steadman	NASA Jet Propulsion Laboratory, California Institute of Technology, Pasadena, CA	kimberly.b.steadman@jpl.nasa.gov
Benjamin P. Weiss	Department of Earth, Atmospheric, and Planetary Sciences, Massachusetts Institute of Technology, Cambridge, MA	bpweiss@mit.edu
Alyssa Werynski	Malin Space Science Systems, San Diego, CA.	awerynski@msss.com
Amy J. Williams	Department of Geological Sciences, University of Florida, Gainesville, FL	amywilliams1@ufl.edu
Roger C. Wiens	Los Alamos National Laboratory, Los Alamos, NM	rwiens@lanl.gov
Kenneth H. Williford	1) NASA Jet Propulsion Laboratory, California Institute of Technology, Pasadena, CA, 2) Blue Marble Space Institute of Science, Seattle, WA	ken@bmsis.org
Katherine Winchell	Malin Space Science Systems, San Diego, CA.	kwinchell@msss.com
Brittan Wogsland	Department of Earth and Planetary Sciences, University of Tennesee, Knoxville, TN	bwogsla1@vols.utk.edu
Anastasia Yanchilina	Impossible Sensing, St. Louis, MO	ayanchilina@impossiblesensing.com
Rachel Yingling	Malin Space Science Systems, San Diego, CA.	yingling@msss.com
Maria-Paz Zorzano	Centro de Astrobiología (CSIC-INTA), Madrid, Spain	zorzanomm@cab.inta-csic.es

Materials and Methods

S1. SHERLOC operation

SHERLOC is a deep-ultraviolet Raman and fluorescence spectrometer (Bhartia et al., 2008) mounted on the turret at the end of *Perseverance*'s robotic arm, alongside a high-resolution camera named WATSON

(Wide-Angle Topographic Sensor for Operations and eNgineering) (Bhartia et al., 2021). SHERLOC operates by scanning the target surface with a 110 μm diameter, 248.5794 nm pulsed laser, collecting any back-scattered Raman scattering and fluorescence emissions produced by illuminated material in the near-subsurface, which are detected by a 512x2048 pixel e2v 42-10 CCD kept at –28 ºC by a phase change material. The laser spot is moved from point to point in a grid by an internal scanning mirror, acquiring a combined Raman and fluorescence spectrum for each point. Spectra are measured between 250 and 354 nm, at a spectral resolution of 0.269 nm (~40 cm^{-1} in the Raman region) and 0.071 nm/pixel (~10 cm^{-1}/pixel). By using deep-ultraviolet excitation, the Raman spectrum is compressed into a narrow spectral range (250–275 nm) that is relatively free of fluorescence signal, allowing for spectral separation of the two phenomena in a single measurement. SHERLOC scans can be up to 1296 points, and cover an area of up to 7x7 mm. The hollow cathode NeCu laser spot is annular in shape, with an outer diameter of ~110 μm, and is fired in 40 μsecond pulses at 80 Hz, with an estimated pulse energy of ~9 μJ at the start of mission. The instrument has a working distance of 48 mm, and focusing is achieved using an autofocus context imager (ACI), which also acquires a high-resolution, grayscale image of the target surface at ~10.1 μm/pixel. SHERLOC typically operates after local sunset, to maximize the time that the phase change material (PCM) can maintain the detector's ideal operating temperature of −28 ºC (Bhartia et al., 2021).

Arm placement accuracy

Based on pre-launch assessments of arm placement accuracy under terrestrial gravity, *Perseverance*'s robotic arm is capable of placing SHERLOC within 12 mm of a targeted location. Lateral arm drift during operation is expected to be <100 μm/min (Bhartia et al., 2021). The SHERLOC scanning mirror itself has a positioning error of <22 μm at the target.

Spectral calibration, resolution and accuracy

The SHERLOC spectral calibration during surface operations on Mars has an estimated uncertainty of ±5 cm^{-1} (±0.004 nm) in the 700–1800 cm^{-1} region (253.0–260.2 nm). The uncertainty was estimated by analyzing observed Raman peak positions for the ten SHERLOC calibration target materials mounted to the front of the rover, which were measured on sols 59 and 181, and comparing them to pre-launch values obtained on a laboratory instrument (Fries et al., submitted). This comparison was done to evaluate any potential changes in calibration that may have occurred during launch, cruise, or landing, and determined that a small linear correction was needed, as described by (Fries et al., submitted). The stated spectral uncertainty reflects the updated calibration, which was applied to all spectra reported in this article.

Once selected, each target was abraded by *Perseverance*'s abrasion tool prior to characterization by SHERLOC (Farley et al., 2020). The abraded patch is circular, approximately 45 mm in diameter, and 8–10 mm deep (Fig. 6.1). The abraded patch was then cleaned of dust/tailings using a jet of compressed gas from the gas Dust Removal Tool (gDRT), providing a clean, flat rock surface for proximity science analysis (Farley et al., 2020). SHERLOC operates by scanning the target surface in a grid in order to construct Raman mineral and fluorescence maps, and analyses generate three different types of scans, referred to as survey (coverage: 5x5 mm, resolution: 140 μm), high-dynamic range (HDR) (coverage: 7x7 mm, resolution: 740 μm), and detail scans (coverage: 1x1 mm, resolution: 100 μm). In addition, survey scans are shot with 15 pulses per point (ppp), HDR scans are shot with between 250-500 ppp, and detail scans are shot with 500 ppp. This means survey scans will have low SNR Raman spectra compared with Raman spectra from HDR and detail scans. Hence, fluorescence and low SNR Raman mineral maps in Fig. 6.3-6.4 were created from survey scan results. High SNR Raman mineral maps were created from HDR scans in Fig. 6.2-6.4. Both fluorescence detail and Raman detail maps were created from detail scans in Fig. 6.2. Further detail for the scans performed on each target can be read below.

Guillaumes: The Guillaumes abraded target was characterized over sols 161–162. On sol 161, SHERLOC conducted one survey scan of 36x36 points in a 5x5 mm area at 15 pulses per point (ppp), and three co-located high dynamic range (HDR) scans of 10x10 points in a 7x7 mm area at 100, 100, and 300 ppp respectively. On sol 162, SHERLOC was positioned over a second area of the abraded target (Fig. 6.3) and conducted one survey scan of 36x36 points in a 5x5 mm area at 15 ppp and two co-located HDR scans of 10x10 points in a 7x7 mm area, both at 250 ppp. The results of the sol 162 survey and HDR #2 scans are shown in Fig. 6.3.

Bellegarde: The Bellegarde abraded target was characterized on sol 186 using one survey scan of 36x36 points in a 5x5 mm area at 15 ppp, and two HDR scans of 10x10 points in a 7x7 mm area, both at 250 ppp. The results of the survey and HDR #2 scans are shown in Fig. 6.4.

Garde: The Garde abraded target was characterized over sols 207–208. On sol 207, SHERLOC conducted one survey scan of 36x36 points in a 5x5 mm area at 15 ppp, and two HDR scans of 10x10 points in a 7x7 mm area, both at 500 ppp. On Sol 208, SHERLOC conducted three detail scans of 10x10 points in three different 1x1 mm areas that overlapped with the survey area, all at 500 ppp. The results of the fluorescence survey, HDR #2 scans, and the central detail scan are shown in Fig. 6.2.

S2. Spectral Processing

Due to the curved projection of the DUV spectrum onto SHERLOC's detector, the SCCD is divided into three vertical binning regions that are read out separately in order to minimize noise. For each region in each spectrum, an active frame is acquired while the laser is firing and a dark frame is acquired with the same duration without triggering the laser, which is then subtracted from the active frame. The full 250–354 nm spectrum can be obtained by recombining the three regions, but this introduces additional noise in the Raman region that may obscure weak Raman signals. To avoid this when generating Raman data products, Region 1 (250–284 nm) is processed separately without recombination.

Initial data processing was done using NASA internal software produced at the Jet Propulsion Laboratory by K. Uckert, named Loupe. Full processing includes dark frame subtraction, normalization to measured laser output, and cosmic ray removal using the method described in (Uckert et al., 2019). Loupe also provides functionality for correlating individual spectra to specific points on the ACI image based on scanning mirror positioning. Further data processing was done using custom Python scripts, following methods developed by (Razzell Hollis et al., 2021a). This includes polynomial baseline subtraction, automatic peak detection, and determining peak positions via Gaussian fitting. The requirements for automatic peak detection are local maxima that are at least 50 cm^{-1} apart, >5% of the spectrum's maximum intensity (after baseline subtraction), and >2 times the background noise (estimated as the standard deviation of baselined intensity in the peak-free region between 2000 and 2100 cm^{-1}). Furthermore, peak identification was also performed semi-quantitatively and subsequently compared to automated detections. Semi-quantitative detections were performed by identifying peaks with intensity >2 times the noise and a full-width half maximum that is >3 pixels (> ~30 cm^{-1}) wide. In all cases, peak fitting was performed by assigning a Gaussian function to each peak, and freely fitting the sum Gaussian curve to the data via either linear least square regression using the LMFIT python package (Newville et al., 2014) or the Levenberg-Marquardt method using the Scipy python package (Virtanen et al., 2020).

Mineral identification

Mineralogical assignments were done by comparing baselined SHERLOC spectra and fitted peak positions to the SHERLOC spectral library, a database of spectral standards for minerals and organic compounds measured on Earth using the Brassboard instrument, an optical analog of the SHERLOC flight model that was adapted to function under terrestrial ambient conditions (Razzell Hollis et al., 2021a). The mineral standard spectra shown in Figs. 6.2-6.4 are taken from the database and described in detail by (Razzell Hollis et al., 2021a) with the exception of subsequently obtained perchlorate spectra, which are detailed below. Following mineral identification of each automated and semi-quantitatively

defined peak through above-described methods, we constructed mineral maps of each obtained grid point within Figs. 6.2-6.4. Deriving quantitative concentrations of minerals from the Raman spectra is not currently possible (Razzell Hollis et al., 2020). Details outlining different Mars-relevant minerals and rocks ability to attenuate UV radiation and thus the SHERLOC DUV laser are detailed in (Carrier et al., 2019). As different minerals have different Raman scattering cross sections and thus peak intensities, not all points scanned exhibit peaks above the level of detection for a mineral phase. These are unclassified.

Raman and fluorescence intensity maps

Spectral intensity maps of both Raman and fluorescence spectra were generated using three pre-defined spectral bands, and assigning the summed intensities of each band in each spectrum to the R, G, B values of the corresponding pixel, normalized to the 2% and 98% percentiles for all three bands across the entire map. For fluorescence maps, R, G, B values represent the 330–350 nm, 295–315 nm, and 265–285 nm bands, respectively, of the full composition spectrum; for Raman maps, R, G, B values represent the 1075–1125 cm^{-1}, 995–1045 cm^{-1}, and 945–995 cm^{-1} bands of the baselined Region 1 spectrum. The Raman spectral intensity maps were compared to the mineral identification maps for secondary validation, and the resulting product is the presented mineral maps in Figs. 6.2-6.4.

Olivine convolution

SHERLOC detection of olivine in Garde was based on the appearance of a single Raman peak at 820–840 cm^{-1}, rather than the doublet at ~820 and ~850 cm^{-1} that has been widely reported for olivines in the literature (Kuebler et al., 2006). The convolution of the olivine doublet into a single peak was also observed in laboratory measurements of olivines using the Brassboard, SHERLOC's terrestrial analog instrument, and is due to the 40–50 cm^{-1} spectral resolution of both instruments, as described in (Razzell Hollis et al., 2021a). It may still be possible to quantitatively derive olivine Fo# compositions from the convoluted peak position, based on the shifting doublet positions reported in (Kuebler et al., 2006), but current analysis is limited to qualitatively associating lower Raman shifts to lower Fo#.

S3. Image processing

SHERLOC includes two imaging subsystems, each equipped with a CCD camera: the Wide Angle Topographic Sensor for Operations and eNgineering (WATSON) and the Autofocus Context Imager (ACI) (Bhartia et al., 2021; Minitti et al., 2021; Edgett et al., 2021). WATSON provides color imaging (1600 x 1200-pixel) of analysis targets from 2.5-40cm standoff distances. WATSON is able to contextualize the SHERLOC and PIXL instrument data, acquire stand-alone observations of rock surfaces, and image rover components and calibration targets to maintain the instruments onboard. The

ACI acquires high-resolution grayscale images (1600 x 1200-pixel, ~10.1 um/pixel spatial scale) at a working distance of 4.5-5 cm to focus SHERLOC's laser and provide context for spectroscopic measurements (Bhartia et al., 2021; Minitti et al., 2021). Both of these imaging subsystems' camera heads are mounted atop a rotatable turret on the robotic arm of the Perseverance rover, and can be independently positioned on a chosen target to provide complementary information, though they are not co-boresighted (Bhartia et al., 2021; Minitti et al., 2021).

The ACI focus merge products used here were created on Earth and flat-fielded using "sky flat" images acquired by ACI of the Martian sky on Sol 77. ACI focus stacks consist of 31 images obtained at different focus positions that capture the scene in increments of ~0.2 mm focus range (e.g., 45.0 mm to 50.4 mm in 31 steps). Images outside the below ranges were not in focus and thus not used in the creation of the focus merge products. The images used in each focus merge product were as follows:

Guillaumes_161 - sol 161 - images 16-26 of 31
Guillaumes_162 - sol 162 - images 13-31 of 31
Bellegarde_186 - sol 186 - images 15-20 of 31
Garde_207 - sol 207 - images 15-19 of 31
Dourbes_257 - sol 257 - images 14-21 of 31
Dourbes_269 - sol 269 - images 14-20 of 31

Image registration and processing was performed using a custom Python script that utilized corresponding ACI (non-focus merged) and WATSON (onboard focus merge) images for a target to create an overlay. Keypoint detection was performed using the Binary Robust Invariant Scalable Keypoints (BRISK) method (Leutenegger et al., 2011) and subsequently matched using the Fast Library for Approximate Nearest Neighbors (FLANN) based matcher utilizing the OpenCV python package (Bradski, 2000). Colors from the two images were blended in hue, saturation, value (HSV) space to create a "colorized" ACI. Each colorized ACI was then overlaid with a map of laser points targeted by SHERLOC and generated in Loupe for each scan type (see S2).

S4. Perchlorate laboratory measurements

The measurement of reference DUV Raman spectra for synthetic perchlorate salts was done using the SHERLOC brassboard instrument, an optical analog of the flight model that was designed to work under terrestrial ambient conditions (Razzell Hollis et al., 2021a). The salts and their sources were as follows: sodium perchlorate monohydrate (Sigma Aldrich 310514), potassium perchlorate (Alfa Aesar A11296),

magnesium perchlorate (Sigma Aldrich 63102), and calcium perchlorate hydrate (Alfa Aesar 11655), all of which had reported purities of >95%. Each salt was characterized as a powder on a clean Aluminum wafer and all measurements were done under ambient conditions; the calcium perchlorate hydrate deliquesced during measurement. Spectra were collected and processed using the method described in Razzell Hollis et al., 2021a.

S5. Assessment of perchlorate species

Detailed consideration of multiple different chemical compounds were considered for assignment of Guillaumes perchlorate spectra. Fig. S4 demonstrates several potential minerals that were assessed as an alternative to a perchlorate origin, including carbonate, phosphates, and sulfates. We compared our strongest SHERLOC spectra to a number of different perchlorate salts, including anhydrous and hydrated species, that were obtained through laboratory measurements with the SHERLOC Brassboard, an analog DUV Raman and fluorescence instrument at the NASA Jet Propulsion Laboratory with similar sensitivity and spectral resolution to SHERLOC. The position of the major 950–955 cm^{-1} peak observed on Mars places it between the observed major peak positions of Na-perchlorate and fluorapatite. However, the observation of two minor peaks at 1090–1095 cm^{-1} and 1150-1155 cm^{-1} are both consistent with Na-perchlorate rather than fluorapatite, which only has a single secondary mode at 1050 cm^{-1} (Fig. S4). Of the perchlorates we measured in the laboratory, only Na-perchlorate exhibits the two minor peaks we observe, the others exhibit a single minor peak at 1095–1115 cm^{-1}. Therefore, despite the ~5–10 cm^{-1} difference in major peak position compared to our Na-perchlorate reference, we are confident that we have observed Na-perchlorate on Mars. When comparing SHERLOC spectra to hydrous and anhydrous versions of Na-perchlorate from (Wu et al., 2016) and unpublished recent efforts (Fischer et al., 2021; Mason & Elwood Madden, 2021, Clark J., personal communication), we find that there is no conclusive difference in match to minor peaks. However, the only spectral evidence we have for hydration (the O–H stretching mode around 3300 cm^{-1}) was observed in locations that exhibited sulfate peaks, indicating a hydrated sulfate species rather than a hydrated perchlorate species. Last, we compared our spectra to those obtained for other oxygen chloride species by a previous study (Wu et al., 2016). Higher oxidative states will systematically shift the peak position upwards and will also alter the position of minor peaks. No examined alternative Na oxygen chlorides yielded a match with either major or minor peaks of the SHERLOC spectra. It is possible that – yet unexamined – down-shifting of peaks related to other cation oxygen chlorides, such as Ca and Mg species, could explain the major 950–955 cm^{-1} peaks. However, these would not be able to explain the position and shape of the two minor peaks that appeared in our strongest spectra.

S6. Assessment of fluorescence correlation with Supercam LIBS shots

The two bright ~275 nm spots in Guillaumes, which are co-located with previous LIBS shots, are likely fluorescence emission from 1-ring aromatics either created by the LIBS plasma, or exposed by ablation of surface material. Given that this was done on an already abraded surface, it seems unlikely that we are examining pristine 1-ring aromatics in the sub-surface, instead we suspect that we are seeing the 1-ring aromatics produced by LIBS-induced photochemical breakdown of MMC (macromolecular carbons) present within the rock. However, we cannot currently rule out the possibility that LIBS-induced crystal defects within the exposed rock may be producing the observed luminescence.

S7. Comparison between SHERLOC mineral identifications and other instruments

SHERLOC Raman detections of sulfates within the Bellegarde target correlate directly with Ca-sulfate detections and minor Mg-sulfate components by the PIXL elemental maps, cementing the interpretation of secondary mm-scale Ca/Mg-sulfate crystals (Fig. S5). The PIXL elemental maps also reveal closely spaced Ca-sulfate and Na-Cl phases correlating with white, anhedral patches within the Guillaumes target, but the maps were not measured over the same area as the SHERLOC Raman map (Fig. S6). Lastly, Supercam LIBS and Raman observations also confirm the presence of mixed Na-Mg-Cl phases, Na-perchlorate, and Ca/Mg-sulfates within partially overlapping measurements compared to SHERLOC in Guillaumes and Bellegarde (Farley et al., submitted).

In the remaining measured spots that cover the primary texture within the Guillaumes and Bellegarde targets, we did not detect definitive mineral Raman peaks. However, the average spectra for each scan of Guillaumes and Bellegarde reveal the presence of a broad peak centered at 1060 cm^{-1} with a full width half maximum (FWHM) of 160 cm^{-1} and low intensity, consistent with amorphous silicate. This spectrum was similar to the single-point detection of amorphous silicate found within Garde. PIXL observations of Bellegarde and Guillaumes indicate primary phases consist of pyroxene, plagioclase, and olivine, which were not observed in the SHERLOC data (Fig. S5-S6) (Farley et al., submitted). SHERLOC cannot report on the presence of plagioclases, as the dominant Raman peak of plagioclase (around 500 cm^{-1}) falls within the spectral range of SHERLOC's edge filter, which significantly attenuates signal below 700 cm^{-1} and makes peaks in this range harder to detect (Razzell Hollis et al., 2021a). PIXL-determined olivine were analyzed to be Fe-rich fayalite, which cannot easily be observed with SHERLOC due to strong DUV absorption by Fe, which reduces overall signal (Razzell Hollis et al., 2021a). Pyroxenes may not have been detected for a number of reasons, for example low abundance or crystallographic orientation. Alternatively, some of these phases may also be significantly disordered giving rise to broader, weaker Raman peaks similar to amorphous silicate signatures. Modelling of orbital data from the Thermal Emission Spectrometer predicted ~24% and ~15% amorphous silicate components within the Máaz and

Seitah formations (Salvatore et al., 2018). The Curiosity rover also detected 15-70 wt% X-ray amorphous components within samples of sedimentary rocks in Gale crater, suggesting the presence of amorphous silicates may be a common phenomenon on Mars (Smith et al., 2021). While the SHERLOC Raman detections of amorphous silicates at present cannot distinguish between the proposed origin as volcanic glass, impact glass, or aqueous alteration of previously crystalline silicate phases, the amorphous silicates within Gale crater have been found to be more consistent with aqueous alteration of previously crystalline silicate phases (Smith et al., 2021).

S8. SHERLOC sensitivity to organics

SHERLOC is capable of detecting organic material via DUV fluorescence emission and Raman scattering, and is most sensitive to compounds containing 1- and 2-ring aromatic units and/or aromatic heterocycles, which typically fluoresce within SHERLOC's spectral range (Bhartia et al., 2008; Eshelman et al., 2015; 2018). Fluorescence provides an exceptionally strong signal, enabling detection of fluorescent compounds even at very low concentrations (Bhartia et al., 2021), while Raman is generally multiple orders of magnitude weaker than fluorescence but provides a spectrum highly specific to chemical structure, enabling identification of particular compounds. Aromatic organic compounds typically dominate SHERLOC spectra, due to strong fluorescence emission and molecular resonance enhancement of Raman scattering (Bhartia et al., 2008). Measured Raman and fluorescence intensities are determined by laser energy at the target, the size of the illuminated volume within the target, the concentration and scattering cross-section/quantum yield of the organic molecule, and optical attenuation by surrounding material (Razzell Hollis et al., 2020). The presence of certain metals that have strong absorptions in the DUV, such as Fe (Bhartia et al., 2008; Carrier et al., 2019; Shkolyar et al., 2018) or Ce (Shkolyar et al., 2021), may attenuate measured signals from any organic molecules within the same sample. Because of such dependencies, quantification of organic concentrations from either Raman or fluorescence signal yields is limited to estimations that utilize a set of assumptions and known instrument performance characteristics, and provide upper/lower bounds for concentration rather than specific values. While some inorganic complexes, specifically $CePO_4$, are also known to fluoresce between 250 and 355 nm (Shkolyar et al., 2021), the observed fluorescence is consistent with data from the SaU 008 martian meteorite calibration target where those inorganic features do not exist (Farley et al., submitted). Additionally, the organic observations of Guillames, Bellegarde, and Garde are associated with carbonates and sulfates, whereas inorganic complexes that can incorporate Ce have not been detected by observations from other instruments aboard the rover.

To estimate the localized concentration and bulk concentrations observed, we utilized the optical performance model that was used to design and verify the performance of the SHERLOC instrument (Farley et al., submitted; Bhartia et al., 2015) . The model incorporates all the primary SHERLOC instrument parameters such as the laser energy at the target, the collection performance, the noise as a function of CCD operation temperature, CCD gain, background subtraction effects to noise, dark noise, and read noise to generate an expected analog to digital count for both signal and noise. This value is dependent on the interrogation volume, the quantum yield of the compound, and its concentration within the interrogation volume. The interrogation volume is approximated by the product of the illumination area and the depth of penetration. We assume that the instrument is focused (within ±500 μm of the optimal focus) and generates a 106 μm diameter annular beam (Razzell Hollis et al., 2020). The depth of penetration into a Mars simulate with similar Fe concentrations was shown to be up to 150 μm (Carrier et al., 2019). The current estimation in the model conservatively assumes a 75 μm depth of penetration. Using an average density of an igneous rock of 2.7 g/cm^3, the total mass analyzed in a single point measurement is 0.6 μg. Over a 1296 point map, this equates to a total mass of ~800 μg.

To determine the concentration of organics in a single point in the map, we use a highly conservative fluorescence cross-section for benzene (1.5 x 10^{-24} cm^2 sr^{-1} nm^{-1} $molecule^{-1}$ (Suto et al., 1992)) at the SHERLOC excitation wavelength, 248.5794 nm. Based on these values, the model adjusts the concentration within a single spot to achieve the detected CCD counts (Fig. S7). The mass of organics is determined for a single point. To assess bulk concentration for comparison the average fluorescence spectrum of the map is used to determine the total mass of organics detected (Fig. S7). This is then divided by the total mass in the scanned volume to derive a concentration in terms of ppm. These values are used to bound the concentration for comparison to previous analyses on Mars and of Martian meteorites and provide a means to compare the difference as we traverse through Jezero crater.

Fig. S1. SHERLOC context and WATSON image merge showing the textures of mineral assemblages within the Guillaumes target. (A) Mineral detections within survey and HDR scans of the Guillaumes target from Fig. 6.3. (B-D) Texture of high intensity Na-perchlorate detections (orange outline and arrows), low intensity less certain Na-perchlorate detections (yellow outlines and arrows) as well as occasional Ca-sulfate detections (white arrows). The mineral detections are mixed within anhedral, white, tan to reddish brown patches of material that are secondary to the primary lithology of the Guillaumes target.
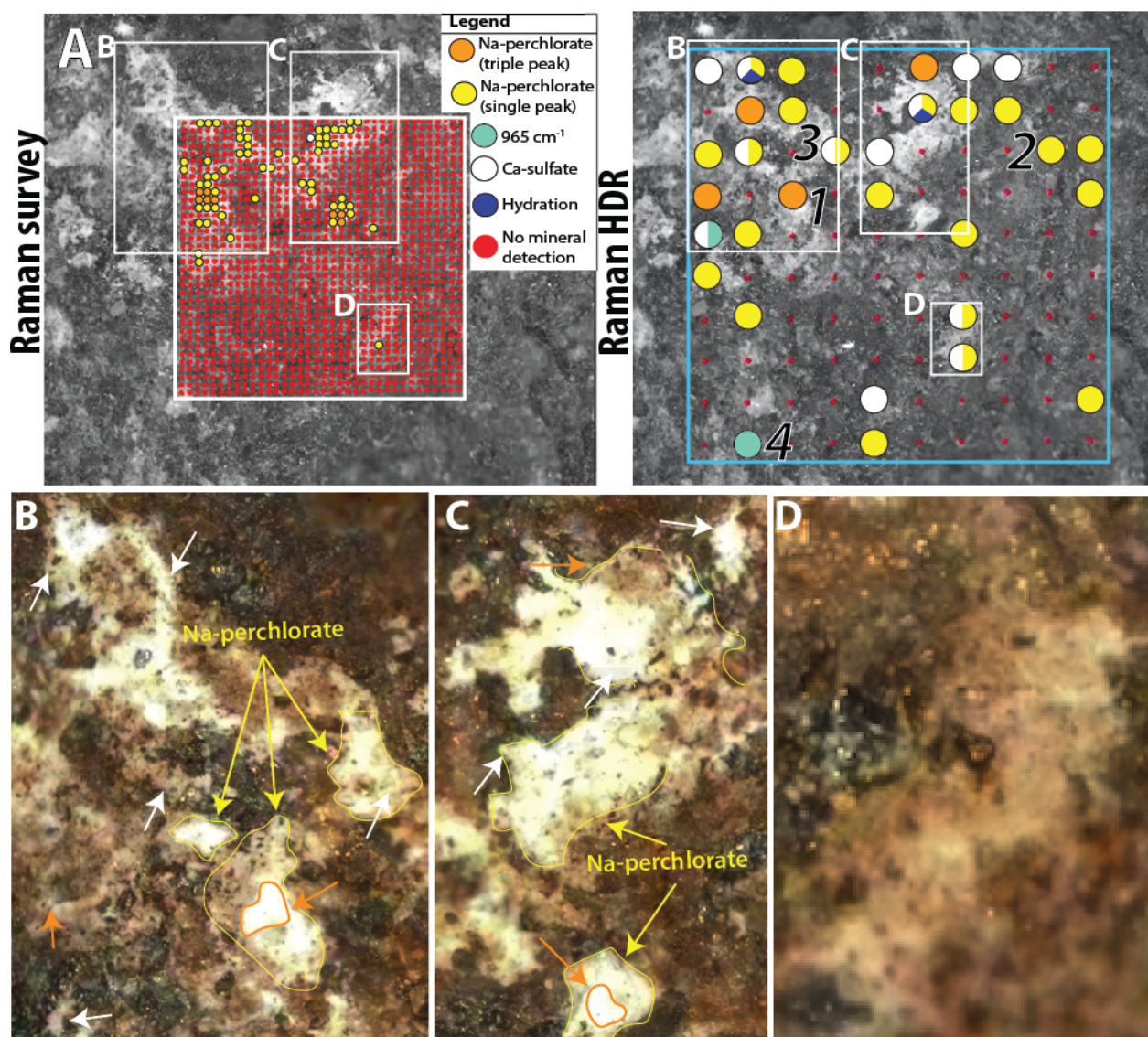
Fig. S2. SHERLOC context and WATSON image merge showing the textures of mineral assemblages within the Bellegarde target. (A) Mineral detections within HDR scans of the Bellegarde target overlain on the PIXL elemental chemistry map of SO_3, MgO, and CaO from Fig. S5. (B-F) Texture of Ca-sulfate detections (white arrows) and possible phosphate materials with a 975 cm^{-1} peak (turquoise arrow). Ca-sulfates are detected within white anhedral to sub-euhedral crystals that have a reddish rim around them that appear secondary to the primary lithology. Textures of possible phosphate minerals are more nebulous.
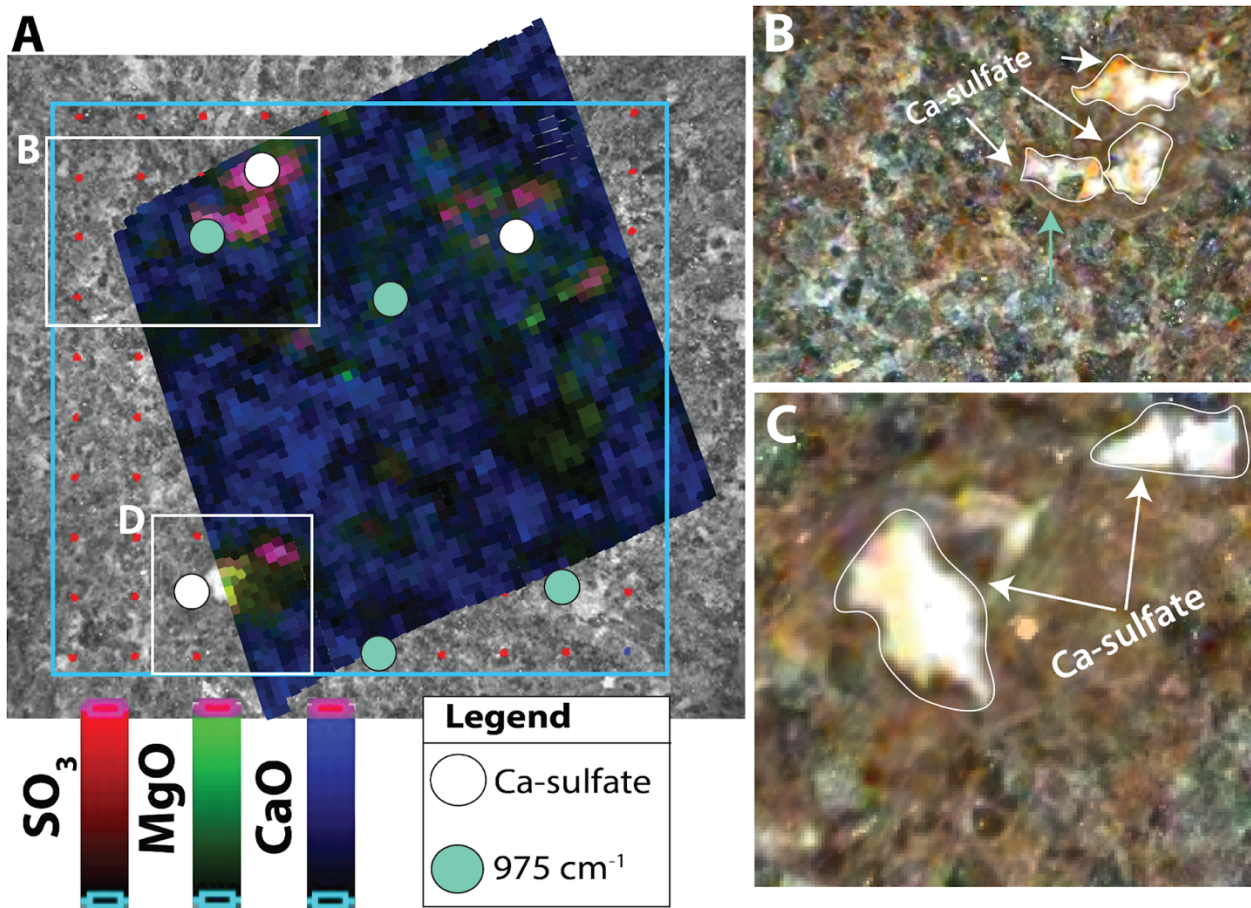
Fig. S3. Hydration feature recorded within Bellegarde sulfates. (A) Average SHERLOC spectrum of the sulfate material within the yellow ROI in panel B showing weak hydration feature at 3560 cm^{-1}. Same spectrum as spectrum no. 1 in Fig. 6.4. (B) Low SNR Raman map from Fig. 6.4E.
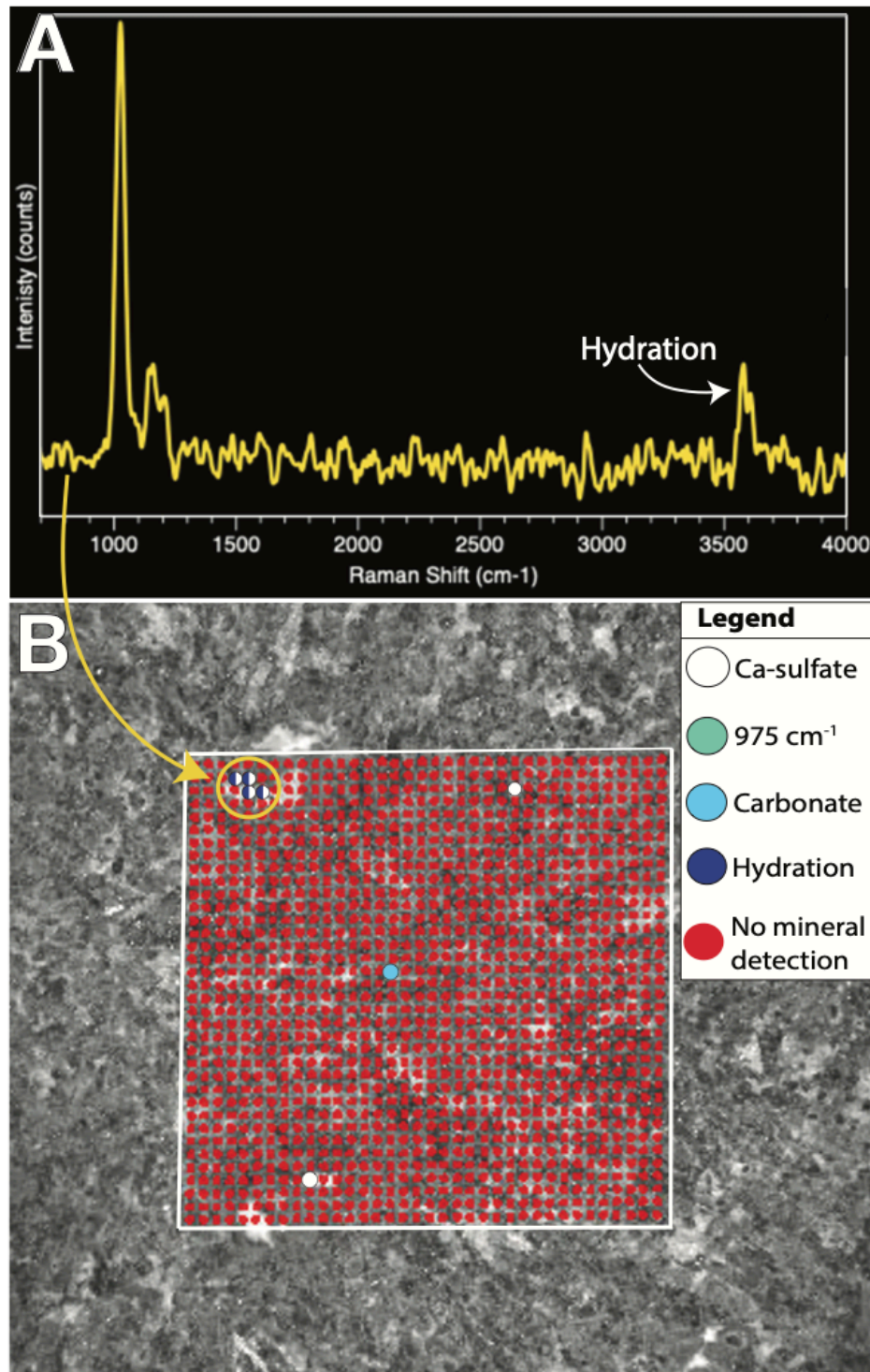
Fig. S4. Comparison between SHERLOC spectra of perchlorate in Guillaumes target and laboratory measurements of a variety of materials. (A,B) Spectrum 5 and spectrum 37 of HDR 2 of Guillaumes from Sol 162, compared to normalised spectra of representative perchlorate, phosphate, sulfate, and carbonate standards, showing that overall spectrum shape is most like that of perchlorate. (C) Secondary peak position plotted against primary peak position for the 4 strongest perchlorate spectra from Guillaumes, compared to all perchlorate and phosphate standards, showing that correlated peak positions are best matched to sodium perchlorate. Vertical dotted line indicates the primary peak position of SHERLOC's best phosphate detection.
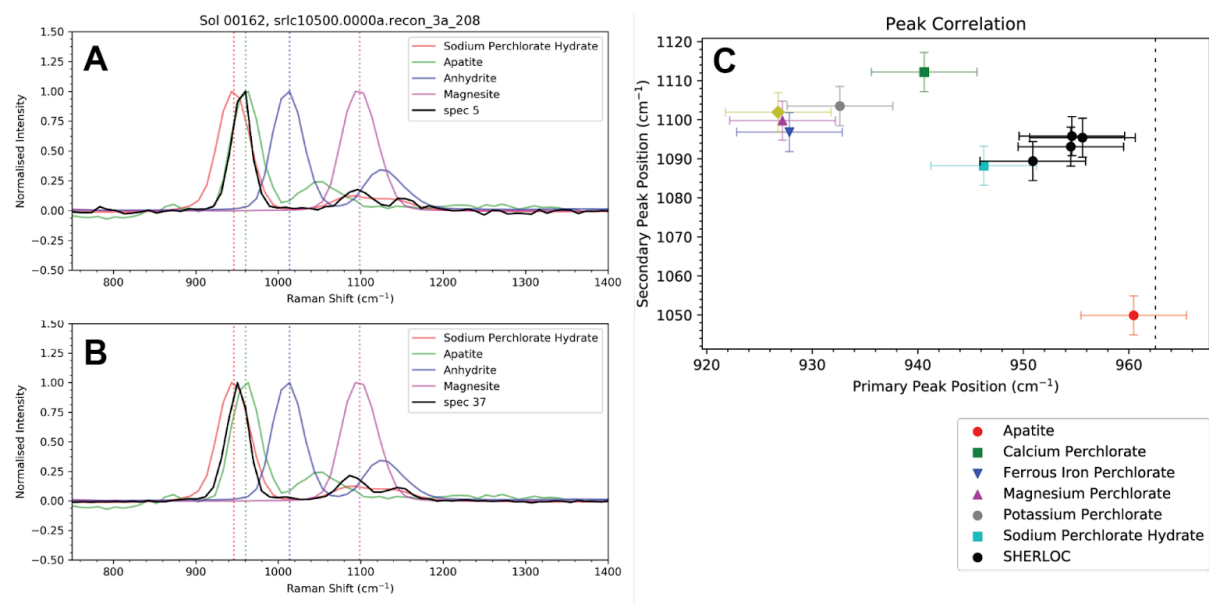
Fig. S5. Elemental chemistry maps of the Bellegarde target produced by the PIXL instrument on the Perseverance rover in comparison to SHERLOC mineral detections. (A) SHERLOC context image of survey scan (white rectangle) and HDR scan (cyan rectangle) superposed on WATSON image of the Bellegarde abraded target from Fig. 6.4. (B-C) Heatmaps of Cl and Na_2O suggest the presence of a Na- and Cl-rich phase. One SHERLOC 975 cm^{-1} peak correlates with a Na-Cl hotspot. (D) Correlations between SO_3 and CaO suggest the presence of Ca-sulfates (pink), which correlate with Ca-sulfate detections in HDR scans (white circles). (E) Distribution of phosphorus (green) does not obviously correlate with 975 cm^{-1} peaks. (F) Correlations between SiO_2, FeO_T, and Al_2O_3 in the PIXL map show that the primary lithology consists of silicates (cyan and purple) and Fe-oxides (red) and does not correlate with SHERLOC detections. (G) Correlations between SO_3 and CaO suggest the presence of Ca-sulfates (pink), which correlate with Ca-sulfate detections in survey scans (white circles).
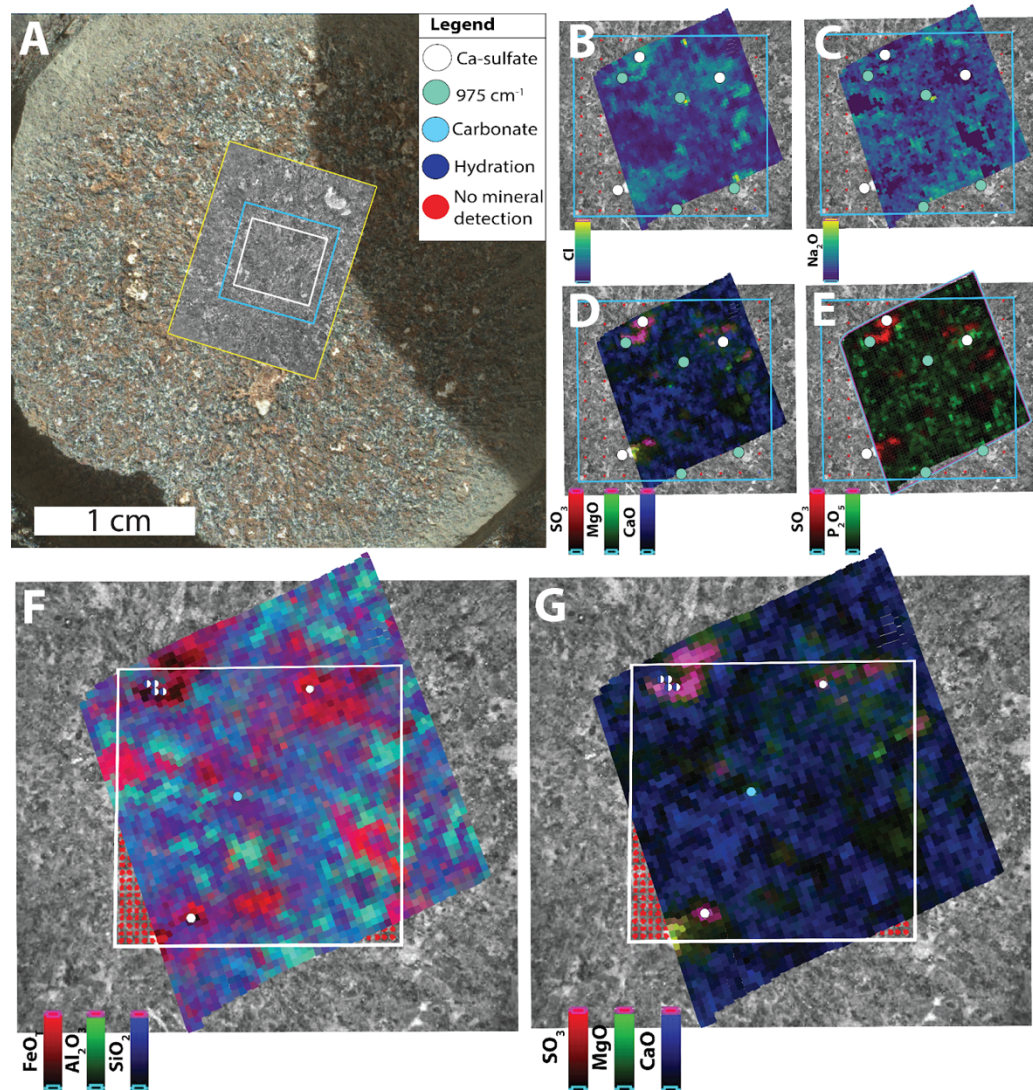
Fig. S6. Elemental chemistry maps of the Guillaumes target produced by the PIXL instrument on the Perseverance rover. (A) PIXL footprint (cyan and purple outline) on PIXL context image showing the location of elemental maps in panel B-G. (B-C) Heatmaps of Cl and Na_2O suggest the presence of a Na- and Cl-rich phase. (D) Spatial relationships between Ca-sulfate (red) and Na- and Cl-rich phases (cyan). (E) Distribution of phosphorus (green) in relation to SO_3 (red). (F) Correlations between SiO_2, FeO_T, and Al_2O_3 showing that the primary lithology consists of silicates (cyan and purple) and Fe-oxides (red). (G) Correlations between SO_3 and CaO suggest the presence of Ca-sulfates (pink).
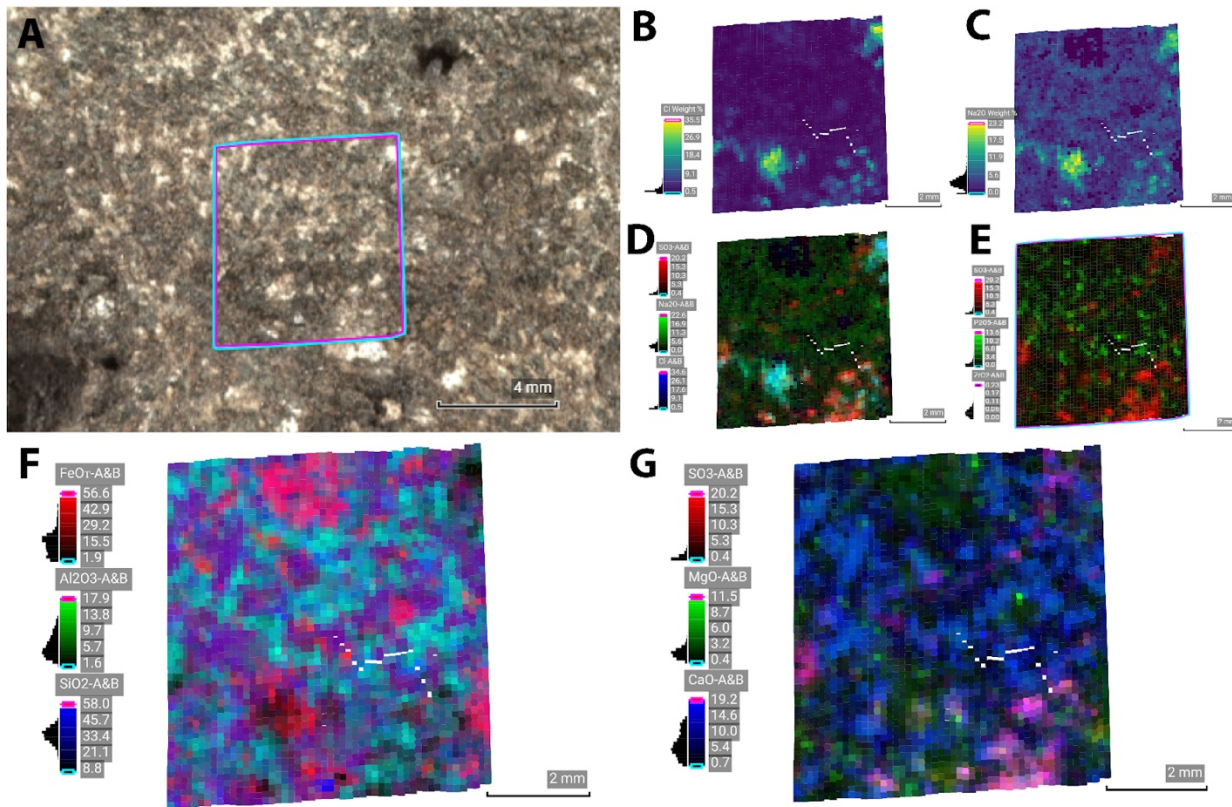
Fig. S7. SHERLOC fluorescence spectra compared to laboratory measurements of simple aromatic organics. Three regions of interest (ROIs) were selected within the fluorescence maps of the three targets, Guillaumes, Bellegarde, and Garde in Fig. 6.2-6.4. These demonstrate the variability in fluorescence signatures throughout the rocks that peak at ~275 nm, ~305 nm, and ~340 nm as described in the main text. Below we show laboratory fluorescence measurements of L-phenylalanine, benzoic acid, and naphthalene made with the Brassboard analogue instrument to demonstrate that aromatic organics fluoresce at these same wavelengths. Note that for Guillaumes spectra, ROI 1 is shown according to the left-hand y-axis, while ROIs 2 and 3 are shown according to the right-hand y-axis.
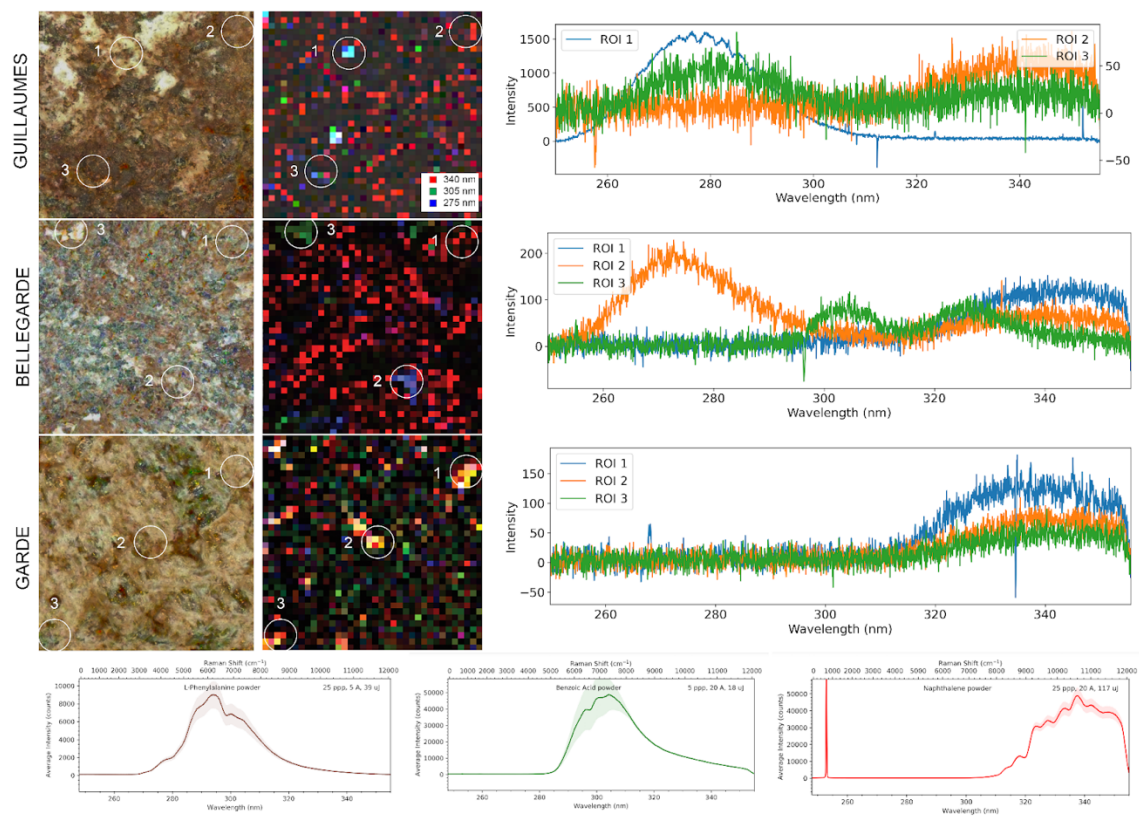
Supporting information for Chapter 7: Materials, methods, and supplementary text and figures

Materials and Methods

S1. Current water reservoirs and D/H compositions

The size of the current exchangeable water reservoir is based on the (negligible) concentrations of water vapor in the modern atmosphere; orbital detections of H_2O ice within the volume of the North Polar layered deposits (NPLD) (~12 m GEL; Zuber et al., 1998), the North Pole Basal Unit (~1.5 m GEL; Nerozzi & Holt, 2019), the South Polar layered deposits (~11 m GEL; Plaut et al., 2007); and the broader south polar deposits, glaciers, and high- and mid-latitudinal subsurface ice (Whitten & Campbell, 2018). Most estimate that mid-latitudinal ice deposits contain <1-1.1 m GEL (Mustard et al., 2001; Dundas et al., 2018; Bramson et al., 2017; Karlsson et al., 2015). Thus, the minimum size of the current water reservoir is the volume of NPLD and SPLD (~20 m GEL). However, it has also been suggested that the total south polar water reservoir may be twice as large as the total north polar reservoir and that mid-latitudinal glaciers and subsurface ice may be larger reservoirs, collectively totaling ~35 m GEL (Christensen et al., 2006). As the size of the modern surface exchangeable reservoir is a subject of study, we conservatively allow a maximum size of 40 m GEL.

The present-day D/H composition has been evaluated by astronomical global and latitudinal measurements (Donahue et al,. 1995; Villanueva et al., 2015, Owen et al., 1988), atmospheric and surface fine samples measured with the Sample Analysis at Mars (SAM) instrument on the Curiosity rover (Webster et al., 2013; Leshin et al., 2013), and measurements of young Shergottite, Nakhlite, and Chassignite (SNC) meteorites (Leshin et al., 2000; Hu et al., 2014) (Fig. S1). Global averages from telescopic data combined with models are estimated to be 6 ± 3 × SMOW (Owen et al., 1988) or 5.2 ± 0.2 × SMOW (Webster et al., 2013). latitudinal seasonal differences in atmospheric D/H of 1-10 × SMOW have been observed, with a general global value of 7 × SMOW (Villanueva et al., 2015). Most of the exchangeable reservoir is present in the NPLD and SPLD today. The NPLD has been modelled to have D/H compositions of 2.7 – 8 × SMOW (Villanueva et al., 2015; Fischer, 2007; Montmessin et al., 2004). SAM measurements of the atmosphere yielded 5.95 ± 1 × SMOW (Webster et al., 2013) while

measurements of surface fines yielded 4.8-8 × SMOW (Webster et al., 2013; Karlsson et al., 2015).
Young meteorites with ages <1 Ga record a range of 5-7 × SMOW (Leshin et al., 2000, Hu et al., 2014).
Hence, estimated D/H compositions of the exchangeable reservoir today vary considerably based on
observational methods. We approximate the present-day D/H composition of the exchangeable reservoir
with the estimates that range from 5-10 × SMOW (Fig. S1) (Donahue et al., 1995; Webster et al., 2013;
Villanueva et al., 2015; Owen et al., 1988; Leshin et al., 2013; Hu et al., 2014; Fischer, 2007; Montmessin
et al., 2014).

S2. Initial and Hesperian atmospheric D/H composition

D/H measurements within the ALH84001 meteorite (3.9-4.1 Ga; Borg et al,. 1999; Lapen et al., 2010)
provide the oldest available measurement of D/H of the Martian atmosphere, yielding D/H compositions
of 4 × SMOW or 2 × SMOW based on Secondary Ion Mass Spectrometry (SIMS) analysis of apatites and
carbonates, respectively (Fig. S1, Table S1) (Boctor et al., 2003; Greenwood et al., 2008). The only other
meteorite, NWA7034 (Black Beauty), which contains materials of similar age (~4.4 Ga) does not record
atmospheric D/H values (Hu et al., 2019; Barnes et al., 2020).

   SAM has measured several rock samples for hydrogen isotopes using its Tunable Laser
Spectrometer (TLS) and Quadruple Mass Spectrometer (QMS). TLS measurement of the Cumberland
sample has been used to infer a D/H composition of 3 ± 0.2 × SMOW (Mahaffy et al., 2015) for the
exchangeable reservoir during sediment deposition in Gale Crater (3.5-2.6 Ga (Grant et al., 2014; Le Deit
et al., 2013; Martin et al., 2017). This measurement was part of a combustion experiment in which only
water released at 550°C and 920°C was analyzed (Mahaffy et al., 2015). Water released in this
temperature range is inferred to be the structural hydroxyl hydrogen from the octahedral layer of smectite
(Mahaffy et al., 2015). In general, SAM measurements will only record the D/H composition of the
ancient surface environment in combustion experiments performed at high temperature, as water released
at lower combustion temperatures would be from a range of mineral sources and yield high, modern
atmospheric D/H values (Mahaffy et al., 2015). Samples from rock strata explored later in the mission
were also measured with the TLS at high combustion temperatures of 374-862°C associated with
dehydroxylation of clay minerals and include Cumberland, Quela, Duluth, Kilmarie, and Glen Etive
samples. These yield a D/H range of 3-5 × SMOW (Fig. S1) available on the Planetary Data System
(PDS) as SAM TLS level 2 data, following processing and corrections according to (Mahaffy et al., 2015;
2012). We adopt 3-5 × SMOW as the D/H range for mineralization within lake sediments in Gale Crater.

   We adopt the age of ALH84001 (~4.1 Ga) as our model starting point as this is the earliest data point
for the atmosphere, corresponds approximately to the earliest geologic units (Tanaka et al., 2014), and
occurs after the generally unconstrained conditions of the Pre-Noachian. We do not enforce any

constraints on the composition of the exchangeable reservoir during the Hesperian, unlike previous studies (Alsaeed & Jakosky, 2019; Carr & Head, 2019). This is due to the large uncertainty in the SAM data that still needs to undergo a detailed assignment of mineral sources for released water. However, we do perform a qualitative comparison between model simulations and the 3-5 × SMOW range of all SAM data measured from high temperature combustion experiments (Fig. 7.2, Fig. 7.3).

S3. Crustal hydration volume

Remote sensing data show globally widespread hydration of the upper crust of Mars during the Noachian, exhibited by hydrated minerals exposed from current crustal depths of 7-10 km in the walls of tectonic features like Valles Marineris and central uplifts of complex craters and basins (Mustard et al., 2019; Murchie et al., 2009; Sun & Milliken, 2015). More geographically restricted hydrated mineral formation continued during the Hesperian, observed at the Meridiani and Gale crater landing sites as well as in Hesperian and early Amazonian hydrated mineral deposits seen from orbit (Mustard et al., 2019; Grotzinger et al., 2015; Grant et al., 2014; Le Deit et al., 2013; Martin et al., 2017; Vaniman et al., 2014). Observations at the Gale landing site support water contents of 1-5 wt. % in stratigraphic units (Vaniman et al., 2014; Sutter et al., 2017; Thomas et al., 2020), and infrared and neutron spectrometer data acquired globally show water contents of 2.5-9 wt.% and 2-15 wt. % in the upper half-meter of ice-free terrains, respectively (Audouard et al., 2014; Maurice et al., 2011). Meteorite NWA7034, an aqueously altered crustal regolith breccia, contains ~0.6 wt% bulk water content (Agee et al., 2013; Humayun et al., 2013). More conservative estimates report an average crustal water content range of 0.5-3 wt% (Mustard, 2019; Wernicke et al., 2019), which we adopt as bounding scenarios of hydrated mineral formation to depths of 5-10 km during the Noachian, yielding a range of 100-900 m GEL, i.e., loss of 0.25-2.25 m GEL Myr^{-1} to Noachian crustal hydration (Fig. 7.1, Table S1). Similarly, this range of water contents for a scenario of hydrated mineral formation to depths of 1 km during the Hesperian yields a range of 10-100 m GEL of water or a loss of 0.014 – 0.14 m GEL Myr^{-1} to Hesperian crustal hydration (Table S1) (Mustard, 2019). Amazonian crustal hydration also likely occurred but, due to limited water and limited erosion rates, was restricted to the uppermost crust and was negligible by comparison (a few meters and a few wt. %, totaling ≲1 m GEL).

The observational range of crustal hydration volumes is consistent with the 400 m GEL water reservoir proposed to have been incorporated within the crust to form serpentines (Chassefiere & Leblanc, 2011). Later observations have shown smectite clays and hydrous phases other than serpentine are more volumetrically dominant (see section S4). It is possible that crustal hydration could initially have occurred as unexchangeable subsurface ice or water volumes trapped in the subsurface and out of contact with the active hydrosphere (Carr & Head, 2019; Grimm et al., 2017; Carter et al., 2013). Some models have

hypothesized an undetected subsurface water/ice reservoir of 100-1000 m GEL (Kurokawa et al., 2014; Grimm et al., 2017; Carter et al., 2013), and 100s of m GEL subsurface water might be present on Mars today (Grimm et al., 2017; Carter et al., 2013). While such large quantities of subsurface ice or water have not been directly observed, these estimated volumes are within the range of the observed amount of hydrated minerals within the Martian crust. One possibility is that the majority of subsurface water/ice could eventually have been incorporated into the crust in the form of hydrated minerals. As such, the crustal hydration reservoir presented in our model (Fig. 7.1) reflects the entire reservoir of unexchangeable water, approximated as a single reservoir. Observations indicate some or all of this water is as mineral structural water but any as-yet-unobserved deep subsurface ice or deep liquid water would also be part of this reservoir.

S4. D/H fractionation associated with crustal hydration

Fe/Mg-smectite clays are the most volumetrically abundant hydrated minerals on Mars by orders of magnitude (Grotzinger et al,. 2015; Ehlmann et al,. 2011; Vaniman et al., 2014; Thomas et al., 2020; Carter et al., 2013), and their formation would cause a D/H fractionation of the exchangeable reservoir. Clays preferentially incorporate hydrogen into their crystal structure over deuterium, which is approximated by the equilibrium fractionation factor between water and smectite ($\propto_{smectite-H_2O}$). Geochemical experiments and models that evaluate this fractionation factor span a possible range of 0.91-0.99 for $\propto_{smectite-H_2O}$ (Table S3). These fractionation factors have generally been evaluated for Al-rich smectites, commonly formed on Earth, as opposed to Fe/Mg-rich smectites, commonly formed on Mars. Fe-rich smectites yield fractionation factors of 0.91, while Al-rich smectites yield higher fractionation factors of 0.98 (Sheppard & Gilg, 1996). No experimental constraints are available on the fractionation factors related to the exact chemical composition of smectites on Mars. However given the restricted possible range of fractionation factors (0.91-0.99), we adopt the median value of $\propto_{smectite-H_2O}= 0.95$ as our assumed approximation of the exchange between the exchangeable reservoir and Fe/Mg-smectites on Mars (Table S1).

S5. Volcanic degassing volume

The volcanic degassing through geological time has previously been estimated by photogeology and by modelling the thermophysical and chemical evolution of the mantle and crust. The initial upper mantle temperature governed the amount and timing of water loss from the mantle (Hauck & Phillips, 2002). two models have been proposed (Grott et al., 2011) that differ in assumptions regarding the surface fraction (f_p) of "hot upwellings" in which melting is taking place, which changes the time-dependence of volcanism and cumulative volatile release. Assuming an initial mantle water content (f_{mantle}) of 100 ppm,

melting on a global scale ($f_p = 1$; "the Global Melts model") results in 61 GEL of degassed water while melting restricted to mantle plumes ($f_p = 0.01$; "the Mantle Plume model") results in 17 GEL of degassed water (Grott et al., 2011) (Fig. 7.3). Time-dependent degassing curves estimated by (Hauck & Phillips, 2002) with 15-25 GEL outgassing are similar to the Mantle Plume model, when assuming an initial mantle water content of 100 ppm, and are encompassed by this scenario. These models also match within uncertainties the photogeological estimates of crustal production rates (Greeley & Schneid, 1991; Grott et al., 2013).

Volcanic degassing models scale directly with assumed initial water content (f_{mantle}) of the volcanic source region, which is constrained by Martian meteorite data. These data reveal a possible range of water contents in source regions from few ppm to 1000 ppm (Lammer et al., 2013) (Table S1). Previous works adopted 100 ppm (Grott et al., 2011; Morschhauser et al., 2011). However, assuming mantle water contents of 1000 ppm, which are extreme but within proposed ranges (Lammer et al., 2013; McSween et al., 1993), the Mantle Plume model and Global Melts model would yield 170 and 610 GEL outgassed water, respectively. For the difference in time-dependent degassing, we utilize the Global Melts model scaled to 300 ppm instead as an upper bound – equivalent in cumulative degassing to the Mantle Plume model at 1000 ppm (Fig. 7.3).

With these 4 different volcanic degassing models (Fig. 7.3), we provide representative time-dependent volcanic outgassing fluxes ($F_{volcanic}$) scenarios that bracket all previously proposed models (Table S1) (Grott et al., 2011; Hauck & Phillips, 2002; Greeley & Schneid, 1991; Grott et al., 2013; Morschhauser et al., 2011, Fraeman & Korenaga, 2010). Volcanic outgassing of H_2O is also dependent on redox conditions (Gaillard & Scaillet, 2009; Schaefer & Fegley, 2017) as well as mantle overturn and heterogeneity (Plesa, 2014) adding additional uncertainty. In general, these one-dimensional volcanic degassing models (Fig. 7.3) are first-order approximations. The effects of other relevant magmatic model parameters (e.g., outgassing efficiency, initial temperature profiles, thermal properties of the mantle, and crustal thickness, and 3D processes) are encompassed by the parameters that we vary: melt fraction, water content, and timing (Fig. 7.3, Table S1). These scenarios are representative of the general range of model results that suggest either 40-80 % (Morschhauser et al., 2011; Fraeman & Korenaga, 2010) or 5-10% (Hauck & Phillips, 2002) of the initial mantle reservoir has outgassed through time.

From 0-2.5 Ga, the volcanic degassing in our simulations is changed from the thermochemical model (Grott et al., 2011) because these predict no crustal production during this time interval. To account for observations of Middle-Late Amazonian-formed volcanic units on the surface, during the Amazonian time interval, we instead utilize a surface melt production 0.1 km^3 year^{-1} (Greeley & Schneid, 1991; Carr & Head, 2010) and f_{mantle} of 100 ppm yielding an Amazonian volcanic degassing flux $F_{volcanic,A}$ of 2×10^{-4} m GEL Myr^{-1} (Table S1). In comparison, the assumed Amazonian escape flux of 5×10^{26} H atoms s^{-1} is

equivalent to the loss of 1.6 x 10^{-3} m GEL Myr^{-1}; the loss rate greater than degassing rate results in slight increases to the D/H composition of the exchangeable reservoir during the Amazonian (Fig. 7.2 and Fig. 7.3).

S6. D/H composition of volcanic gas

We assume that the D/H composition of the Martian mantle dictates the D/H of outgassed waters and is constrained by measuring the D/H composition of water-containing phases, e.g., melt inclusions, glasses, apatites, amphiboles, and biotites, in Martian meteorites. Previous studies have used the lowest measured D/H composition to represent the mantle/igneous end-member of a D/H mixing line, recording exchange between multiple D/H reservoirs (Leshin et al., 2000; Usui et al., 2012; Barnes et al., 2020). These analyses provide an upper bound on the D/H composition of the mantle (R_{mantle}), yielding a large range of possible D/H values from ~0.8-2 × SMOW for the mantle (Fig. S1, Table S1), which we include as lower and upper bounds in our model. We adopt the result of D/H = 1.275 × SMOW from melt inclusions within shergottites (Usui et al., 2012) as a representative value for the mantle and a middle-case scenario in our preferred model.

We do not model fractionation of D/H compositions in outgassed water compared to the initial source nor any fractionation dependency on the redox state of the melt. Fractionation between water vapor and water in melts is relatively small (tens of permille or maximally up to 100s of permille depending on redox conditions (Chacko et al., 2001; Dobson et al., 1989; Sarafian et al., 2017). Compared to the observed isotopic variability within Martian meteorites, these fractionations are negligible for our simulations. Limited retention of water in any crystallizing hydrous mineral phases leads us to assume that most water outgases. This minimizes the effect of any such fractionations if Rayleigh distillation is complete as the accumulated gas will have a D/H composition similar to the initial composition of the melt (Sarafian et al., 2017). Assimilation of hydrated minerals or subsurface water within crust that formed prior to the melting event or partial H$_2$O outgassing within the crust rather than full outgassing of the vapor to the atmosphere may have occurred. This crust could alter the D/H composition of the melt towards the crustal "intermediate" D/H composition (2-3 × SMOW), which has been proposed based on meteorite measurements (Usui et al., 2015; Liu et al., 2018; Barnes et al., 2020). However, there is no evidence that pluton formation and melting of pre-existing crust was a widespread phenomenon (Day et al., 2018; Baratoux et al., 2013). The upper and lower bounds on mantle D/H used in our model encompass the range that would result with moderate assimilation, partial degassing and redox-dependent fractionation, and the typical mantle D/H.

S7. Present-day atmospheric escape

The present-day H escape flux has previously been measured using instruments aboard the Mars Atmosphere and Volatile EvolutioN (MAVEN) spacecraft (1-11 × 10^{26} H atoms s^{-1}; (Jakosky et al., 2018; Stone et al., 2020) and the Ultraviolet and Infrared Atmospheric Spectrometer (SPICAM) aboard the Mars Express spacecraft (10^{25}-10^{27} H atoms s^{-1}; (Chaffin et al., 2014; 2017; Heavens et al., 2018; Bhattacharyya et al., 2015). The range of measured H escape fluxes reflects seasonal changes, related to the variable amounts of water vapor at high-altitude on seasonal time scales (Jakosky et al., 2018; Chaffin et al., 2014; 2017; Stone et al., 2020; Heavens et al., 2018; Bhattacharyya et al., 2015). Dust storms effect this rate, with the escape flux reaching 10^{28} H atoms s^{-1} during the dust storm of MY28 (Stone et al., 2020; Heavens et al., 2018). The enhanced H escape flux due to dust storms is thought to be related to deep convection and enhanced transport of water vapor to high altitudes (Chaffin et al., 2017; Stone et al., 2020; Heavens et al., 2018). The integrated present-day H escape fluxes can only account for the loss of few to tens of m GEL water to space (Jakosky et al., 2018; Chaffin et al., 2014). We adopt the median present-day value of 5 × 10^{26} H atoms s^{-1} for the average H escape flux during the Amazonian ($F_{esc,A}$) (Table S1).

S8. Modelling past Mars H escape fluxes

Most previous studies invoked higher past H escape flux on Mars when considering the high D/H composition of the present-day atmosphere (Fig. S1). However, there have been few attempts to calculate H escape fluxes for Mars during Noachian and Hesperian conditions, presumably due to the large number of unknown parameters. We adapt the chemical transport model KINETICS, (Allen et al., 1981; Nair et al., 1994) for the early Mars atmosphere. The original KINETICS software, including all reactions and rate constants used in this study, are described in original references (Allen et al., 1981; Nair et al., 1994). Additional input and output files from our study can be found in a Caltech online repository (see acknowledgements). We consider the chemistry of 27 species linked by 150 reactions on an altitude grid with 2 km spacing that extends to 240 km. Our model calculates and outputs chemical abundances for each species at every level by computing the chemical production and loss rates at each altitude as well as the diffusive flux between each altitude grid with the 1-D continuity equation:

$$\frac{dn_i}{dt} = P_i - L_i - \frac{\partial \phi_i}{\partial z} \ (S1)$$

where n_i is the number density of species i, φ_i the vertical flux, P_i the chemical production rate, and L_i the chemical loss rate, all evaluated at time t and altitude z. The vertical flux is given by

$$\phi_i = -D_i\left(\frac{\partial n_i}{\partial z} + \frac{n_i}{H_i} + \frac{1-\alpha_i}{T}\frac{\partial T}{\partial z}n\right) - K\left(\frac{\partial n_i}{\partial z} + \frac{n_i}{H_a} + \frac{1}{T}\frac{\partial T}{\partial z}n\right) \quad (S2)$$

where D_i is the species' molecular diffusion coefficient, H_i the species' scale height, H_{atm} the atmospheric scale height, α_i the thermal diffusion parameter, K_{zz} the vertical eddy diffusion coefficient, and T the temperature (Yung & DeMore, 1998). The flux consists of two parts: i) molecular diffusion which can be derived from the molecular theory of ideal gases and ii) eddy transport. We calculate the eddy diffusion coefficient profile using an existing formulation (Ackerman & Marley, 2001). The H escape flux was evaluated using this model with present-day conditions (surface pressure (P_S) of 6.36 mbar, calculated H_2 mixing ratio (M_{H2}) of 3.3×10^{-5}, surface temperature (T_{surf}) of 214 K, H_2O concentration profile from derived from calculated saturation vapor pressure), which yielded $\Phi = 2.9 \times 10^{26}$ H atoms s^{-1} (1.89×10^8 cm^{-2}s^{-1}), validating the model relative to spacecraft measurements *(16-17)*.

We consider 84 atmospheric environments for ancient Mars by varying the surface pressure as 2, 50, 200, 1000, 2000, 5000 mbar; the surface temperature as 190, 210, 240, 270, 300 K; and the mesospheric temperature as 130, 150, 170 K (Table S2). We consider surface temperatures $\geq$ 270 K in the 2 mbar case to be unphysical; a sufficiently strong greenhouse effect would not be provided by such a thin atmosphere and the assumption of saturation vapor pressure for water would exceed the total surface pressure. We use a solar spectrum corresponding to 4.4 Ga (Claire et al., 2012)*.

For each of the 84 environments, we consider three scenarios. In our standard scenario, we fix the H_2O profile to the saturation vapor pressure and allow the H_2 profile to be computed to steady state.. The standard KINETICS model does not include advection. However, a second scenario injects a high-altitude layer of water vapor (60 ppm centered at 100 km), using published atmospheric profiles (Chaffin et al., 2017)*, and functions as a proxy for advection. This scenario is thought to be caused by dust storms at present-day Mars (Stone et al., 2020; Heavens et al., 2018; Chaffin et al., 2017; Bhattacharyya et al., 2015), but may be applicable during periods of strong convection in an earlier atmosphere. A third scenario fixes the water vapor profile to the saturation vapor pressure but fixes the surface H_2 mixing ratio to 10^{-3}. This is about two orders of magnitude larger than the present day H_2 mixing ratio (Allen et al., 1981). However, higher H_2 mixing ratio have been proposed to have been produced via surface processes, such as volcanic outgassing and serpentinization (*e.g.* Wordsworth et al., 2017). For standard and fixed, high surface H_2 scenarios, we calculated steady-state photochemical output, which is typically taken to be from $>10^8$ simulated terrestrial years. We do not consider obliquity cycles, which may affect the steady-state solutions. Because the high-altitude water vapor layer is likely only applicable under transient timescales, we show results after 10^7 seconds (~1 year) as shown in the results of (Chaffin et al., 2017).

The dominant source of hydrogen is photolysis of water (Allen & Yung, 1981; Nair et al., 1994; Yung & DeMore, 1998). In the standard case with water fixed to the saturation vapor pressure, the dominant region for hydrogen production resides near the surface, where water vapor is abundant, but at an altitude sufficiently high that atmospheric extinction of ultraviolet (UV) photons is minimal. In dense atmospheres, escape becomes inefficient as diffusion slows the transport of H_2 to the upper atmosphere. In thin atmospheres, it is easier for hydrogen to diffuse to the exobase, where escape occurs. Hence, under standard conditions, the escape rate is inversely related to the surface pressure (Fig. S3). Atmospheric escape rates increase slightly as the mesospheric temperature is warmed due to the greater thermal energy of H_2 and increased water abundance (Fig. S3). The surface temperature appears less relevant, likely because photolysis is photon-limited at low altitudes and the hydrogen produced is collisionally bound. The mean escape rate appears to decrease at the greatest surface temperatures (Fig. S3), but we attribute this to bias from the six unphysical cases we do not consider. Injecting a high-altitude water layer exposes the water to a greater UV flux, allowing rapid hydrogen production and enhanced escape due to fewer collisions in this less dense region (Fig. S3). Likewise, fixing the surface mixing ratio of H_2 affects the full profile, lofting more to the upper altitudes. The increased presence of high-altitude hydrogen results in an increased escape rate for the denser atmospheres (Fig. S3).

We performed simulations in our D/H model of our entire parameter space, yielding Noachian and Hesperian escape fluxes ranging from 10^{25}-10^{30} H atoms s^{-1}. We find that our D/H model is compatible with a Noachian H escape flux ($F_{esc,N}$) of 10^{25} to 4×10^{29} H atoms s^{-1} and a Hesperian escape flux ($F_{esc,H}$) of 10^{25} to 7×10^{28} H atoms s^{-1} (Table S1, Fig. S3). If past escape fluxes were higher than the ranges presented in Fig. S2, the average of model simulations would produce much higher present-day D/H values than $10 \times$ SMOW and the full span of model simulation results will vary over 10,000s of ‰, which are not observed for Mars. Lower H escape fluxes than 10^{25} H atoms s^{-1} are improbable, based on higher measured modern escape rates, the KINETICS results, and cannot reproduce modern D/H compositions $>5 \times$ SMOW.

S9. D/H fractionation associated with atmospheric escape

H escape causes major fractionation of the atmospheric D/H as hydrogen preferentially escapes compared to deuterium. This fractionation factor, $\propto_{escape}$, can be calculated as

$$\propto_{escape} = \frac{\varphi_D/\varphi_H}{[HDO]_s/2[H_2O]_s} \quad (S3)$$

where, φ_H and φ_D are the escape flux of H and D and $[HDO]_s$ and $[H_2O]_s$ are the concentrations of HDO and H_2O at the surface approximating the total amounts of hydrogen and deuterium in the atmosphere (derivations in Cangi et al., 2020; Krasnopolsky et al., 2000; Yung et al., 1988). $\propto_{escape}$ describes the relative efficiency of D versus H escape, where H_2 and HD are the dominant escaping species. H_2 primarily sources from H_2O in the Martian atmosphere. Hence, the efficiency of H escape can be written as the H escape flux as a function of the surface concentration of H_2O (and equivalent for the deuterated species). The factor of two in eq S3 derives from a single H_2O molecule sourcing two H atoms, but HDO sourcing only one D atom (derivations in Cangi et al., 2020; Krasnopolsky et al., 2000; Yung et al., 1988). These escape fluxes and concentrations have previously been modelled through photochemistry with a range of results: $\propto_{escape}$ = 0.32 (Yung et al., 1988); 0.016 or 0.135 (Krasnopolsky, 2000); and ~0.002 (Cangi et al., 2020) using revised photochemical models (Chaffin et al., 2017). Hence, the range of $\propto_{escape}$ we consider is 0.002-0.32 (Table S1).

S10. Step-wise Rayleigh distillation numerical modelling equations

D/H fractionations related to clay formation and atmospheric escape were evaluated assuming Rayleigh distillation.

$$R = R_0 \times \left(\frac{X}{X_0}\right)^{\propto - 1} (S4)$$

where R is the isotope ratio of the residual reservoir, R_0 is the initial isotope ratio, X is the residual amount of the light isotope, X_0 is its initial amount, and α is the fractionation factor. Our model evaluates the isotope ratio at each 10-Myr time step i through eq. S5-S10. First, the size of the exchangeable reservoir X_{ex} at time step i (t_i), where t_0 is the starting point, is evaluated by integrating the time-dependent volcanic degassing rate ($F_{volcanic}$), H escape flux (F_{esc}), and crustal hydration rate (F_{crust}) and accounting for the initial reservoir size ($X_{ex,0}$) (eq S5).

$$X_{ex_i} = X_{ex,0} + \int_{t_0}^{t_i} F_{volcanic,t_i} - \int_{t_0}^{t_i} F_{esc} - \int_{t_0}^{t_i} F_{crust} (S5)$$

Second, the D/H composition of the exchangeable reservoir (R_{ex}) is corrected (R_{mix}) to account for the contribution of depleted volcanic gas (R_{mantle}) by linearly mixing with the composition of the exchangeable reservoir (R_{ex}) in eq S6.

$$R_{mix_i} = \frac{\int_{t_{i-1}}^{t_i} F_{volcanic,t_i}}{X_{ex_i}} \times R_{mantle} + \left(1 - \frac{\int_{t_{i-1}}^{t_i} F_{volcanic,t_i}}{X_{ex_i}}\right) \times R_{ex_i} \ (S6)$$

Third, fractionation of the exchangeable reservoir related to crustal hydration is then calculated using eq S4 by integrating the rate of crustal hydration (F_{crust}) for the next 10-Myr time step.

$$R_{res_i} = R_{mix_i} \times f_{res_i}{}^{\propto_{smectite-H_2O}-1} \ (S7)$$

$$\text{where } f_{res_i} = \left(1 - \frac{\int_{t_i}^{t_{i+1}} F_{crust}}{X_{ex_i}}\right) \ (S8)$$

We then use mass balance to determine the relationship between the isotopic composition of the exchangeable reservoir and the reservoir of crustal hydration at the time step.

$$R_{mix_i} = R_{crust_i} \times \left(1 - f_{res_i}\right) + R_{res_i} \times f_{res_i} \ (S9)$$

Rearrangement of eq. S9 provides the isotope composition of the crustal reservoir (R_{crust}) formed at the evaluated time step.

$$R_{crust_i} = \frac{R_{mix_i} - R_{res_i} \times f_{res_i}}{\left(1 - f_{res_i}\right)} \ (S10)$$

Last, the fractionation related to atmospheric escape is modelled through Rayleigh distillation and calculated by integrating the H escape flux for the current 10-Myr time step.

$$R_{ex_{i+1}} = R_{res_i} \times \left(1 - \frac{\int_{t_i}^{t_{i+1}} F_{esc}}{f_{res_i} \times X_{ex_i}}\right)^{\propto_{escape}-1} \ (S11)$$

S11 Modelled 3-period time evolution

The model is divided into 3 intervals. Interval 1 ($\sim$ 3.7 - 4.1 Ga) simulates the Noachian when the H escape flux ($F_{esc,N}$) was high and the rate of crustal hydration ($F_{crust,N}$) was high (Fig. 7.1, Table S1). Interval 2 ($\sim$ 3.0 - 3.7 Ga) simulates the Hesperian when the H escape flux may have decreased compared to the Noachian ($F_{esc,H}$) and rate of crustal hydration ($F_{crust,H}$) was lower (Fig. 7.1, Table S1). Interval 3 simulates the Amazonian (now to $\sim$3.0 Ga) where we assume negligible active crustal hydration processes (Fig. 7.1, Table S1). During the Amazonian interval, we ignore eq. S7-S11 that account for crustal hydration and calculate the D/H composition of the exchangeable reservoir following eq. S12.

$$R_{ex_{i+1}} = R_{mix_i} \times \left(1 - \frac{\int_{t_i}^{t_{i+1}} F_{esc,A}}{X_{ex_i}}\right)^{\alpha_{escape}-1} \quad (S12)$$

The absolute age of the Noachian/Hesperian boundary (t_{N-H}) and the Hesperian/Amazonian boundary (t_{H-A}), when crustal hydration ceased, are uncertain. Estimates of t_{N-H} vary from 3.7 to 3.5 Ga (Hartmann, 2005); therefore we investigate t_{N-H} of 3.7 Ga and 3.5 Ga (Fig. 7.3, Table S1). Estimates of the Hesperian/Amazonian boundary vary from 3.2 to 2 Ga and the Early Amazonian interval may have occurred between 3.2 and 1 Ga (Hartmann, 2005). We adapt t_{H-A} of 3 Ga to represent a short Hesperian interval within the uncertainty (Hartmann, 2005) (Fig. 7.3, Table S1). We also adapt t_{H-A} of 1.5 Ga to encompass the crater chronology uncertainties and hydrated mineralogy observed in the early Amazonian (Martin et al., 2017) (Fig. 7.3, Table S1).

Supplementary Text

S12. Oxygen sinks

Crustal hydration can be an oxygen sink as well as a source of liberated H_2 because both H_2O and OH are incorporated into a mineral structure during hydrated mineral formation. There are a multitude of reactions in which the formation of minerals can liberate H_2 that could have occurred on ancient Mars. The most well-studied of these include serpentinization and the formation of magnetite. Serpentinization reactions alone have a large possible range of ratios of H_2O incorporated into the crust and H_2 released (H_2O_{in}/H_{2out}) that may vary from $\sim 4 - 43$ (Chassefiere et al., 2013). During magnetite formation, often coupled to phyllosilicate formation, H_2O_{in}/H_{2out} may be as small as 2 (Tosca et al., 2018). Clay minerals, such as smectites that dominate the Martian crustal reservoir, may also release H_2 due to incorporation of OH-groups. In contrast, minerals such as hydrated sulfates and hydrated silica sequester only H_2O, without releasing any H_2.

We consider this effect on the oxygen and hydrogen balance in our model simulations. In the minimum escape cases (Fig. 7.4 and Fig. S4-S6) in which the crustal hydration sink dominates over the atmospheric escape sink, the liberation of H_2 would either balance H escape or cause the accumulation of H_2 in the atmosphere. However, any such accumulation of H_2 in the atmosphere would have increased the H escape flux calculated in the KINETICS simulations (Fig. S3), suggesting that the accumulation of H in the atmosphere could be short-lived and readily removed by atmospheric escape. In this scenario many of our simulations do not require an additional oxygen sink in addition to crustal hydration. H_2 present in the atmosphere for a short period after release may provide greenhouse warming (e.g. Wordsworth et al.,

2017).

In contrast, our simulations, where the atmospheric escape sink dominates over the crustal hydration sink, would likely need additional oxygen sinks (Fig. 7.4 and Fig. S4-S6). Atmospheric escape of oxygen can account for between 18-58 m GEL of (1 O in each H_2O) (Kurokawa et al., 2014; Lammer et al., 2003; Jakosky et al., 2018). In simulations, where the H escape flux is larger than both the oxygen escape flux by a factor of 2 and the flux of H liberated through crustal hydration, there must be another sink to account for oxygen liberated by water loss. One possibility is the co-occurrence of crustal oxidation with crustal hydration, in particular oxidation of Fe(II) and S_2 in igneous rocks. Oxidation of FeS minerals in the upper crust can account for the oxygen loss of ~10 m GEL of water (Chassefiere & Leblanc, 2011). Oxidation of volcanically degassed H_2S may have consumed oxygen up to 10-15 m GEL of water (Chassefiere & Leblanc, 2011). In addition, (Heard & Kite, 2020) proposed that oxidation of Fe(II), SO_2, and H_2S within young (<3.5 Ga) sedimentary deposits could account for oxygen loss of 5 m GEL of water.

However, the volumetrically dominant basaltic Martian crust consists of ~20 wt% total iron oxide (FeO_T), including both Fe(II) and Fe(III) components, based on rover and orbital measurements (Taylor et al., 2010; McSween et al., 2006; Morris et al., 2006; Ehlmann et al., 2017). Ratios of Fe(III) to total iron (Fe^{3+}/Fe_T) measured in situ are < 0.2-0.3 for basalts with little alternation on Mars and 0.6-0.9 for highly altered basalts (120). Assuming oxidation of 10-60% of all Fe(II) to Fe(III), requiring 0.5 mol O per mol Fe over the entirety of the crustal reservoir (5-10 km global thickness), the upper and lower bounds of the Fe oxidation oxygen sink are 30-380 m GEL. The total oxygen sink could therefore range between 18-470 m GEL; the minimum is set by the minimum amount of escaped oxygen and the maximum is set by combined maximum oxygen escape and maximum crustal oxidation. In our modeled maximum escape case where the initial reservoir size is 1300 m GEL (Fig. S4-S6), 530 m GEL of H_2O (1 H_2 molecule per H_2O) is lost through atmospheric escape and 740 m GEL of water is lost through crustal hydration. If we assumed an approximate H_2O_{in}/H_{2out} of ~7 (Chassefiere et al., 2013) during crustal hydration, this would cause the liberation of ~100 m GEL of H_2. To balance the integrated H escape sink, a 410 m GEL oxygen sink is then required, within the estimated range for the oxygen sink.

Volcanic degassing could also have been a source of H_2. Simulations at low pressures found that H_2:H_2O ratios of volcanic gas could be approximately between 1:2 and 1:1 for a redox buffer at QFM-2 (Gaillard & Scaillet, 2009). If conditions were more reduced, the H_2:H_2O ratios of volcanic gas may have been >1. When considering our 4 volcanic degassing models we use (Fig. 7.3), this could have been an additional integrated H_2 source of approximately 5-120 m GEL with H_2-equivalent water over Martian history. In cases of high volcanic H_2 contribution, as with significant release of crustal H_2 from crustal hydration, the increased atmospheric H_2 levels would cause an increase in the H escape flux. This flux

would not require balancing by an oxygen sink, thus lowering the upper bound on the O_2 sink if H_2:H_2O were high in volcanic degassing. However, as the H escape flux increases it would consequently reduce atmospheric H_2 levels, ultimately causing the atmosphere to return to the loss rate before the H_2 outgassing.
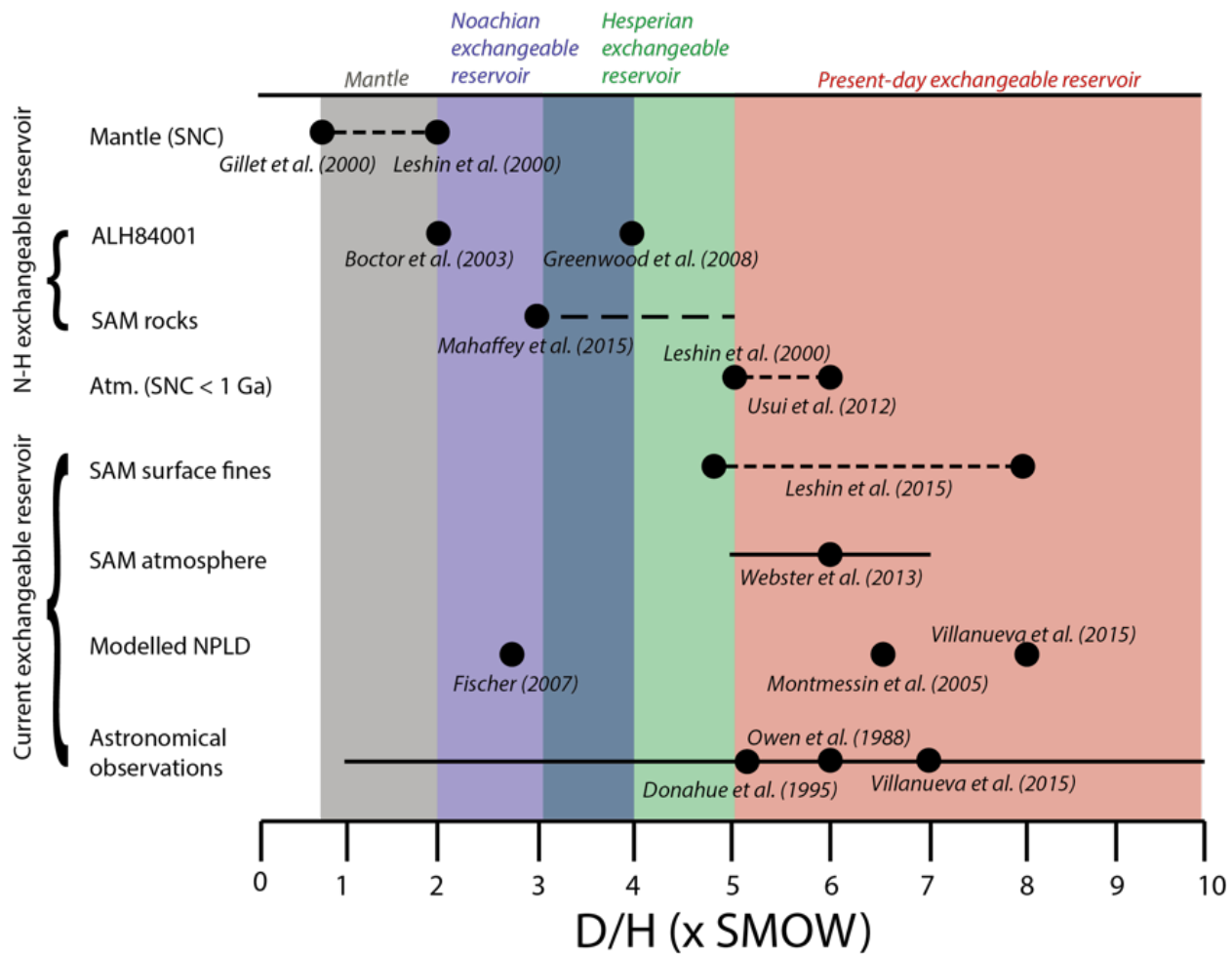
Fig. S1. Previous measurements of Noachian, Hesperian, and current D/H compositions of the exchangeable reservoir. We use these D/H data to provide ranges for the Noachian exchangeable reservoir at 4.1 Ga (blue shading), Hesperian exchangeable reservoir (green shading), the current exchangeable reservoir (red shading), and the mantle (grey shading). Black points show D/H values from previous studies with the references given either beneath or above the point. Solid black lines for SAM atmosphere shows standard error of mean as given in Webster et al., 2013. Solid black lines for SAM surface fines shows full data range given in Leshin et al., 2013 while the dot shows the mean of these data. Solid black lines for astronomical observations shows the full range of data given in Villanueva et al., 2015. Dashed black lines indicate multiple measurements within the range of values. Dashed black line for SAM rocks show the range of SAM measurements of high temperature combustion experiments of Hesperian rocks as found on the PDS.

Table S1. Parameter ranges used in simulations of D/H model. This is a summary compilation of all the observational constraints on parameter ranges explored within the D/H model of this study. More details with respect to selected value ranges are given in Materials and Methods sections S1-S11.

| Variable	Meaning	Value Range	Units	Reasoning
$R_{ex,0}$	Initial D/H of exchangeable reservoir	2-4 × SMOW	N/A	D/H measurements of ALH84001 (Boctor et al., 2003; Greenwood et al., 2008)
$R_{ex,end}$	D/H of present-day exchangeable reservoir	5-10 × SMOW	N/A	Compilation of astronomical, meteorite, and SAM data (Fig. S1) (Donahue, 1995; Webster et al., 2013; Villanueva et al., 2015; Owen et al., 1988; Leshin et al., 2013; Hu et al., 2014; Fischer, 2007; Montmessin et al., 2004)
R_{mantle}	D/H of mantle	0.8-2 × SMOW	N/A	D/H measurements of various meteorites (Gillet et al., 2002; Leshin, 2000; Usui et al., 2012; Mane et al., 2016)
$\alpha_{smectite-H2O}$	D/H fractionation factor between smectite and water	0.95	N/A	Literary review of geochemical experiments (Table S2)
α_{escape}	D/H fractionation factor of atmospheric escape	0.002-0.32	N/A	Compilation of photochemical model results (Cangi et al., 2020; Krasnopolsky et al., 2000; Yung et al., 1988)
$X_{ex,end}$	Present-day size of exchangeable reservoir	20-40	m GEL	Remote sensing evidence (Zuber et al., 1998; Plaut et al., 2007; Christensen, 2006; Nerozzi & Holt, 2019; Whitten & Campbell, 2018; Mustard et al., 2001; Dundas et al., 2018; Bramson et al., 2017; Kralsson et al., 2015)
$F_{crust,N}$	Rate of water drawdown by crustal hydration during the Noachian	0.25-2.25	m GEL Myr^{-1}	Remote sensing evidence (Mustard, 2019; Murchie et al., 2009; Sun & Milliken, 2015; Vaniman et al., 2014; Sutter et al,. 2017; Thomas et al., 2020; Audouard et al., 2014; Maurixe et al., 2011; Humayun et al., 2013; Wenicke & Jakosky, 2019; Chassefiere & Leblanc, 2011; Kurokawa et al., 2016; Grimm et al., 2017; Carter et al., 2013)
$F_{crust,H}$	Rate of water drawdown by clay formation during the Hesperian	0.014-0.14	m GEL Myr^{-1}	Remote sensing evidence (Mustard, 2019; Murchie et al., 2009; Sun & Milliken, 2015; Vaniman et al., 2014; Sutter et al,. 2017; Thomas et al., 2020; Audouard et al., 2014; Maurixe et al., 2011; Humayun et al., 2013; Wenicke & Jakosky, 2019; Chassefiere & Leblanc, 2011; Kurokawa et al., 2016; Grimm et al., 2017; Carter et al., 2013)
f_{mantle}	Water content of mantle	100-1000	ppm	(Grott et al., 2011; Lammer et al., 2013; Grott et al,. 2013; McSween & Harvey, 1993)
$F_{volcanic}$	Rate of volcanic degassing of H$_2$O	Time-dependent fluxes, see text	m GEL Myr^{-1}	Compiling thermal evolution models (Grott et al., 2011; Hauck & Phillips, 2002; Greeley & Schneid, 1991; Grott et al,. 2013; Morschhauser et al., 2011; McSween & Harvey, 1993; Fraeman & Korenaga, 2010)
$F_{volcanic,A}$	Rate of volcanic production after 2.5 Ga	2×10^{-4}	m GEL Myr^{-1}	Remote sensing evidence (Greeley & Schneid, 1991; Carr & Head, 2010)
$F_{esc,A}$	Present-day H escape flux	1-11×10^{26}	H atoms s^{-1}	Measured by MAVEN/Mars Express (Jakosky et al., 2018; Chaffin et al., 2014)
$F_{esc,N}$	H escape flux during the Noachian	5×10^{26}-4×10^{29}	H atoms s^{-1}	Modelled in this study (Fig. S2-S3)
$F_{esc,H}$	H escape flux during the Hesperian	5×10^{26}-5×10^{28}	H atoms s^{-1}	Modelled in this study (Fig. S2-S3)
t_{N-A}	End of deep, "Noachian" crustal alteration	3.7 - 3.5	Ga	Uncertainty regarding crater statistics (Hartmann, 2005)
t_{H-A}	End of shallow , "Hesperian" crustal alteration	3 - 1.5	Ga	Orbital observations of Hesperian and Amazonian hydrated mineralogy and uncertainty regarding crater statistics (Martin et al., 2012; Hartmann, 2005)
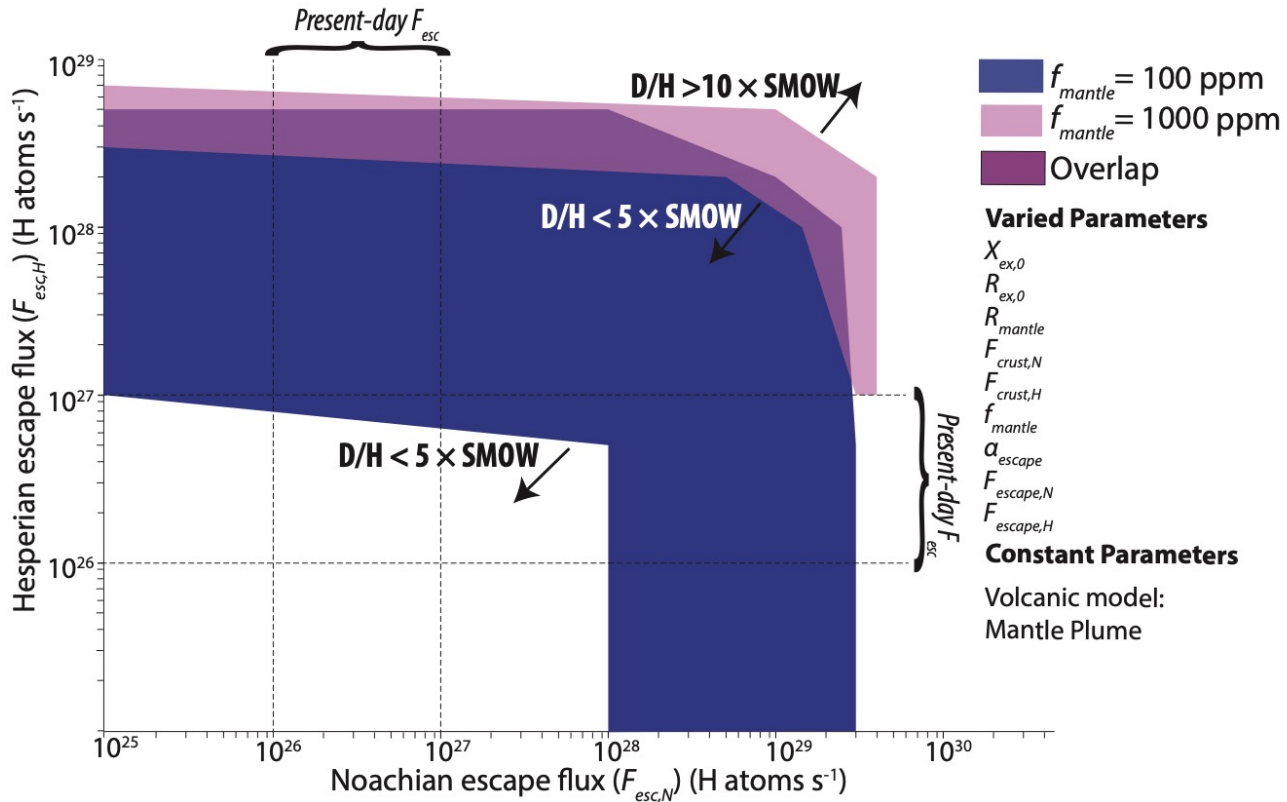
Fig. S2. Hesperian and Noachian escape fluxes in our simulations. Hesperian and Noachian H escape fluxes for the present-day exchangeable reservoir ($R_{ex,end}$) evaluated at the initial D/H compositions ($R_{ex,0}$) between $2 \times$ SMOW and $4 \times$ SMOW and run for the 2 Mantle Plume models. Parameter combinations were accepted when present day D/H was between 5-10 $\times$ SMOW, shown where f_{mantle} was assumed 100 ppm (dark blue region) and 1000 ppm (fuchsia region) (Fig. 7.3) as well as their overlap (purple region). The range of present-day escape fluxes of $\sim 10^{26}$-10^{27} H atoms s^{-1} is shown with dashed vertical lines for comparison. Some Noachian and Hesperian escape flux combinations that are similar to present-day escape fluxes satisfy the 5-10 $\times$ SMOW convergence condition for the Mantle Plume, f_{mantle} = 100 ppm volcanic degassing model.

Table S2. Parameter ranges used in the KINETICS simulations.

| Variable	Meaning	Value	Units	Reasoning
P_s	Surface pressure	0.002 – 5 with intermediate cases of 0.05, 0.2, and 1, 2 bar	Bar	Minimum level based on current pressure (Haberle, 2015) Intermediate cases consider proposed pressures for early Mars (Hu et al., 2015) Maximum level considers an extreme case
T_s	Surface temperature	190-300	K	Minimum level based on current average temperature (Clancy et al., 2000) Maximum level based on room temperature
T_{meso}	Temperature of mesosphere	130-170	K	Extrapolation from temperature structure of atmosphere today (Nair et al., 1994; Seiff, 1987)
F_{EUV}	Solar extreme ultraviolet flux	N/A	N/A	Solar spectrum by (Claire et al., 2012)
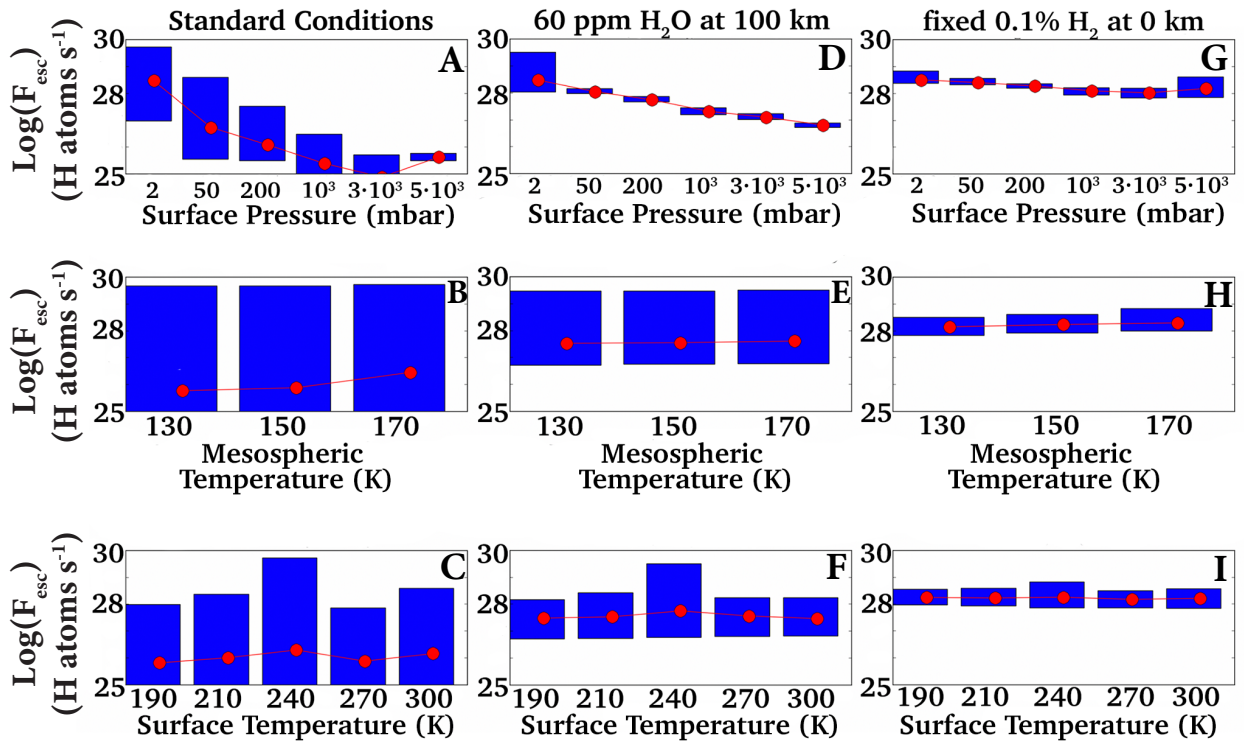
**Fig. S3.** Results of the KINETICS simulations. Mean global escape rates (red points) in units of H atoms s⁻¹, with the full range (blue bars) spanning from the minimum to maximum escape rates for ranges of surface pressure, mesospheric temperature, surface temperature. Columns show results from the 3 considered scenarios: (A-C) standard ancient Mars (see text), (D-F) high altitude water injection, and (G-I) fixed high surface H_2 mixing ratio of 10^{-3}.

Table S3. Previous experimental measurements of the D/H fractionation between smectite and water ($\alpha_{smectite-H_2O}$).

| Mineral	Evaluated Expression	$\alpha_{smectite-H_2O}$ at 25°C	Reference
Smectite/illite	$1000 \ln(\alpha) = \dfrac{-45.3 * 10^3}{T} + 94.7$	0.94	(Capuano et al., 1993; Hyeong & Capuano, 2004)
Smectite	$1000 \ln(\alpha) = -65 \ to -10$	0.94-0.99	(Sheppard & Gilg, 1996)
Al-smectite/Fe-smectite	$1000 \ln(\alpha) = -20 \ to -90$	0.91-0.98	(Sheppard & Gilg, 1996)
Smectite/illite	$1000 \ln(\alpha) = \dfrac{-19.6 * 10^3}{T} + 25$	0.94	(Yeh et al., 1980)
Montmorillonite/kaolinite	$\alpha = 0.97$	0.97	(Lawrence & Taylor, 1972)
Montmorillonite	$\alpha = 0.94$	0.94	(Savin & Epstein, 1970)
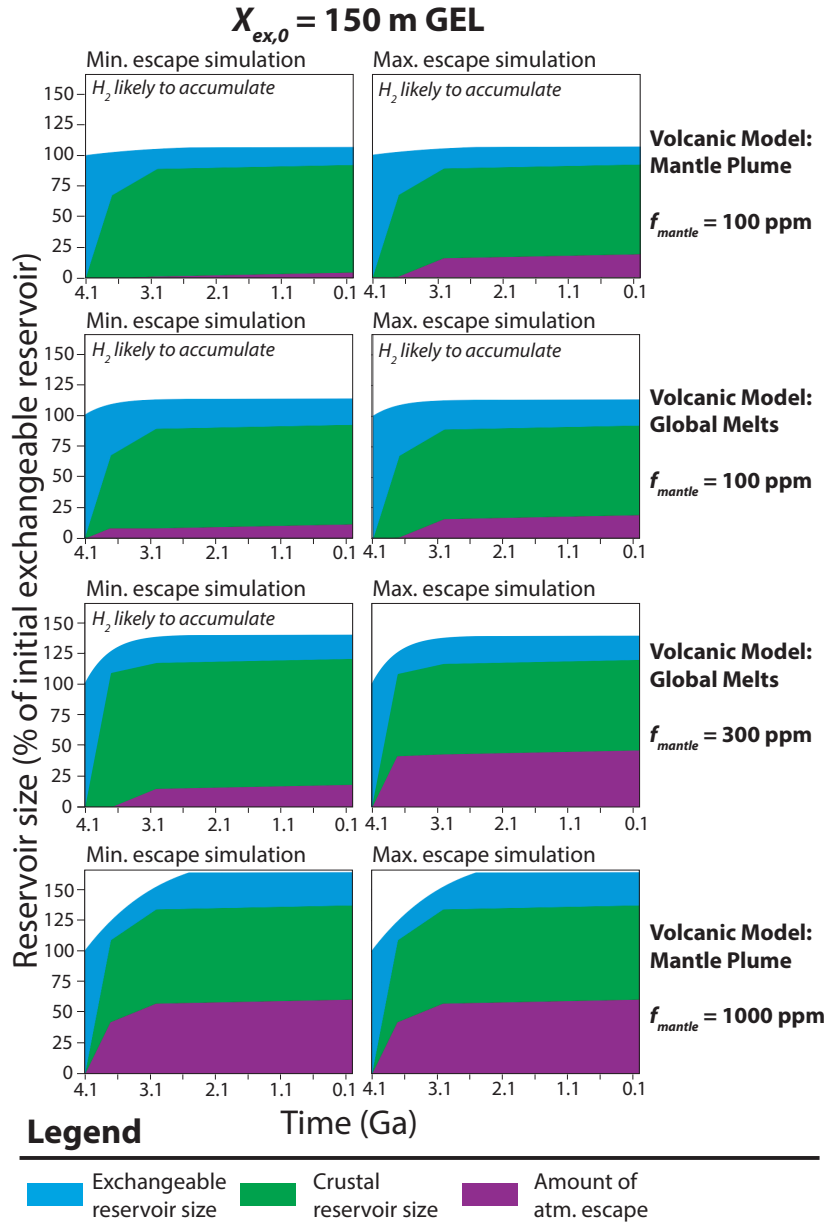
Fig. S4. Cumulative percentage of water in the exchangeable reservoir, crustal reservoir, and escaped water for the full range of model parameters part 1. Same as Fig. 7.4.C-D but showing results from a different set of parameter combinations. The min. and max. escape simulations from each set of simulations are shown beside each other. Each row of min. and max. escape simulations are organized according to assumptions regarding volcanic degassing model. The initial exchangeable reservoir ($X_{ex,0}$) size was set to be 150 m GEL at 4.1 Ga for all simulations in this figure. All other parameters were varied. In cases where the crustal hydration sink strongly dominates over the atmospheric escape sink, H_2 is likely to accumulate in the exchangeable reservoir. The simulations where H_2 are likely to accumulate have been marked with a sentence inside the figure panel.
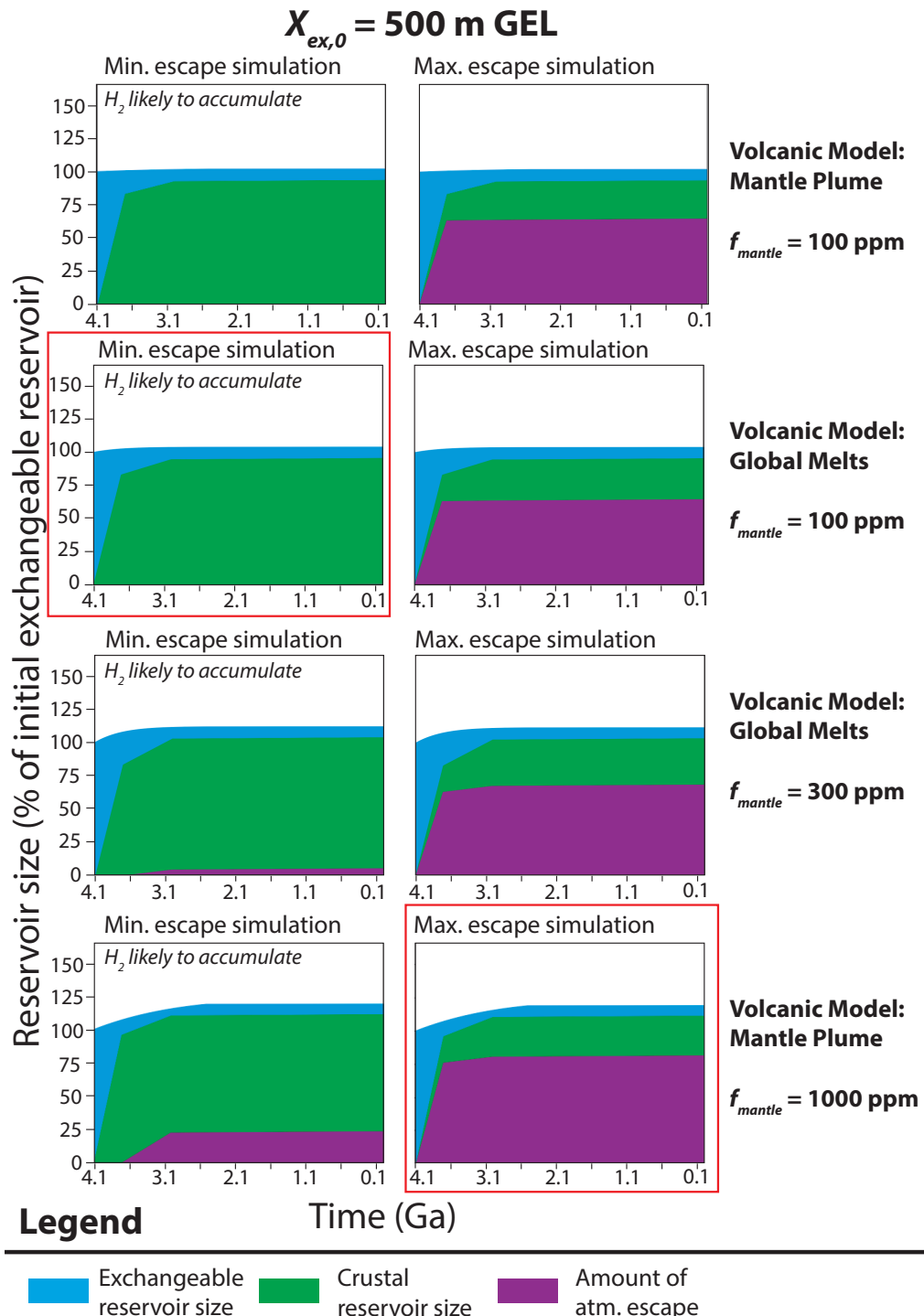
Fig. S5. Cumulative percentage of water in the exchangeable reservoir, crustal reservoir, and escaped water for the full range of model parameters part 2. Same as Fig. S4 but the initial exchangeable reservoir ($X_{ex,0}$) size was set to be 500 m GEL at 4.1 Ga for all simulations in this figure. Plots outlined in red are the minimum and maximum endmembers of the entire examined solution space and are the ones shown in Fig. 7.4.C-D.
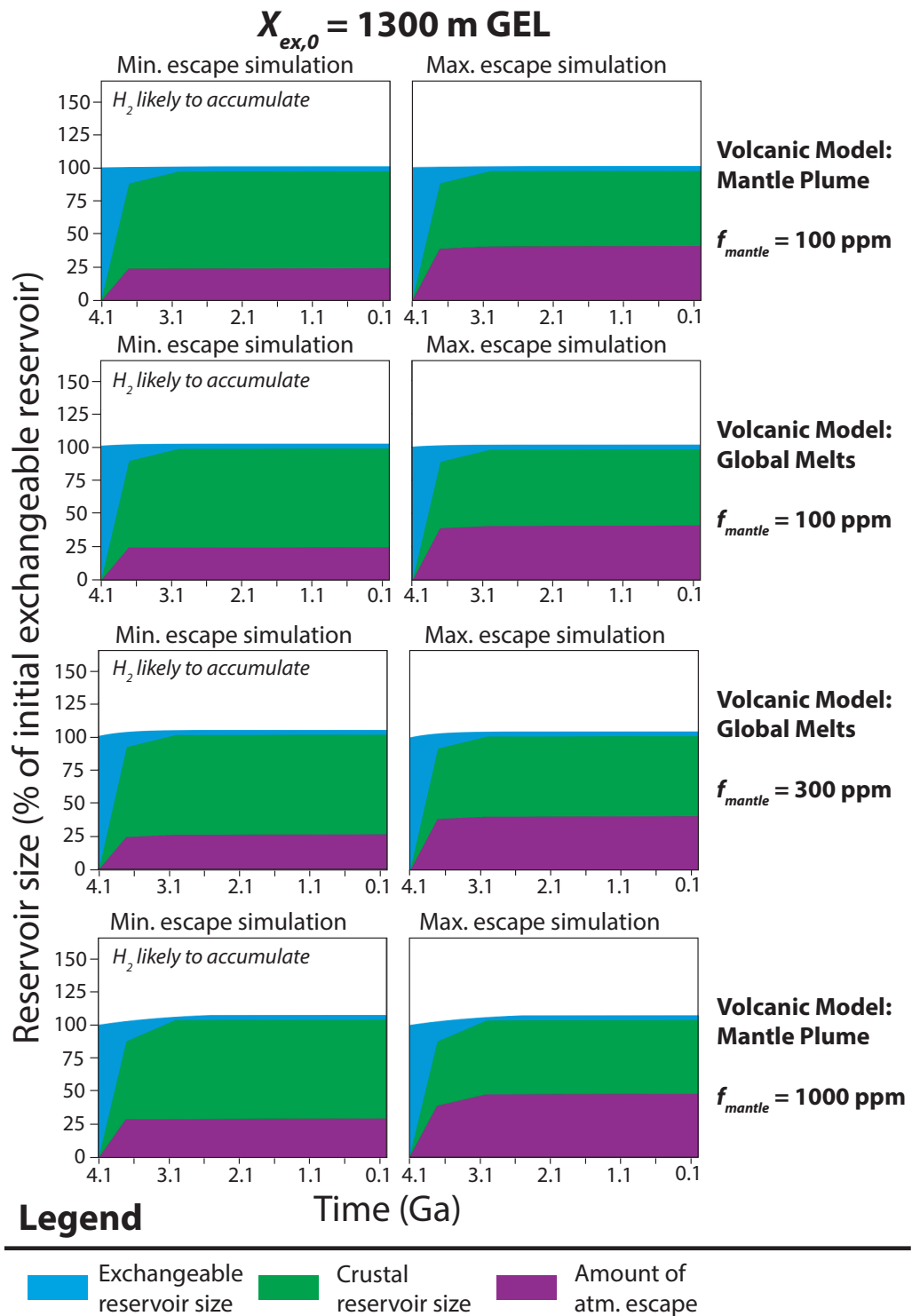
Fig. S6. Cumulative percentage of water in the exchangeable reservoir, crustal reservoir, and escaped water for the full range of model parameters part 3. Same as Fig. S4 but the initial exchangeable reservoir ($X_{ex,0}$) size was set to be 1300 m GEL at 4.1 Ga for all simulations in this figure.